





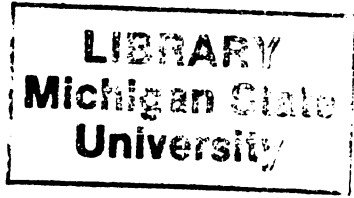
This is to certify that the  
dissertation entitled  
Electrical Properties and Physical Characteristics  
of Polycrystalline Diamond Films Deposited in A  
Microwave plasma Disk Reactor,  
presented by

Bohr-ran Huang

has been accepted towards fulfillment  
of the requirements for  
Ph.D degree in Electrical Engineering

Donnie K Rembar  
Major professor

Date Jan 8, 1992



PLACE IN RETURN BOX to remove this checkout from your record.  
TO AVOID FINES return on or before date due.

DATE DUE	DATE DUE	DATE DUE
<del>NOV 12 1998</del>	_____	_____
AUG 01 1999	_____	_____
SEP 22 2000	_____	_____
SEP 23 03	_____	_____
OCT 07 2005	_____	_____
_____	_____	_____
_____	_____	_____
_____	_____	_____
_____	_____	_____

MSU is An Affirmative Action/Equal Opportunity Institution

c:\circ\datedue.pm3-p.1

**ELECTRICAL PROPERTIES AND PHYSICAL  
CHARACTERISTICS OF POLYCRYSTALLINE  
DIAMOND FILMS DEPOSITED IN A MICROWAVE  
PLASMA DISK REACTOR**

By

*Bohr-ran Huang*

A DISSERTATION

Submitted to  
Michigan State University  
in partial fulfillment of the requirements  
for the degree of

DOCTOR OF PHILOSOPHY

Department of Electrical Engineering

1992

692-3781

Copyright by  
Bohr-ran Huang  
1992

**ABSTRACT**

**ELECTRICAL PROPERTIES AND PHYSICAL  
CHARACTERISTICS OF POLYCRYSTALLINE  
DIAMOND FILMS DEPOSITED IN A MICROWAVE  
PLASMA DISK REACTOR**

By

*Bohr-ran Huang*

Diamond possesses many excellent properties which motivate investigations of the potential of diamond for a wide range of electronic, mechanical, and optical applications. This work experimentally investigates techniques for high quality diamond synthesis and develops means for electrical and physical characterization of the films. The films are deposited by plasma assisted chemical vapor deposition using a methane/hydrogen plasma in a microwave plasma disk reactor system.

Both a diamond paste nucleation method and a diamond powder nucleation method are studied in this research. Although as indicated by Raman spectroscopy both methods produced similar quality diamond films, the powder nucleation method produced fine grain, sub-micron sized crystallite, films whereas the paste nucleation method produced large grain, several-micrometer size crystallite, films. This difference is due to a higher density of surface nucleation sites in the powder polished films. Grain size could also be varied by using microwave power, pressure, and the methane/hydrogen ratio as processing variables, however, the effect is smaller than

the differences caused by the two nucleation methods.

For electrical characterization, a new sample preparation method was developed in cooperation with the University of Wuppertal which allows metallic access to both sides of the diamond film. Using this technique, the properties of a variety of metal/diamond contacts were investigated. Although films were not intentionally doped, thermo-power measurements show all films to be p-type with activation energies between 0.1 and 0.5 eV.

For powder polished films, all metallic contacts were ohmic. These samples were used to explore the high electric field properties of diamond. It was discovered that for fields larger than approximately  $1 \times 10^5$  V/cm the electrical properties are dominated by defects, where defect is used generically for either an impurity or a structural defect. For low electric fields, the electrical conductivity was constant which resulted in ohmic behavior. But for high fields, the conductivity was field activated according to Poole's law. This behavior was modeled as being due to ionizable defects and indicates that there is approximately one ionizable defect per 10,000 host atoms. As a result of such defects, the breakdown field for these films was somewhat less than  $1 \times 10^6$  V/cm. A large concentration of defects is compatible with the observation of ohmic contact behavior regardless of metallic work function since contact space charge layers would be sufficiently thin to allow tunneling.

Non-ohmic, Schottky barrier contacts were achievable on the paste polished films. For Al/diamond/silicon structures diode characteristics were observed. These I-V characteristics were modeled as an ideal Schottky barrier diode in series with bulk diamond, for which the property of the bulk diamond follows an  $I \propto V^m$  relationship, indicative of space charge limited current in an insulating material. The rectifying behavior was determined to be at the Al/diamond surface rather than the diamond/silicon surface. The best rectification ratios were  $2 \times 10^5$ .

To my parents  
Chien-Ching, Tsui-Kuan C. Huang  
and my wife  
Pey-Nan C. Huang

## **ACKNOWLEDGEMENTS**

The author would like to thank Dr. Donnie K. Reinhard for his guidance , support, and encouragement. Special thanks is extended to Dr. Jes Asmussen Jr. and Dr. Timothy Grotjohn for their valuable discussions, and Dr. Peter A. Schroeder for his comments. Additional thanks is given to Dr. Engemann and Mr. Hans Keller in Wuppertal University (Germany) for their help on fabricating back-etched diamond samples, Dr. Kevin Gray of Norton Company and Dr. Mark Holtz in the Physics department of Michigan State University for providing the Raman spectra, and Dr. Kevin Hook in the Composite and Structural Materials Center of Michigan State University for performing the XPS analysis.

This work was supported in part by grants from Wavemat, Corp. and the Michigan Research Excellence Fund.

# TABLE OF CONTENTS

<b>LIST OF TABLES</b>	<b>x</b>
<b>LIST OF FIGURES</b>	<b>xi</b>
<b>1 Introduction</b>	<b>1</b>
1.1 Motivation for Diamond Research . . . . .	1
1.2 Research Objectives . . . . .	3
1.3 Dissertation Outline . . . . .	4
<b>2 Synthetic Diamond : Background Review</b>	<b>5</b>
2.1 Introduction . . . . .	5
2.2 Brief History of Diamond Synthesis . . . . .	6
2.2.1 Historical Background . . . . .	6
2.2.2 Growth Mechanism of Diamond Films . . . . .	13
2.3 Review of Diamond Film Technologies . . . . .	17
2.3.1 Hot Filament Chemical Vapor Deposition Techniques . . . . .	18
2.3.2 Plasma Assisted Chemical Vapor Deposition Techniques . . . . .	20
2.3.3 Other Deposition Methods . . . . .	24
2.3.4 Nucleation Methods. . . . .	24
2.4 Physical Attributes of Diamond . . . . .	27
2.4.1 Comparison of Bulk and Film Material Properties . . . . .	27
2.4.2 Comparison of Semiconductor Properties . . . . .	30
2.5 Review of Diamond Diodes and Transistors . . . . .	33
<b>3 Film Deposition and Sample Preparation</b>	<b>38</b>
3.1 Introduction . . . . .	38
3.2 The MPDR System . . . . .	38
3.2.1 The Microwave Cavity . . . . .	38
3.2.2 The Deposition System . . . . .	41
3.3 The Nucleation Methods . . . . .	45

3.4	Diamond Film Deposition . . . . .	48
3.4.1	Operation of The System . . . . .	48
3.4.2	Experimental Parameters . . . . .	53
3.4.3	Substrate Temperature . . . . .	54
3.5	Fabrication of Electrical Samples . . . . .	61
3.5.1	Four-Point Probe Samples . . . . .	61
3.5.2	The Metal/Diamond/Silicon Samples . . . . .	65
3.5.3	Back-Etched Samples . . . . .	65
<b>4</b>	<b>Physical Characterization</b>	<b>72</b>
4.1	Introduction . . . . .	72
4.2	Raman Spectroscopy . . . . .	73
4.3	X-ray Photoelectron Spectroscopy . . . . .	79
4.4	Dek-Tak Analysis . . . . .	89
4.5	Scanning Electron Microscope Analysis . . . . .	94
4.6	Film Uniformity Analysis . . . . .	107
<b>5</b>	<b>Electrical Characterization</b>	<b>113</b>
5.1	Introduction . . . . .	113
5.2	Four Point Probe Characterization . . . . .	113
5.2.1	Experimental Method . . . . .	113
5.2.2	Theory of Conductivity vs. Temperature . . . . .	116
5.2.3	Comparison with Physical Characterization . . . . .	118
5.2.4	Experimental Results and Match with Theory . . . . .	122
5.3	Back-Etched Samples. . . . .	130
5.3.1	The Back-Etched Samples and I-V Measurement Set-Up . . . . .	130
5.3.2	Contact Effects on Back-Etched Samples . . . . .	132
5.3.3	High Field Effect . . . . .	132
5.3.4	Photo Effect . . . . .	145
5.4	The Metal/Diamond/Silicon Samples . . . . .	147
5.4.1	The I-V Measurement Set-up . . . . .	147
5.4.2	Contact Effects on Metal/Diamond/Silicon Samples . . . . .	151
5.4.3	Photo Effect . . . . .	158
5.4.4	Diamond Schottky Barrier Diode . . . . .	165
<b>6</b>	<b>Summary and Future Research</b>	<b>183</b>
6.1	Summary of Important Results . . . . .	183
6.1.1	Nucleation Method . . . . .	184

6.1.2	Quality of Diamond Films . . . . .	185
6.1.3	Back-Etching Technique . . . . .	185
6.1.4	Diamond/Silicon Interface . . . . .	186
6.1.5	Activation Energy of Diamond Films . . . . .	186
6.1.6	Electric Field Dependent Conductivity of Diamond Films . . .	187
6.1.7	Diamond Schottky Barrier Diode . . . . .	188
6.2	Future Research . . . . .	188
6.2.1	Improvement for Diamond Deposition . . . . .	189
6.2.2	The Techniques for Physical Characterization . . . . .	189
6.2.3	The Role of <i>SiC</i> at the Diamond/Silicon Interface . . . . .	190
6.2.4	Defects States in Diamond Films . . . . .	191
6.2.5	Diamond Devices . . . . .	191
<b>A Deposited Diamond Films</b>		<b>193</b>
<b>B Electrical Samples</b>		<b>198</b>
<b>BIBLIOGRAPHY</b>		<b>202</b>

## LIST OF TABLES

2.1	Physical properties of bulk natural diamond.[68] . . . . .	28
2.2	Properties of bulk natural diamond and synthetic diamond films.[13] .	29
2.3	Properties of diamond, i-C, and graphite.[21] . . . . .	31
2.4	Working definition for different carbon coatings.[69] . . . . .	32
2.5	Comparison of semiconductor properties for diamond, Si, GaAs, $\beta$ Sic.[70]	34
4.1	Relation of average grain size vs. methane concentration, microwave power and plasma pressure by the paste-polished method. . . . .	105
4.2	Relation of average grain size vs. microwave power and plasma pressure by the powder-polished method. . . . .	106
4.3	Relation of deposition rate vs. methane concentration, microwave power and plasma pressure by the paste-polished method. . . . .	108
4.4	Relation of deposition rate vs. methane concentration, microwave power and plasma pressure by the powder-polished method. . . . .	109

## LIST OF FIGURES

2.1	The atomic structure of (a) diamond (b) graphite. . . . .	7
2.2	Phase diagram of carbon.[12] . . . . .	8
2.3	Illustration of free energy difference between diamond and graphite. .	10
2.4	Low pressure CVD diamond synthesis in the phase diagram of carbon.[13]	12
2.5	Relationship between diamond properties and engineering applica- tions.[70] . . . . .	35
3.1	The cross section of the MPDR and processing chamber, and a schematic display of the electric (E) and magnetic (H) field patterns of the $TM_{011}$ mode. . . . .	39
3.2	The microwave power source, circuit, and cavity applicator. . . . .	42
3.3	The diagram of the MPDR CVD system. . . . .	44
3.4	SEM pictures of the silicon substrate prepared by <i>diamond paste method</i> .	47
3.5	SEM pictures of the silicon surface prepared by <i>diamond powder method</i> .	49
3.6	The MPDR CVD system during the diamond film deposition. . . . .	52
3.7	Top view of the MPDR processing chamber. . . . .	56
3.8	(a) Typical temperature profile and (b) better temperature uniformity of the silicon substrate. . . . .	58
3.9	Si substrate temperature vs. microwave input power for 1 % and 0.5 % methane concentration at 50 Torr. . . . .	59
3.10	Si substrate temperature vs. microwave input power for 1 % and 0.5 % methane concentration at 60 Torr. . . . .	60
3.11	Si substrate temperature vs. microwave input power for 50 and 60 Torr at 0.5 % methane concentration. . . . .	62
3.12	Si substrate temperature vs. microwave input power for 50 and 60 Torr at 1 % methane concentration. . . . .	63
3.13	Temperature difference between silicon and silicon nitride for 0.5 % methane concentration at 50 Torr. . . . .	64

3.14	Fabrication of the four-point probe samples. The actual surface was more uneven than is indicated here. (a) The starting point is a silicon nitride substrate which has received a nucleation procedure. (b) Since the substrate is insulating, the sample is ready for the 4 point probe measurement. . . . .	66
3.15	Fabrication of the metal/diamond/silicon samples. (a) The surface is nucleated by diamond powder or diamond paste, (b) the diamond film is deposited, and (c) top contacts are evaporated through a shadow mask. Aluminum is shown here as an example. . . . .	67
3.16	Fabrication of back-etched diamond samples for surface analysis. (a) Silicon is coated with diamond using conventional method. (b) The sample is secured to an epoxy substrate. (c) The silicon is removed by chemical etching. . . . .	69
3.17	Fabrication of dual-sided metal contacts on isolated diamond films. (a) The silicon is coated with diamond and (b) a metallic contact is evaporated on the first diamond surface. (c) A wire lead is attached to the evaporated metal and (d) the substrate is placed face down in epoxy. (e) The silicon is removed by etching and (f) metal contacts are evaporated on the second diamond surface. . . . .	70
4.1	Raman spectroscopy is based on a process of inelastic scattering of photons by phonons. . . . .	74
4.2	Raman spectra for diamond and silicon on (a) absolute wave number scale and (b) relative wave number scale. . . . .	76
4.3	Raman Spectroscopy set-up for the Raman spectrum analysis.(From Dr. Gray) . . . . .	78
4.4	Raman spectra of 0.5% methane samples at (a) 936 °C (b) 1040 °C and (c) 1090 °C. (From Dr. Gray) . . . . .	80
4.5	Raman spectra of samples with conditions : (a) 0.5% methane, 1000 °C (b) 0.5% methane, 1040 °C (c) 1% methane, 1000 °C and (d) 1% methane, 1040 °C. (From Dr. Gray) . . . . .	81
4.6	Raman spectra of samples of 0.5% methane at 1000 °C for (a) 10 hours' deposition and (b) 6 hours' deposition. (From Dr. Gray) . . . . .	82
4.7	Raman spectra of samples with 0.5% methane at 1040 °C by (a) powder-polished method and (b) paste-polished method. (From Dr. Gray) . . . . .	83

4.8	Raman spectra of (a) the as-deposited film and (b) the free standing film of the sample with 1.5% methane at about 1040 °C. (From Dr. Gray) . . . . .	84
4.9	Principle of X-ray Photoelectron Spectroscopy. When a core level electron absorbs a photon of energy ( $h\nu$ ) greater than its binding energy ( $E_B$ ), the electron is ejected from the atom with kinetic energy (K.E.).	86
4.10	ESCA spectra of samples exposed to air for (a) a long time and (b) no time before the analysis. (From Dr. Hook) . . . . .	88
4.11	(a) Elemental survey scan of the sample before the Ar sputtering (b) higher resolution narrow scan of (a) in the carbon region. (From Dr. Hook) . . . . .	90
4.12	(a) Elemental survey scan of the sample after the Ar sputtering (b) higher resolution narrow scan of (a) in the carbon region. (From Dr. Hook) . . . . .	91
4.13	SEM view of the paste-polished produced diamond film on a cleaved sample showing the silicon substrate, the interface, and the side view and top surface of the diamond film. . . . .	93
4.14	The surface profile on (a) the top surface of an as-deposited paste-polished produced diamond film and (b) the back surface of the film after transfer to the epoxy substrate. . . . .	95
4.15	SEM view of the powder-polished produced diamond film on a cleaved sample showing the silicon substrate, the interface, and the side view and top surface of the diamond film. . . . .	96
4.16	The surface profile on (a) the top surface of an as-deposited powder-polished produced diamond film and (b) the back surface of the film after transfer to the epoxy substrate. . . . .	97
4.17	The extreme top surface profiles of (a) large-grain-size and (b) small-grain-size diamond films. . . . .	98
4.18	Typical SEM photo of the top view of the diamond film prepared by the paste-polished method. The triangular shapes indicate [111] crystallite faces. (MW power: 600 W, plasma pressure: 60 Torr, methane concentration: 0.5%) . . . . .	101
4.19	Typical SEM photo of the top view of the diamond film prepared by the powder-polished method. (MW power: 600 W, plasma pressure: 60 Torr, methane concentration: 0.5%) . . . . .	102

4.20	Growth mechanism of diamond film prepared by (a) paste-polished and (b) powder-polished method. The latter has a higher nucleation density and therefore a finer grain film. . . . .	103
4.21	This SEM photo shows large and small grain size diamond growth on the same substrate. . . . .	104
4.22	(a) Cross section view of laser scan from plane A to D. (b) Thickness ( $\mu\text{m}$ ) uniformity analysis on an area of 1 cm X 2 cm of a sample. . .	112
5.1	The set-up of the four point probe method. . . . .	115
5.2	Raman spectra of (a) NDF-S3, (b) NDF-S4, and (c) NDF-S6. (From Dr. Holtz) . . . . .	120
5.3	Raman spectrum of NDF-S1. (From Dr. Gray) . . . . .	121
5.4	Conductivity vs. $1000/T$ of NDF-S1 . . . . .	125
5.5	Conductivity vs. $1000/T$ of NDF-S3 . . . . .	126
5.6	Conductivity vs. $1000/T$ of NDF-S4 . . . . .	127
5.7	Conductivity vs. $1000/T$ of NDF-S6 . . . . .	128
5.8	Raman spectrum of the diamond film as deposited on the silicon substrate with substrate temperature at $1000\text{ }^\circ\text{C}$ . (From Dr. Gray) . . .	131
5.9	The I-V measurement set-up of the back-etched samples. . . . .	133
5.10	I-V characteristics of a small grain size sample with gold contacts top and bottom. It shows linear and symmetric behavior at low voltages. (Electrical sample : P47-T1) . . . . .	134
5.11	I-V characteristics of a small grain size sample with gold contacts top and bottom. It shows nonlinear behavior at high voltages. (Electrical sample : P47-T1) . . . . .	136
5.12	The $I - V^{3/2}$ characteristic and (b) the $I - V^2$ characteristic of Figure 5.11. (Electrical sample : P47-T1) . . . . .	137
5.13	I-V characteristic of diamond film with gold contacts top and bottom. Experimental data is shown by data points. The solid line represents the model results of Eq. (5.12) with $G_{00}=2.6\times 10^{-10}\ \Omega^{-1}$ , $G_0 = 2.1\times 10^{-11}\ \Omega^{-1}$ , and $a = 0.042\ \text{V}^{-1}$ . (Electrical sample : P47-T1)	139
5.14	I-V characteristic of diamond film with top indium contacts and bottom gold contact. Experimental data is shown by data points. The solid line represents the model results of Eq. (5.12) with $G_{00}=2.1\times 10^{-10}\ \Omega^{-1}$ , $G_0 = 2.0\times 10^{-11}\ \Omega^{-1}$ , and $a = 0.045\ \text{V}^{-1}$ . (Electrical sample : P47-T3) . . . . .	140

5.15	I-V characteristic of diamond film with silver contacts top and bottom. Experimental data is shown by data points. The solid line represents the model results of Eq. (5.12) with $G_{00}=2.9\times 10^{-10} \Omega^{-1}$ , $G_0 = 4.0\times 10^{-12} \Omega^{-1}$ , and $a = 0.08 V^{-1}$ . (Electrical sample : P49-T2)	141
5.16	The photoconductance is nearly independent of the applied voltage. Shown here are data for different photon fluxes corresponding to different optical density (O.D) filter values. (Electrical sample : P47-T1)	143
5.17	(a) The calibration factors corresponding to different optical wavelength for Si and Ge photodetector. (b) The relative power intensity factors for Si and Ge photodetector at different wavelength of the optical monopass filters. . . . .	148
5.18	Relation of photoconductance vs. photon energy for Au-Au contact sample (a) before normalization and (b) after normalization. (Electrical sample : P47-T1) . . . . .	149
5.19	Relation of photoconductance vs. photon energy for In-Au contact sample (a) before normalization and (b) after normalization. (Electrical sample : P47-T3) . . . . .	150
5.20	The I-V measurement set-up of the metal/diamond/silicon samples. .	152
5.21	I-V characteristic of the small grain size Au/diamond/silicon samples. (Electrical sample : P39) . . . . .	154
5.22	I-V characteristic of the small grain size In/diamond/silicon samples. (Electrical sample : P39) . . . . .	155
5.23	I-V characteristic of the large grain size Al/diamond/silicon samples. The average grain size is $2.1 \mu\text{m}$ . (Electrical sample : P6) . . . . .	156
5.24	I-V characteristic of the large grain size Al/diamond/silicon samples. The average grain size is $1.4 \mu\text{m}$ . (Electrical sample : P7) . . . . .	157
5.25	Photoconductance versus photon energy (a) before normalization and (b) after normalization for the small grain size Au/diamond/silicon sample. (Electrical sample : P39) . . . . .	159
5.26	Photoconductance versus photon energy (a) before normalization and (b) after normalization for the small grain size In/diamond/silicon sample. (Electrical sample : P39) . . . . .	160
5.27	Photoconductance versus photon energy (a) before normalization and (b) after normalization for the large grain size Al/diamond/silicon sample. The average grain size is $2.1 \mu\text{m}$ . (Electrical sample : P6) . . . .	161

5.28	Photoconductance versus photon energy (a) before normalization and (b) after normalization for the large grain size Al/diamond/silicon sample. The average grain size is 1.4 $\mu\text{m}$ . (Electrical sample : P7) . . . .	162
5.29	Photoconductance versus photon energy (a) before normalization and (b) after normalization for the large grain size Al/diamond/silicon sample. The average grain size is 1.1 $\mu\text{m}$ . Electrical sample : P20) . . . .	163
5.30	The energy band diagram at the Al/p-type diamond interface. . . . .	164
5.31	The I-V characteristic of the point contact/diamond/silicon structure showed ohmic behavior. The top contact is a tungsten point probe and the bottom contact is the silicon wafer. (Electrical sample : P20) . .	166
5.32	The best Schottky barrier diode (SBD) characteristic of the large grain size Al/diamond/silicon samples. The top contact is aluminum and the bottom contact is the silicon wafer. (Electrical sample : P20) . . . . .	167
5.33	The Raman spectrum of NDF-P20. The peak between $1550\text{cm}^{-1}$ and $1600\text{cm}^{-1}$ indicates that the existence of graphitic component in the film. . . . .	168
5.34	The SBD I-V characteristic of a film with coplanar surface contacts. One contact is aluminum and the other contact is a tungsten point probe. (Electrical sample : P20) . . . . .	169
5.35	The $\log(I)$ -V characteristic of the SBD. (Electrical sample : P20) . . .	171
5.36	The forward bias I-V characteristic of the SBD. The $\diamond$ represents the experimental data, the solid line shows the ideal diode with $\eta = 1$ , $I_0=5.2\times 10^{-16}$ A and the dashed line shows the ideal diode with $\eta = 2$ , $I_0=2.9\times 10^{-14}$ A. (Electrical sample : P20) . . . . .	173
5.37	Conductance-bulk voltage characteristic. It follows the field activated model above 10 V. (Electrical sample : P20) . . . . .	174
5.38	The $I-V_b^{3/2}$ characteristic of the SBD. (Electrical sample : P20) . . .	176
5.39	The $I-V_b^2$ characteristic of the SBD. (Electrical sample : P20) . . . .	177
5.40	(a) The energy band diagram of the SBD. The barrier height $\phi_p$ equals to the sum of built-in potential $V_i$ and activation energy $E_a$ . (b) The equivalent circuit of the SBD. . . . .	178
5.41	Capacitance versus frequency characteristic at different reverse bias. (Electrical sample : P20) . . . . .	180
5.42	Capacitance versus reverse bias characteristic at 50 kHz. (Electrical sample : P20) . . . . .	182

# CHAPTER 1

## Introduction

### 1.1 Motivation for Diamond Research

Diamond is well known as one of the most valuable gems and possesses many excellent properties, such as an extremely high degree of hardness, high thermal conductivity, high electrical resistivity, chemical inertness, and good optical transparency. When properly doped with impurities, diamond also has potential as a useful semiconducting material.

Currently in industry, diamonds are mostly used in hard-surfacing and abrasive applications. The general methods to get synthetic diamond are variations on the high pressure and high temperature technique (HPHT), reported by Bundy et al. [1] at General Electric several decades ago. That process is a mature and economically feasible technology, but it has some limitations. First, commercial HPHT diamond synthesis needs a large, expensive system. Secondly, low impurity diamond is rather difficult and costly by this method. Finally, and most important it is only suitable for production of diamond in the form of small pieces, grit, and powder. It is not practical for many technological applications where a continuous film is required.

Now there appears to be a high likelihood that these limitations can be overcome by new diamond thin film deposition techniques which allow large area coating with

lower cost. These new methods are based on metastable synthesis of diamond at pressures of an atmosphere or less. So far this new method of synthesis has motivated a major international research effort aimed at developing techniques for high quality, low cost, large area, and high deposition rate diamond thin film production. This research raises the possibility of many new potential applications in mechanical, electronics, and optical industries.

Following are some of the potential diamond film applications:

- \* Tribology and abrasive coating applications.
- \* Thermal heat sinks.
- \* Electronic packaging and passivation.
- \* Electrical isolation.
- \* High temperature, high speed electronic devices.
- \* Optical windows.
- \* Microwave and millimeter wave power devices.
- \* Corrosion resistant applications.

Significant issues still remain that hinder widespread commercial applications of diamond films. These include reproducibility, film quality, film uniformity, and high deposition rate of the diamond films.

The initial steps of this research were to develop techniques on new apparatus for producing high quality diamond films. Subsequent steps focused on the correlation between processing techniques and diamond film physical properties and specifically on studying electrical properties of the diamond films.

## 1.2 Research Objectives

One objective of this research was to develop techniques for high quality diamond film synthesis using a microwave plasma disk reactor (MPDR) chemical vapor deposition system developed by Asmussen et al. [2, 3] which had previously been proven successful in plasma assisted etching of semiconductors [4, 5, 6, 7] and in plasma oxidation techniques [8, 9]. This objective, which was part of a group effort, was met, and in fact during the past year a commercial version of the MPDR was placed in use on an industrial processing line.

A second objective was to correlate diamond film properties with substrate preparation methods and synthesis conditions, providing insight into the factors affecting diamond quality. Two different nucleation methods were shown in this research to produce films of similar diamond quality as measured by Raman spectroscopy, but considerably different morphology and different electrical characteristics. A variety of physical characterization methods were used for film analysis.

The third and final objective was to specifically focus on the electrical properties of the films in order to provide insight into the relationship between synthesis variables and electrical properties, and to investigate electron device related film properties. Toward this objective, new sample preparation methods were used to study the role of metal contacts. New information about the role of defects in limiting the use of diamond films at very high electrical fields, above  $10^5$  V/cm, was provided by this research. Also, the importance of nucleation procedures on the properties of metal-diamond junctions, specifically on the properties of diamond Schottky barrier diodes, was demonstrated.

## 1.3 Dissertation Outline

This dissertation is divided into four subjects. These are (1) background literature review, (2) diamond film deposition and sample fabrication, (3) physical characterization, and (4) electrical properties analysis.

Chapter 2 of this dissertation reviews the diamond synthesis theory, diamond film production methods, and previous diamond electronic device results from the literature. Chapter 3 describes diamond film deposition by using the MPDR chemical vapor deposition system and also describes the sample preparation techniques used in this research. Chapter 4 reviews characterization results of the diamond films by Raman spectroscopy, scanning electron microscope, X-ray photoelectron spectroscopy, and surface profiling, The electrical conductivity versus temperature of the diamond films as measured by the four point probe method is presented in chapter 5 (section 2). Chapter 5 (section 3 and 4) also analyzes the electrical contact effects on back etched diamond samples and on diamond/silicon structures. Chapter 6 concludes this work with a summary of important results and discussions for future research.

C

S

F

2

T

h

pr

m

pr

p

ti

o

te

ca

# **CHAPTER 2**

## **Synthetic Diamond : Background Review**

### **2.1 Introduction**

This chapter begins by describing the historical background of diamond synthesis from high pressure high temperature methods to low pressure low temperature metastable production methods. Then the growth mechanisms of the metastable production methods are covered. In chapter 2 (section 3), several categories of the diamond film production technologies are discussed, such as chemical vapor deposition techniques, plasma assisted chemical vapor deposition techniques, and ion beam deposition techniques. Then several nucleation methods are also described. The physical attributes of diamond, such as material properties and semiconductor properties, and some of the potential applications are explained in chapter 2 (section 4). Finally, some of the diamond device work is reviewed in chapter 2 (section 5).

2.

2.

Di

dia

str

arr

in

lat

dia

hav

the

sci

und

per

dia

can

the

tan

the

diag

pres

A

und

de

## 2.2 Brief History of Diamond Synthesis

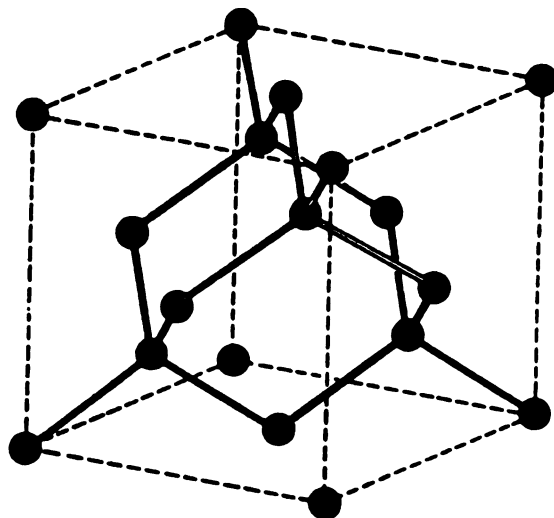
### 2.2.1 Historical Background

Diamond was first known to be a form of carbon in 1797. Later it was discovered that diamond is formed by carbon atoms which are arranged in a particular crystalline structure. It has a cubic lattice which is built up from  $sp^3$ -hybridized, tetrahedrally arranged carbon atoms. A much more common form of solid state carbon is graphite, in which carbon atoms are arranged in a hexagonal crystalline structure. The graphite lattice consists of layers of condensed  $sp^2$ -hybridized rings. The atomic structure of diamond and graphite are shown in Figure 2.1. Most recently, however, scientists have just found the third form of carbon, the fullerenes [11]. With the knowledge of the fact that diamond is formed by the  $sp^3$  bonding arrangement of carbon atoms, a scientific approach was open for research on synthetic diamond technologies.

Thermodynamic calculations based on the Gibb's free energy show the conditions under which carbon atoms prefer to form diamond or graphite. At ordinary temperatures and pressures, diamond is a metastable form of carbon. This means that diamond is not the most stable form of carbon compared to graphite in nature, because the hexagonal structure of graphite has a lower thermodynamic potential than the diamond crystal structure. Therefore, graphite is favored in terms of thermodynamic stability. However, at very high pressures, greater than 100,000 atmospheres, the phenomenon is reversed and diamond becomes the preferred state. The phase diagram of carbon, shown in Figure 2.2, illustrates the regions of temperature and pressure corresponding to diamond, graphite, liquid carbon, and vapor carbon [12].

Although diamond is metastable, it does not degrade to graphite spontaneously under ordinary conditions. A significant potential energy barrier prevents such degradation except at very high temperatures as shown in Figure 2.3. However, the phase

(a) Diamond ( $sp^3$  bonding)



(b) Graphite ( $sp^2$  bonding)

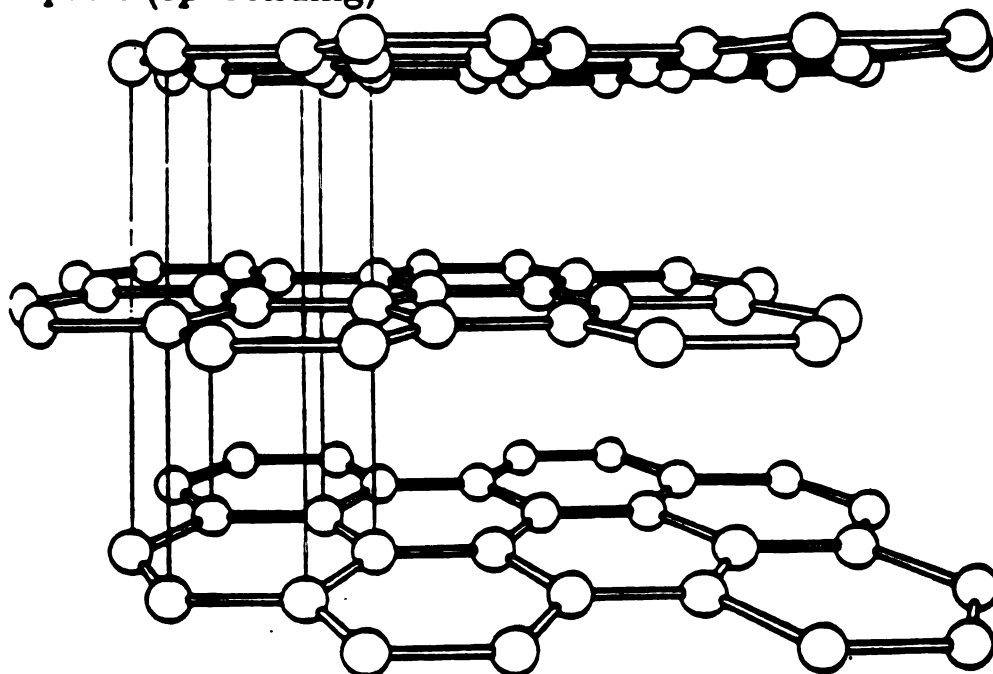


Figure 2.1. The atomic structure of (a) diamond (b) graphite.



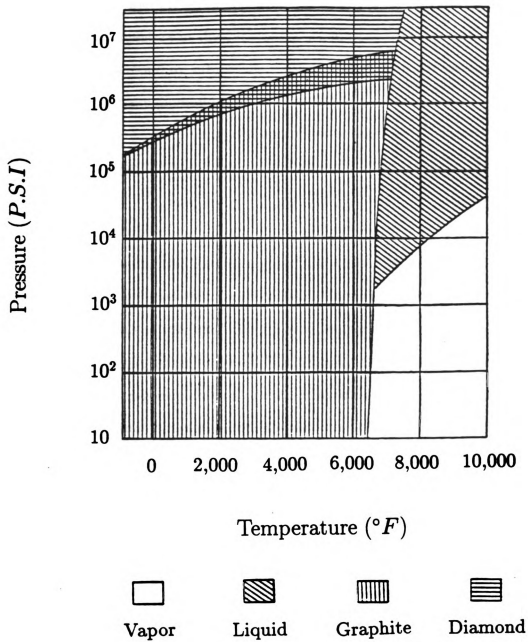


Figure 2.2. Phase diagram of carbon.[12]

diagram does show that at ordinary conditions graphite can't transform to diamond because graphite has the lower thermodynamic potential under such conditions.

Many experimenters in the 19th century and early 20th century tried unsuccessfully to make diamond by subjecting graphite and many other carbon compounds to the conditions where diamond is the favored state of carbon, namely under high heat and great pressure. Eventually, a group of researchers at GE successfully developed the first technique to make "*synthetic diamond*", or "*man-made diamond*" in 1955 [1].

This technique involves processing at high temperatures and high pressures, which are in the range of 30,000-100,000  $kg/cm^2$  and 1000-3000  $^{\circ}K$  respectively. It also involves a metal, such as iron, nickel, cobalt, manganese, chromium, or tantalum to serve as a solvent and catalyst. The GE work not only lead directly to present industrial production of synthetic diamond for abrasive applications, but also to advanced carbon research in general with more understanding of the carbon phase diagram.

There is another important high pressure method to synthesize diamond which is the so-called shock wave technique. Diamond containing material was achieved first by means of shock waves by Paul S. DeCarli and John C. Jamieson in 1961. This technique, industrialized by Du Pont, utilizes the high pressure in the shock wave of explosions to directly convert crystalline graphite into diamond. The particles are then separated from the starting material by sedimentation [13].

With the success of these two techniques, over 30 tons of industrial diamond abrasive grain are made each year around the world. However, it has long been recognized that there is a possibility that diamond may be formed in the metastable portion of the phase diagram, i.e. in the graphite stable region, under the conditions where "nascent" (un-combined) carbon atoms are liberated [12]. Such synthetic conditions would be easier to achieve and also better suited for diamond film coating at relatively

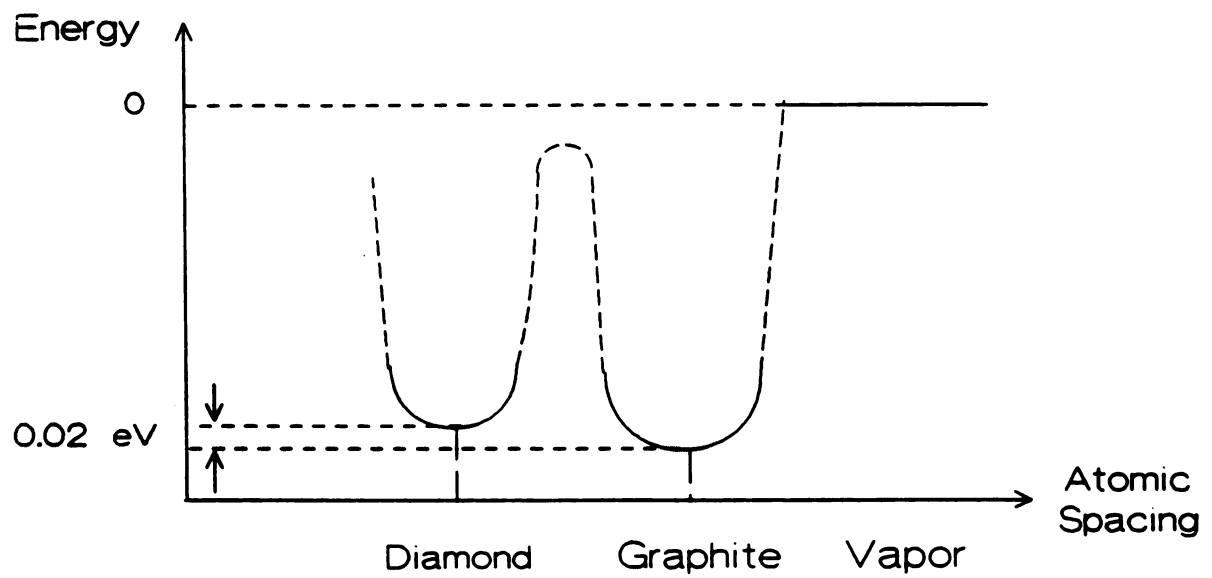
Ere

002

LEI

LEI

Fig



$$\Delta E (\text{ free carbon, graphite } ) = 170 \text{ Kcal/g-atom}$$

$$\Delta E (\text{ diamond, graphite } ) = 0.5 \text{ Kcal/g-atom}$$

Figure 2.3. Illustration of free energy difference between diamond and graphite.

low co

For

1970's

at rel

Th

iment

ion be

differe

section

A

Physic

mond

appro

film

attent

ter's

featur

the de

thesis

with r

(CVD

develo

pushee

Sim

all kin

technic

low cost over larger areas.

Following this spirit of thought, attempts were made in the 1950's, 1960's, and 1970's to form diamond films on non-diamond substrates by depositing carbon atoms at relatively low pressures and low temperatures under a variety of conditions.

The first results of the diamond film work were the development of a few experimental methods to form diamond-like-carbon (DLC) films by vapor deposition or ion beam deposition. [14, 15, 16, 17] However, the atomic structure of DLC films is different from that of diamond films. The difference will be explained in chapter 2 (section 4).

A significant breakthrough occurred when researchers at the Moscow Institute of Physical Chemistry developed methods for depositing diamond films on both diamond and, for the first time, non-diamond substrates. They suggested three different approaches to achieve a "super-equilibrium" with atomic hydrogen : *catalysis, heated filament, and electric-discharge plasma* [18]. However, their work did not get much attention in the west until Japan's National Institute for Research in Inorganic Materials (NIRIM) repeated the work and also reported true diamond films. The key feature of this work is the addition of hydrogen gas associated with methane gas into the deposition chamber [19]. This result confirmed the hypothesis that diamond synthesis techniques can take place under the conditions in which diamond is metastable with respect to graphite. The region for low pressure chemical vapor deposition (CVD) technique of diamond synthesis is illustrated in Figure 2.4. Not only did this development trigger many research efforts on diamond film technology but it also pushed the synthetic diamond films towards industrial applications.

Since 1983, many groups successfully deposited diamond films or DLC films on all kinds of non-diamond substrates by all kinds of techniques. Some representative techniques and their experiment parameters will be described in details in chapter 2

Pressure ( Kbar )

Figure

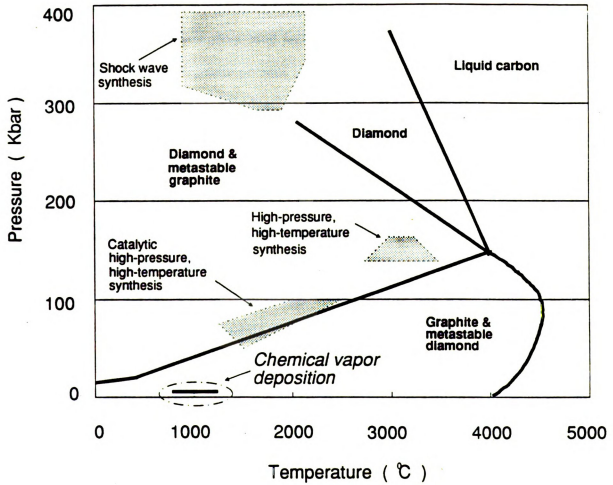


Figure 2.4. Low pressure CVD diamond synthesis in the phase diagram of carbon.[13]

(section 3).

## 2.2.2 Growth Mechanism of Diamond Films

In general, there are two ways to form metastable crystal:

1. *If a stable crystal is brought into a new temperature or pressure range in which it doesn't transform into the more stable form;*

2. *A precipitate or transformation may form a new metastable phase.* [20]

Metastable crystal will remain present because the high activation energy required for the conversion into more stable phase causes a low rate of transition. This explains why diamond doesn't spontaneously degrade to graphite at ordinary temperature and pressure.

The possibility of synthesis of diamond in the graphite region of the phase-diagram is based on the fact that the free energy difference between diamond and graphite (0.5 Kcal/g-atom) is so small under ambient conditions. See Figure 2.3. There is some probability that diamond and graphite can both nucleate and grow simultaneously from nascent carbon atoms, especially under conditions in which kinetic factors can dominate, e.g. high energy. If graphite can be prevented from forming, or if it can be removed preferentially, diamond can be recovered. [21] A sampling of theories and models for diamond growth mechanism from methane/hydrogen mixture are briefly described below.

In 1986, M. Tsuda, et al proposed the "*Epitaxial Growth Mechanism of Diamond Crystal in CH<sub>4</sub>-H<sub>2</sub> Plasma.*" They believe that no phase transition of graphite or amorphous carbon takes places under the conditions of low temperature plasma reaction. Rather, the diamond formation in vacuum is considered to proceed by chemical reactions which are different from the phase transition of graphite under ultrahigh pressure at very high temperature. By a quantum chemical calculation a mechanism

was found to explain the process in two steps. First, the (111) plane of diamond surface is covered by methyl groups ( $CH_3$ ) via methylene insertion or hydrogen abstraction followed by methyl radical addition. Second, epitaxial growth occurs when three neighboring methyl groups standing on the (111) plane of the diamond surface bind spontaneously to form the diamond structure via methyl cation intermediates [22]. However, S. J. Harris also proposed a mechanism for homo-epitaxial growth on an finite (100) diamond surface from the methyl radicals ( $CH_3$ ) [23].

In 1987, M. Frenklach and K. E. Spear proposed a different growth mechanism of vapor-deposited diamond. This central postulate is that the monomer growth species is "acetylene" ( $C_2H_2$ ). This mechanism basically consists of two alternating steps. The first is surface activation by the H abstraction of a bonded hydrogen atom from a surface carbon. Then the activated carbon radical acts as a site for the addition of one or two acetylene molecules. During the addition reaction cycle a number of solid C-C bonds are formed and hydrogen atoms migrate from a lower to a upper surface layer. This paper also discusses the two possibilities for the production of graphite on a growing diamond layer. First, graphite precursors may form in the gas phase followed by surface deposition and further growth. Second, the initiation and growth of graphite may happen directly on the surface [24].

Additional insight into growth mechanism is provided by the fact that methane and hydrogen is not a unique recipe for diamond film growth. For example, Hirose and Terasawa reported that diamond thin films with good crystallinity and quality were quickly synthesized by thermal CVD using several organic compounds, some of which include oxygen [25]. However, the specific roles of oxygen were not discussed in that work.

T. Kawato and K-I Kondo were the first to specifically study the effects of oxygen. With the addition of oxygen, the deposition of graphitic or amorphous carbon could be

suppressed, the growth rate of diamond was increased and the pressure range for the synthesis of diamond was extended. It was suggested that these effects resulted from the fact that the acetylene concentration is significantly reduced upon the addition of oxygen [26].

S. J. Harris and A. M. Weiner also reported that  $O_2$  can reduce the effective initial hydrocarbon mole fraction, which is important because higher quality diamond is grown at a lower initial hydrocarbon mole fraction. Perhaps more importantly, it was also noted that there is a possibility the formation of sufficient gas phase  $OH$  will remove non-diamond (pyrolytic) carbon from the film [27]. Y. Liou, et al. also found that the addition of oxygen was critical for diamond growth at temperatures below  $500\text{ }^\circ C$  [28].

It is likely that details of the growth mechanism depend on the synthesis method. For example, with the acetylene flame technique, Y. Matsui, et al. [29] proposed that stable species such as  $CH_4$  and  $C_2H_4$  are rapidly produced, followed by the methyl radical formation. Then the C-radicals adsorbed on the diamond surface are etched by H-atoms to form  $CH_4$ . The growth rate depends both on the substrate temperature and on the  $C_2H_2/O_2$  ratio. This result is also confirmed by Y. Tzeng, et al. [30].

Although there are many postulates attempting to explain diamond synthesis, the experimental evidence in support of any particular growth mechanism is limited. However, there are several hypotheses most researchers believe that can explain parts of the growth mechanism for the diamond synthesis. There are listed as follows.

First, the best quality diamond films have been generally obtained in a predominantly hydrogen atmosphere, with only small amounts of hydrocarbon (typically methane, 1 % or less) present in the reaction mixture. That is, the hydrogen atoms should be in a super-equilibrium state for a successful diamond growth. Moreover, H

atoms play a very crucial role in enhancing the film growth. The effects of hydrogen are described in the following [31].

**1. Hydrogen acts as the etching agent for non-diamond carbon :**

The formation of diamond kinetically competes with the formation of graphite. When graphite and diamond are formed simultaneously, the atomic hydrogen created from the hydrogen gas either by thermal energy or by electric energy is considered a preferential etching agent of graphite over diamond.

**2. Hydrogen provides stabilization of  $sp^3$  bonding :**

Atomic hydrogen serves to satisfy the dangling bonds of surface carbon atoms, keeping them in the  $sp^3$  configuration and thus preventing the diamond surface from reconstruction into graphitic ( $sp^2$ ) or carbonic ( $sp$ ) structures.

**3. Hydrogen promotes the main monomer of the gas-phase production for diamond growth :**

Either acetylene ( $C_2H_2$ ) [24, 32] or methyl radical ( $CH_3$ ) [22, 23] is the main monomer for the diamond growth and hydrogen is believed to support the formation of these species.

Secondly, the temperature dependence of the rate of diamond growth exhibits a maximum. That is, it initially increases with temperature and then decreases. Graphite formation rates also exhibit a temperature maximum, but at higher temperatures than that of diamond.

Finally, the addition of oxygen not only increases the deposition rate but also improves aspects of the film quality. The roles of oxygen are suggested as follows [32].

**1. Oxygen may increase the H atom concentration which selectively etches graphitic and amorphous carbons.**

**2. Oxygen may cause the reduction of pyrocarbon-forming species.**

Consequently, it will increase the growth rate of diamond.

### **3. Oxygen may also act as a good selective etchant of non-diamond carbons.**

Oxygen is better than hydrogen in the efficiency of etching graphite, however, the addition of an excessive amount of oxygen may result in a decreased growth rate, because the diamond crystals are also etched.

Besides the growth mechanism of the diamond synthesis, the nucleation mechanism still needs to be briefly considered. The initial nucleation mechanism of a diamond crystallite is distinct from the mechanism for the extension of a preexisting diamond lattice. Without special substrate preparation, the initial nucleus density of diamond is extremely low, and a continuous film does not result. To improve the amount of nucleation sites becomes necessary. Generally speaking, it is well recognized that the nucleation rate can be enhanced prominently both by scratching the substrate surface or by attaching small seed crystallites to the substrate before the deposition. Nucleation methods will be described further in chapter 2 (section 3).

Until now, the understanding of the growth mechanism is only at the ice-breaking stage. Many more experiments with better control of experiment parameters are needed to verify the physics and chemistry of the diamond film synthesis.

## **2.3 Review of Diamond Film Technologies**

In the past few years the potential applications of diamond films have stimulated a great deal of research interest on various synthesis technologies, each of which has advantages and disadvantages. A broad sampling of these technologies is briefly presented in this section in which the synthesis methods are grouped into three categories. These are (1) **hot filament assisted chemical-vapor-deposition (CVD)**; (2) **plasma assisted CVD**; and (3) **other deposition methods**. Additionally, in the last part of this section, several nucleation methods will be described.

### 2.3.1 Hot Filament Chemical Vapor Deposition Techniques

Generally, CVD is a reaction in which two types of gas, C(g) and D(g), react at a high temperature to form a solid phase A(s) and a gas phase B(g). Sometimes, more than two kinds of gases are introduced for certain applications. One way of enhancing the reaction rate is to add thermal energy. In hot filament CVD the thermal energy comes from a hot filament located in the reaction chamber into which the gases are introduced.

In 1982, Matsumoto, et al. reported synthesis of microcrystal diamond using a hot filament CVD process from a mixture of methane and hydrogen gas. This technique involves the use of a hot tungsten filament in the vicinity of the substrate. The hot filament causes the dissociation of the gas as well as heating of the substrate, providing appropriate conditions for the growth of diamond [19].

A modified version of the thermal CVD method has been used by Sawabe, et al. to improve the growth rate of diamond films. It involves the electron bombardment of the substrate surface by biasing the substrate positively with respect to the hot filament. It is suggested that the decomposition of  $CH_4$  and  $H_2$  by electrons occurs mainly at the substrate surface, because the scattering cross section for electrons is fairly small in space under these conditions. It is also found that the number of nucleation sites on the substrate surface is increased by electron bombardment. Thus, growth rates as high as 3 - 5  $\mu\text{m}/\text{hour}$  were achieved [33].

Hirose and Terasawa experimented with many organic gases other than methane using the hot filament CVD method. These experiments were based on their hypothesis that the methyl radical ( $CH_3$ ) with  $sp^3$  hybridized orbits and atomic hydrogen ( $H$ ) play important roles in the synthesis of diamond. Consequently, they choose methyl alcohol ( $CH_3OH$ ), ethyl alcohol ( $C_2H_5OH$ ), acetone ( $CH_3COCH_3$ ), dimethyl ether ( $C_2H_5OC_2H_5$ ), and some other organic gases which can generate methyl radicals

more easily in order to increase the growth rate. They found that good quality diamond films can be grown on silicon substrates with high growth rates (8 - 10  $\mu\text{m}/\text{hour}$ ) under the pressure range 1 - 800 Torr. The growth rate is about 10 times faster than thermal CVD method using  $\text{CH}_4$  or  $\text{C}_2\text{H}_2$  gas [34].

H. Aikyo and K.-I. Kondo reported diamond synthesis by a new hot filament CVD method in which methane is decomposed mainly by an abstraction reaction of  $\text{CH}_4$  with atomic hydrogen. The film obtained by this method was compared with that obtained by the method which involves the thermal decomposition of  $\text{CH}_4$  near a filament. They found that the film quality of the former method was better in terms of the ratio of crystalline to amorphous carbon, but slightly lower in deposition rate compared to that by the latter method. They hypothesize that production of acetylene ( $\text{C}_2\text{H}_2$ ) is suppressed by the separate introduction of the gases and that there is consequently an improvement in the film quality [35].

Y. H. Lee, et al. used the bias-controlled thermal CVD method to do diamond synthesis. They found that high quality films with highly faceted cubo-octahedral diamond growth was observed under low current bias conditions, in which the substrate is negative with respect to the filament. In contrast, multiply twinned microcrystal growth incorporating  $sp^2$ -bonded carbon was obtained under high current bias conditions. They suggested that this is due to a decrease in electron and ion bombardment of the sample during the low bias conditions which minimizes surface damage. Clearly this observation is quite different from Sawabe's point of view about the role of the electrons [36].

Lately, M. Ihara, et al. reported that they successfully deposited good quality diamond on silicon substrates at a temperature as low as 135  $^\circ\text{C}$  by controlling the temperature of the substrate holder. A tantalum filament was typically used and maintained at 2300  $^\circ\text{C}$  in this experiment [37].

There are some advantages and limitations associated with the hot filament CVD process. The fact that the apparatus is inexpensive and easy to operate is the most attractive advantage. However, film non-uniformity due to the high temperature gradient of the filament and the difficulty to scale up the size limits the possibilities for a production process. Also, the hot filament can be a source of impurities in the films.

### **2.3.2 Plasma Assisted Chemical Vapor Deposition Techniques**

Plasma assisted chemical vapor deposition (PACVD) processes used for the synthesis of diamond and diamond-like films involve the decomposition and dissociation of hydrocarbon gas in a plasma by direct-current (dc), radio-frequency (rf), or microwave excitation. Several variant techniques of the PACVD process as applied to diamond are described in the following.

#### **DC Plasma CVD Techniques**

In 1987, K. Suzuki, et al. first successfully deposited good quality diamond films by the DC plasma parallel plate CVD method. Films with growth rates of about 20  $\mu\text{m}/\text{hour}$  were grown on silicon and  $\alpha$ -alumina substrates from a methane/hydrogen mixture gas at a pressure of 200 Torr without surface scratching by diamond or c-BN powder. By experiment they also observed that electrons could enhance the film growth. [38] Later epitaxial growth of diamond thin films on cubic boron nitride (111) surfaces [39] and deposition of diamond onto an aluminum substrates at low temperature (below 480 °C) [40] by dc plasma CVD technique were also reported by other groups.

K. Kurihara, et al. reported diamond synthesis with the use of a DC plasma jet

(chamber pressure: 100 - 400 Torr). A plasma jet, formed by the dc arc discharge of  $CH_4$  diluted with  $H_2$ , was sprayed onto a water-cooled substrate. Because of the high density of radicals, a high growth rate of  $80 \mu\text{m}/\text{hour}$  was achieved by this technique [41].

Diamond films synthesized by dc arc discharge plasma CVD in a hydrogen/argon/ethanol mixture gas was reported by F. Akatsuda, et al. (chamber pressure: 200 - 400 Torr). The growth rate of diamond films was reported to be about  $200 - 250 \mu\text{m}/\text{hour}$  which is higher than that of other CVD techniques [42].

S. Matsumoto, et al. also studied the substrate bias effect on diamond deposition by the dc plasma jet method. When they applied a positive bias voltage to substrates in a dc plasma jet of the  $Ar-H_2-CH_4$  system, the deposition rate increased more than twice, and a maximum rate of  $15 \mu\text{m}/\text{min}$  was obtained. The deposition area also increased but the uniformity of film thickness did not improve. They deduced that positive bias on the substrate enlarges the plasma region near the substrate by inducing a secondary discharge between the arc plasma and bias electrode. As the concentration of activated species increased near the substrate, the deposition of diamond also increased. However, too much bias current changes the secondary discharge from glow-like to an arc discharge, causing the over heating of the substrate and deposition of graphite instead of diamond [43].

### **RF Plasma CVD Techniques**

In 1987, S. Matsumoto, et al. developed a technique using an rf (4 MHz) inductive heating of an argon-hydrogen-methane mixture plasma under 1 atm pressure. Micro-crystals of diamond and continuous polycrystalline films were deposited on molybdenum substrates with a  $1 \mu\text{m}/\text{min}$  deposition rate, however the films were not uniform in thickness and had poor adhesion [44].

D. E. Meyer, et al. studied the 13.56 MHz inductive coupled plasma CVD tech-

nique. They found that the diamond-like carbon scratching only enhanced the formation of diamond particles on silicon and niobium, but not on stainless-steel substrates [45].

### **Microwave Plasma CVD Techniques**

Based on the number of journal articles, the literature indicates that the microwave plasma CVD process is the most often used technique by diamond film researchers. Various techniques for this approach are described in the following.

For microwave (usually 2.45 GHz) plasma excitation, typically a quartz tube is positioned inside a microwave waveguide, a gas flow is introduced through the tube, and a plasma is produced and confined in the center of the tube. Substrates are mounted in the tube and exposed directly to the plasma which is formed at a gas pressure in the range of 10 to several hundred Torr.

In 1983, M. Kamo, et al. reported diamond synthesis from the gas phase in a microwave plasma [46]. With a methane/hydrogen plasma the deposition rates were approximately 0.5 - 1  $\mu\text{m/hr}$ . A number of subsequent investigations used similar apparatus for diamond synthesis or used a variation where a bell jar is placed in a stub-tuned microwave reactor. For example, single-crystal growth rates over 20  $\mu\text{m/hour}$  were obtained from a methane/hydrogen/oxygen gas mixture by C.-P. Chang, et al. [47]. I. Watanabe and K. Sugata used a microwave plasma to synthesize diamond with different organic gases. Films with deposition rates higher than methane/hydrogen plasmas and with a uniform film thickness over a 5 cm by 3.3 cm area were achieved [48]. J. S. Ma, et al. studied the selective nucleation and growth of diamond on a  $\text{SiO}_2$  dot-patterned Si substrate exposed to a microwave  $\text{CO}/\text{CH}_4/\text{H}_2$  plasma [49]. Epitaxial growth of high quality diamond film on diamond substrate [50] and local epitaxial diamond growth on Si (100) substrate [51] have also been studied by different microwave plasma CVD (MPCVD) techniques.

In an alternative microwave approach, Y. Mitsuda, et al. developed a microwave plasma torch (MW plasma jet) system, which can generate a pure  $H_2$  plasma jet at atmospheric pressure from the end of a center electrode. The electric field has maximum strength at the end of the electrodes, so the plasma is initially ignited by the electric breakdown. Then the plasma jet was powered and sustained by the electromagnetic field generated between the electrodes and/or in the chamber. Diamond films were successfully synthesized at a high rate ( $30 \mu\text{m}/\text{hour}$ ) on an area of  $2.5 \times 2.5 \text{ cm}^2$  from a  $Ar-H_2-CH_4$  mixture gas [52].

Recently, low temperature ( $\leq 500 \text{ }^\circ\text{C}$ ) CVD of diamond films has been addressed as an important task for diamond synthesis because many materials will melt or become unstable at high temperature deposition conditions. Microwave plasma systems have played an important role in this effort. Usually, low temperature deposition is achieved by lowering the gas pressure and the microwave power from normal deposition conditions. For example, a magneto-microwave plasma for deposition of wide area diamond films was reported by Hiraki and his coworkers. In this case, the pressure was reduced to 0.1 Torr and a magnetic field higher than that required for ECR resonance was added to the plasma. The plasma, which is 16 cm diameter wide, filled the reactor. High quality diamond films were formed on a positively biased silicon substrate from a mixture gas of  $CH_4/H_2$  or  $CO/H_2$  [53]. Later, they also successfully deposited low temperature ( $500 \text{ }^\circ\text{C}$ ) diamond films on Al substrates at 0.1 Torr from the  $CH_4/CO_2/H_2$  mixture gas [54].

Growth of diamond films on silicon at  $500 \text{ }^\circ\text{C}$  has been accomplished in a MPCVD system by W. L. Hsu, et al. [55]. Y. Liou, et al. also found that they could deposit diamond films on silicon, MgO, and fused silica at about  $400 \text{ }^\circ\text{C}$  in a bell jar MPCVD system [56]. D. J. Pickrell, et al. successfully deposited diamond both in the plasma and downstream at about  $400 \text{ }^\circ\text{C}$  by using the same system [57]. However, all low

temperature techniques have the disadvantage of extremely low growth rates because of the reduction in the plasma density.

Recently, Norton Company has begun a unique microwave reactor approach, called the microwave plasma disk reactor (MPDR), which was developed at Michigan State University. This is the reactor type used for the research in this dissertation. It is described in detail in chapter 3 (section 2).

### 2.3.3 Other Deposition Methods

In addition to hot filament and plasma approaches to diamond thin film deposition, a number of other interesting methods have been reported. At Rice university, researchers showed that diamond can also be deposited by using the mixture gas of halogen, hydrogen and carbon atoms on a variety of substrates at temperatures as low as 300 °C [58]. In perhaps the simplest procedure in terms of experimental apparatus, acetylene torches ( $C_2H_2$  and  $O_2$ ) have been used for diamond synthesis. Ion beam deposition, in which  $C^+$  ions are directed at a substrate, have been reported by several groups [14, 15, 59, 60, 61, 62, 63, 64] for "diamond-like" carbon films. These films do not have the diamond crystal structure and the 1332  $cm^{-1}$  Raman signal, but they do have some diamond-like properties in terms of transparency and hardness, although generally to a lesser extent than diamond. The method appears less successful at this time for true diamond synthesis. In all diamond film deposition approaches, the challenge is to produce high quality diamond films over large areas with useful deposition rates.

### 2.3.4 Nucleation Methods.

In chapter 2 (section 2) it was noted that enhancing the number of nucleation sites on the surface of the substrates is a precursor to most diamond deposition processes.

Typically the substrates are either abraded with diamond powder or diamond paste, in the size of approximately  $0.1 \mu\text{m}$  to  $40 \mu\text{m}$ , or seeded with small diamond crystallites in order to increase the number of nucleation sites. After a surface abrasion treatment, a cleaning procedure is always followed to remove residue and minimize the contamination. Substrates are cleaned by one or more organic solvents, such as acetone, methanol, ethyl alcohol, ... etc. Sometimes, ultrasonic treatment or acid solutions are also used in order to clean more effectively. There are many kinds of nucleation methods [11-70]. Only a sampling of nucleation methods will be described in the following.

1. C. P. Chang, et al. described that they abraded polished silicon substrates with diamond powder ( $0.5 \mu\text{m}$ ), rinsed the substrate in de-ionized water and blew it dry [47].
2. I. Watanabe and K. Sugata reported that the substrates were roughened for 40 min by diamond powder with a particle size of  $40 \mu\text{m}$  suspended in ethyl alcohol where ultrasonic waves were passing [48].
3. H. Shiomi, et al. reported that the substrates were polished with a diamond paste of  $1/4 \mu\text{m}$  size for 5 min and were de-greased in acetone. Then the substrates were treated in a 1:1 solution of  $\text{HF}$ ,  $\text{HNO}_3$  and in a 1:3 solution of  $\text{HNO}_3$ ,  $\text{HCl}$ . Substrates were finally treated with de-ionized water and acetone [50].
4. J.-I. Suzuki, et al. reported that the substrates received ultrasonic treatment for 30 min in a suspension of diamond powder ( $20 - 40 \mu\text{m}$ ) and ethyl alcohol. After that, they were cleaned in organic solvents [53].
5. Dr. Richard Guarnier, senior engineer in IBM Watson research center, described an electrophoresis seeding method [65]. Diamond powder ( $0.1 \mu\text{m}$ ) is first put in an ethyl alcohol solution and mixed homogeneously. The substrate is positively biased

at 40 V and placed face to face with a 2 cm gap away from a reference electrode for about 30 sec. The substrate is gently taken out of the solution and dried on a spinner. As a result, nuclei are homogeneously seeded on the substrate. In this case there is no subsequent cleaning procedure since that would remove the seeds. In a similar technique, the diamond powder is dispensed on the substrate by an aerosol mist.

6. Professor Aslam and colleagues have described a seeding method whereby diamond powder is in solution with photo-resist, which allows patterned seeding and patterned growth of diamond films [66].

For the nucleation techniques involving direct seeding by diamond powder, the nucleation action is clear. The diamond particles serve as sites for homo-epitaxial growth and the crystallites size increases. Eventually a continuous polycrystalline film results. For nucleation methods which involve abrasion, the nucleation action is less obvious since microscopy generally indicates a clear surface. However, recently S. Iijima, et al. [67] reported that extremely high power transmission electron microscopy (TEM) indicates that abrasion does, even after cleaning, leave very small plaques of diamond,  $\leq 50 \text{ \AA}$  in size, that serve as homo-epitaxial growth sites for individual crystallites in the polycrystalline film. Therefore a hypothesis is that nucleation methods work by providing sites for homo-epitaxial growth. However, it should be noted that the literature does contain some cases where nucleation of substrates is claimed without the use of diamond powder at all. For example, D. E. Meyer, et al. reported that all the substrates were polished or roughened by sandpaper, sand-blasting, or silicon to silicon abrasion. Substrates were cleaned by sonicating in trichloroethylene and acetone [45].

## 2.4 Physical Attributes of Diamond

### 2.4.1 Comparison of Bulk and Film Material Properties

The great interest in diamond is due to its several extreme properties. It has the highest atom number density of any material. Because of its high atom number density and the strong covalent bonding, diamond has the highest hardness and elastic modulus of any material and is the least compressible substance known [64]. These properties contribute to its wide use as an abrasive and cutting material.

But, if you look further into diamond's physical properties as listed in Table 2.1 [68], you will find that the thermal conductivity of diamond is higher than that of any other material, even 5 times that of copper at room temperature. Its thermal expansion coefficient is very low. Electrical resistivity is extremely high and chemical reactivity is extremely low. The combination of these excellent properties makes diamond unique, special, and attractive for many applications.

However, these are the properties of bulk natural diamond. There are some differences between natural diamond and synthetic diamond films which are synthesized by the different kinds of techniques mentioned in chapter 2 (section 3). Those major differences are shown in Table 2.2 [13]. The most prominent difference is that the properties reported for natural diamond are for single crystalline material, but synthetic diamond films on non-diamond substrates are polycrystalline. "Diamond-like" carbon is often amorphous. Consequently, the properties of synthetic diamond films are often not as great as natural diamond. Thermal conductivity, electrical resistivity, and hardness are smaller depending on the techniques used for the diamond synthesis and their experimental parameters.

It should be noted that the "diamond films" produced by those techniques may exist as composites of crystalline diamond and/or amorphous diamond-like carbon

Property	Diamond's Value
Chemical Reactivity	Extremely Low
Hardness	9000 kg / mm <sup>-2</sup>
Heat Conductivity	20 W / cm / degree K @ 30° C
Tensile Strength	0.5 x 10 <sup>6</sup> psi (natural )
Compressive Strength	14 x 10 <sup>6</sup> psi (natural )
Thermal Expansion Coeff.	.8 x 10 <sup>-6</sup> / degree K
Refractive Index	2.41 @ 590 nm
Transmissivity	225 nm - far IR
Friction Coefficient	0.05 (dry)
Band Gap	5.4 eV
Electrical Insulation	10 <sup>16</sup> ohm-cm (natural )
Young's Modulus	10.35 x 10 <sup>12</sup> dynes / cm <sup>2</sup>

Table 2.1. Physical properties of bulk natural diamond.[68]

<b>Property</b>	<b>Bulk Diamond</b>	<b>Diamond and Diamond-like Films</b>
<b>Crystal structure</b>	<b>Face-centered cubic</b>	<b>Amorphous, micrograined polycrystalline</b>
<b>Density ( gm / cm <sup>3</sup> )</b>	<b>3.51</b>	<b>1.8 - 3.4</b>
<b>Hardness ( Mohs )</b>	<b>10</b>	<b>7 - 9</b>
<b>Coefficient of friction ( against steel )</b>	<b>0.05 - 0.15</b>	<b>0.002 - 0.2</b>
<b>Refractive Index</b>	<b>2.42</b>	<b>1.5 - 3.0</b>
<b>Optical transparency ( visible region )</b>	<b>Yes</b>	<b>Yes, but shows interference color</b>
<b>Optical transparency ( infrared region )</b>	<b>Yes</b>	<b>Yes</b>
<b>Electrical resistivity ( Ohm.cm )</b>	<b>Type Ia, b, and IIa: 10<sup>16</sup> Type IIb: 10<sup>3</sup></b>	<b>10<sup>2</sup> - 10<sup>14</sup></b>
<b>Thermal conductivity ( W / cm<sup>2</sup>.K )</b>	<b>10 - 20</b>	<b>5 - 18</b>
<b>Chemical inertness</b>	<b>Most inorganic acids and solvents</b>	<b>Many inorganic acids and solvents</b>

Table 2.2. Properties of bulk natural diamond and synthetic diamond films.[13]

(i-C) and/or graphite. The relative concentration of these phases depend on the synthetic processing conditions. Likewise, the properties of the film strongly depend on the relative concentration of each respective phases. The characteristic properties of these three phases are given in Table 2.3 [21].

So far, we have mentioned diamond films and diamond-like films very often. Sometimes in the literature, particularly for early papers, the terms "diamond films" and "diamond-like films" are used without a clear distinction. But most researchers are trying to clearly specify these two as different categories. Table 2.4 carefully sets the definitions for diamond films, diamond-like films, carbon and graphite coatings [69].

It should be noted that film properties can vary considerably for different deposition techniques. The chemical structure, crystallinity, and thickness have a significant influence on the final film properties. Consequently, the physical, mechanical, electrical, optical and thermal properties of the films are not solely determined by the intrinsic properties of the bulk diamond. In some cases this may be advantageous since film properties can be tailored to the specific requirements of certain applications.

## 2.4.2 Comparison of Semiconductor Properties

Diamond is a very wide bandgap semiconductor ( $E_g=5.45$  eV). Table 2.5 compares diamond semiconductor properties to Si, GaAs, and SiC. Diamond's thermal conductivity is nearly 20 times that of silicon. Also, diamond's saturated carrier velocity, the velocity at which electrons move in a high electric field, is nearly 3 times that of Si and GaAs. The saturated carrier velocity of diamond is also greater than the peak velocity of GaAs. Unlike GaAs, the saturated carrier velocity of diamond maintains its high rate even in a large electric field. The Johnson's figure of merit, of which saturated carrier velocity and peak electric field at breakdown are factors, predicts

<i>Property</i>	<i>Diamond</i>	<i>i-C</i>	<i>Graphite</i>
Crystal structure	Cubic ( $sp^3$ )	Amorphous with small crystal regions mixed with $sp^2$ and $sp^3$ bonds	Hexagonal ( $sp^2$ )
Density ( gm / cm <sup>3</sup> )	3.51	1.8 - 2.0	2.26
Chemical stability	Inert, inorganic acids and solvents	Inert, inorganic acids and solvents	Inert, inorganic acids
Hardness ( Vickers, kg / mm <sup>2</sup> )	7000 - 10000	900 - 3000	---
Thermal conductivity ( W / cm <sup>2</sup> . K )	20	---	K // 30 - 40, K $\perp$ 1-2
Optical properties: Refractive Index Transparency	2.42 UV - VIS - IR	1.8 - 2.2 VIS - IR	2.15 ( // c ), 1.8 ( $\perp$ c ) Opaque
Electrical properties: Resistivity ( Ohm.cm ) Dielectric constant	$10^{16}$ 5.7	$10^{10} - 10^{13}$ 4 - 9	0.04 ( // c ), 0.2 ( $\perp$ c ) 2.6 ( // c ), 3.28 ( $\perp$ c )

Table 2.3. Properties of diamond, i-C, and graphite.[21]

**1. Diamond Film**

- \* semi-transparent to transparent.
- \* hard.
- \* resistivity :  $10^3$  to  $10^{16}$  ohm-cm.
- \* chemically unreactive.
- \* crystalline to X-ray diffraction.
- \* shows Raman peak at  $1332\text{ cm}^{-1}$  .

**2. Diamond-Like Film**

- \* opaque to semi-transparent.
- \* hard.
- \* insulating.
- \* chemically unreactive.
- \* non-crystalline to X-ray diffraction.
- \* shows only a single broad Raman peak around  $1550\text{ cm}^{-1}$  .

**3. Carbon**

- \* black.
- \* hard.
- \* electrically conducting.
- \* non-crystalline to X-ray diffraction.
- \* Raman shows broad peaks centered at  $1350 - 1360\text{ cm}^{-1}$  and  $1580 - 1610\text{ cm}^{-1}$ .

**4. Graphite**

- \* black.
- \* soft.
- \* electrically conducting.
- \* X-ray diffraction showing d value of about 3.3 to 3.4 Angstroms.
- \* Raman shows well defined peak at  $1590\text{ cm}^{-1}$  , may or may not show well developed peak at  $1355\text{ cm}^{-1}$  depending on crystal size and ordering.

Table 2.4. Working definition for different carbon coatings.[69]

the suitability of a semiconductor for high power applications [70, 71]. The Keyes' figure of merit, of which saturated carrier velocity, dielectric constant and thermal conductivity are factors, indicates the thermal limitation of a material on its high frequency electrical performance [70, 71]. From Table 2.5 the combination of high Johnson's figure of merit and high Keyes' figure of merit make it an excellent potential material for high power microwave and millimeter wave devices. It is expected to outperform GaAs and  $\beta$ SiC in microwave device application based on the available data [70, 71]. Moreover, due to the large bandgap of diamond, it can also be used for UV detectors. The combination of high bandgap and high resistivity would reduce the contribution to the photocurrent of thermal and background radiation, thereby make it possible to fabricate low noise UV detectors.

Diamond is also of interest in electronic systems for uses other than as an active electronic material. For example, diamond heat sinks can be fabricated for high power, high temperature, electronic and photonic devices. Diamond windows may be used to permit viewing of an object over a wide optical range from infrared to UV light.

In Figure 2.5 diamond's physical properties are related to various potential engineering applications. But can diamond films really be used to fabricate diamond devices? Yes, however, the fabrication techniques for diamond devices are not quite mature yet. Some of the preliminary diamond devices results will be reviewed in the next section.

## **2.5 Review of Diamond Diodes and Transistors**

In this section selective examples of diamond device work are briefly reviewed.

In 1982, J. F. Prins demonstrated a bipolar transistor action in ion implanted diamond. P-type semiconducting natural diamond was used as the substrate. Then

<b>PROPERTY</b>	<b>DIAMOND</b>	<b>B-SIC</b>	<b>SI</b>	<b>GaAs</b>
<b>Bandgap ( eV )</b>	<b>5.45</b>	<b>2.3</b>	<b>1.11</b>	<b>1.43</b>
<b>Saturated Electron Velocity ( <math>10^7</math> cm / s )</b>	<b>2.7</b>	<b>2.5</b>	<b>1.0</b>	<b>2.0 peak velocity</b>
<b>Carrier Mobility ( <math>\text{cm}^2/\text{V}\cdot\text{s}</math> )</b>				
<b>electron</b>	<b>2200</b>	<b>1000</b>	<b>1350</b>	<b>8500</b>
<b>hole</b>	<b>1600</b>	<b>50</b>	<b>480</b>	<b>400</b>
<b>Dielectric Constant</b>	<b>5.7</b>	<b>9.7</b>	<b>11.9</b>	<b>12.5</b>
<b>Dielectric Strength ( MV / cm )</b>	<b>10</b>	<b>4.0</b>	<b>0.5</b>	<b>0.6</b>
<b>Thermal Conductivity ( W / cm . C )</b>	<b>20</b>	<b>5.0</b>	<b>1.45</b>	<b>0.5</b>
<b>Johnson' s Fig. Merit ( ratio to silicon )</b>	<b>8206.0</b>	<b>1137.8</b>	<b>1.0</b>	<b>6.9</b>
<b>Keyes' Fig. Merit ( ratio to silicon )</b>	<b>32.2</b>	<b>5.8</b>	<b>1.0</b>	<b>0.5</b>

Table 2.5. Comparison of semiconductor properties for diamond, Si, GaAs,  $\beta$ Sic.[70]

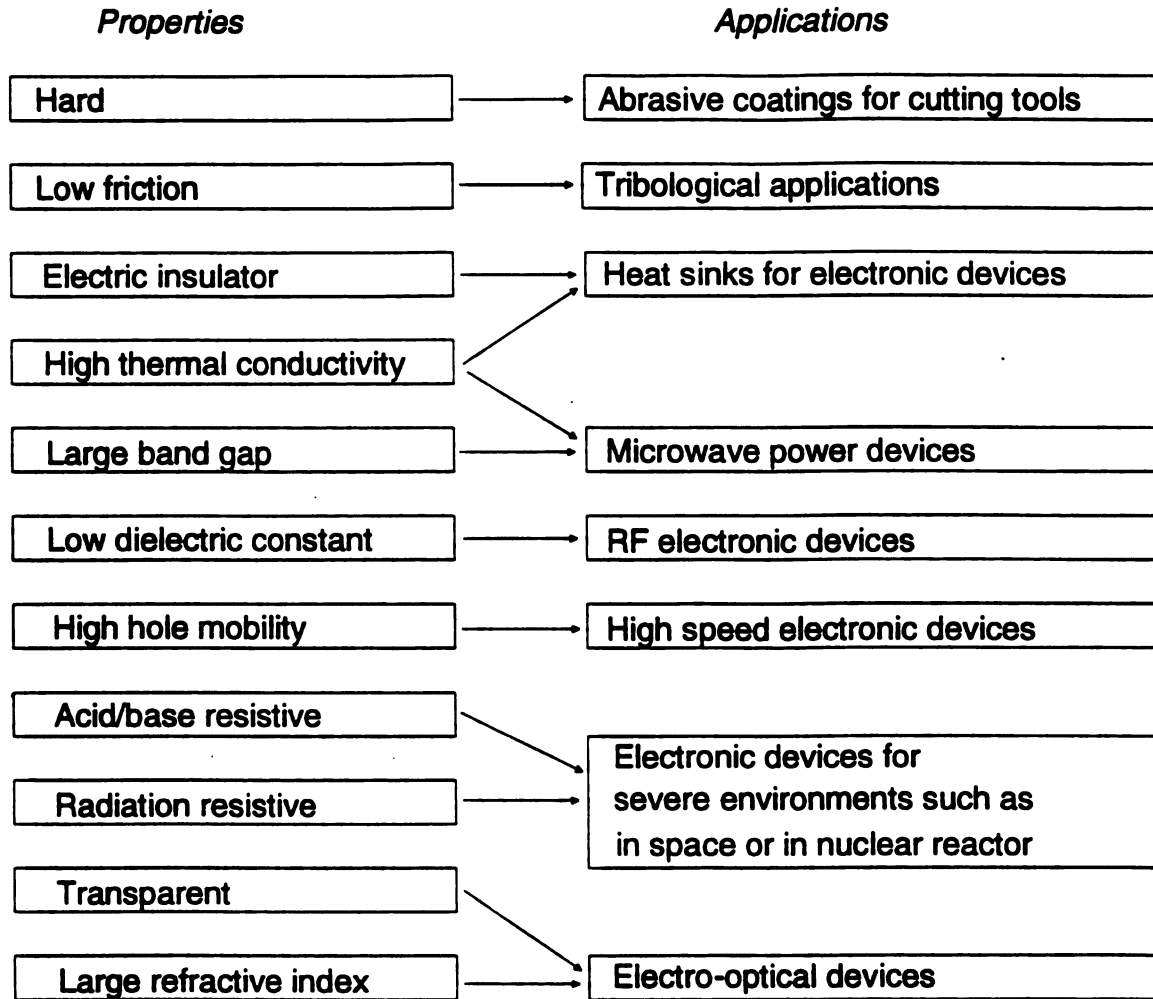


Figure 2.5. Relationship between diamond properties and engineering applications.[70]

n-type layers were induced by implantation of carbon ions. However, very low current gain was obtained by this configuration [72].

In 1987, M. W. Geis and coworkers fabricated high-temperature point-contact transistors and Schottky diodes formed on synthetic boron-doped diamond. The boron-doped single crystal diamond was produced by the high-temperature high-pressure process. The transistors exhibited power gain at 510 °C and the Schottky diodes were operational even at 700 °C [73].

Since 1986 several groups developed methods to synthesize boron-doped diamond films by the microwave plasma CVD technique or the hot-filament CVD technique. A mixture gas of  $B_2H_6/CH_4$  [74, 75, 76, 77] or a saturation solution of  $B_2O_3$  powder in  $CH_3OH$  mixed with acetone [78] are the most often used methods. Also, placing boron powder [79] or boric acid [51] near the substrate during the diamond synthesis is also used to get boron-doped films.

In 1989, H. Shiomi et al. fabricated metal-semiconductor field-effect transistors (MESFET) using boron-doped diamond epitaxial films. This is the first report of a planar type transistor using a diamond film. The single crystal diamond substrate was prepared by the high-temperature and high-pressure process. A high-quality boron-doped epitaxial diamond film was then obtained on the single crystal diamond by a plasma assisted chemical vapor deposition method. Ti was evaporated for the source and drain ohmic contacts by the electron beam method. Al was thermally evaporated for the gate Schottky contact. Basic transistor operation was observed [81].

In 1991, K. Okano et al. made a diamond p-n junction diode by the hot-filament CVD method. Since silicon was used as the substrate, the synthetic diamond films were polycrystalline.  $P_2O_5$  and  $B_2O_3$  were used for the doping source. Rectifying characteristics were observed [82].

G. Sh. Gildenblat and coworkers fabricated a high-temperature thin-film diamond field-effect transistor by using a selective growth method. A natural single crystal diamond was used as the substrate. Selective growth of boron-doped homo-epitaxial diamond films was achieved using sputtered  $SiO_2$  as a masking layer. The device was operational at 300 °C. [83]

W. Tsai, et al. developed a diamond MESFET using ultra-shallow rapid thermal processing (RTP) boron doping. A novel doping technique was used to drive in and activate boron in natural type IIa diamond. An ultra-shallow p-doped channel of less than 500 Å was created by RTP solid-state diffusion using cubic boron nitride as the dopant source. A device pinch-off phenomenon was observed for the first time [84].

M. W. Geis and coworkers also found that the metal- $SiO_2$ -diamond structure on (100)-oriented substrate is more acceptable for a depletion-mode metal-oxide-semiconductor field-effect transistor (MOSFET). Type IIb natural diamond was used as the substrate in this work [85].

It is noted that commercial fabrication of diamond electronic devices is not a reality, however, many researchers are devoted to optimize the deposition processes and develop techniques for the fabrication of diamond devices. For example, the technique of selective growth of diamond has been much improved in recent years [86, 87]. N-type doping has been performed by incorporation with lithium [88] and by using  $P_2O_5$  as a doping source in the process [82]. In terms of achieving hetero-epitaxial films, large-area mosaic diamond films approaching single crystal quality has been obtained on the silicon substrate [89]. Consequently, significant progress is being made on overcoming technological problems associated with the fabrication of diamond devices.

# **CHAPTER 3**

## **Film Deposition and Sample Preparation**

### **3.1 Introduction**

In this chapter, the detailed configuration of the MPDR deposition system will be explained in chapter 3 (section 2). Then the description of the nucleation methods and the film deposition process will be presented in chapter 3, section 3 and section 4 respectively. Finally, the fabrication processes of the samples for physical characterization and electrical studies, such as four-point probe samples, metal-diamond-silicon samples, and back-etched diamond samples, are described in chapter 3 (section 5).

### **3.2 The MPDR System**

#### **3.2.1 The Microwave Cavity**

A tunable microwave plasma disk reactor (MPDR) system [2, 3] is used for microwave plasma assisted CVD (MPACVD) diamond synthesis. The cross section of the MPDR and quartz processing chamber are shown in Figure 3.1.

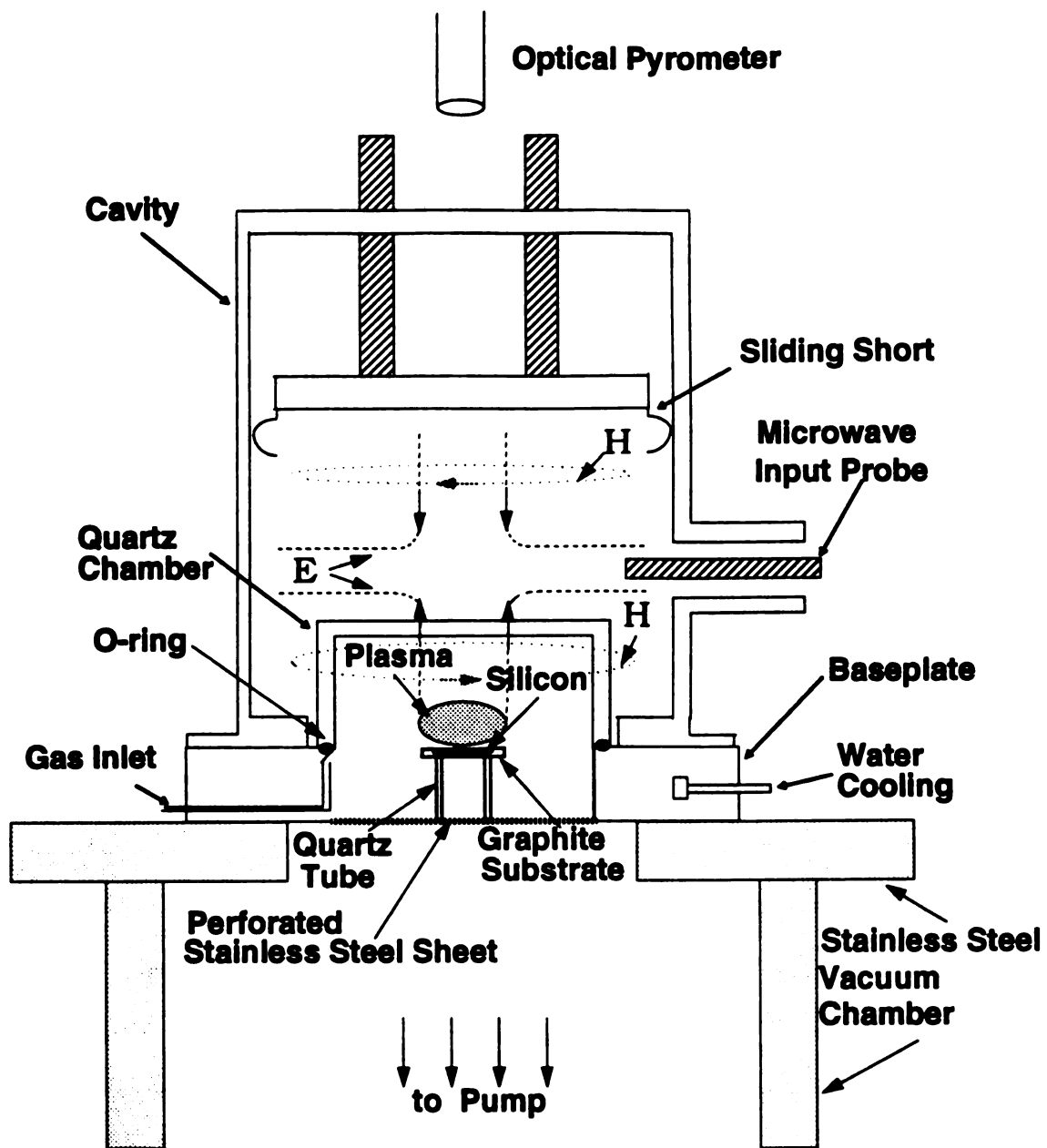


Figure 3.1. The cross section of the MPDR and processing chamber, and a schematic display of the electric (E) and magnetic (H) field patterns of the  $TM_{011}$  mode.

The body of the cavity is a 17.8 cm (7 inch) inner diameter double-wall brass cylinder, with water cooling between the walls. The upper end of the cylinder is terminated by a movable sliding short. The baseplate and quartz chamber are in the lower end of this structure. Microwaves are introduced into the system via a short antenna, which is a coaxial microwave input probe. The length of the probe inside the cavity,  $L_p$ , is adjustable and serves as one of the two tuning parameters. The other tuning parameter, the length of the cavity ( $L_s$ ), may be varied by adjusting the sliding short. Using these two degrees of tuning, it is possible to match the impedance of the cavity/plasma system to the microwave power source. A perforated stainless steel sheet is affixed to the baseplate in the bottom part of the processing chamber and serves to terminate the cavity and still allow gas to flow through.

The baseplate consists of an opening for the discharge chamber, gas inlets, and water cooling. The plasma is centrally contained under a quartz disk which is vacuum sealed to the baseplate by a viton O-ring. The height of the discharge chamber measured from the bottom of the baseplate to the top surface of the quartz disk is 9.5 cm. It is 3.5 cm from the perforated stainless steel sheet to the stage where the quartz disk sits on, and 2 cm from the stage to the top surface of the cavity bottom respectively. The height of the quartz disk is 6 cm and its inner diameter is 9.25 cm. Thus, the top of the quartz disk is 4 cm above the cavity bottom surface.

There are 16 small holes which serve as the gas inlets located in the inner surface of the baseplate. Pre-mixed gas from multiple gas tanks is uniformly distributed to each of these gas inlets by a common gas channel, which is located at the inner region of the baseplate.

Water cooling of the system is accomplished through the double wall cylinder and through a circumferential channel inside the baseplate. The latter cooling channel protects the viton O-ring. Also, the baseplate is designed to allow low pressure

electron cyclotron resonance (ECR) operating conditions. For such operation, eight rare-earth magnets are placed inside the baseplate. [6] Since the magnets are sensitive to high temperature, cooling is achieved through the water channel surrounding the magnets. However in this work, plasma pressures were too high to allow ECR operation, so the magnets were removed.

### 3.2.2 The Deposition System

The input microwave system consists of a 2.45 GHz Cheung power source (model MPS2450-1200), a three port circulator, a matched dummy load, a cross waveguide directional coupler, power meters and waveguides as shown in Figure 3.2 [90]. The Cheung microwave power source can produce stable power from 200 to 1200 watts. The output of the microwave source is attached to a three port circulator, which protects the magnetron from reflected power by directing radiation toward the microwave source into a  $50 \Omega$  matched dummy load. Incident and reflected power are sampled by a cross waveguide direction coupler and are further diminished by 30 db attenuators before being measured by the power meters. Microwave power is then coupled from a waveguide to the cavity input probe.

The HP 435A microwave power meters are used to measure incident power  $P_i$  and reflected power  $P_r$  at the cavity. The microwave power coupled into the plasma loaded applicator, which is the microwave absorbed power, is given by  $P_a = P_i - P_r$ . By tuning the wall probe and sliding short,  $P_r$  is generally less than or equal to 10 % of  $P_i$ . Due to losses in the input system, waveguide and cavity, about 15 % of the power is dissipated as heat. Consequently, the microwave absorbed power is about 75 % of the the power supplied from the microwave source.

Figure 3.3 gives a schematic diagram of the MPDR CVD system. Up to four different gases may be mixed by a 4-channel (model MKS 1159A) mass flow controller.

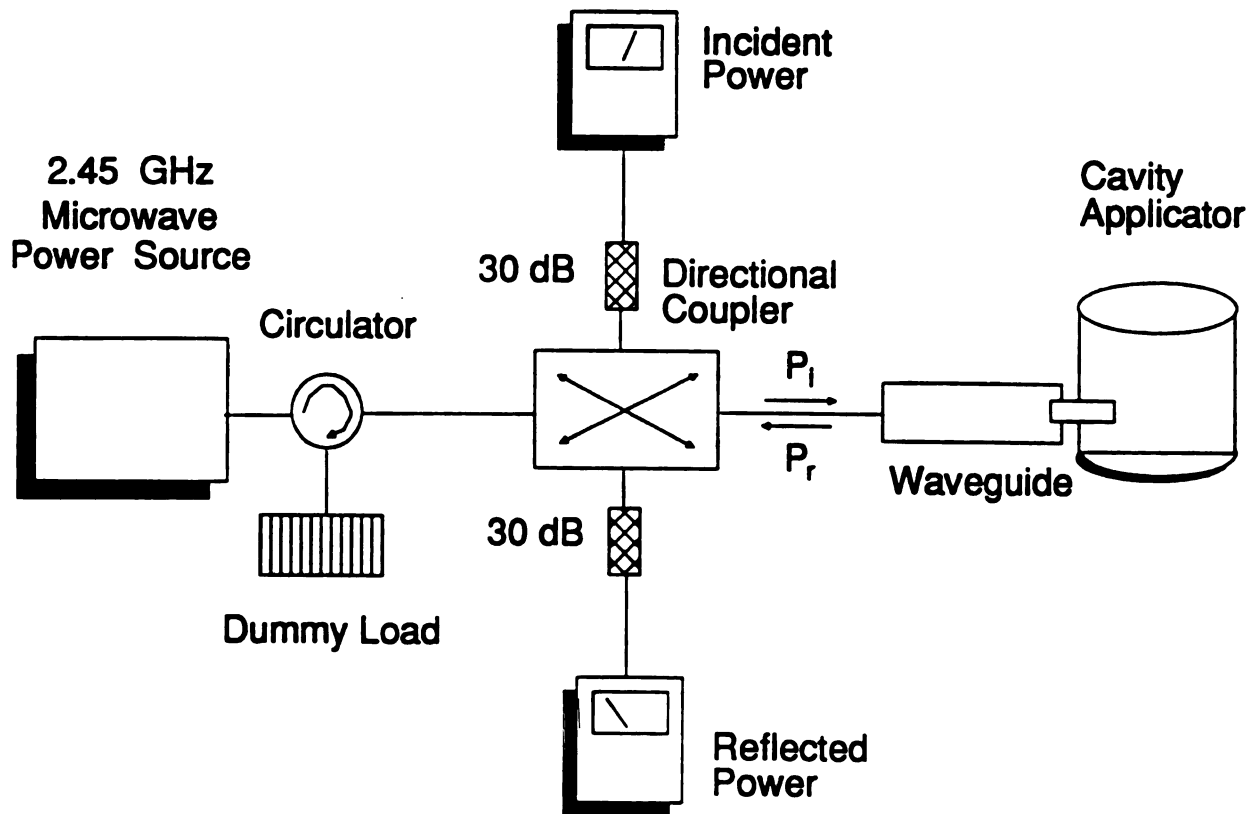


Figure 3.2. The microwave power source, circuit, and cavity applicator.

The flo

respect

a single

A la

In some

not use

is perfo

stainless

vacuum

122A) c

vacuum

to 1 Torr

region (1

the range

condition

same op

pump (n

The s

pump is

gases. In

between

gases, nit

The flow controllers have maximum operating flows of 10,000, 500, 100, and 10 sccm respectively. The gas output of each mass flow controller is mixed simultaneously into a single gas channel which feeds the quartz processing chamber through the baseplate.

A large stainless steel vacuum chamber is below the baseplate and quartz chamber. In some cases, this could be used as a downstream processing chamber, although it was not used as such in this research. [6] Pressure measurement within the vacuum system is performed through four vacuum gauges. There are three gauges connected to the stainless steel vacuum chamber; a baratron pressure gauge, a thermal conductivity vacuum gauge, and an ion pressure gauge. The baratron pressure gauge (model MKS 122A) can determine pressure from 0.1 Torr to 1000 Torr. The thermal conductivity vacuum gauge (TC2) (model MKS 286) can accurately measure pressure from 1 mTorr to 1 Torr, and the ion gauge (model MKS 290) is able to measure in the high vacuum region ( $10^{-3}$  to  $10^{-9}$  Torr). These three different pressure gauges can therefore cover the range from very good vacuum to above an atmosphere depending on the operating conditions. In addition, a second thermal conductivity vacuum gauge (TC1) with the same operating pressure range is located between the roughing valve and roughing pump (mechanical pump).

The system is pumped down by a Alcatel 2033 roughing pump. The mechanical pump is filled with Alcatel 200 oil which is safe for pumping hydrogen and methane gases. In order to minimize the backstream oil from the pump, a baffle trap is placed between the pump and the chamber. Because the hydrogen and methane are explosive gases, nitrogen gas is also used to purge the gas exhaust for safety reasons.

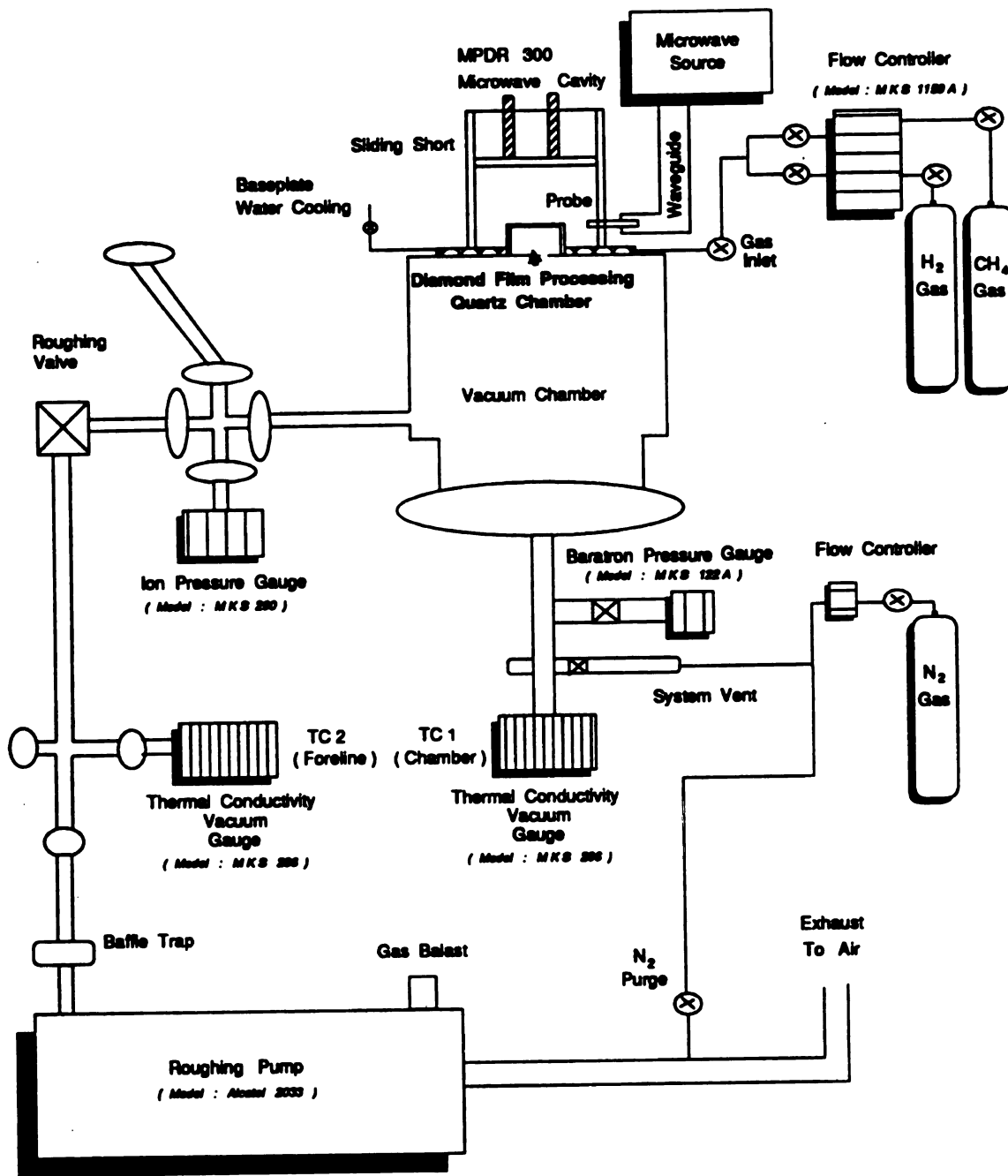


Figure 3.3. The diagram of the MPDR CVD system.

### 3.3 The

A wide variety of approaches to diamond synthesis. The diamond powder is described in detail as follows:

The diamond

1. 0.25  $\mu\text{m}$  diamond powder (TEXMET powder) is used. Metadi lubricant is used for diamond paste. The diamond is rubbed back and forth on the substrate surface.
2. Step 1 procedure is repeated, finishing a kimura substrate surface.
3. Next the substrate is rinsed immediately with water for about 10 minutes.
4. The substrate is treated with a solution of  $1\text{H}_2\text{O}_2 : 1\text{NH}_4\text{OH}$ . The solution is left overnight and then rinsed with  $\text{N}_2$ .
5. The substrate is treated with a solution of  $2\text{H}_2\text{O}_2 : 1\text{HCl}$ . The solution is left overnight. Again, it is rinsed with  $\text{N}_2$ . Step 4 and 5 from

### 3.3 The Nucleation Methods

A wide variety of nucleation methods are described in chapter 2. In this research, two approaches were used to do the sample polishing and cleaning before the diamond synthesis. They are **1. the diamond paste nucleation method**, and **2. the diamond powder nucleation method**. The two nucleation methods will be described in detail as follows.

#### **The diamond paste nucleation method :**

1. 0.25  $\mu\text{m}$  Buehler Metadi synthetic diamond paste was placed on a Buehler TEXMET polishing cloth sheet, which is water and oil resistant. Then Buehler Metadi lubricant oil was sprayed onto the paste. The substrate was placed onto the diamond paste position and was gently polished by hand for about 20 min by using rubbing back and forth motions.
  2. Step 1 produces a substrate surface which has a dirty appearance. After the polishing, a kimwipe with some acetone was used to get rid of the dirty stain on the substrate surface as much as possible.
  3. Next the substrate was placed in a boiling TCE solution for 3 min. Then it was rinsed immediately in running acetone, running methanol, and running de-ionized(DI) water for about 60 sec each. Finally it was dried with nitrogen gas ( $N_2$ ).
  4. The substrate was then immersed in a freshly prepared degrease etch ( $5H_2O : 1H_2O_2 : 1NH_4OH$ ) for 10 min at about  $70^\circ\text{C}$  to remove residual organic contamination left over from the solvent cleaning. Then it was rinsed in DI water and dried with  $N_2$ .
  5. The substrate was next immersed in a freshly prepared de-metal etch ( $8H_2O : 2H_2O_2 : 1HCl$ ) for 10 min at about  $70^\circ\text{C}$  to remove ionic and metallic contaminants. Again, it was rinsed in DI water and dried with  $N_2$ .
- Step 4 and 5 from the RCA cleaning procedure are widely used in the silicon industry.

(

i

v

s

s

li

ti

1.

m

2.

si

pr

3.

to

4.

bi

sti

ma

nov

and

scri

cas

[91]

6. After the RCA clean, the substrate was placed in a 9:1  $H_2O:HF$  diluted solution in order to get rid of the thin oxide layer. This was again followed by a rinse in DI water and a dry with  $N_2$ .

The substrate at this point was ready for the diamond film deposition. If the substrate was a silicon wafer polished to a mirror finish, then after step 6 one cannot see scratches easily on the shining surface by eye unless it is observed under a strong light. No diamond particle residue was found either by the optical microscope or by the scanning electron microscope as shown in Figure 3.4.

**The diamond powder nucleation method :**

1. The substrate was cleaned by following step 3 to step 6 of the diamond paste method.
2. Dry 1  $\mu\text{m}$  natural diamond powder was spread on a 3-inch diameter sacrificial silicon wafer which was used as a lapping surface. The substrate surface was then prepared by gentle polishing by hand on the sacrificial wafer for about 2 min.
3. Following the polishing process, the substrate receives an ultrasonic acetone/methanol cleaning for 5 min respectively.
4. The substrate also received a diluted  $HF$  solution treatment, DI water rinse and blow dry with nitrogen.

At this point the substrate was ready for the diamond film deposition. If the substrate was originally mirror-polished silicon, after step 4 one can easily see a marked difference of the surface. The surface is filled with a lot of scratches and is now hazy compared to the previous mirror-like surface. Under the optical microscope and the scanning electron microscope, the surface is seen to be rough and full of scratches as compared to the diamond paste nucleation method. In Figure 3.5 one can easily see the difference of the surface prepared by the powder nucleation method.

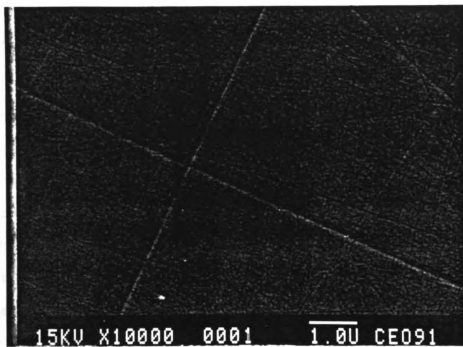


Figure 3.4. SEM pictures of the silicon substrate prepared by *diamond paste method*.

W

In ot

treat:

### 3.4

#### 3.4.1

In the

are se

a given

by virt

MW p

Alt

[92], th

geomet

single c

have be

mode w

pressure

tuned to

Torr. by

the quar

operatin

length an

$TM_{011}$  m

What are the effects of the nucleation mechanism on the diamond film growth? In other words, is there any difference on the film growth after different surface treatments? The answer is yes! It will be described in the next section.

## 3.4 Diamond Film Deposition

### 3.4.1 Operation of The System

In the MPDR, a microwave (MW) plasma is generated within a resonant cavity. There are several advantages over radio-frequency (rf) and direct current (dc) plasma. For a given power input and plasma size, the electron density is higher in a MW plasma by virtue of the higher frequency, so its reactivity is expected to be very high. Since MW plasma can be electrodeless, electrode contamination can be eliminated.

Although the electromagnetic modes of a perfect cylindrical cavity are well known [92], the introduction of a plasma into the cavity can significantly alter the field geometry. However, the MPDR can create a microwave discharge when excited in a single cavity electromagnetic mode. For example, in the past experimental discharges have been sustained in the  $TE_{111}$  [93],  $TE_{211}$  [3],  $TM_{012}$  and  $TM_{011}$  modes [94]. Each mode was experimentally evaluated for its potential to deposit films at discharge pressures of 30 - 90 Torr. The cavity applicator was first length ( $L_s$ ) and probe ( $L_p$ ) tuned to a specific mode. Then a discharge was started at a gas pressure of 5 - 10 Torr, by applying microwave power which then ignited a discharge that entirely filled the quartz processing chamber. The discharge pressure was then increased to an operating condition of 30 - 90 Torr by manually adjusting the roughing valve while length and probe tuning the cavity to a matched condition. It was found that the  $TM_{011}$  mode is superior to the others in this pressure range and set-up. [10]

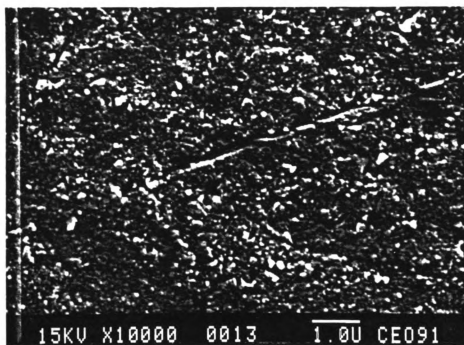


Figure 3.5. SEM pictures of the silicon surface prepared by *diamond powder method*.

The experimental parameter space is large, since the microwave power,  $CH_4/H_2$  ratio, substrate material, shape of the substrate, position of the substrate, discharge pressure (plasma pressure) all may contribute to the quality of the diamond deposition. A systematical operation procedures should be conducted in order not to inadvertently introduce new parameters. Consequently, a well defined procedure of operation for "turning on" and "shutting off" the MPDR CVD diamond system was developed as follows.

**The procedures of turning on the system :**

1. The substrate received the surface treatment either by diamond powder nucleation method or diamond paste nucleation method before putting it into the quartz processing chamber. The size of the substrate was always 2 cm × 2cm for silicon and 1.2 cm × 1.2 cm for silicon nitride.
2. The system stand-by condition is under vacuum. So the first step was to close the baratron valve, open the system vent valve, and allow the nitrogen gas to flow into the quartz chamber until the chamber pressure reaches atmosphere. Then the quartz disk and the sliding short are removed from the system.
3. Silicon substrates were typically mounted on a 0.1 inch thick graphite holder with a 2 cm × 2 cm recessed area. The graphite holder was placed on a quartz tube, typically 3.25 cm high, which stands on the perforated stainless steel sheet, contained in the quartz processing chamber. The silicon nitride substrates were mounted directly on the quartz tube without a graphite susceptor. In both cases, the substrates were in a position along the cavity axis.
4. The quartz disk was positioned such that it smoothly fit the viton O-ring. The system vent valve was closed and the processing chamber was evacuated by the roughing pump with an ultimate pressure of  $10^{-4}$  Torr. The baratron readout was then adjusted to zero.

5.

ap

$L_r$

im

6.

w

99

ga

an

7.

T

th

30

th

T

tu

th

T

99

8.

th

pro

ure

me

5. The sliding short was placed in the cavity, then the cavity length  $L_s$  was set to approximately 7 cm which is the position for the  $TM_{011}$  mode. The probe position  $L_p$  was set at about 1.8 cm which corresponds to maximum absorbed power and minimum reflected power.
6. After the reading in both of the thermal conductivity vacuum gauges (TC1, TC2) was almost zero, gas was introduced into the discharge chamber. 99.999 %  $H_2$  and 99.99 %  $CH_4$  Airco gases are used in this research. The flow rate and ratio of the gases were monitored through the 4-channel gas flow controller. The nitrogen purge and water cooling were on from this point throughout the whole process .
7. The roughing valve was "throttled" to increase the chamber pressure up to 5 to 10 Torr as measured by the baratron gauge, then MW power was applied. At ignition the discharge completely filled the quartz chamber, but as the pressure increased to 30 - 90 Torr (It takes about 5 - 15 min), the discharge contracted and separated from the surrounding quartz walls and formed a roughly semi-spherical shape when the  $TM_{011}$  mode was used. During the plasma pressure increase, cavity length and probe tuning are still necessary to minimize the reflected power. Visual inspection showed that the discharge uniformly covered the whole substrate under this particular mode. Typically, the microwave input power and plasma pressure are in the range of 400 - 900 watts and 50 - 80 Torr respectively.
8. Typically the system ran for 5 - 10 hours in order to get the desired thickness of the diamond films. For the duration of the run, the roughing valve was monitored to provide the desired plasma pressure.

Operation of the MPDR CVD system during the film growth is shown in Figure 3.6. One can see the discharge glowing inside the cavity through a transparent metal-screened side window.

**The procedures of shutting off the system :**



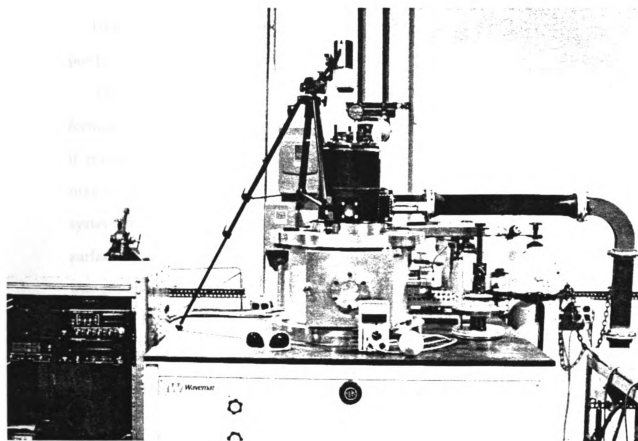


Figure 3.6. The MPDR CVD system during the diamond film deposition.

1. The MW power was reduced from several hundred watts down to 0 immediately and the gas flow of both hydrogen and methane gases were turned off. Also the roughing valve was fully open to rapidly eliminate the gases from the discharge chamber. At this point, the TC1, TC2, and baratron pressure gauges all read almost zero.
2. A 20 min period was allowed to let the system cool down. Then the water cooling was turned off and the system was vented to nitrogen and the sample was removed.

Unless otherwise noted, these were the procedures for starting and ending a deposition process.

The procedure to terminate the deposition process is crucial to the question of formation of a surface conducting layer on top of the diamond film. For example, if reactive gases continue to flow while the substrate is cooling, a graphite layer may be formed. Early in the research, another approach was used to turn off the system. First, the methane flow was turned off to prevent graphite formation on the surface of the diamond film but the hydrogen was left on. Second, the hydrogen flow was gradually reduced, and then the microwave power was turned down immediately. However, Raman characterization showed a graphite peak instead of the diamond peak on one of the samples under this procedure. The energy of the hydrogen plasma is high enough to convert diamond into carbonaceous conducting layer. [32, 79]

### **3.4.2 Experimental Parameters**

The experimental deposition parameters varied in this research are summarized as follows.

**Methane Concentration** : The percentage of methane in the methane/hydrogen mixture was varied from 0.5% to 1.5%.

**Microwave Power** : The microwave input power was varied from 400 W to 900 W.

**Plasma Pressure** : The plasma pressure range investigated was from 50 to 80 Torr.

**Gas Flow :** Total gas flow was varied from 100 sccm to 250 sccm.

**Substrate Position :** The quartz pedestal length was varied from 2.5 cm to 3.5 cm.

Additional deposition parameters, as described elsewhere in this chapter, are the choice of substrates (silicon or silicon nitride) and the nucleation procedures (diamond paste method or diamond powder method). It should be noted that there is a big difference between the deposited diamond films which are prepared by diamond powder method and diamond paste method. Large grain (greater than 1  $\mu\text{m}$ ) size diamond films were obtained by the diamond paste prepared method, and small grain (sub-micron) size films were achieved by the diamond powder prepared method. A more detailed study of the grain size difference will be discussed in chapter 4.

### 3.4.3 Substrate Temperature

In the last subsection, it was noted that during the film growth the position of the substrate, flow rate,  $\text{CH}_4/\text{H}_2$  concentration, microwave power, and plasma pressure are all experimental parameters. Each of these may contribute to the film properties either directly or indirectly in that they affect the substrate temperature. In this research, the substrate was self-heated by the plasma and microwave power. Consequently, changing the deposition conditions generally changed the substrate temperature.

Temperature is a very important parameter in any CVD process, including diamond film deposition. Most often, good quality diamond films are deposited with a substrate temperature between 800  $^\circ\text{C}$  and 1100  $^\circ\text{C}$  [10-60]. Usually, there are two ways to determine the substrate temperature. One way is to determine the substrate temperature by direct contact as for example by a thermocouple through the substrate holder, which is on the down side of the substrate. However, microwave coupling to the thermocouple wire is a potential problem in this approach. Another

way is to determine the temperature without direct contact as for example with an optical or infrared pyrometer. For a microwave applicator one means of optical access is through the system window, which is on the top side of the substrate. Generally the windows are shielded by a metal screen which provides microwave power leakage protection. In this case the measurement goes through the metal screen, transparent window quartz wall, and discharge to the substrate. Pyrometer calibration is always a questionable matter in such a situation. The temperatures reported for good quality diamond films by direct contact with a thermocouple (800 °C to 950 °C) are often lower than those reported by the pyrometer methods (900 °C to 1050 °C).

In our design, the original sliding short on the MPDR can be replaced with a short constructed with an axial opening to allow vertical optical access to the substrate as shown in Figure 3.7. A brass collar is used for shielding the MW leaks. The advantage of this set-up is that one can measure the temperature through only quartz and plasma to the substrate. Without a metal screen, calibration for the measuring device is much easier and temperature measurement accuracy improved. Generally these vertical pyrometer measurements produced higher (100 °C - 150 °C) readings than pyrometer readings through the metal screened window.

An Ircon Ultimax optical pyrometer (model UX-20), with working temperatures between 600 to 3000 °C, was used for measuring the substrate temperature. This is a small spot size instrument which has a spot size approximately equal to  $D/100$  mm where  $D$  is the focusing distance. This device has a focal range from 500 mm to infinity, but close focus lenses can be used to reduce the focal range. There are four different close focus lens with focal ranges of 100 - 130 mm, 130 - 180 mm, 180 - 290 mm, and 250 - 540 mm respectively. The unit was generally used with a 370 mm focus distance, which corresponds to a spot size of 3.7 mm. This makes it possible to measure the temperature distributions across the substrates.

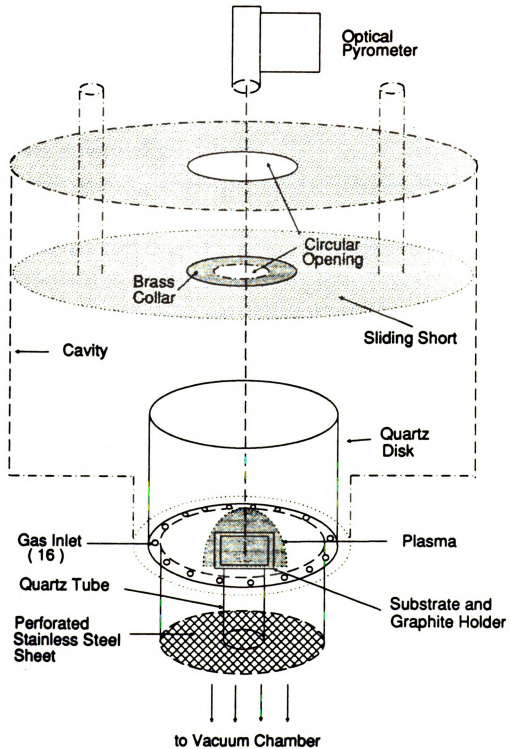


Figure 3.7. Top view of the MPDR processing chamber.

Eac

this de

0.92 is

comes

respect

temper

For

on eac

mm fro

Howev

In som

in Figu

of the c

less tha

Fig

for 1 %

and 60

graphit

obvious

temper

Fig

the pre

higher

shrinks

microw

supply.

Each material has different emissivity, which is the main calibration factor for this device. When the silicon emissivity of 0.89 and the silicon nitride emissivity of 0.92 is multiplied by the quartz correction factor of 0.95, the corrected emissivity comes to 0.85 and 0.88 for measuring the temperatures of silicon and silicon nitride respectively. Then the calibration is also confirmed using silicon wafers at comparable temperatures in thermal diffusion furnaces.

For several runs at various deposition conditions, 9 spot measurements were made on each substrate. The corner and side measurement points were approximately 2 mm from the edge of the substrate. Figure 3.8 (a) shows a typical temperature profile. However the uniformity is quite dependent on substrate position and cavity tuning. In some cases much better profiles were observed. A better uniformity case is shown in Figure 3.8 (b). Generally, all points showed temperatures within plus/minus 5 % of the center temperature. However, better uniformity was sometime achieved within less than 1 %.

Figure 3.9 and Figure 3.10 show the substrate temperature dependence on power for 1 % and 0.5 %  $CH_4/H_2$  concentrations for two different plasma pressures, 50 Torr and 60 Torr. At both cases, a 2 cm  $\times$  2 cm silicon wafer was placed on a 0.1 inch thick graphite holder which is supported by a 3.25 cm high quartz pedestal. There is no obvious temperature difference for the 1 % and 0.5 % concentration depositions. The temperature increases with increasing microwave power in a nearly linear fashion.

Figure 3.11 and Figure 3.12 show the the same data plotted so as to demonstrate the pressure dependence of substrate temperature. With higher plasma pressure, higher substrate temperatures were observed. At higher pressures, the plasma ball shrinks and the energy is concentrated nearer the substrate. In all the above cases, the microwave input powers listed are shown as measured by the Cheung microwave power supply. The actual power delivered into the cavity is about 75 % of the microwave

(a)

(b)

Figure 3  
the silico

(a)

905°C	930°C	960°C
910°C	950°C	980°C
915°C	950°C	985°C

Microwave  
Probe

Screened Window

(b)

1070°C	1070°C	1060°C
1075°C	1076°C	1080°C
1080°C	1085°C	1090°C

Microwave  
Probe

Screened Window

Figure 3.8. (a) Typical temperature profile and (b) better temperature uniformity of the silicon substrate.

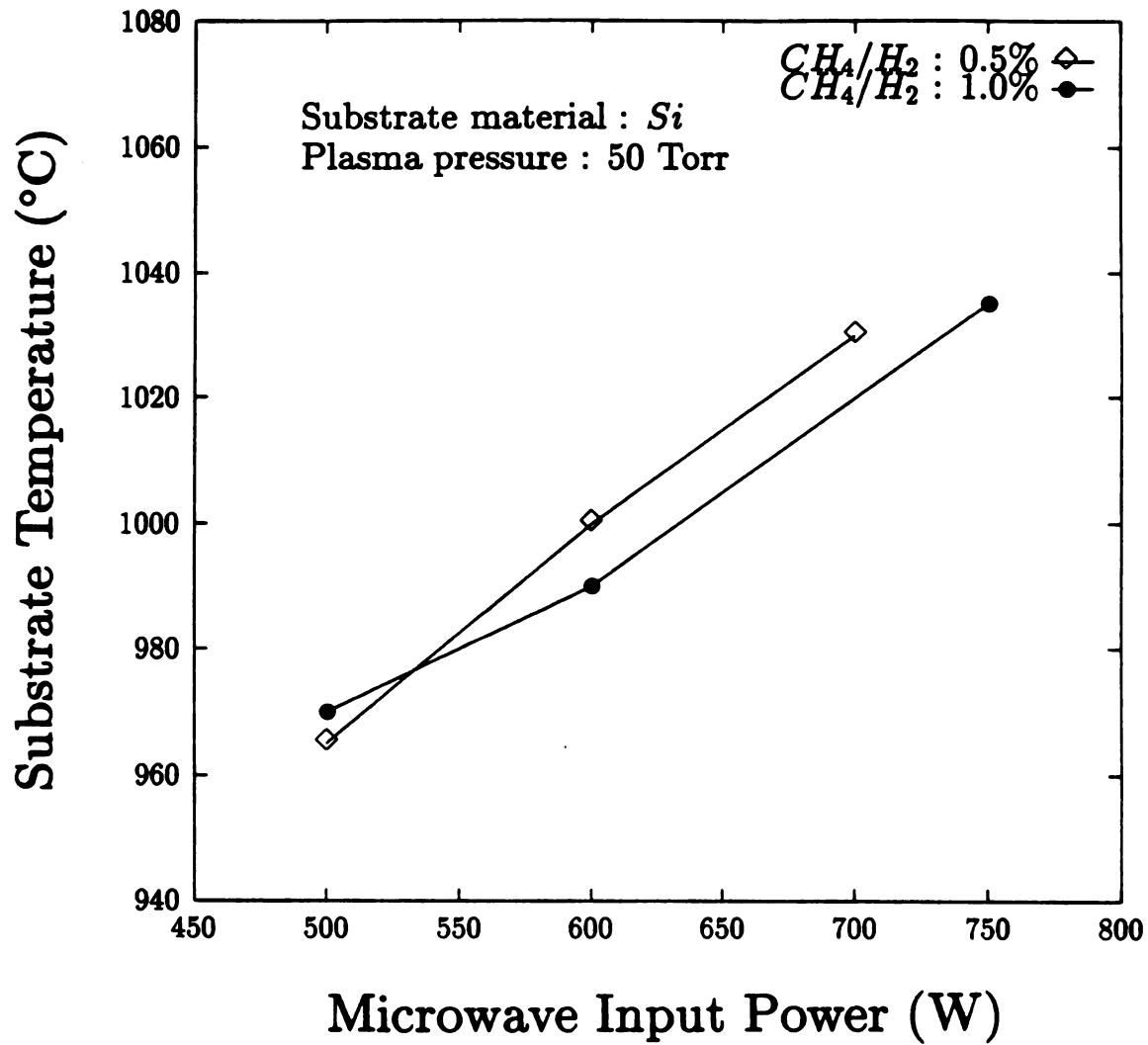


Figure 3.9. Si substrate temperature vs. microwave input power for 1 % and 0.5 % methane concentration at 50 Torr.



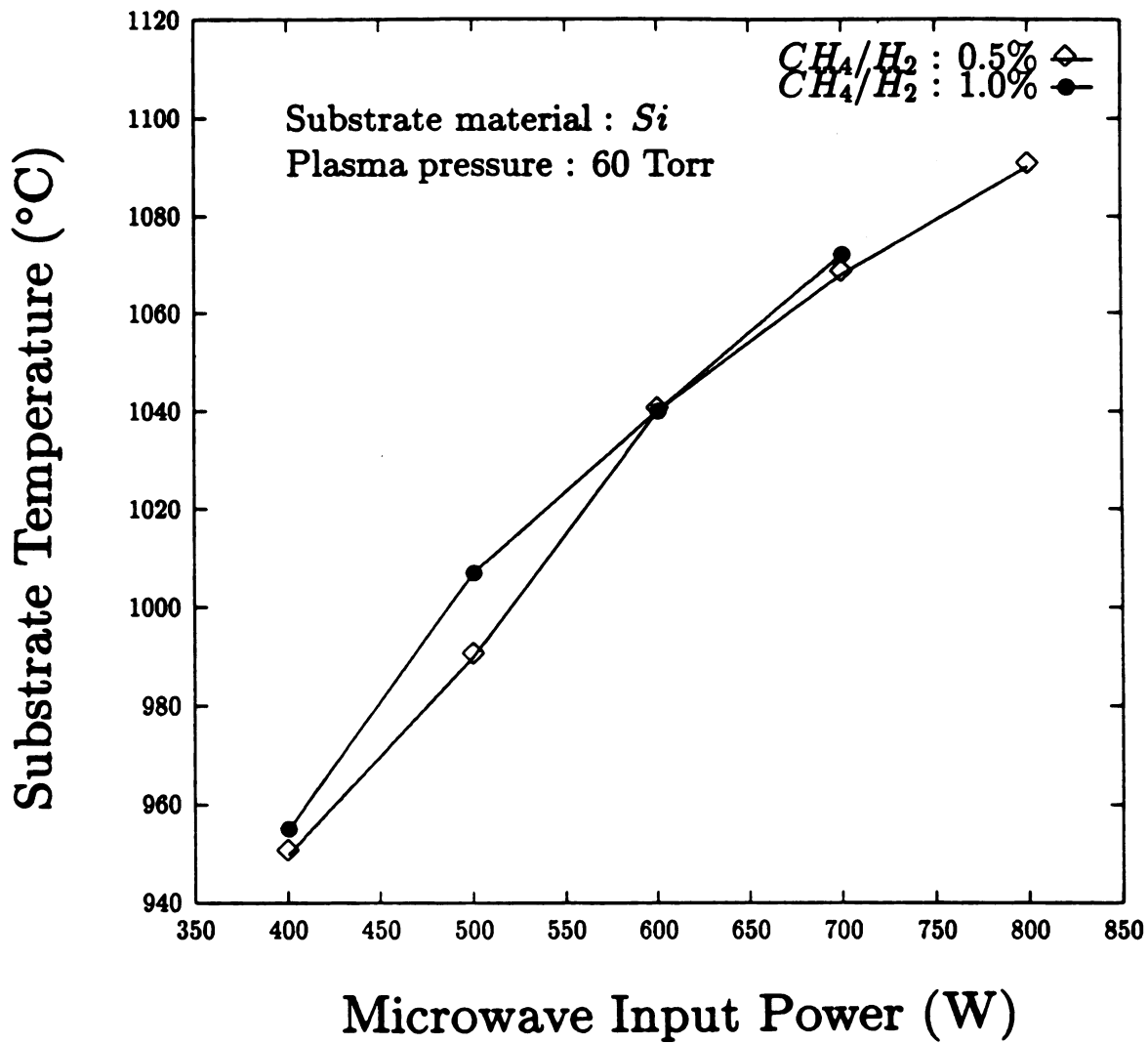


Figure 3.10. Si substrate temperature vs. microwave input power for 1 % and 0.5 % methane concentration at 60 Torr.

powers from the Cheung microwave source.

When silicon nitride substrates were used, a  $1.2\text{ cm} \times 1.2\text{ cm} \times 0.5\text{ cm}$  substrate was supported on a 2.75 cm high quartz pedestal without a graphite holder. Figure 3.13 shows the temperature difference between silicon and silicon nitride for 0.5 % methane concentration at 50 Torr. The substrate temperature of silicon nitride increases almost linearly with microwave power and is higher than that of silicon at the same deposition conditions. The reason for the higher temperature with silicon nitride is that the surface area is smaller than the silicon. The plasma will then contribute more energy per unit area on the silicon nitride samples as compared to the silicon samples.

## **3.5 Fabrication of Electrical Samples**

### **3.5.1 Four-Point Probe Samples**

Silicon nitride, which is an insulating composite ceramic material, was used as the substrate for fabricating four-point probe samples. As described in chapter 3 (section 4), a  $1.2\text{ cm} \times 1.2\text{ cm} \times 0.5\text{ cm}$  silicon nitride sample was placed directly on a 2.75 cm high quartz pedestal for deposition. Both diamond powder and diamond paste nucleation methods were used to prepare the substrate. The as-received silicon nitride substrates showed an uneven surface upon microscope examination, with multiple trenches and ridges which were on the order of a few micrometers wide and deep. However, the deposited diamond film followed the surface topography and successfully covered this uneven surface.

As shown in Figure 3.14, as-deposited diamond films were ready for the four-point probe measurements which determines the sheet resistance of the diamond films. Results of the 4 point probe resistivity measurements will be discussed in chapter 5



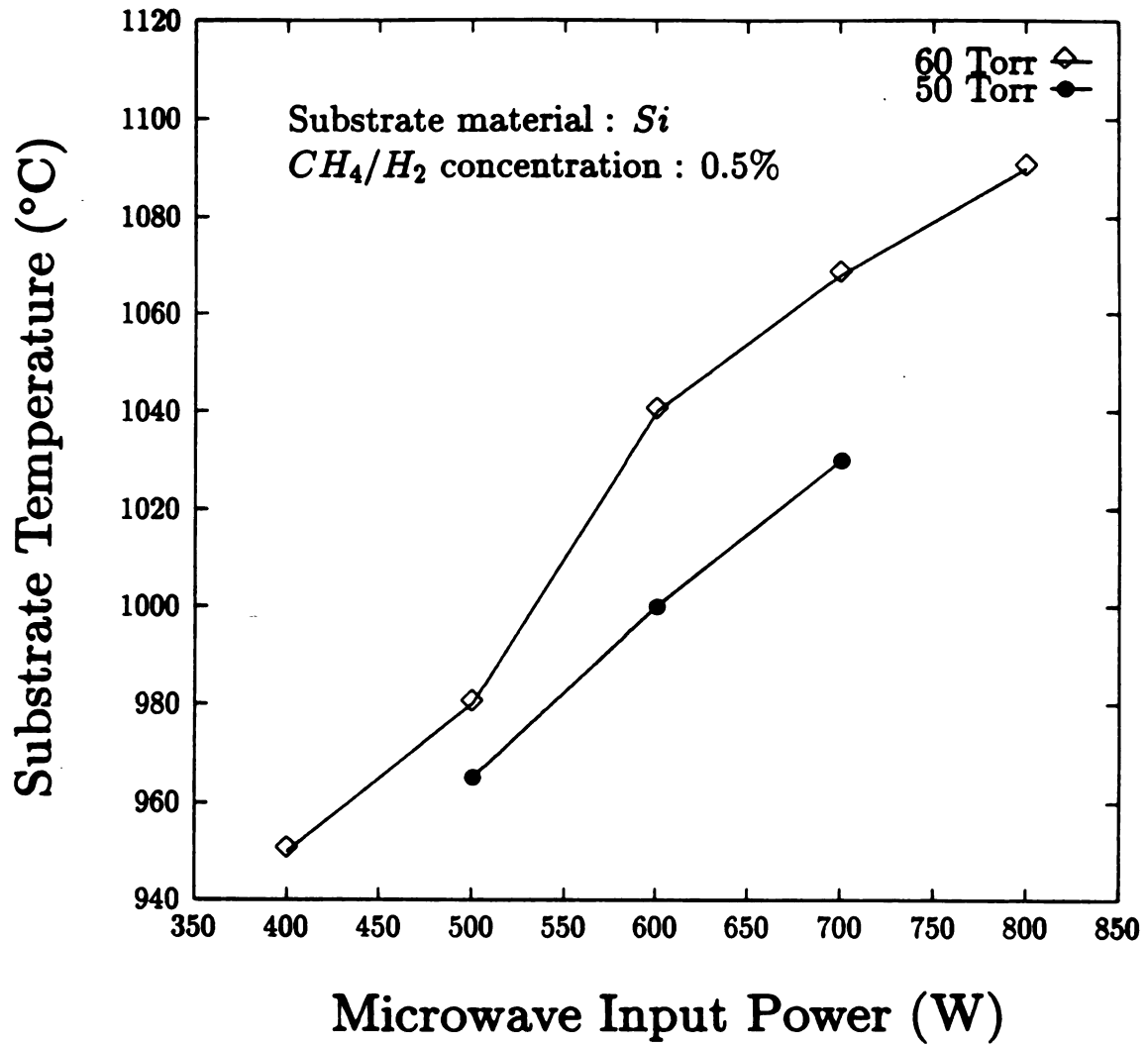


Figure 3.11. Si substrate temperature vs. microwave input power for 50 and 60 Torr at 0.5 % methane concentration.



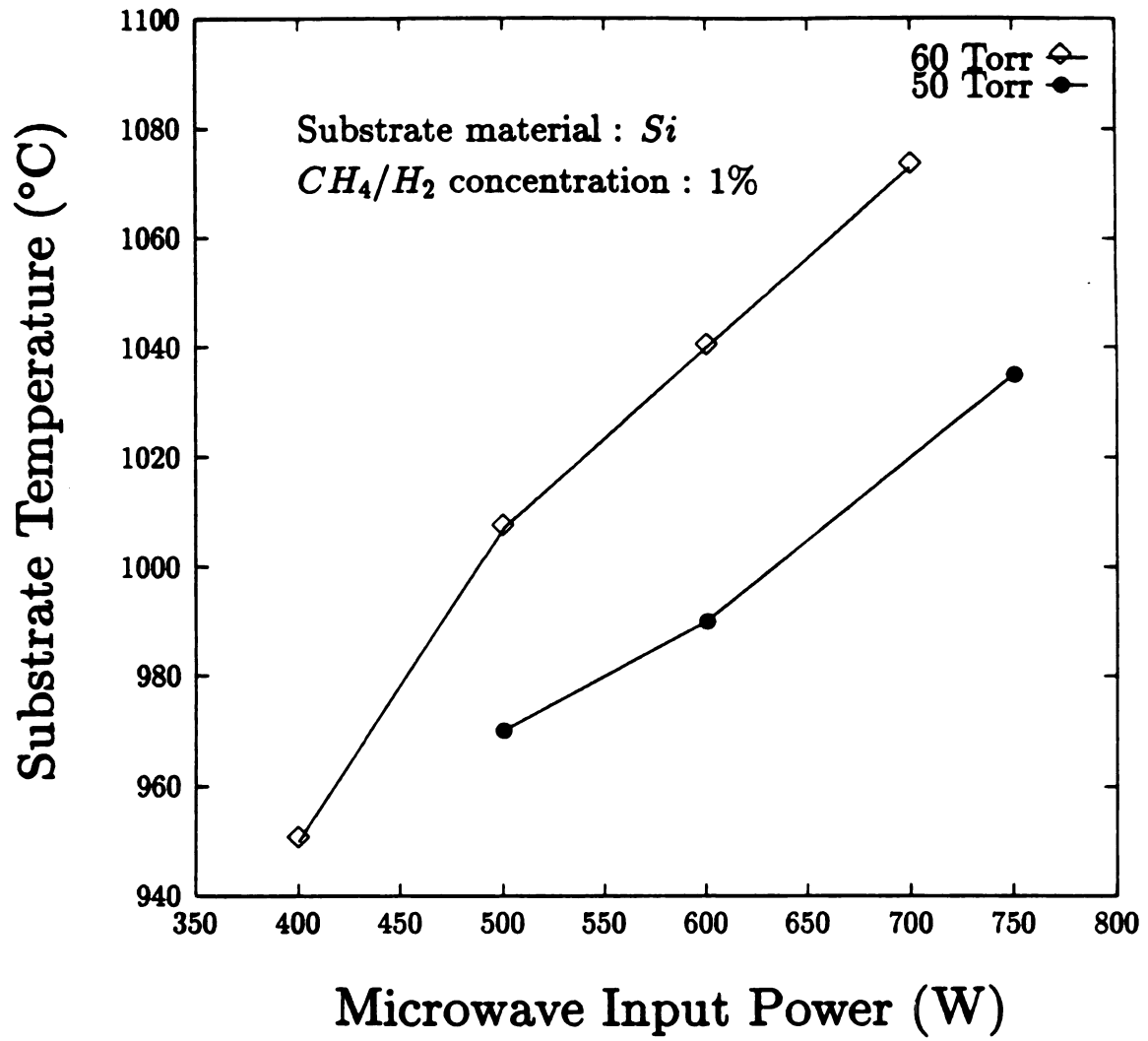


Figure 3.12. Si substrate temperature vs. microwave input power for 50 and 60 Torr at 1 % methane concentration.

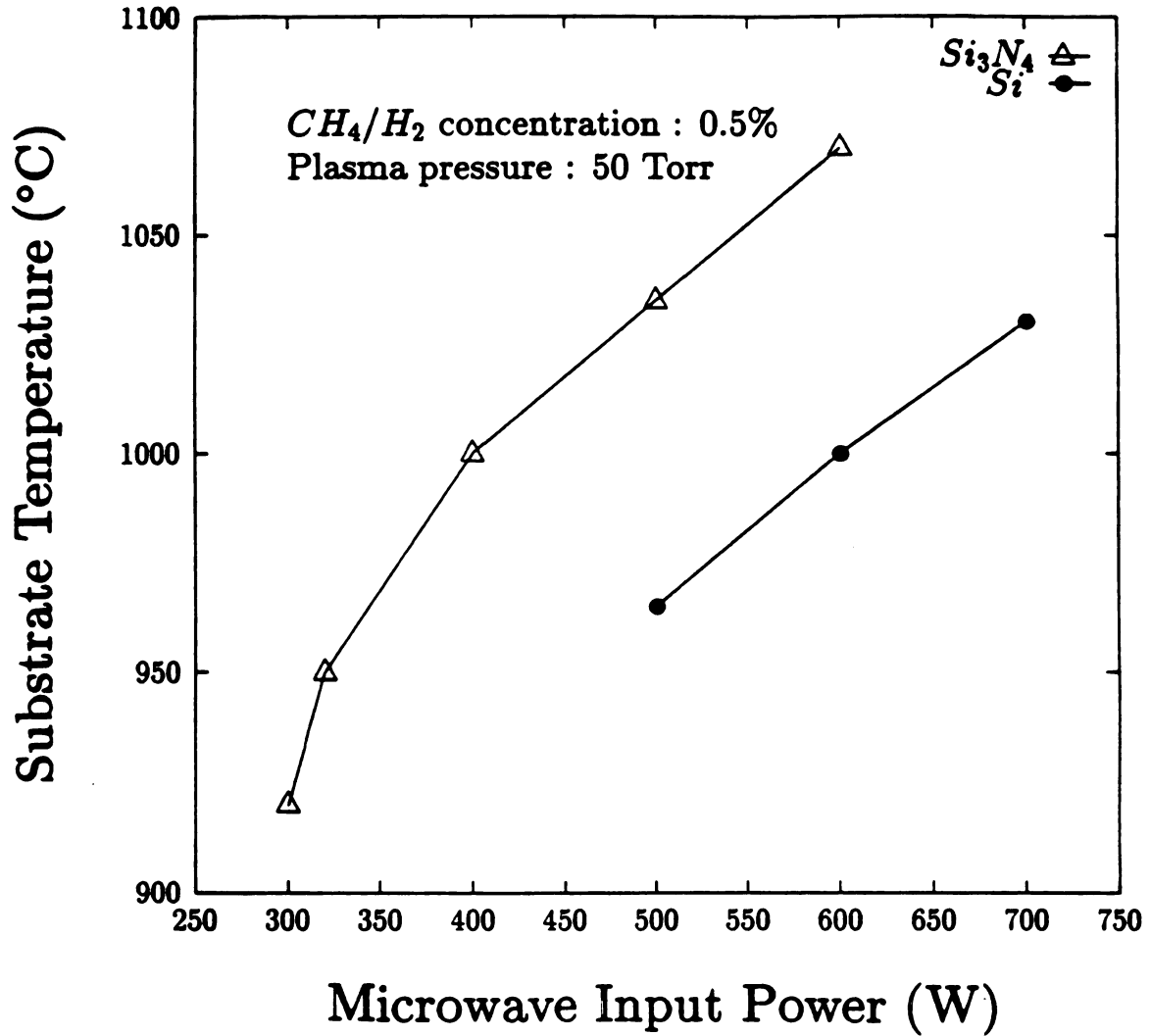


Figure 3.13. Temperature difference between silicon and silicon nitride for 0.5 % methane concentration at 50 Torr.

(section 2).

### 3.5.2 The Metal/Diamond/Silicon Samples

For the metal/diamond/silicon samples, both n and p-type silicon substrates with (100) orientation and resistivity of 1-2  $\Omega\cdot\text{m}$  were used, with a area of 4  $\text{cm}^2$ . Some samples were prepared with the diamond paste nucleation method and some by the diamond powder nucleation method. After deposition, a shadow mask with 900  $\mu\text{m}$  diameter openings was used to form metal contacts on the top of the diamond films. Typically, Al contacts were most often used in the diamond paste prepared samples as shown in Figure 3.15. But on the diamond powder prepared samples, a shadow mask with smaller openings (400  $\mu\text{m}$ ) was used. Au, Ag, and In were used as the top metal contacts in this case. The electrical properties will be described in chapter 5 (section 4).

### 3.5.3 Back-Etched Samples

For film characterization, it is useful to have access to both sides of the film. Towards this purpose, a procedure suggested by Dr. J. Engemann from the University of Wuppertal was used. Some of the preparation details were developed by H. Keller at the University of Wuppertal. Specifically, after the diamond deposition on the silicon substrate, a back-etched process was performed to transfer the diamond film from the silicon substrate to an epoxy substrate.

For samples intended for back surface analysis, the coated silicon was cleaved into approximately 5 mm  $\times$  5 mm samples which were placed diamond film down into a *Torr - Seal*<sup>TM</sup> [96] mixture formed by 1 part of hardener and 2 parts of resin on an aluminum oxide substrate. After a 70  $^{\circ}\text{C}$  anneal for 30 min, the silicon was removed by etching. Both NaOH (25 % by weight to water) and KOH (44 % by

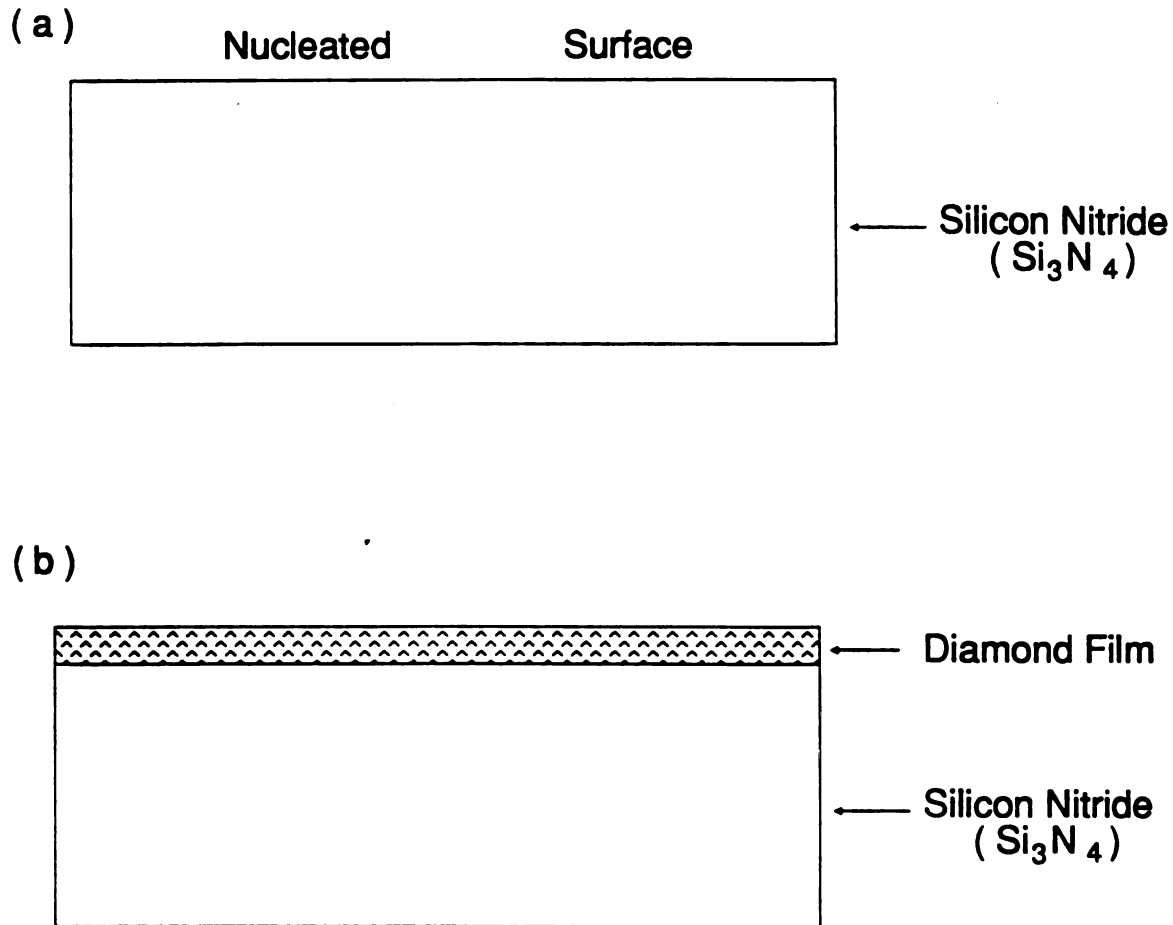


Figure 3.14. Fabrication of the four-point probe samples. The actual surface was more uneven than is indicated here. (a) The starting point is a silicon nitride substrate which has received a nucleation procedure. (b) Since the substrate is insulating, the sample is ready for the 4 point probe measurement.

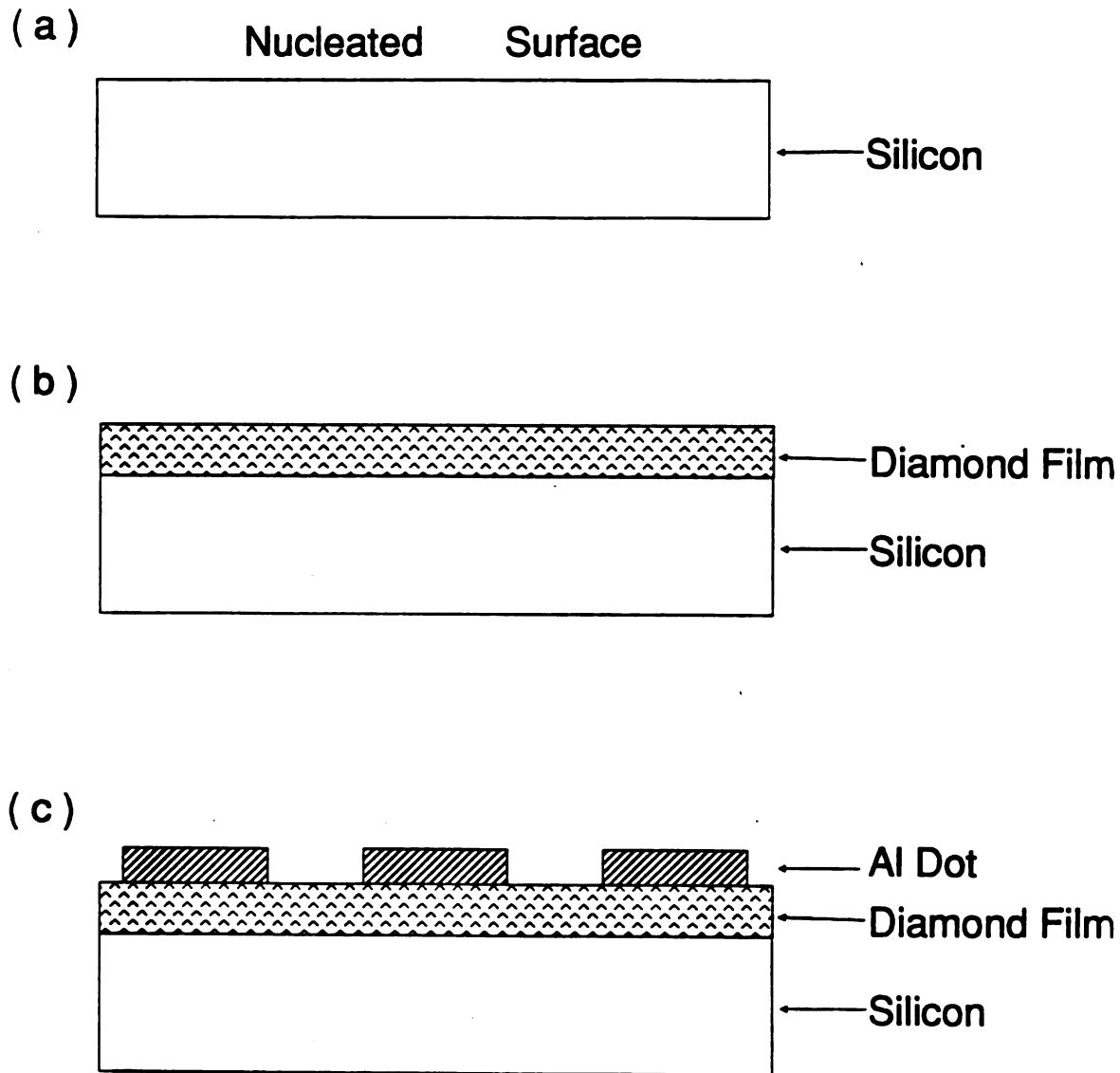


Figure 3.15. Fabrication of the metal/diamond/silicon samples. (a) The surface is nucleated by diamond powder or diamond paste, (b) the diamond film is deposited, and (c) top contacts are evaporated through a shadow mask. Aluminum is shown here as an example.

weight to water) were successfully used with a bath temperature of 58 °C. For a substrate thickness of 15 mils, it takes about 25 hours to etch the silicon. With lower temperature, longer time is needed to finish the etching process. There is sufficient adhesion between the top polycrystalline surface of the diamond film and the epoxy that the intact film remains, attached to the hardened epoxy substrate, thereby providing the back surface for analysis as shown in Figure 3.16. In some cases, however, film peeling and wrinkling were observed from the epoxy, indicating either films with higher internal strain or poor film-epoxy adhesion [95]. Some of the diamond/silicon interface (back-etched diamond surface) characterization results will be discussed in chapter 4.

For electrical access to both sides of the film, the sample preparation procedure was modified as follows. After diamond deposition on the silicon substrate, the first (bottom) metal contact was evaporated onto the diamond surface through a shadow mask. Then a wire lead is attached to the evaporated metal with *Epo - Tek™* polyimide silver conducting epoxy [97] which is cured first for 30 min at 50 °C and then 60 min at 150 °C. The sample is placed top down in the *Torr - Seal™* epoxy and the silicon is removed by back etching. At this point, the evaporated metal contact is visible through the transparent diamond film, and the second diamond surface is available for electrical contacts as shown in Figure 3.17. The second (top) metal contacts then can be evaporated onto the back-etched surface through another shadow mask with much smaller openings. A careful study of diamond film samples prepared by this method will be discussed in chapter 5 (section 3).

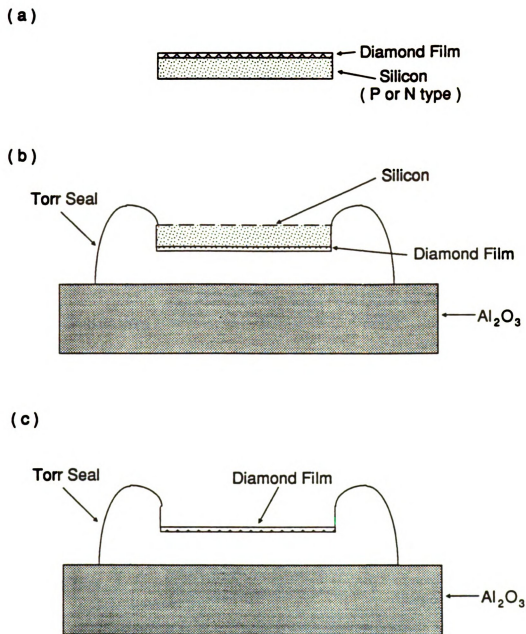


Figure 3.16. Fabrication of back-etched diamond samples for surface analysis. (a) Silicon is coated with diamond using conventional method. (b) The sample is secured to an epoxy substrate. (c) The silicon is removed by chemical etching.

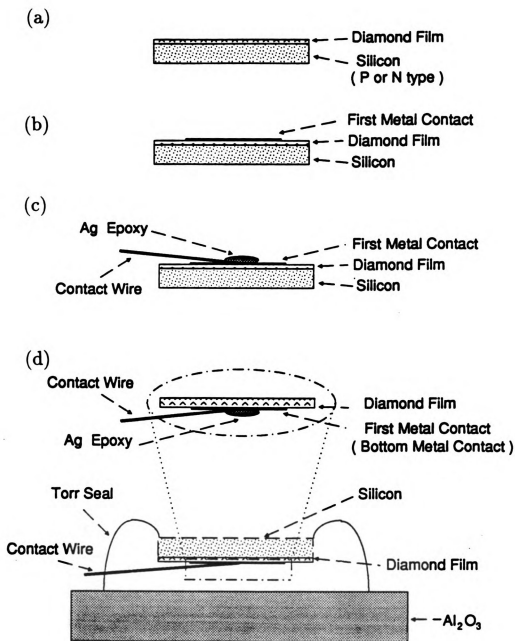
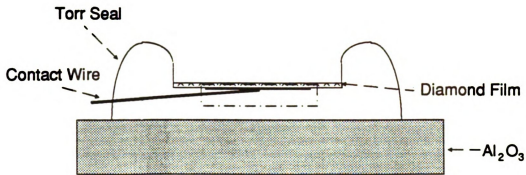


Figure 3.17. Fabrication of dual-sided metal contacts on isolated diamond films. (a) The silicon is coated with diamond and (b) a metallic contact is evaporated on the first diamond surface. (c) A wire lead is attached to the evaporated metal and (d) the substrate is placed face down in epoxy. (see also Engemann, et al. [95])

(e)



(f)

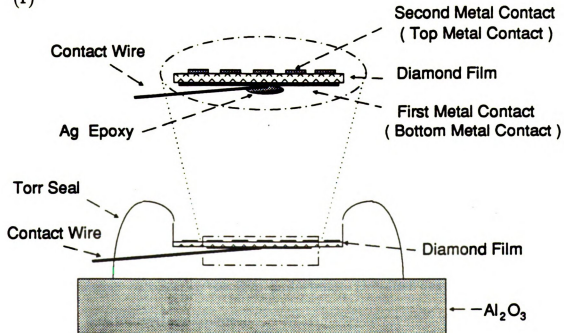


Figure 3.17 (cont'd): Fabrication of dual-sided metal contacts on isolated diamond films. (e) The silicon is removed by etching and (f) metal contacts are evaporated on the second diamond surface.

# CHAPTER 4

## Physical Characterization

### 4.1 Introduction

Physical characterization of the deposited film is very important to determine whether the film is in fact diamond and if it is indeed diamond, the film quality. There are several methods which may be used for film characterization, such as Raman spectroscopy, X-ray diffraction, reflection high-energy electron diffraction (RHEED), scanning electron microscope (SEM), X-ray photoelectron spectroscopy (XPS), Auger analysis, and others. In this chapter, we will use Raman spectroscopy to study the film quality in terms of  $sp^3$  bonding, XPS to perform surface analysis, SEM to examine the surface morphology, a Dektak profiler to evaluate the surface profile, and laser scanning microscopy to observe the film uniformity. Detailed descriptions of these methods are in the following sections.

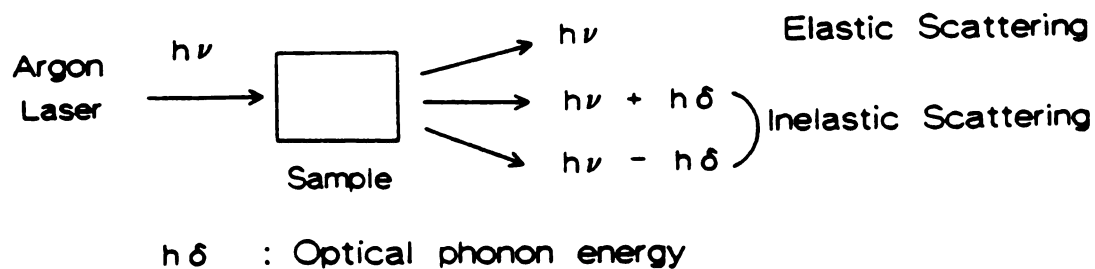
## 4.2 Raman Spectroscopy

Raman spectroscopy is based on an inelastic light scattering process. The incident photons, which are monochromatic, interact with the material either by creating or annihilating one or several phonons and then emerge with energies different from the incident photons. As in Figure 4.1, the strong line centered at  $h\nu$  is due to elastic scattering of photons and is known as *Rayleigh scattering*. The weak lines at  $h\nu \pm h\delta$  originate from inelastic scattering of photons by phonons and constitutes the *Raman spectrum*. The Raman bands at frequencies  $\nu - \delta$  are called *Stokes lines*, corresponding to phonon generation, and those at frequencies  $\nu + \delta$  are known as *anti-Stokes lines*, corresponding to phonon absorption. The intensity of the anti-Stokes lines are usually considerably weaker than those of the Stokes lines [98] and the Raman spectra reported in this chapter are based on the Stokes-line signals.

Figure 4.2 shows the Raman spectra for diamond and silicon on the absolute wave number scale and on the relative wave number scale. Most traditionally Raman spectra on the relative wave number scale were presented. For example, in this research, a wavelength of 488 nm laser was used by the Raman operators. It corresponds to the photon energy of 2.541 eV and wave number at  $20492 \text{ cm}^{-1}$ . Since only the first-order Raman scattering, which involves the optical phonons with wave vector  $\mathbf{k} \simeq 0$ , is considered, for diamond the energy of optical phonon involved is 0.165 eV. Considering only the *Stokes* signal, the photon energy becomes 2.376 eV after the phonon generation. Photon energy of 2.376 eV corresponds to wavelength of 522 nm and wave number of  $19160 \text{ cm}^{-1}$ . A strong peak of diamond is then observed at  $19160 \text{ cm}^{-1}$  if an absolute wave number scale is used. It is  $1332 \text{ cm}^{-1}$ , which is called the *Raman shift* for diamond, between  $19160 \text{ cm}^{-1}$  and  $20492 \text{ cm}^{-1}$ . The reported natural diamond peak at  $1332 \text{ cm}^{-1}$  is on the relative wave number scale [99]. Similarly, for silicon the optical phonon energy is 0.063 eV. After calculation, the silicon peak will

## Raman Spectroscopy

(a)



(b)

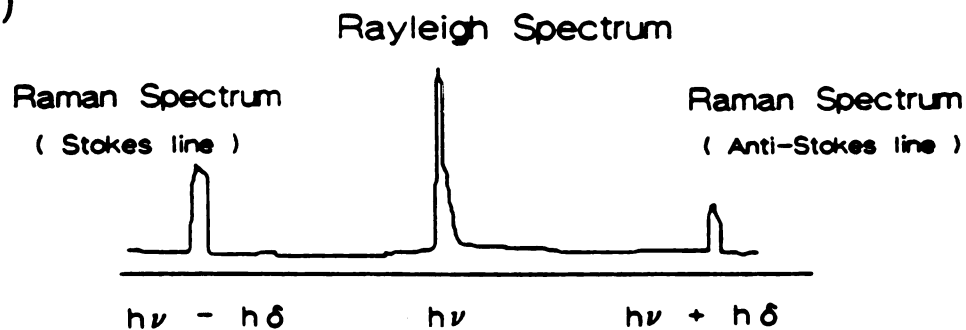


Figure 4.1. Raman spectroscopy is based on a process of inelastic scattering of photons by phonons.

be at  $19984\text{ cm}^{-1}$  on the absolute wave number scale and  $508\text{ cm}^{-1}$  on the relative wave number scale.

It is also known that graphite shows broad peaks at about  $1360\text{ cm}^{-1}$ ,  $1590\text{ cm}^{-1}$  [100] and amorphous carbon at about  $1600\text{ cm}^{-1}$  [41]. Diamond-like carbon, which is amorphous but has properties close to those of diamond, is reported to have a broad peak at about  $1500 - 1550\text{ cm}^{-1}$ . [101, 102, 103] The larger the Raman signal at  $1332\text{ cm}^{-1}$  and the smaller the other peaks, the higher quality of the diamond films in that the results indicate a preponderance of  $sp^3$  bonding (diamond) rather than  $sp^2$  bonding (graphite). At the present time, Raman spectroscopy is considered to be the best technique to distinguish between the diamond, diamond-like carbon and graphite.

Dr. Kevin Gray in Norton Company (Northboro, Massachusetts) performed most of the measurements for the Raman spectrum analysis. The principle set-up of the instrumentation is illustrated in Figure 4.3 [104]. The monochromatic and polarized light of the laser passes through an interference filter that rejects spurious lines and background from the laser source. The light beam then enters the beam-splitter and is focused by the lens to the samples. If micro-Raman analysis is performed, the microscope shown in Figure 4.3 is added to reduce the beam size. Light scattered from the sample through a variable beam-splitter then is focused by the lens onto the entrance slit of the 1/8 meter double-grating monochromator. Before entering the monochromator, a notch filter was used to reduce the laser light. The double-grating monochromator acts as a tunable filter of extremely high contrast; its purpose is to prevent the internally scattered intense Rayleigh light from overpowering the weak Raman lines. Light leaving the final slit of the double-grating monochromator is collected by a 1024 element silicon-array detector, whose output is processed with a "photon counting" electronics. It includes a programmable detector controller and

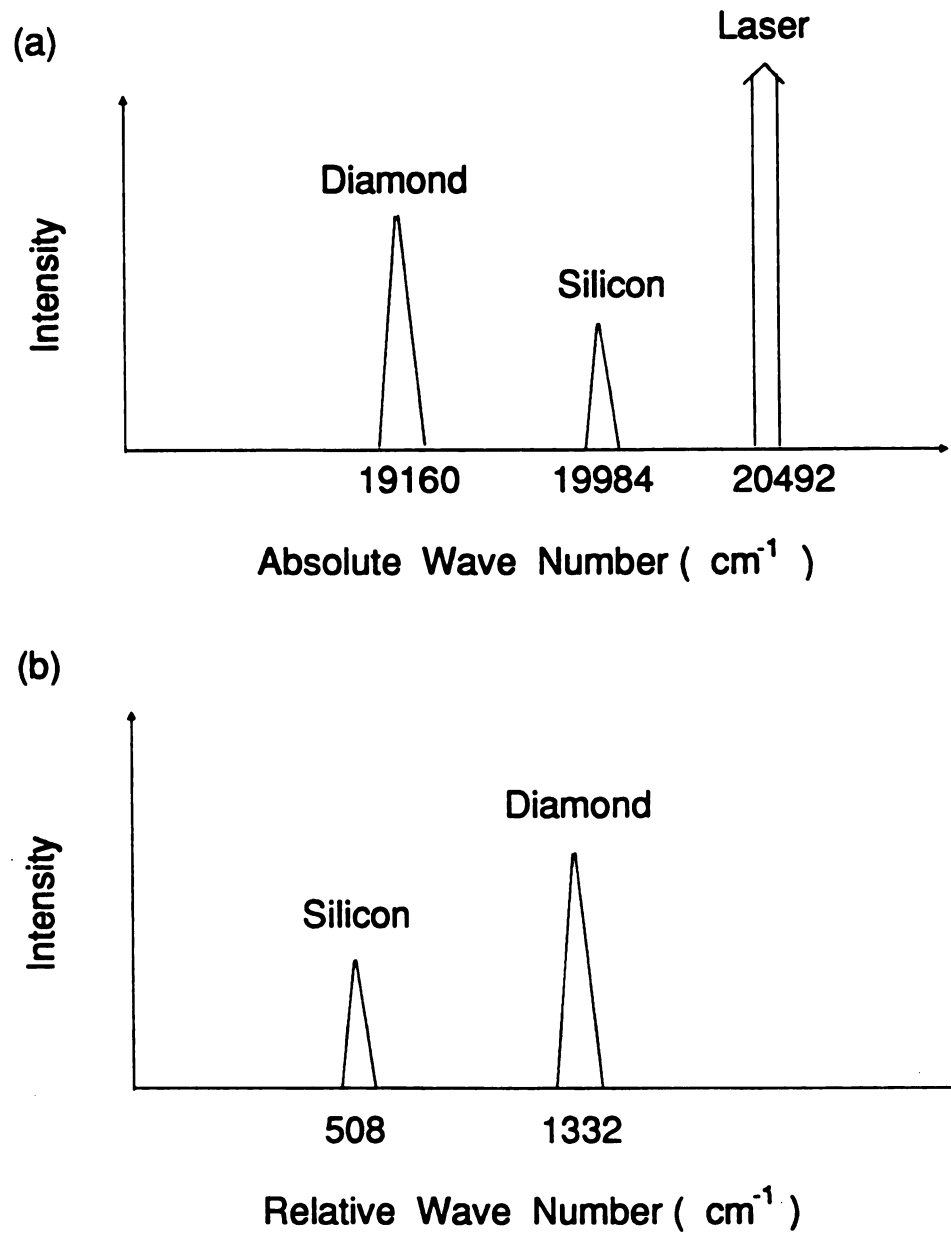


Figure 4.2. Raman spectra for diamond and silicon on (a) absolute wave number scale and (b) relative wave number scale.

an oscilloscope, which is used for monitoring the real time signal synchronously with the spectrometer. Finally, the data processing and data acquisition were collected and processed with the personal computer.

In this work, typically a wavelength of 488 nm from an Argon laser and a laser power of 400 mW was used to excite the Raman signals. In Figure 4.4 Raman spectra of 0.5 %  $CH_4/H_2$  powder-polished samples are compared at different substrate deposition temperatures. All spectra show the characterization peak at  $1332\text{ cm}^{-1}$ . At  $936\text{ }^\circ C$  the  $1332\text{ cm}^{-1}$  peak is quite small and a broad shoulder around  $1500\text{ cm}^{-1}$  indicates amorphous diamond-like component in the film. Around  $1040\text{ }^\circ C$  a better defined diamond peak shows up. Then at  $1090\text{ }^\circ C$  a graphite peak at  $1600\text{ cm}^{-1}$  becomes obvious. In all cases the peak at  $508\text{ cm}^{-1}$  is the silicon Raman signal. For depositing good quality diamond films, the depositing temperature must be in a certain range. If the temperature is too low, an amorphous diamond-like component is dominant in the film. If the temperature is too high, graphitic component will play a major role in the film. It is observed that the preferential temperature range for good quality diamond films is between  $1030\text{ }^\circ C$  and  $1060\text{ }^\circ C$ .

The Raman spectrum is also dependent on gas flow composition. In Figure 4.5 the Raman spectra for 0.5 % and 1 % gas mixture powder-polished samples are compared at a fixed substrate temperature of  $1000\text{ }^\circ C$  and  $1040\text{ }^\circ C$ . It shows that the 1 % samples have a larger graphitic component than the 0.5 % samples for both substrate temperatures. It indicates that for the same temperature, a smaller methane concentration of the gas flow produces better quality diamond films than a higher methane concentration does.

Figure 4.6 shows that at the same growth condition a 10 hours deposition sample has a similar Raman spectrum to a 6 hours deposition sample, but the sample with longer deposition time has a stronger diamond signal and weaker silicon signal because

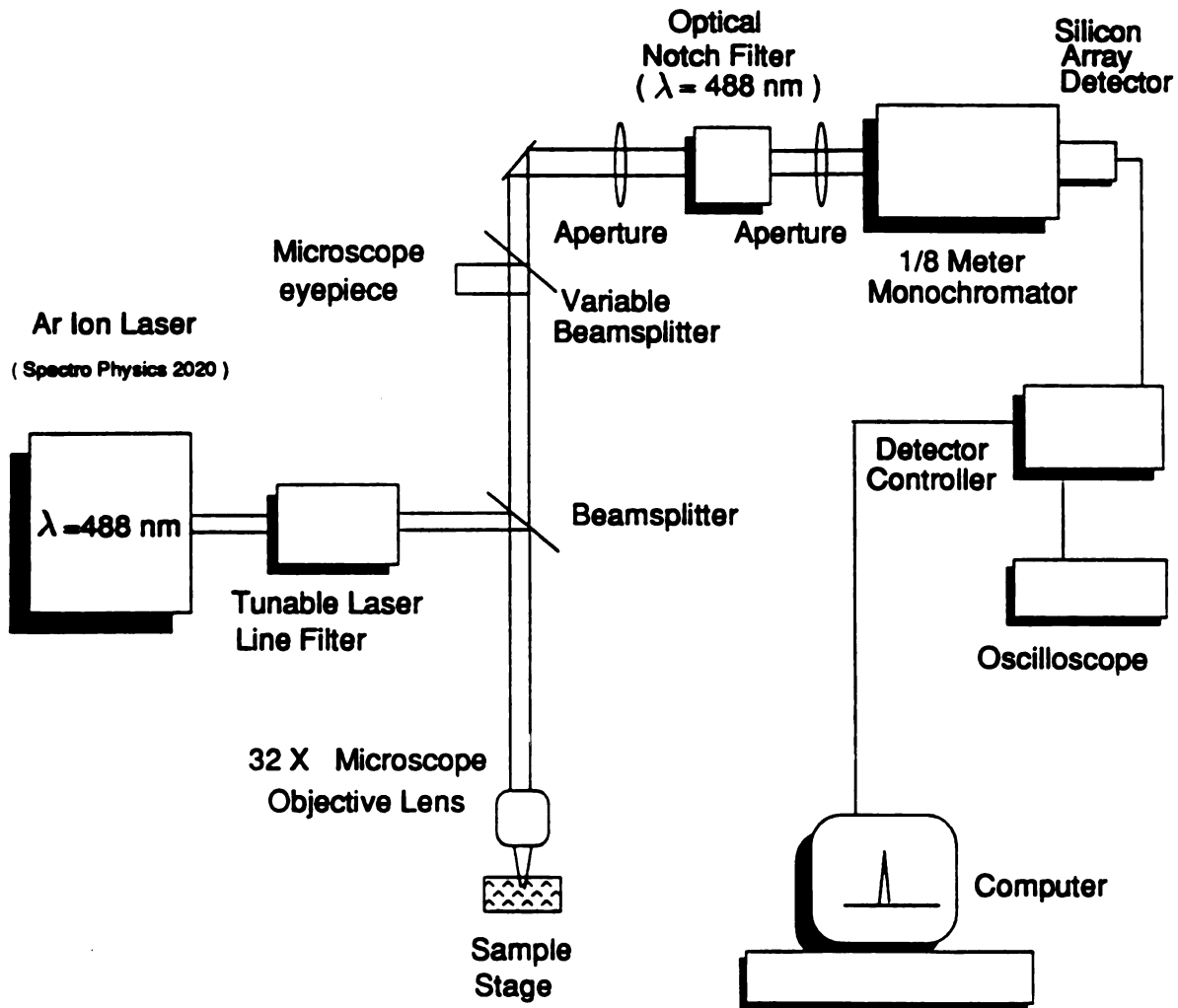


Figure 4.3. Raman Spectroscopy set-up for the Raman spectrum analysis.(From Dr. Gray)

of the thicker diamond film.

In Figure 4.4 to Figure 4.6, only powder-polished samples were analyzed. In Figure 4.7 Raman spectra of samples with the same deposition conditions but with different nucleation methods were examined. It showed that the Raman spectra were similar for samples with 0.5% methane at 1040 °C by both paste-polished and powder-polished methods. Consequently, the quality of diamond films shows no obvious difference between different kinds of preparation methods under the same deposition conditions. Raman spectra are based on bulk properties of the sample rather than on surface or interface characteristics. However, the method was used to indirectly identify the location of the graphite signal in one case.

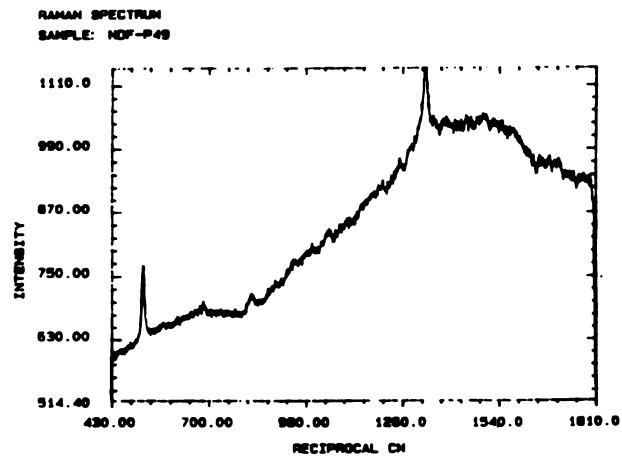
Figure 4.8 shows a good Raman spectrum with a small graphitic peak for a sample prepared with 1.5% methane at about 1040 °C. The temperature was not measured from the pyrometer directly but by estimation from the temperature measurement on the similar deposition conditions. A part of the film peeled off when the sample cleavage was performed. Absence of the graphitic peak was observed on the Raman spectrum of the free standing film. This suggests that some graphitic component exist in the diamond/silicon interface during the film deposition. When the diamond film peeled off, most of that graphitic component stayed on the silicon surface.

Generally, Raman analysis is essential for characterizing the deposited diamond films. However, it is not appropriate to do the surface or interface analysis. Another characterization technique, X-ray photoelectron spectroscopy, is then introduced for the chemical analysis in the surface and interface layers.

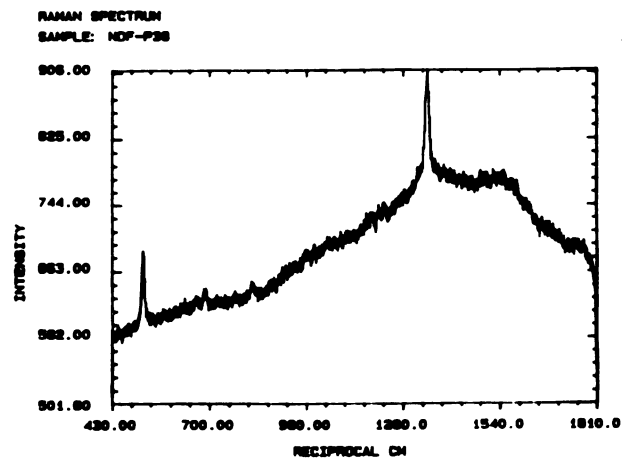
### **4.3 X-ray Photoelectron Spectroscopy**

X-ray Photoelectron Spectroscopy (XPS) is also known as Electron Spectroscopy for Chemical Analysis (ESCA). This technique is able to analyze a wide of variety of

(a)



(b)



(c)

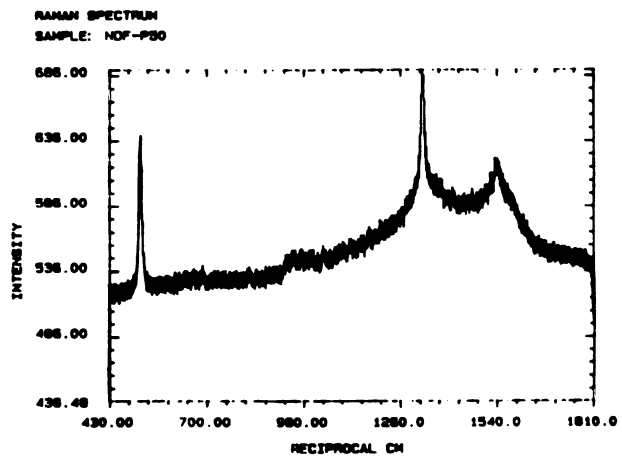


Figure 4.4. Raman spectra of 0.5% methane samples at (a) 936 °C (b) 1040 °C and (c) 1090 °C. (From Dr. Gray)

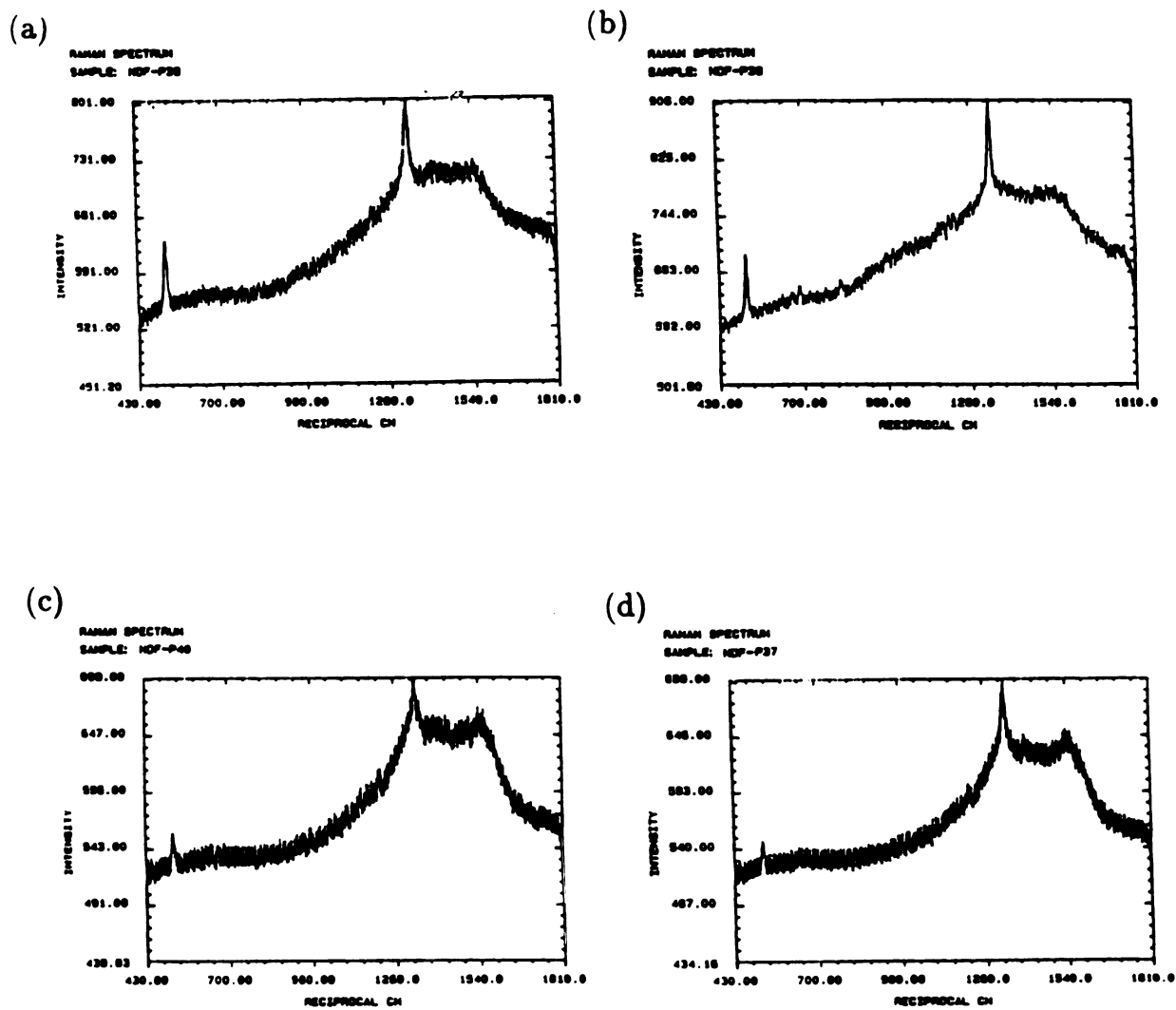
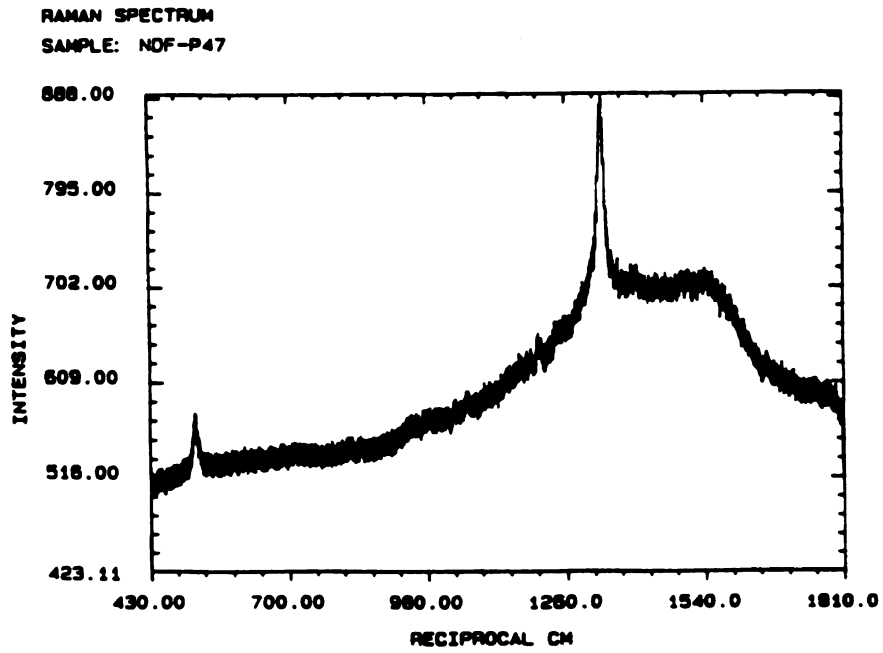


Figure 4.5. Raman spectra of samples with conditions : (a) 0.5% methane, 1000 °C (b) 0.5% methane, 1040 °C (c) 1% methane, 1000 °C and (d) 1% methane, 1040 °C. (From Dr. Gray)

(a)



(b)

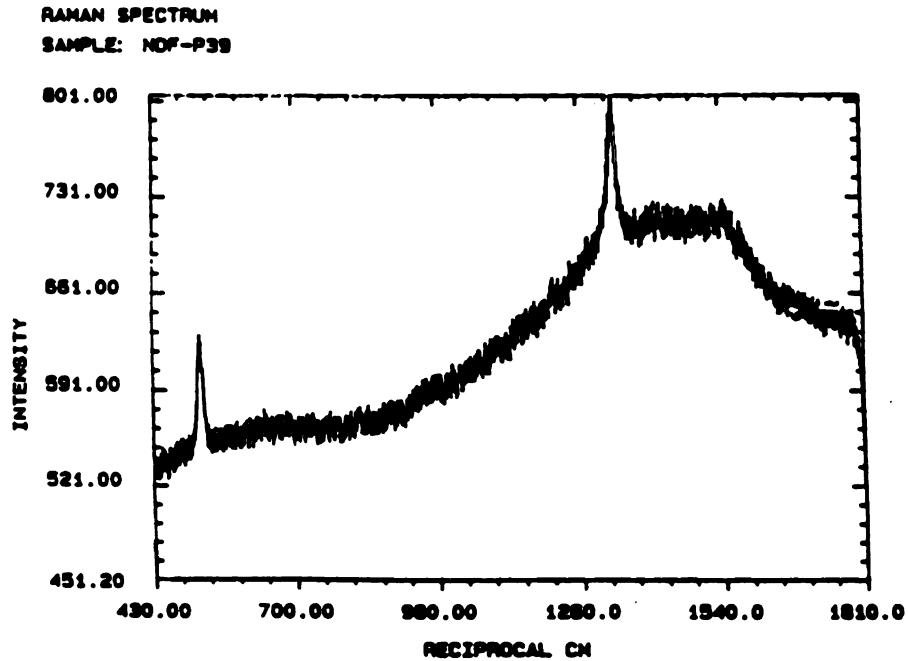
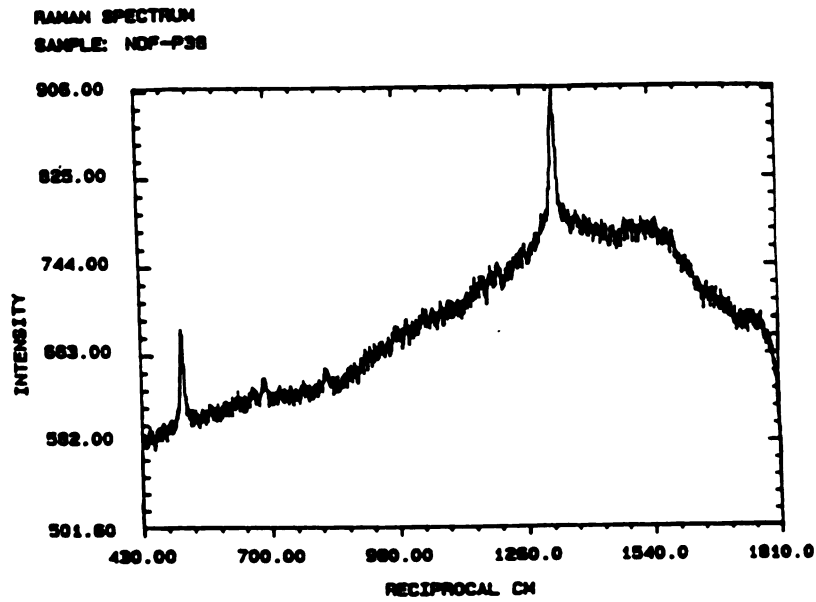


Figure 4.6. Raman spectra of samples of 0.5% methane at 1000 °C for (a) 10 hours' deposition and (b) 6 hours' deposition. (From Dr. Gray)

(a)



(b)

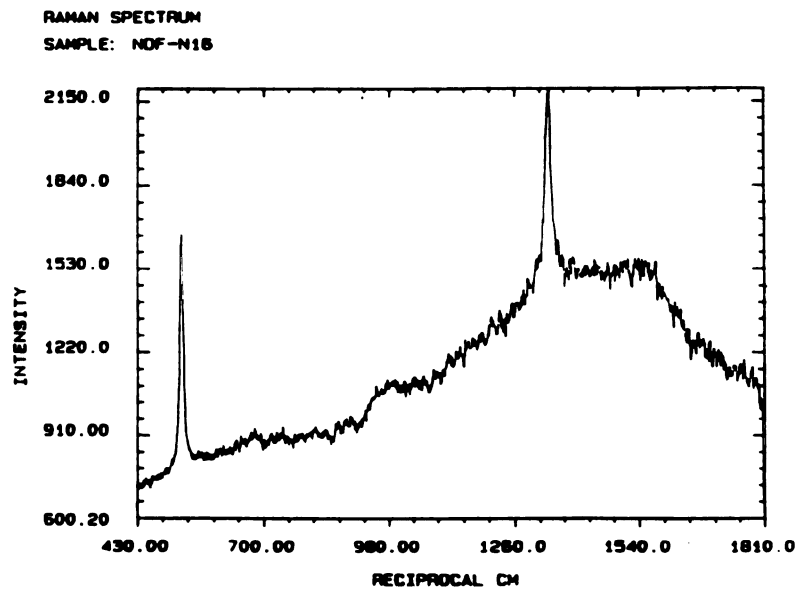
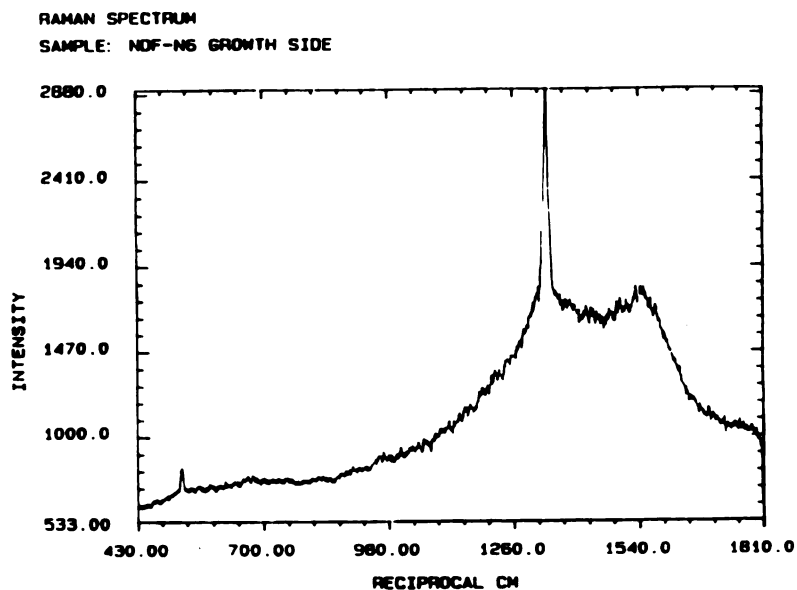


Figure 4.7. Raman spectra of samples with 0.5% methane at 1040 °C by (a) powder-polished method and (b) paste-polished method. (From Dr. Gray)

(a)



(b)

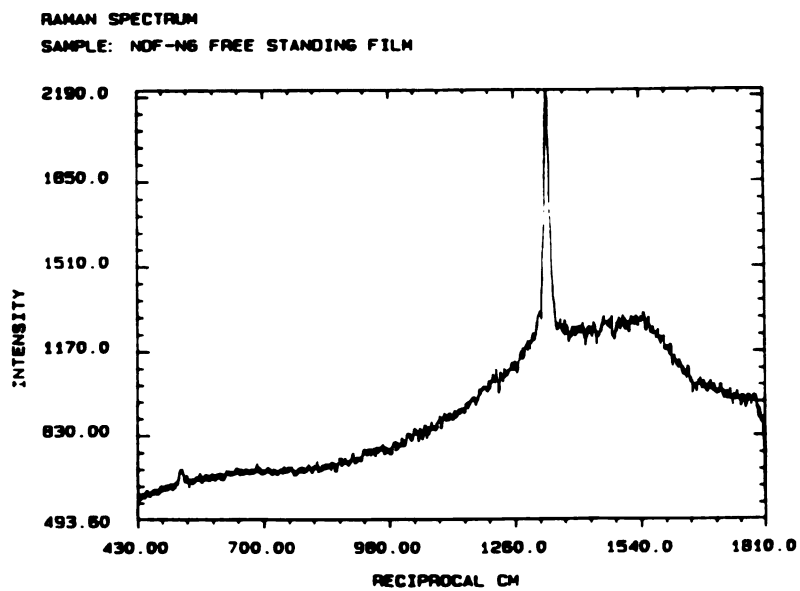


Figure 4.8. Raman spectra of (a) the as-deposited film and (b) the free standing film of the sample with 1.5% methane at about 1040 °C. (From Dr. Gray)

samples in terms of elemental and chemical composition on the surface layer of a sample, typically 5 to 50 Å in depth.

XPS involves the energy analysis of electrons ejected from a surface under energetic bombardment by X-rays as shown in Figure 4.9. The photoelectric process occurs when a core level electron absorbs a photon of energy greater than its binding energy. When this occurs, the electron is ejected from the atom with kinetic energy (K.E.) expressed by the following equation:

$$K.E. = h\nu - E_B \quad (4.1)$$

where  $h\nu$  is the X-ray photon energy and  $E_B$  is the photoelectron binding energy.  $E_B$  provides both elemental information as well as chemical bonding information. For example it is possible to distinguish carbon bonded as diamond from carbon bonded to silicon as *SiC*. Typically,  $K_\alpha$  X-ray emission from the light metals is the photon source used by most XPS [105].

XPS characterization of the samples was performed in a Perkin-Elmer PHI 5400 X-ray Photoelectron Spectrometer in this research. Dr. Kevin Hook of MSU's Composite and Structural Materials Center performed the XPS analysis. Samples were attached directly to the instrument analysis stubs and placed in the system pre-pumping chamber. System pressure during XPS analysis was approximately  $10^{-9}$  mbar. The spectrometer is equipped with both a *Mg K $\alpha$*  standard source and a *Al K $\alpha$*  monochromatic source. The *Al K $\alpha$*  monochromatic source was used mostly in this study and was operated at 600 W (15 KV, 40 mA). A continuously variable stage was used and set to 65° with respect to the sample surface. The portion of the sample was analyzed through an initial lens system in this instrument. For all analyses, the lens system was set in the large area, small solid angle mode. The size of the electron beam was 3.3 mm diameter circle. Data points were collected in the fixed analyzer

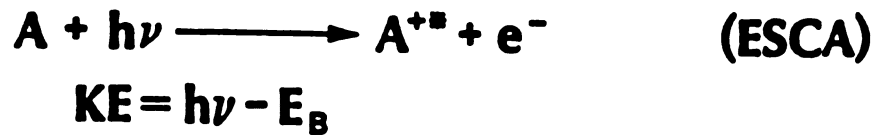
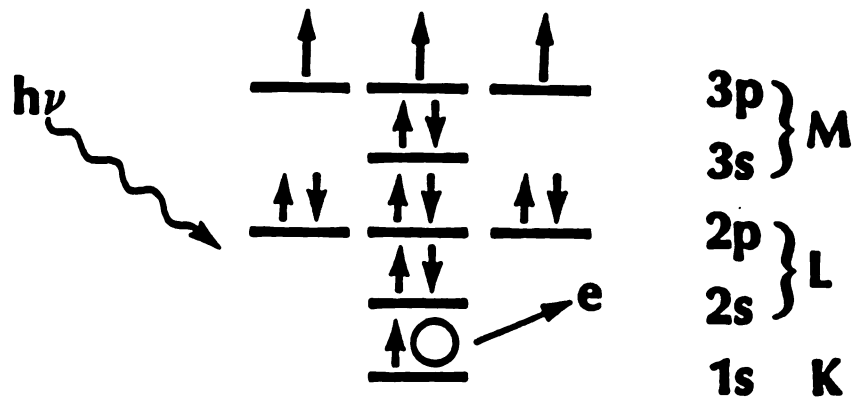


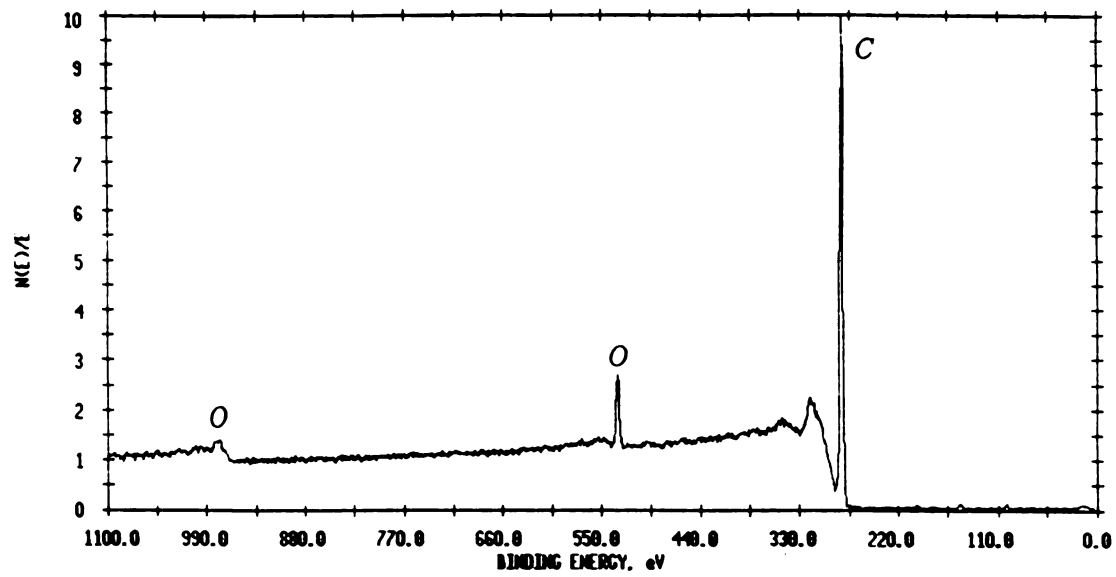
Figure 4.9. Principle of X-ray Photoelectron Spectroscopy. When a core level electron absorbs a photon of energy ( $h\nu$ ) greater than its binding energy ( $E_B$ ), the electron is ejected from the atom with kinetic energy (K.E.).

transmission mode utilizing a position sensitive detector and a 180° hemi-spherical analyzer. There are two types of samples analyzed by this technique : as-deposited samples as shown in Figure 3.16 (a) and back-etched samples as shown in Figure 3.16 (c). All the samples analyzed by XPS were treated by the paste-polished method.

For the as-deposited samples, the top surface of the diamond film was analyzed. Figure 4.10 shows the spectra of two different samples; one was left in the air for several weeks before the analysis and for the other the analysis was performed within 15 minutes after the deposition. Oxygen peaks were observed in addition to the carbon peak on the sample exposed to the air for a long time. Since the sample has some pinholes, silicon dioxide might in principle be a contributor to the oxygen peaks. However, as the analyzing angle (the angle of the beam relative to the surface) decreases the *O* peak increases. This suggested that the contamination came from the diamond film surface rather than pinholes. This does not necessarily mean that the diamond surface has formed carbon-oxygen bonds. The oxygen signal could be simply a result of non-outgassing  $H_2O$  on the surface, since hydrogen is not detectable with XPS. Alternatively, oxidation of impurities in grain boundaries might be a contributor, although no other elemental signal were observed.

Back-etched samples were used to analyze the diamond/silicon interface. In Figure 4.11 (a) *C*, *O*, *K* and *Si* were observed on the surface of the back-etched sample under the elemental survey scans. The *K* peak came from the *KOH* which was in the silicon etching solution. *Si* peaks may have come from the silicon residue or *SiC* (as discussed below) which was not completely etched, or silicon from the etching bath. An additional source of *Si*, as well as *O*, may come from contamination from the quartz disk. Such contamination has been previously reported for microwave CVD diamond deposition. [106] However, it is noted that the *Si* signal was not observed for the top surface XPS analysis. The big *O* peak, may also be due to contamination

(a)



(b)

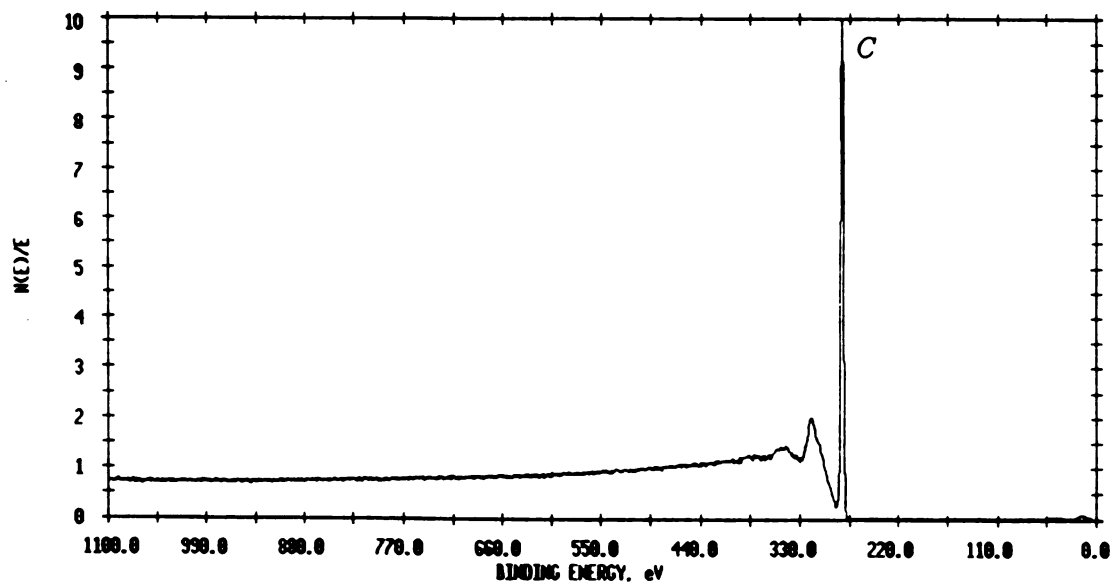


Figure 4.10. ESCA spectra of samples exposed to air for (a) a long time and (b) no time before the analysis. (From Dr. Hook)

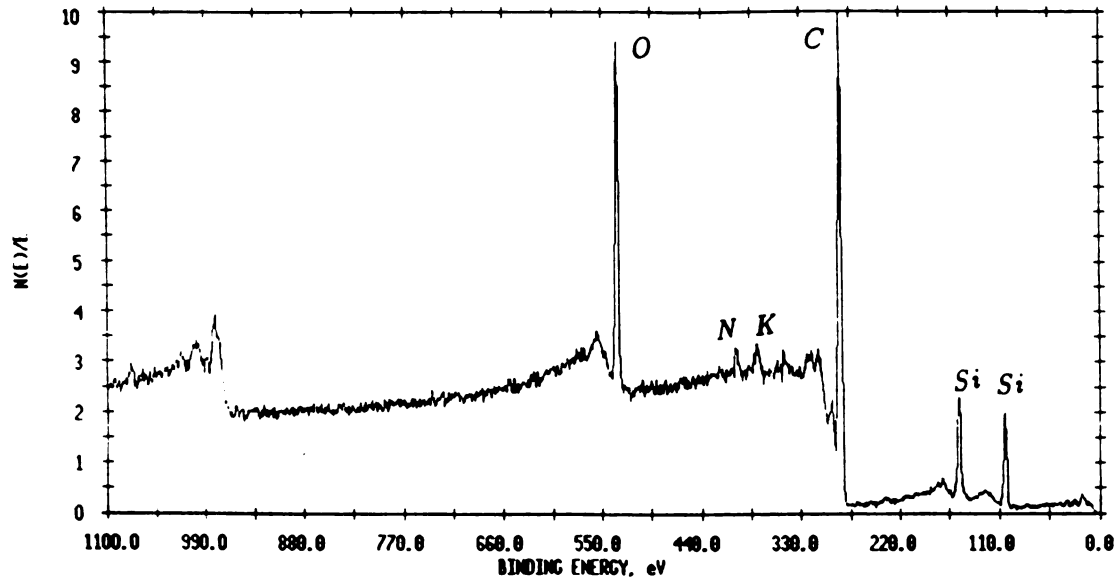
of the torr-seal during the back-etch process. However, another contributor might be the oxidation of the silicon residue after the back-etch process. Figure 4.11 (b) shows more detailed information about the *C* peak. The most intense contribution to the overall peak shape is from the peak centered at 284.25 eV due to the deposited diamond surface layer. The smaller peak present at the lower binding energy side of the diamond peak is a contribution from the *SiC* interface layer (282.75 eV). It has been suggested that the growth of a thin layer of *SiC* (20 - 100 Å) in the early stage of deposition is crucial to the formation of diamond films. [107, 108, 109, 110] In any case, the observation of a *SiC* layer is consistent with several other groups' studies. [111, 112, 113]

Typically Argon sputtering is the most used method to clean the surface impurities from an XPS sample. In this work, 3 KeV Argon sputtering at 15 mPa gun pressure was performed for 30 seconds. After the surface cleaning, it was observed that the *O* peak is obvious reduced from Figure 4.12 (a) which indicates that part of the contamination was removed. Also from Figure 4.12 (b) it is shown that the *SiC* shoulder has completely disappeared. Based on the sputtering rate of *SiC*, it is estimated that the carbide layer was approximately 30 Å thick. However, the *SiC* signal was not observed in some of the back etched samples. For these samples, it is believed that the *SiC* layer was etched by the back-etch solution because the samples were not removed from the etching solution right after the silicon was completely etched.

## 4.4 Dek-Tak Analysis

In chapter 3 (section 3), it was mentioned that the diamond powder preparation approach produced much finer grained films than did the diamond paste preparation method. Microscope examination shows the powder-polished film to be made of fine,

(a)



(b)

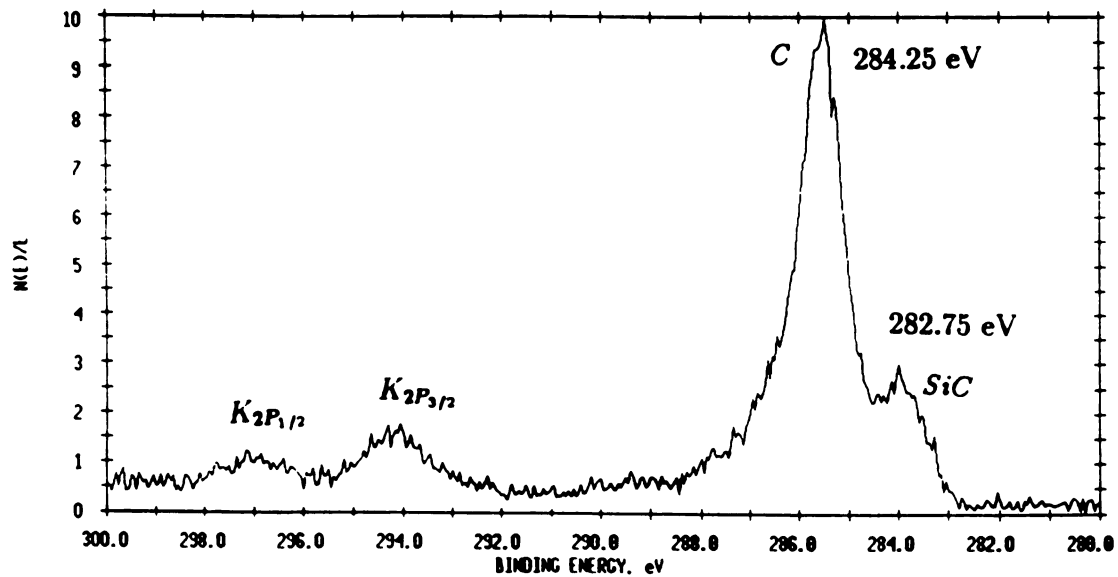
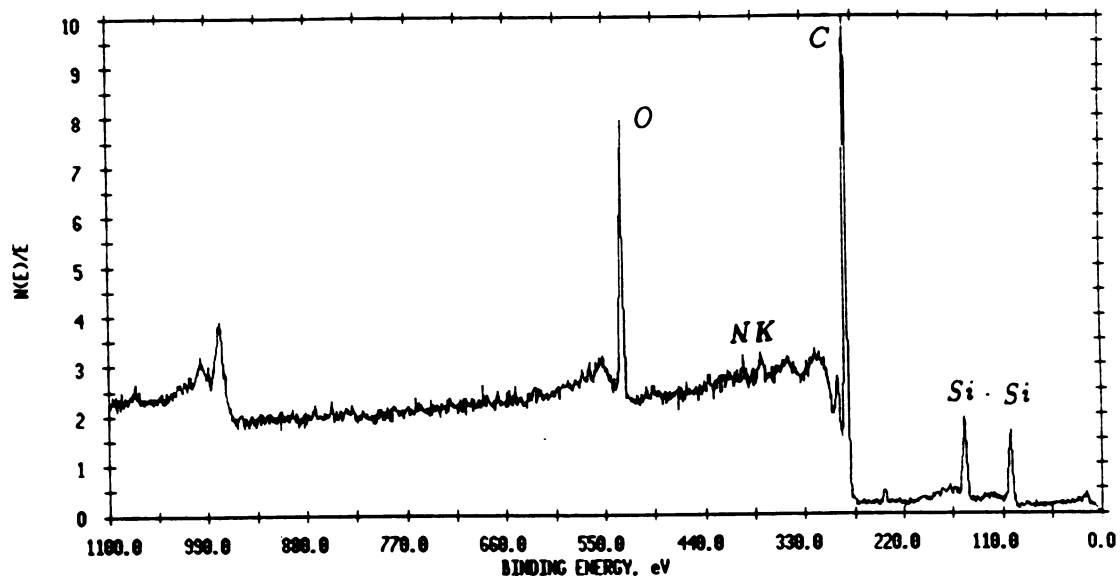


Figure 4.11. (a) Elemental survey scan of the sample before the Ar sputtering (b) higher resolution narrow scan of (a) in the carbon region. (From Dr. Hook)

(a)



(b)

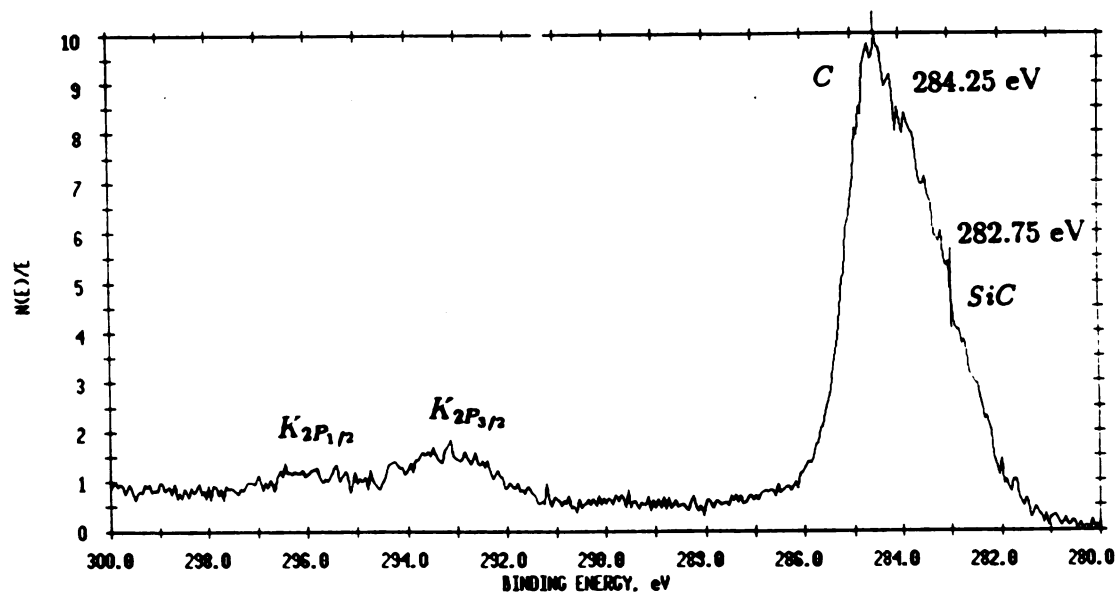


Figure 4.12. (a) Elemental survey scan of the sample after the Ar sputtering (b) higher resolution narrow scan of (a) in the carbon region. (From Dr. Hook)

sub-micron crystallites whereas the paste-polished surface produced crystallites which were larger than one micron for similar deposition conditions. The difference is also obvious to the eyes. Prior to deposition, a silicon substrate has a mirror finish and reflected images are easily observed. After deposition on a paste-polished silicon substrate, the deposited diamond films show a highly specular surface with a gray appearance and no observable reflected images. However, with the powder prepared surfaces, the diamond film is flat and somewhat shiny with some ability to produce reflected images.

There are also some other interesting visual observations. First, both types of films appear glittery under the sun or strong light, but the film produced by the paste-polished method did show a darker background. Secondly, because the film prepared by the powder method is less specular, some of the scratches on the silicon substrate surface could be seen through the film. Third, if the grain sizes are small enough, film produced by the powder-polished method showed colorful interference rings due to thickness variation across the sample.

For the samples produced by the paste-polished method, optical and electron microscopy of the transferred film shows a relatively flat back surface compared to the original top surface of the film. This observation is consistent with the cross-sectional view of the film and underlying substrate shown in Figure 4.13. It shows the relative smoothness of the back surface relative to the top surface.

In order to quantify film smoothness, a Sloan DekTak II surface profiler was used. The relative smoothness of the two surfaces of the paste-polished diamond film is shown in Figure 4.14. Shown here are surface profiles measured over a 50  $\mu\text{m}$  scan across the samples. A standard deviation of 940  $\text{\AA}$  is observed about the mean for the top surface of the diamond film as deposited on the silicon substrate. When the silicon is removed as shown in Figure 3.16 (c) and the back surface is scanned, a

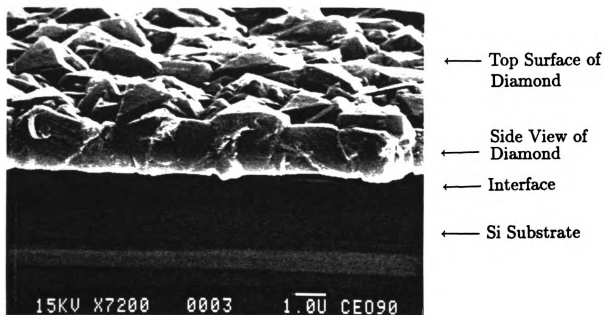


Figure 4.13. SEM view of the paste-polished produced diamond film on a cleaved sample showing the silicon substrate, the interface, and the side view and top surface of the diamond film.

standard deviation of 130 Å is observed.

For the samples produced by the powder-polished method, SEM cross-sectional view shows relative smoothness of the top and bottom surfaces in Figure 4.15. It is clearly seen that the difference between these two surfaces is not as big as that of the paste-polished produced samples. The quantified smoothness of the two surfaces is shown in Figure 4.16. Typically, a standard deviation of 630 Å is observed for the top surface and 570 Å is for the bottom surface of the diamond film. As shown in Figure 3.4 and Figure 3.5, a rougher surface on the back side of the diamond film produced by the powder-polished method is expected.

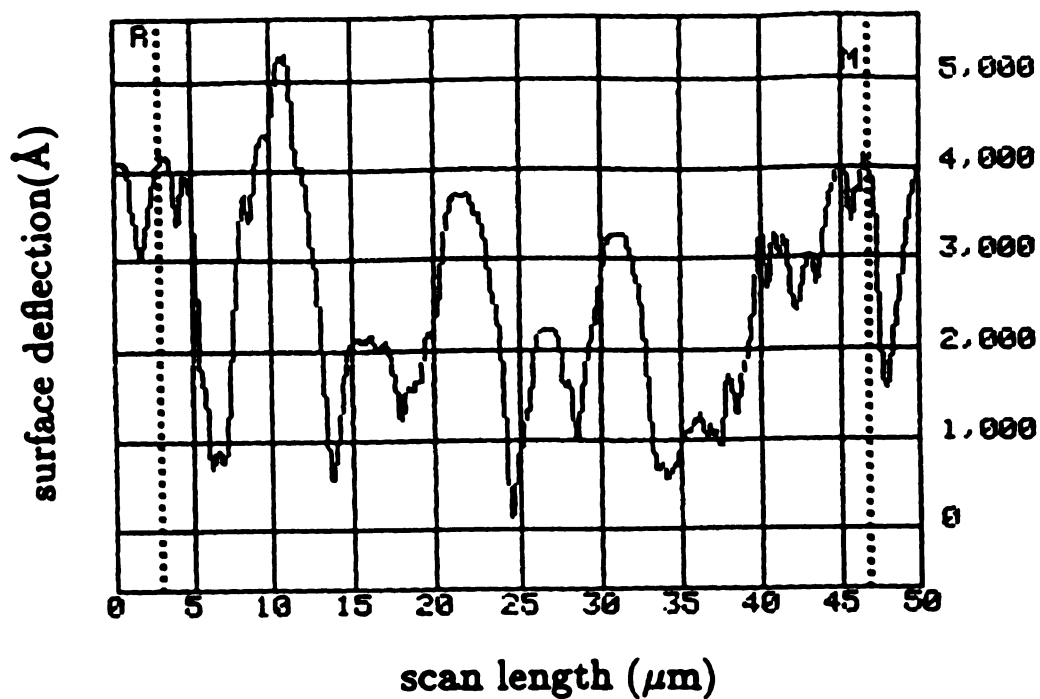
Figure 4.17 shows the top surface profiles of two extreme samples produced by the paste-polished and the powder-polished nucleation methods respectively. Standard deviations of 1600 Å and 420 Å are observed for the large-grain-size and small-grain-size diamond film respectively.

## 4.5 Scanning Electron Microscope Analysis

The scanning electron microscope (SEM) has unique capabilities for analyzing surface. It is analogous to the conventional optical microscope, but a different radiation source serves to produce the require illumination. Whereas the optical microscope forms an image from light reflected from a sample surface, the SEM uses electrons for image formation. The different wavelengths of these radiation source result in dramatically different resolution levels. Electrons have a much shorter wavelength than light photons, and shorter wavelengths are capable of generating high-resolution information. Enhanced resolution then permits higher magnification without loss of details.

The maximum magnification of the optical microscope is about 2000X and the theoretical resolution limit is about 0.17 μm. In practice it is difficult to clearly dis-

(a)



(b)

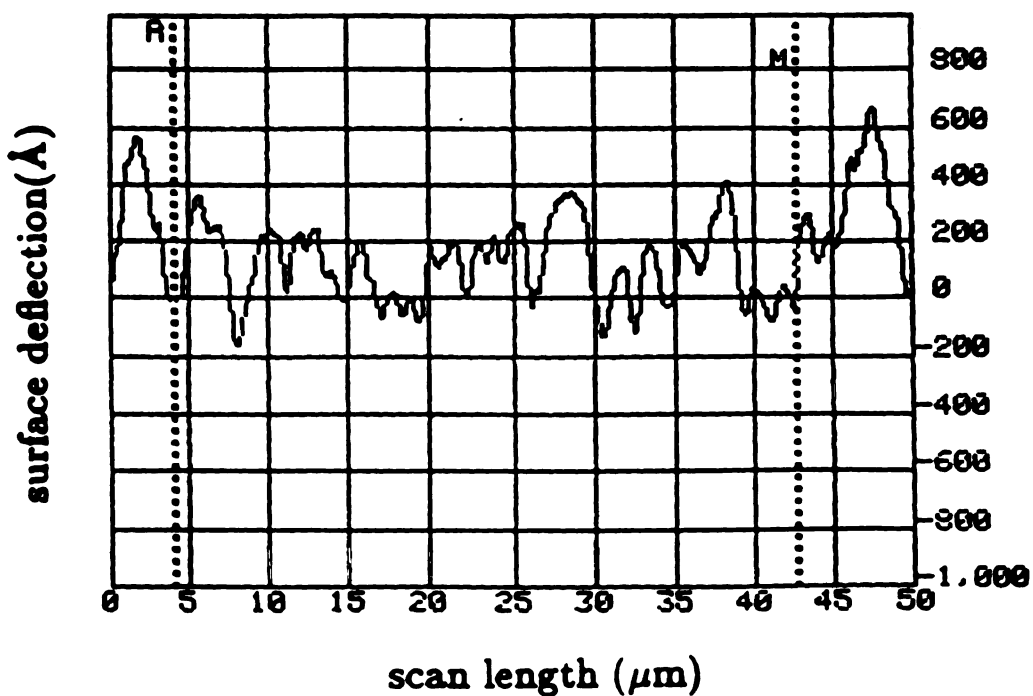


Figure 4.14. The surface profile on (a) the top surface of an as-deposited paste-polished produced diamond film and (b) the back surface of the film after transfer to the epoxy substrate.

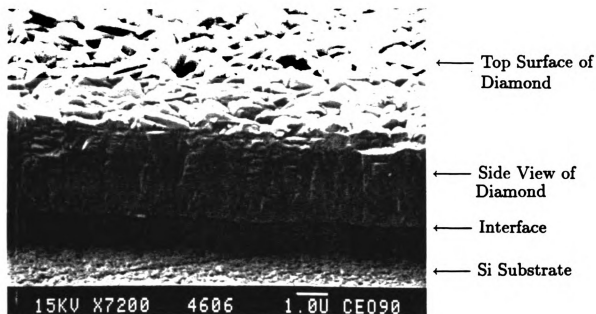
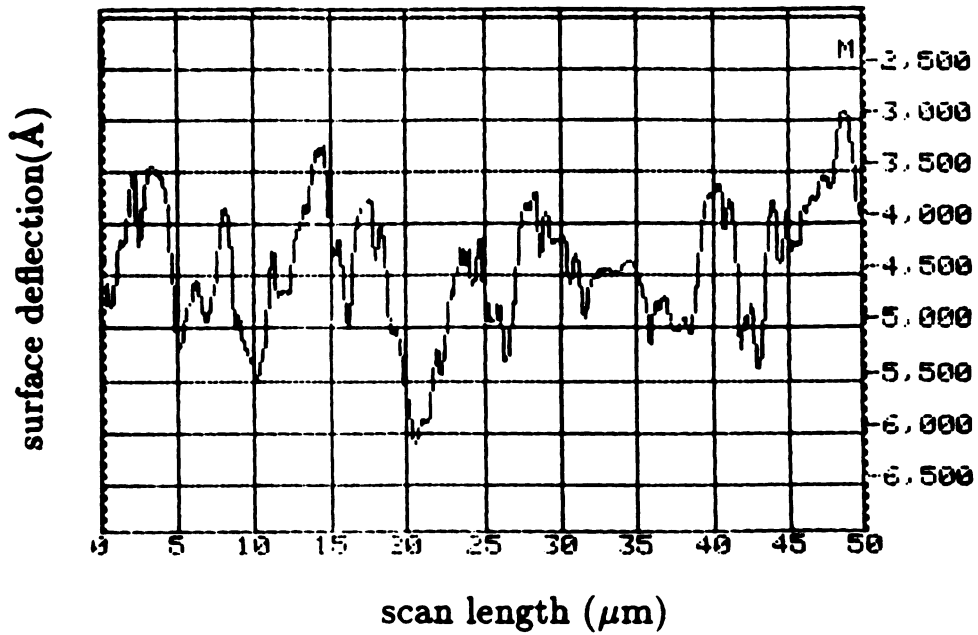


Figure 4.15. SEM view of the powder-polished produced diamond film on a cleaved sample showing the silicon substrate, the interface, and the side view and top surface of the diamond film.

(a)



(b)

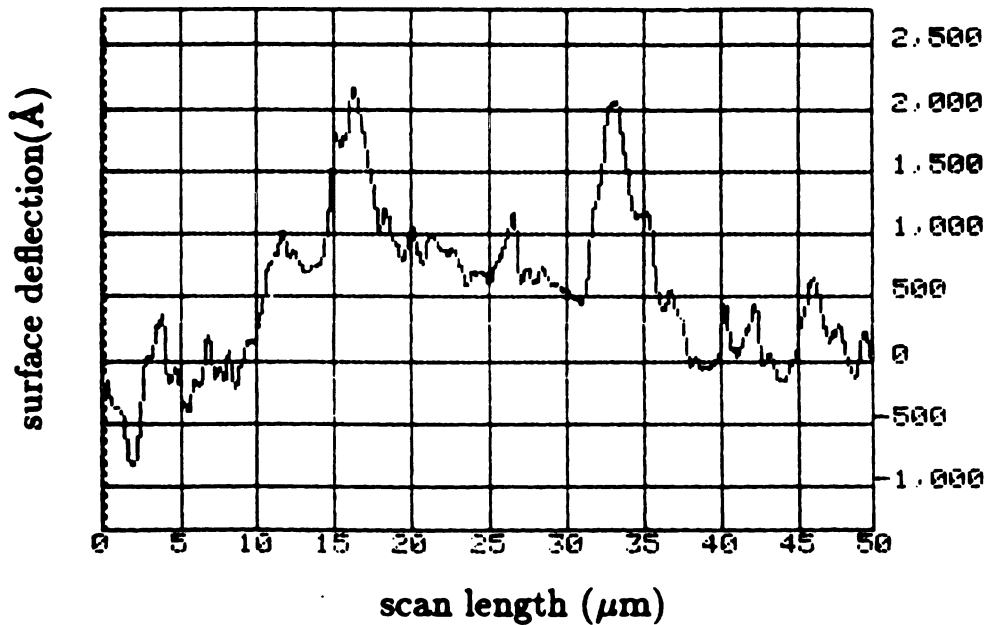
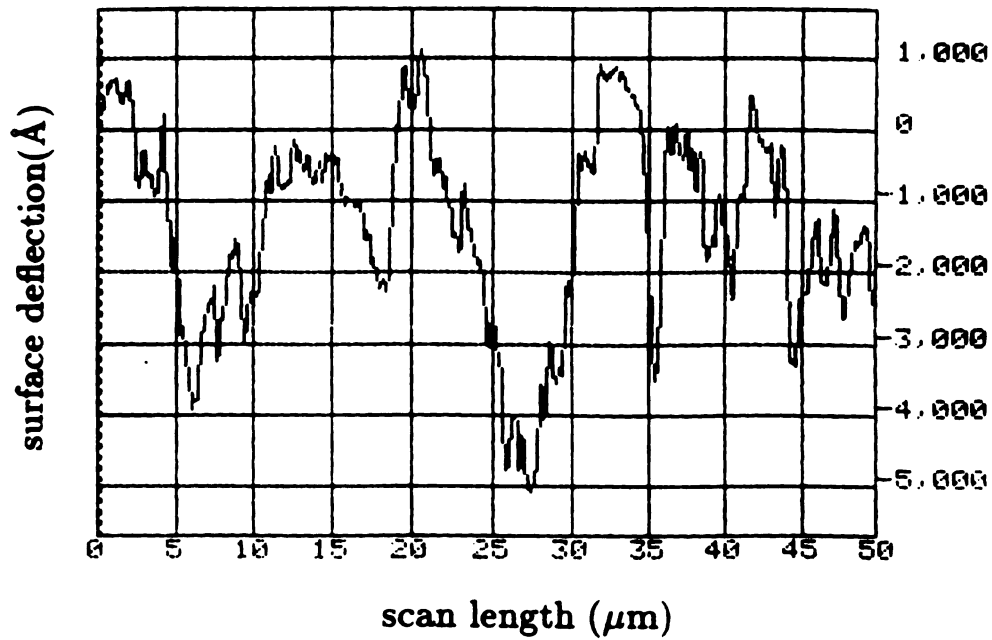


Figure 4.16. The surface profile on (a) the top surface of an as-deposited powder-polished produced diamond film and (b) the back surface of the film after transfer to the epoxy substrate.

(a)



(b)

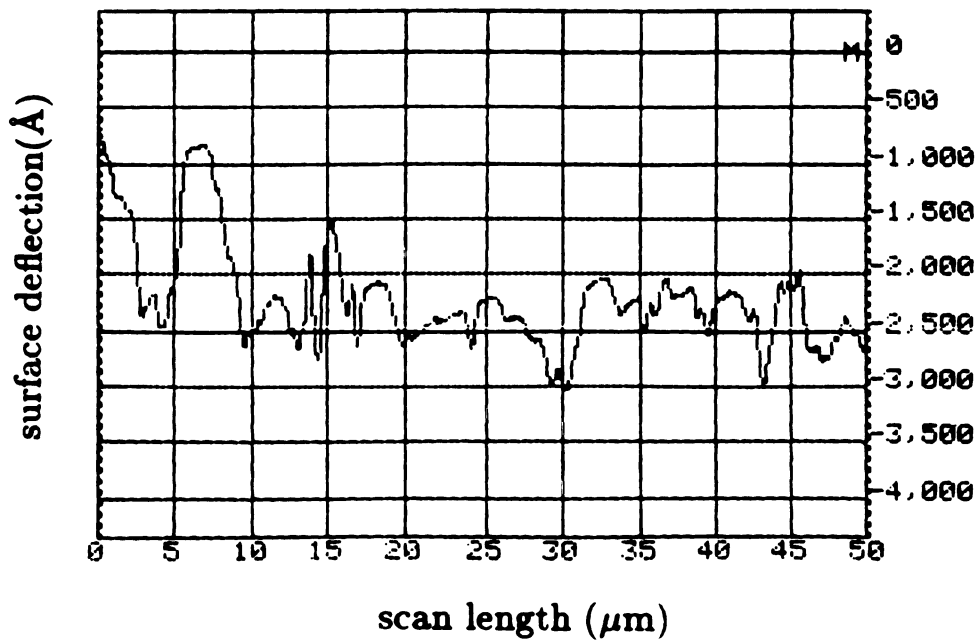


Figure 4.17. The extreme top surface profiles of (a) large-grain-size and (b) small-grain-size diamond films.

tinguish features smaller than  $1\ \mu\text{m}$ . In comparison, the wavelength of the electrons is less than  $0.5\ \text{\AA}$ , and theoretically the maximum magnification of electron beam instruments is beyond 800,000X. However, because of the instrumental parameters, practical magnification and resolution limits are about 75,000X and  $40\ \text{\AA}$  in a conventional SEM [114]. Since polycrystalline diamond films often have sub-micron feature sizes, the high resolution capabilities of SEM are crucial for determining crystal morphology.

In chapter 4 (section 4), it was noted that different grain-size polycrystalline diamond films result from different nucleation techniques. Relatively large-grain-size diamond films, as in Figure 4.18, are formed by the paste-polished method and relatively small-grain-size films, as in Figure 4.19, are formed by the powder-polished method. The major reason for the difference is that the powder-polished method provides a much higher density of nucleation sites than did the paste-polished method. Diamond particle residue and the scratches associated with polishing by diamond particles provide nucleation sites which enhance the local configuration for the diamond growth. As shown in Figure 3.4 and Figure 3.5, more scratches and particle residue were observed by the powder-polished method than the paste-polished method. As the nucleation sites density increases, the space of lateral growth of diamond for each site is limited. Correspondingly, the grain size becomes much smaller as shown in Figure 4.20. This phenomenon also can be proved by a careful experiment described as follows. The surface was intentionally polished with less nucleation sites in one place than in the other places by the powder-polished method. After the deposition, the difference of the crystal growth is obvious under the SEM in Figure 4.21. Large grain size diamond particles show up in the area with less nucleation sites compared to the small grain size diamond particles in the area with a higher density of nucleation sites. This shows that the density of nucleation sites is a major factor in determining

grain

Th

surfac

surfac

of line

T

the a

press

then

plasm

and

ples

incre

more

I

depe

pare

for

the

con

pea

seq

met

grain size. This observation is also confirmed by J. F. DeNatale and coworkers [115].

The main objectives for using SEM analysis in this research are to examine the surface morphology and grain size and to determine the film thickness. From the surface micrograph the average grain size of a film can be estimated by the method of linear intercepts, which is explained by the following equation.

$$\langle \text{grain size} \rangle = \frac{\text{total path length}}{\text{no. of intercepts}} \times \frac{1}{\text{magnification}} \quad (4.2)$$

The results in Table 4.1 and Table 4.2 show that for a given preparation method the average grain size has a tendency to increase as the microwave power or plasma pressure increases. The higher the microwave power, the higher the plasma energy, then the higher the reaction rate, so the bigger the grain size. On the other hand, plasma density increases as the plasma pressure increases, so does the reaction rate and grain size. In Table 4.1 the data also indicates that in the paste-polished samples the  $CH_4/H_2$  concentration plays an important role since the average grain size increases significantly as methane concentration increases. It is understandable since more methyl radicals can form the same crystal at the same time.

It was noted that the samples prepared by the powder-polished method were deposited at lower microwave power and plasma pressure conditions than those prepared by the paste-polished method since the experiment was performed sequentially for these two groups. The samples were prepared by the paste-polished method in the beginning. However, it was found from the Raman spectrum that a sample at the condition of 700 W, 70 Torr, and 1 % methane concentration showed only graphite peaks instead of a diamond peak since the deposition temperature is too high. Consequently the deposition conditions for later samples prepared by powder-polished method were lower.



Fig  
pas  
pow

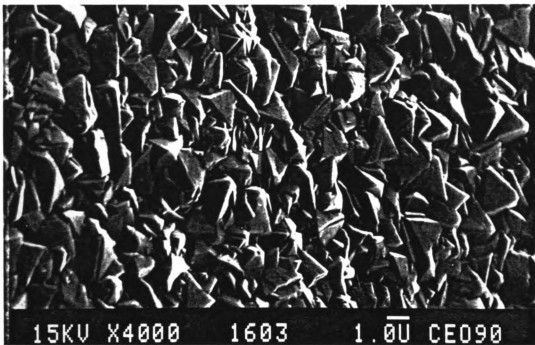


Figure 4.18. Typical SEM photo of the top view of the diamond film prepared by the paste-polished method. The triangular shapes indicate [111] crystallite faces. (MW power: 600 W, plasma pressure: 60 Torr, methane concentration: 0.5%.)

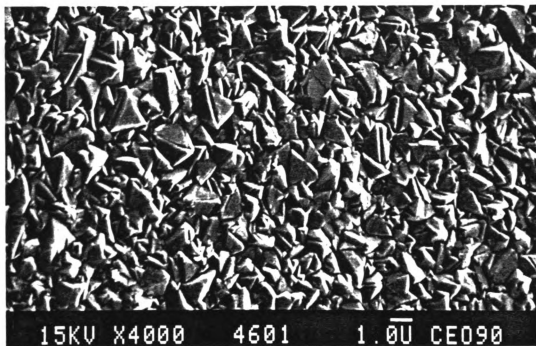


Figure 4.19. Typical SEM photo of the top view of the diamond film prepared by the powder-polished method. (MW power: 600 W, plasma pressure: 60 Torr, methane concentration: 0.5%.)

(a)

Voids

Nucleation  
Sites

(b)

V

Nucleation  
Sites

Figure 4.  
(b) powder  
a finer gr

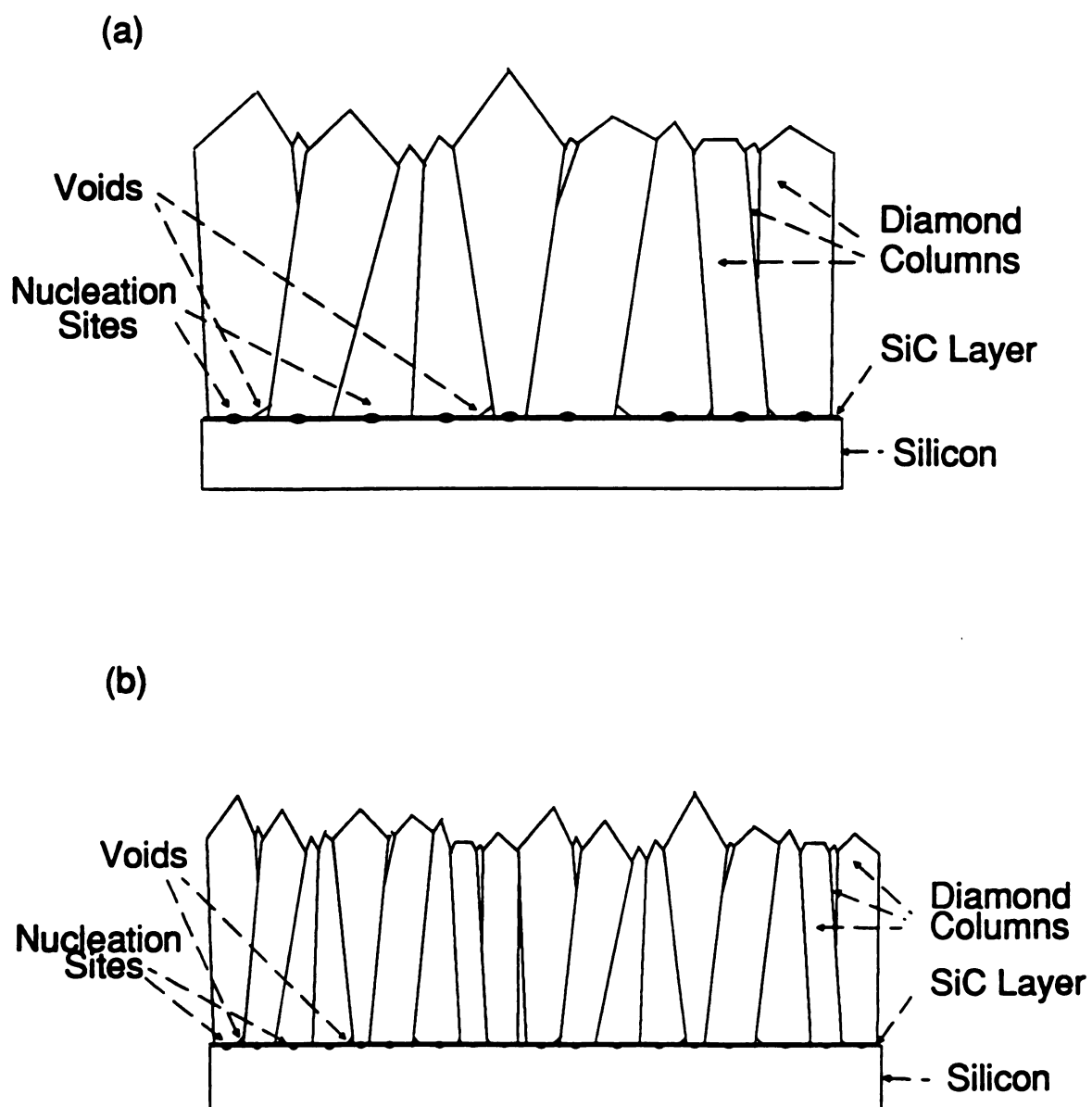


Figure 4.20. Growth mechanism of diamond film prepared by (a) paste-polished and (b) powder-polished method. The latter has a higher nucleation density and therefore a finer grain film.

Figur  
the s

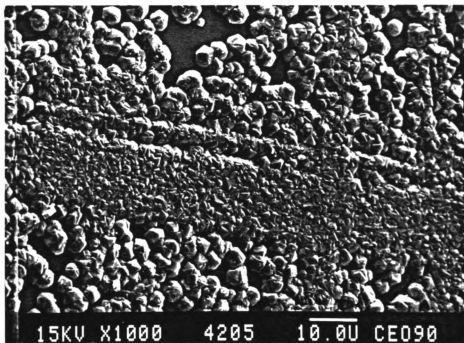


Figure 4.21. This SEM photo shows large and small grain size diamond growth on the same substrate.



(a) **CH<sub>4</sub>/H<sub>2</sub> Concentration : 0.5 %**

*Average grain sizes ( $\mu\text{m}$ ) are listed below.*

Microwave Input Power	Plasma Pressure		
	60 Torr	70 Torr	80 Torr
600 W	0.83	---	---
700 W	0.89	1.18	1.28
800 W	1.01	---	---

(b) **CH<sub>4</sub>/H<sub>2</sub> Concentration : 1.25 %**

600 W, 60 Torr : 1.41  $\mu\text{m}$

(c) **CH<sub>4</sub>/H<sub>2</sub> Concentration : 1.5 %**

600 W, 70 Torr : 2.14  $\mu\text{m}$

Table 4.1. Relation of average grain size vs. methane concentration, microwave power and plasma pressure by the paste-polished method.

**CH<sub>4</sub>/H<sub>2</sub> Concentration : 0.5 %**

*Average grain sizes ( $\mu\text{m}$ ) are listed below.*

Microwave Input Power	Plasma Pressure		
	50 Torr	60 Torr	80 Torr
400 W	---	0.47	---
500 W	---	0.57	---
600 W	0.55	0.63	0.76

Table 4.2. Relation of average grain size vs. microwave power and plasma pressure by the powder-polished method.

ne

re

s

o

re

a

n

i

n

**1**

ic

va

h

a

r

o

v

re

re

o

o

si

e

The relationship of the growth rate or the deposition rate ( $\mu\text{m}/\text{hour}$ ) versus methane concentration, microwave power and plasma pressure by the two different preparation methods are listed in Table 4.3 and Table 4.4. Methane concentration is a major factor for the growth rate since the growth rate increases as the methane concentration increases in both preparation methods. The higher the methane concentration, the more methyl radicals ( $\text{CH}_3$ ) are available for deposition, so the growth rate increases. Likewise, the growth rates also had a tendency to increase as the microwave power and plasma pressure increase since the reaction rate increased as plasma energy or plasma density increased, however, the effect is smaller than the methane concentration effect.

## 4.6 Film Uniformity Analysis

So far, in this chapter Raman Spectroscopy was used for film quality analysis, XPS was performed for diamond/silicon interface studies, DekTak profiles were used for the film surface smoothness test, and SEM were used for the grain size and growth rate studies. But there is another important parameter, which is the film uniformity.

When depositing the diamond film by using the plasma CVD technology described in chapter 3 (section 4), usually an approximately hemispherical shape discharge is formed right above the substrates. This phenomenon becomes particularly evident when the discharge pressure is above 50 Torr. The discharge size increases as the pressure decreases because at about 10 Torr or less the discharge tends to fill the quartz confinement chamber. The deposition rates of the film are dependent on the positions correspond to the density of the discharge. If at low pressures, the discharge volume is large enough to uniformly cover the sample, the deposition rate will be fairly uniform over the sample. At high pressures as the discharge size decreases, the deposition rates over the sample area will show more variation. The trade-off is that

(a) **CH<sub>4</sub>/H<sub>2</sub> Concentration : 0.5 %**

*Deposition rates ( $\mu\text{m}/\text{hour}$ ) are listed below.*

Microwave Input Power	Plasma Pressure		
	60 Torr	70 Torr	80 Torr
600 W	0.34-0.38	---	---
700 W	0.35-0.4	0.36-0.41	0.37-0.42
800 W	0.39-0.44	---	---

(b) **CH<sub>4</sub>/H<sub>2</sub> Concentration : 1.25 %**

600 W, 60 Torr : 0.54 - 0.6  $\mu\text{m}/\text{hour}$

(c) **CH<sub>4</sub>/H<sub>2</sub> Concentration : 1.5 %**

600 W, 70 Torr : 0.92 - 1.06  $\mu\text{m}/\text{hour}$

Table 4.3. Relation of deposition rate vs. methane concentration, microwave power and plasma pressure by the paste-polished method.

(a) **CH<sub>4</sub>/H<sub>2</sub> Concentration : 0.5 %***Deposition rates ( $\mu\text{m}/\text{hour}$ ) are listed below.*

Microwave Input Power	Plasma Pressure		
	50 Torr	60 Torr	80 Torr
400 W	---	0.28-0.32	---
500 W	---	0.33-0.38	---
600 W	0.4-0.42	0.42-0.45	0.58-0.63

(b) **CH<sub>4</sub>/H<sub>2</sub> Concentration : 1 %***Deposition rates ( $\mu\text{m}/\text{hour}$ ) are listed below.*

Microwave Input Power	Plasma Pressure	
	50 Torr	60 Torr
600 W	0.48-0.52	0.56-0.62

Table 4.4. Relation of deposition rate vs. methane concentration, microwave power and plasma pressure by the powder-polished method.

deposition rate goes down as the pressure and plasma density decreases.

To determine the thickness on different parts of the film, SEM is still the most accurate measurement method. However, a gold coating of the sample is necessary to obtain good image resolution and sample cleavage is required. Consequently, the SEM technique is destructive. In order to determine a technique for measuring thickness uniformly non-destructively, a laser scanning confocal microscope (LSM) was used in this research.

The LSM is a light microscope, but one with a difference! In the microscope's name the words "laser" and "scanning" refer to the method of illumination, while "confocal" refers to the method of image formation. The microscope has four light sources: a fiber optic tungsten lamp, a mercury lamp, an argon-ion laser with 488 and 514 nm lines, and a helium-neon laser with a 543 nm line. So the LSM can be operated both as a conventional microscope (using the tungsten or the mercury lamp) and a laser scanning instrument.

The term "confocal" indicates that the microscope is aligned so that the illuminated spot and imaged spot coincide precisely, which is not the case in conventional light microscopes. In a conventional microscope, light reaching the observer comes from all parts of the specimen within the field of view - both from the narrow horizontal plan which is in focus and from out-of-focus regions above and below it. The light from out-of-focus areas, which severely degrades the focal-plane image, generally limits to just a few microns the depth to which a specimen can be examined.

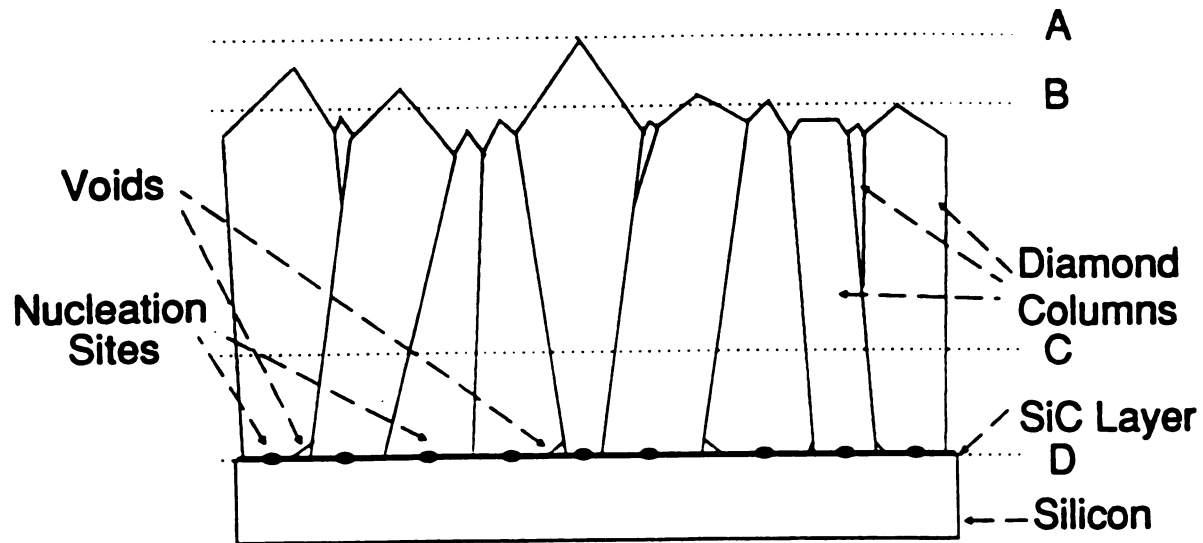
In a confocal instrument the specimen is scanned point-to-point with a finely focused beam, most effectively by a laser, and a pinhole aperture is placed directly in front of the detector at the focal point of light coming from the in-focus part of the specimen. The effect of these modifications is to block light from out-of-focus regions because the focal point of such light falls either in front of or behind the pinhole

aperture. The result of this instrument configuration on the final image is a dramatic increase in resolution and contrast.

The theoretical limit of resolution for a conventional light microscope is about  $0.17 \mu\text{m}$ . But much smaller objects can be easily seen in the LSM. There are multiple reasons for this, chief among them being the elimination of out-of-focus light by the confocal pinhole. In addition, monochromatic light (the laser) eliminates chromatic aberration; scanning a specimen with a small spot, no matter what the light source, always improve resolution; and the photomultiplier detector is more sensitive than the human eye. Magnification in the LSM ranges from  $200\times$  to  $16,000\times$  [116]. This upper limit is significantly higher than a conventional optical microscope.

In our case, however, the samples prepared by paste-polished method have a better resolution in the diamond/silicon interface than those prepared by powder-polished method since the interface was flatter by the former method. A sample with the biggest average grain size and thickest diamond film was used to perform the uniformity study. Under the SEM analysis, the thickness of the diamond film on an area of  $0.2 \text{ cm} \times 0.4 \text{ cm}$  is between  $6.5$  and  $7.5 \mu\text{m}$ . By the LSM technique, a scan in the Z (or vertical) axis of the sample can be carefully observed since diamond is transparent to visible light. A  $488 \text{ nm}$  laser scan was used for the best resolution in our studies. The thickness of the film was then determined by the distance between A plane and D plane as shown in Figure 4.22(a). Eight thickness measurements were performed on an area of  $1 \text{ cm} \times 2 \text{ cm}$  of the same sample in different locations as in Figure 4.22(b). A distribution of thickness between  $5.8$  and  $8.0 \mu\text{m}$  were obtained. This study did show that the LSM technique indeed can perform the uniformity studies efficiently without significant loss of accuracy and also without any sample destruction and contamination.

(a)



(b)

8.0	6.9	6.1
7	6.5	
7.8	7.4	5.8

Figure 4.22. (a) Cross section view of laser scan from plane A to D. (b) Thickness ( $\mu\text{m}$ ) uniformity analysis on an area of 1 cm X 2 cm of a sample.

# CHAPTER 5

## Electrical Characterization

### 5.1 Introduction

In this chapter, conductivity vs. temperature results for the as-deposited diamond films will be described in chapter 5 (section 2). Then current-voltage characteristic of samples with dual-side metal contacts on the isolated diamond films will be discussed in chapter 5 (section 3). Finally, current-voltage characterization of the samples with metal-diamond-silicon structure will be discussed in chapter 5 (section 4).

### 5.2 Four Point Probe Characterization

#### 5.2.1 Experimental Method

The measurement of bulk resistivity, particularly vs. temperature, provides a fundamental means of electrically characterizing materials and is essential to investigate current transport in diamond films. In order to avoid contact effects, a method of choice for measurement of electrical resistivity is the four point probe method. However, on high resistivity thin films (such as diamond films), the measurement technique is nontrivial because of the requirement of accurately measuring small voltages and

e  
a  
o  
(  
e  
H  
te  
o  
d  
th  
ef  
ti  
w  
ex  
wh  
tes  
thi  
spa  
rati

currents. A standard instrumentation approach such as is used on silicon wafers is not adequate. Consequently, a sensitive four point probe apparatus, with the capability of changing the measurement temperature, was constructed as in Figure 5.1.

The sheet resistance of diamond films on insulating silicon nitride substrates ( $Si_3N_4$ ) was measured with a Signatone four point probe station as follows. Four equally spaced point probes are brought into contact with the sample surface. A Hewlett Packard 4145 B Semiconductor Parameter Analyzer is used as the ammeter to measure the current (I), which is supplied by a dc power supply, through the two outer probes. The supply voltage is set at 40 V in this study. A high impedance digital voltmeter (Fluke Model 8840 A) connected to the two inner probes is used for the voltage (V) measurement. This arrangement largely eliminates contact resistance effects, since the voltage measurement probes draw negligible current. The probe station is then placed in a Thermotron Environmental Control Chamber (Model S1.2) which allows the temperature to be varied from  $-75^{\circ}C$  to  $175^{\circ}C$ .

The sheet resistance  $R_{\square}$  has a constant of proportionality between  $V/I$ , and is expressed as follows

$$R_{\square} = \xi \left( \frac{V}{I} \right) \quad (5.1)$$

where  $\xi$  is a correction factor, the value of which is determined by the shape of the test sample and the ratio between the size of the sample and the probe spacing. In this experiment, the size of the  $Si_3N_4$  substrate is  $0.5'' \times 0.5'' \times 0.2''$  and the probe spacing is 0.0625 inches. For a square substrate and a substrate size to probe spacing ratio of 8, the correction factor  $\xi$  is determined to be approximately 4 [117].

The resistivity ( $\rho$ ) of the diamond film is then obtained by

$$\rho = R_{\square} \cdot t \quad (5.2)$$

—  
/—  
—  
—  
—  
—  
—

—

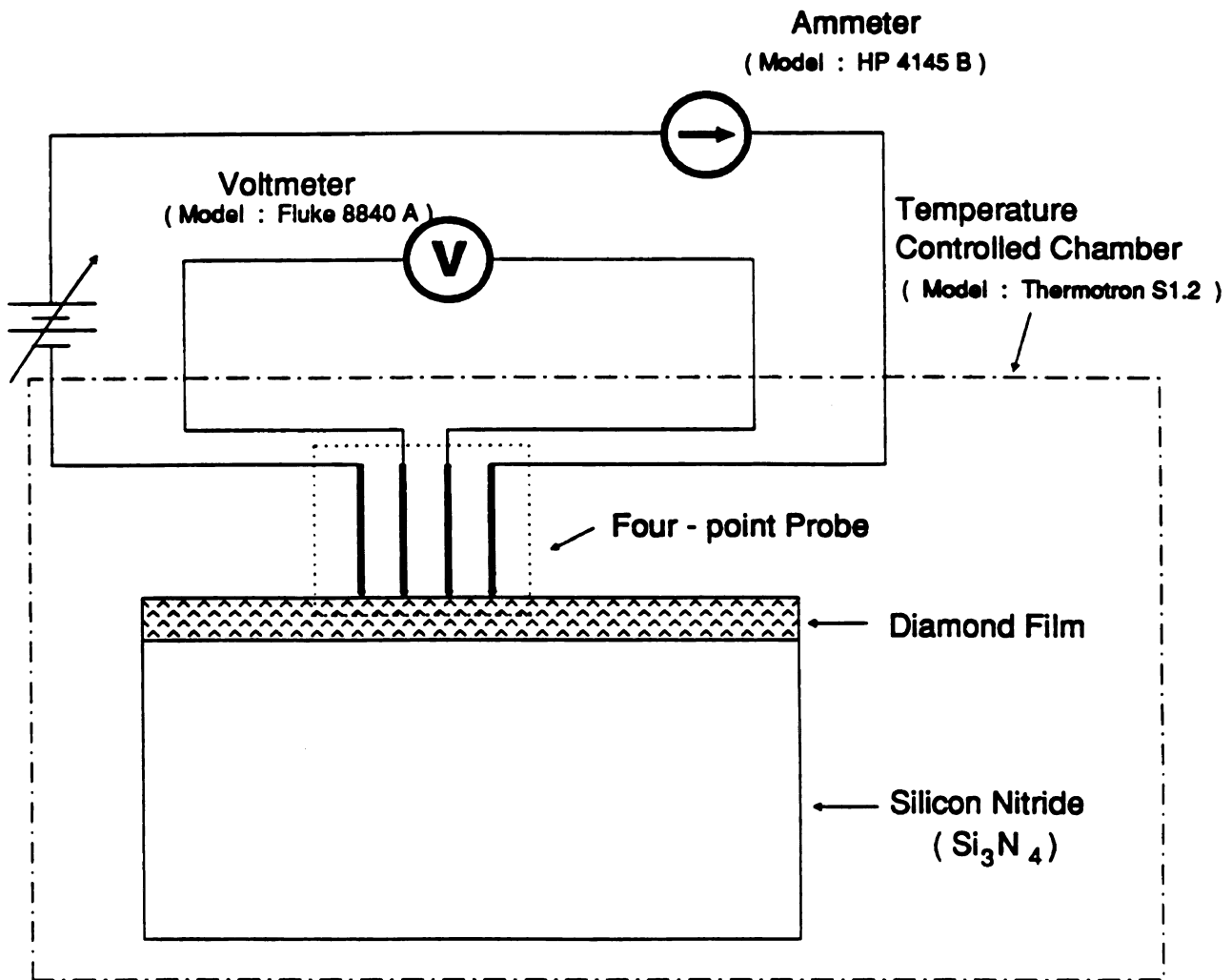


Figure 5.1. The set-up of the four point probe method.

where  $t$  is the film thickness, and the conductivity ( $\sigma$ ) of the film is

$$\sigma = \frac{1}{\rho} \quad (5.3)$$

### 5.2.2 Theory of Conductivity vs. Temperature

The conductivity of the diamond film on insulating material ( $Si_3N_4$ ) was studied at different temperature levels in order to understand the conduction mechanism.

As is generally the case for semiconductors, the electrical properties of diamond are dominated by the effect of dopants and other impurities or defects. Experimental measurements of the electrical conductivity provide information about the concentration of electrically active impurities and defects as well as their energy levels.

Thermopower measurements on the diamond films used in this research show that the films are p-type, indicating the presence of acceptor-type impurities or defects even though the films were not intentionally doped with acceptors. For a semiconductor with a single acceptor level at energy  $E_a$  in the energy gap, the hole concentration,  $p$ , is given by [118, 119]

$$p = N_v \exp - [(E_f - E_v)/kT] \quad (5.4)$$

where  $N_v$  is the effective density of states in the valence band,  $E_f$  is Fermi level,  $E_v$  is top level of the valence band and  $k$  and  $T$  denote the Boltzmann constant and absolute temperature, respectively. From charge neutrality,

$$p = n + N_a^- \quad (5.5)$$

where  $n$  is the electron concentration,  $N_a$  is the concentration of acceptors, and  $N_a^-$

is

T

or

in

or

Fr

Th

pr

wh

va

wh

of

is the concentration of ionized acceptor. Consequently,

$$p = n + \frac{N_a}{1 + 4\exp[(E_a - E_f)/kT]} \quad (5.6)$$

The term on the left side of the equation corresponds to positive charges, and those on the right side correspond to negative charges. However, at the temperature of interest here the electron density in p-type material is very small, so the first term on the right hand side can be neglected and Eq. (5.6) becomes [118]

$$p = \frac{N_a}{1 + 4\exp[(E_a - E_f)/kT]} \quad (5.7)$$

From Eq.(5.4) and (5.7), one obtains

$$p = \frac{1}{2}\exp\left(\frac{E_v - E_a}{kT}\right) \times \left[-N_v/4 + \sqrt{N_v^2/16 + N_a N_v \exp\left(\frac{E_a - E_v}{kT}\right)}\right] \quad (5.8)$$

The hole concentration is directly related to the measured conductivity by the expression

$$\sigma = q\mu_p p \quad (5.9)$$

where  $q$  and  $\mu_p$  are electron charge and carrier mobility respectively. The reported value of hole mobility  $\mu_p$  is  $1200 \text{ cm}^2/\text{V}\cdot\text{s}$ . [120]

In this research,  $N_v$  was calculate from

$$N_v = 2(2\pi m_p^* kT/h^2)^{3/2} \quad (5.10)$$

where  $m_p^*$  is effective hole mass and  $h$  is Planck constant. [121] The reported value of  $m_p^*$  ( $= 0.75 m_0$ ) of natural diamond was used [120], which yields

$$N_v = 3.137 \cdot 10^{15} \cdot T^{3/2} \text{ cm}^{-3} \quad (5.11)$$

From Eq.(5.8), (5.9) and (5.11), and the measured conductivities at different temperatures,  $(E_a-E_v)$  and  $N_a$  may be used as parameters to fit the experimental data. The comparison of the experimental results and theoretical calculation will be discussed in chapter 5 (section 2.4).

### 5.2.3 Comparison with Physical Characterization

There are four samples in this four point probe study, three of which are prepared by the diamond powder nucleation method and one which is prepared by the diamond paste nucleation method. The three powder-polished samples (NDF-S3,S4,S6) have similar sub-micron crystallite morphology and the paste-polished sample (NDF-S1) has a larger (greater than  $1 \mu\text{m}$ ) grain size diamond film based on optical microscope analysis.

The deposition conditions for the samples are described as follows. The deposition times are all 6 hours.

**NDF-S1**,  $CH_4/H_2$  : 0.5 %(1.25 sccm/250 sccm), M.W input power : 600 W, plasma pressure : 60 Torr, temperature : 1060 °C.

**NDF-S3**,  $CH_4/H_2$  : 0.5 %(0.75 sccm/150 sccm), M.W input power : 500 W, plasma pressure : 50 Torr, temperature : 1035 °C.

**NDF-S4**,  $CH_4/H_2$  : 0.5 %(0.75 sccm/150 sccm), M.W input power : 400 W, plasma pressure : 50 Torr, temperature : 1000 °C.

**NDF-S6**,  $CH_4/H_2$  : 0.5 %(0.75 sccm/150 sccm), M.W input power : 320 W, plasma pressure : 50 Torr, temperature : 950 °C.

Samples NDF-S3, S4 and S6 are as-deposited diamond films, for which the deposition was terminated by turning off the microwave power while both methane and hydrogen gas flows were on. However, the deposition for NDF-S1 was terminated by first turning off the methane gas flow, exposing the sample to a hydrogen plasma and

then turning off the microwave power. This sample was subsequently treated in a solution ( $2H_2O:16H_3PO_4:1HNO_3:1$  acetic acid) at  $80\text{ }^\circ C$  for 1 hour in order to remove the conducting layer caused by the hydrogen plasma during the process.

The corresponding Raman spectrum for each sample is shown in Figure 5.2 and Figure 5.3. In Figure 5.2, the Raman spectra, which were performed by Dr. Mark Holtz in Physics department of Michigan State University, of NDF-S3, S4, S6 are compared. Note that the horizontal wavenumber scale is in **absolute wavenumbers** with *photon energy increasing from left to right* and *phonon energy increasing from right to left*. More typically, diamond Raman spectra are plotted vs. shifted wavenumber. In terms of shifted wavenumber, the peak that is apparent in each spectrum is at  $1331\text{ }cm^{-1}$  plus or minus  $1\text{ }cm^{-1}$  and corresponds to the diamond peak. At all temperatures shown in this figure a strong diamond peak is noted. There are two indicators that the diamond films approach the Raman properties of natural diamond as temperature increases from  $950\text{ }^\circ C$  to  $1035\text{ }^\circ C$ . First, the height of the diamond peak relative to the background level increases as the temperature increases. Secondly, the width of the peak increases as the temperature decreases. For natural diamond, the peak is very sharp, with full-width-half-maximum (FWHM) of  $2.1\text{ }cm^{-1}$ . For diamond films, FWHM values are substantially larger, in the range of  $7 - 17\text{ }cm^{-1}$  [102].

In Figure 5.3, the Raman spectrum, which was performed by Dr. Kevin Gray in Norton Company, of NDF-S1 is shown. The spectrum shows a very sharp diamond peak along with a small graphitic peak on the right shoulder. This spectrum is similar to the spectrum of NDF-S3, with a FWHM equal to  $9\text{ }cm^{-1}$ .

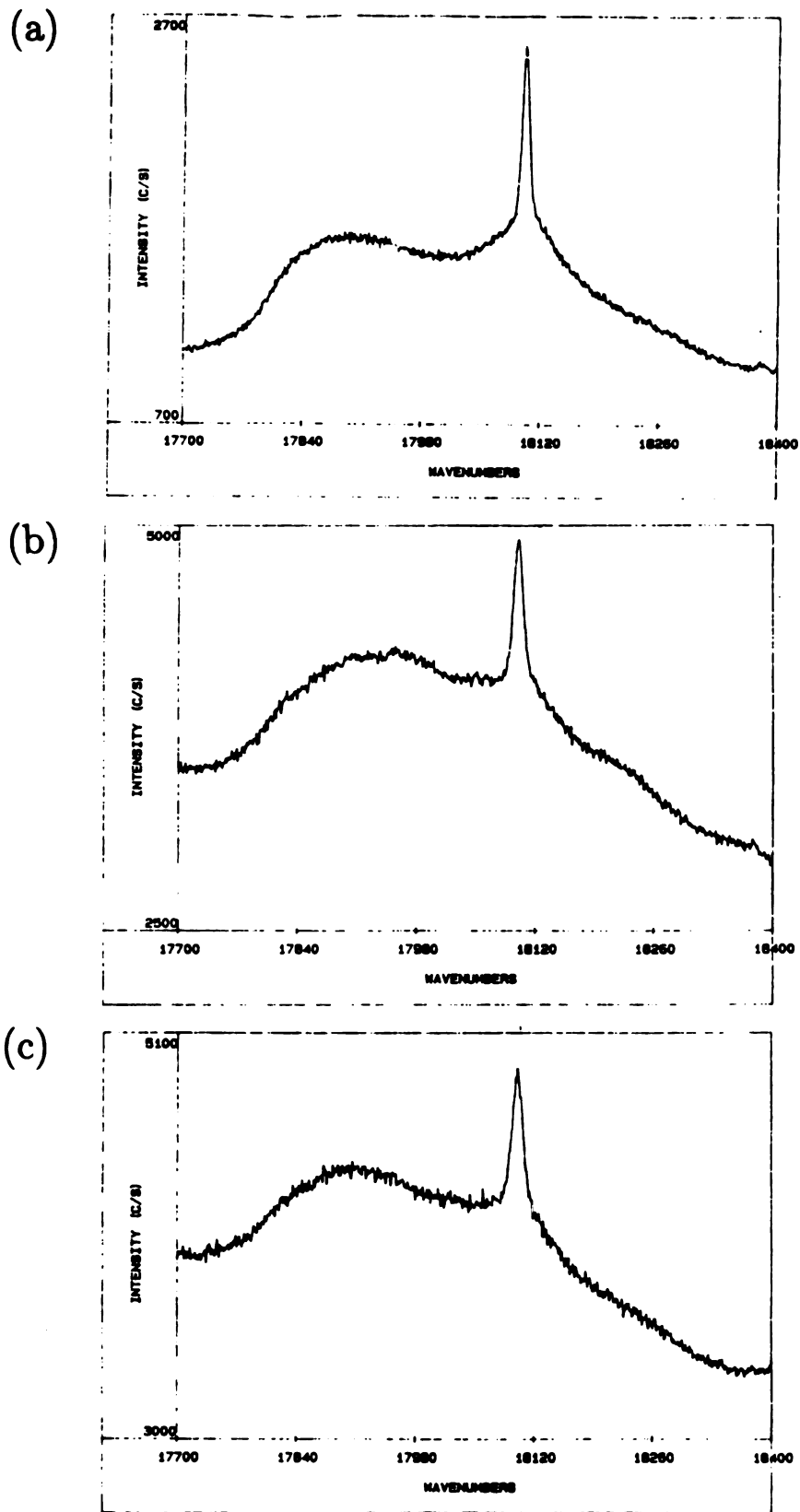


Figure 5.2. Raman spectra of (a) NDF-S3, (b) NDF-S4, and (c) NDF-S6. (From Dr. Holtz)

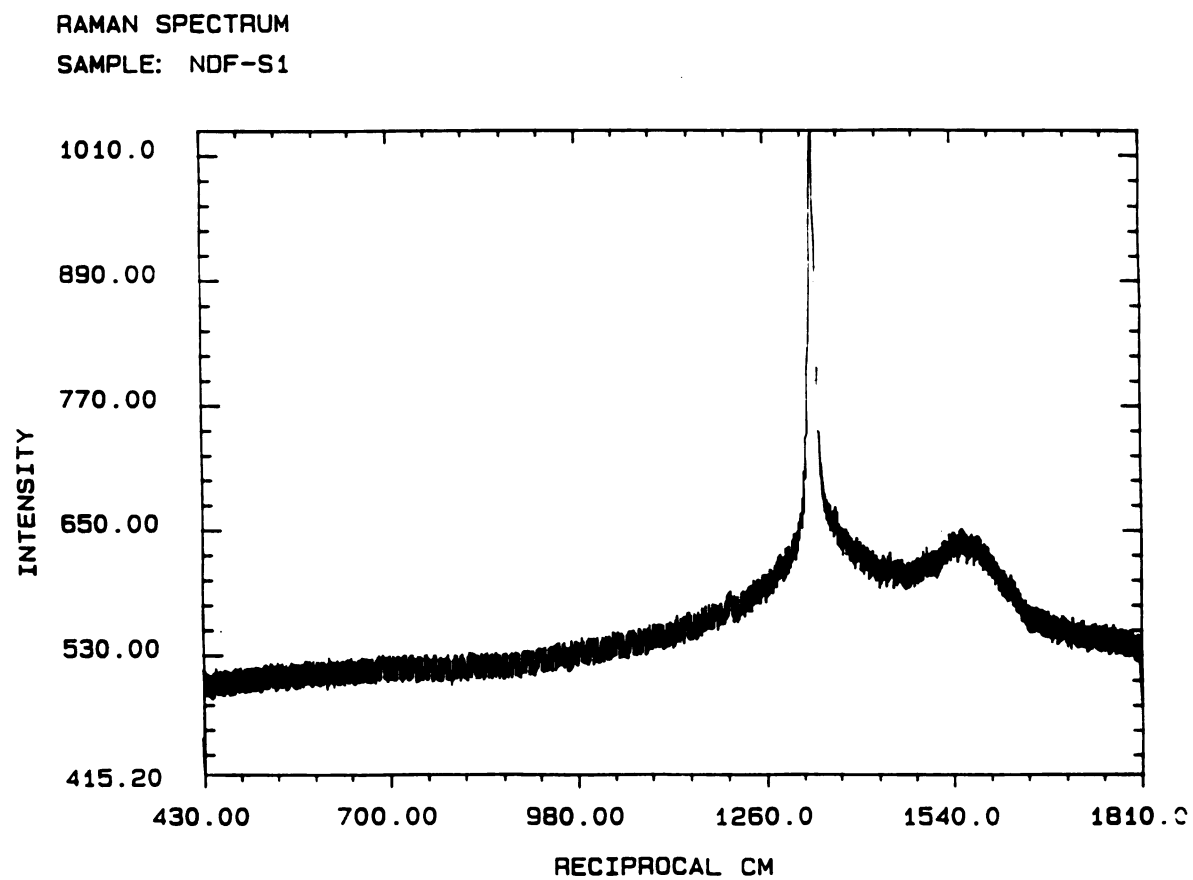


Figure 5.3. Raman spectrum of NDF-S1. (From Dr. Gray)

### 5.2.4 Experimental Results and Match with Theory

The films in this study were not intentionally doped with impurities. However, impurities may come from a variety of sources including impurities in the feed gases. Although the methane used was the highest purity readily available (99.99 %), this is not high purity by semiconductor standards. A methane purity of 99.99 % essentially corresponds to one impurity in 10,000 methane molecules. If, as a case in point, there is one impurity per 10,000 carbon atoms in the diamond film, this would correspond to an impurity density of  $1 \times 10^{19} \text{ cm}^{-3}$  which is more than sufficient to dominate the electrical properties. In conventional semiconductors like silicon, impurity densities in active device regions are typically on the order of  $1 \times 10^{15} \text{ cm}^{-3}$ . Other possible sources of impurities include residual gases in the vacuum system, air leaks, and sample handling. Only a mechanical roughing pump was used to evacuate the system. Furthermore, structural defects in the crystallites and grain boundaries can introduce states in the gap which may act as traps, acceptors, or donors. Consequently, even though the films are not intentionally doped, it is anticipated that electrical properties of the film will be controlled by defects and impurities.

Simple hot probe measurements based on the thermopower phenomenon showed that all of the samples were p-type, indicating that defects and/or impurities play the role of acceptors. By combining the theory of chapter 5 (section 2.2) with experimental results, information is obtained about the concentration of these states, and their energies.

Performing the four point probe measurement, one can get the (V/I) ratio. Then following Eq. (5.1), it was found that the sheet resistances ( $R_{\square}$ ) for NDF-S1, S3, S4 and S6 at room temperature are  $1.2 \times 10^8$ ,  $1.3 \times 10^6$ ,  $5.6 \times 10^5$ , and  $2.1 \times 10^5 \Omega/\square$  respectively. It was also noted that the sheet resistance of NDF-S1 before the cleaning procedure was  $1 \times 10^4 \Omega/\square$ . All of these resistivities are low compared to

natural, un-doped, diamond. However the variation of resistivities among the samples is consistent with the Raman indication that higher deposition temperature produced properties closer to natural diamond since the diamond peak is more similar to that of natural diamond.

Since the thickness of the samples were estimated to be about 3  $\mu\text{m}$  thick for 6 hours' deposition, from Eq. (5.2) the resistivities ( $\rho$ ) at room temperature were calculated to be  $3.6 \times 10^4$ ,  $3.9 \times 10^2$ ,  $1.68 \times 10^2$  and  $6.3 \times 10^1 \Omega \cdot \text{cm}$  for NDF-S1, S3, S4 and S6 respectively. Taking the inverse of the resistivity ( $\rho$ ), then the conductivity ( $\sigma$ ) was determined and plotted.

Figure 5.4, Figure 5.5, Figure 5.6 and Figure 5.7 show the temperature dependence of the conductivity for NDF-S1, S3, S4 and S6 respectively. In all cases, points show experimental results and lines show the results of theoretical calculation from Eq. (5.8), (5.9) and (5.11) assuming a constant mobility ( $\mu_p = 1200 \text{ cm}^2/\text{V}\cdot\text{s}$ ). The values of  $E_a - E_v$  and  $N_a$  are presented in the following.

NDF-S1,  $E_a - E_v = 0.51 \text{ eV}$  and  $N_a = 2.5 \times 10^{12} \text{ cm}^{-3}$ .

NDF-S3,  $E_a - E_v = 0.31 \text{ eV}$  and  $N_a = 2.0 \times 10^{13} \text{ cm}^{-3}$ .

NDF-S4,  $E_a - E_v = 0.24 \text{ eV}$  and  $N_a = 4.0 \times 10^{13} \text{ cm}^{-3}$ .

NDF-S6,  $E_a - E_v = 0.22 \text{ eV}$  and  $N_a = 1.0 \times 10^{14} \text{ cm}^{-3}$ .

However, in reality the carrier mobility for polycrystalline diamond films is much smaller than that in single crystal diamond. If it is assumed that  $\mu_p = 12 \text{ cm}^2/\text{V}\cdot\text{s}$ , the values of  $E_a - E_v$  and  $N_a$  after the same curve fitting procedure are presented in the following.

NDF-S1,  $E_a - E_v = 0.42 \text{ eV}$  and  $N_a = 5.5 \times 10^{14} \text{ cm}^{-3}$ .

NDF-S3,  $E_a - E_v = 0.23 \text{ eV}$  and  $N_a = 3.5 \times 10^{15} \text{ cm}^{-3}$ .

NDF-S4,  $E_a - E_v = 0.15 \text{ eV}$  and  $N_a = 4.0 \times 10^{15} \text{ cm}^{-3}$ .

NDF-S6,  $E_a - E_v = 0.13 \text{ eV}$  and  $N_a = 1.2 \times 10^{16} \text{ cm}^{-3}$ .

Generally, the model calculated data for both  $\mu_p = 1200 \text{ cm}^2/V\cdot s$  and  $\mu_p = 12 \text{ cm}^2/V\cdot s$  fit quite well to the experimental results. However, there are some deviations from the experimental plots. This may indicate the existence of other levels in the forbidden gap or non-monoenergetic states, also the mobility is general not constant with temperature, but may either decrease or increase with temperature depending on whether impurity scattering or lattice scattering dominates.

The paste-polished sample NDF-S1 has a much higher activation energy than the powder-polished samples NDF-S3, S4, S6. Also, the concentration of acceptors is an order of magnitude less than for the other samples. From chapter 4 (section 4), it is known that paste-polished samples usually have bigger grain size diamond crystals than the powder-polished samples. Comparatively, the concentration of grain boundaries for paste-polished samples are smaller than those of powder-polished samples. This is consistent with a hypothesis that acceptor type states are associated with grain boundaries. However, the situation is evidently more complex since the changing value of  $E_a - E_v$  indicates that the nature of acceptor level changes as well as the concentration. For comparison purposes, it is interesting to note that type IIb diamonds which are naturally doped with boron are reported to have an activation energy of 0.37 eV [120].

An annealing process was also performed on all the samples to study if the temperature dependence of the conductivity would change. The samples first were cleaned by acetone, methanol, DI water and dried with  $N_2$ . Then they were annealed at 500 °C for 1 hour in a furnace atmosphere of nitrogen with a 500 sccm flow rate. After the annealing, the sheet resistance of the NDF-S6 is  $1.6 \times 10^9 \Omega/\square$  at room temperature. It increased by nearly 4 orders of magnitude. The sheet resistance of the other samples could not be measured because the current was too small. For these samples, the sheet resistance is beyond the limit of the measuring equipment used in

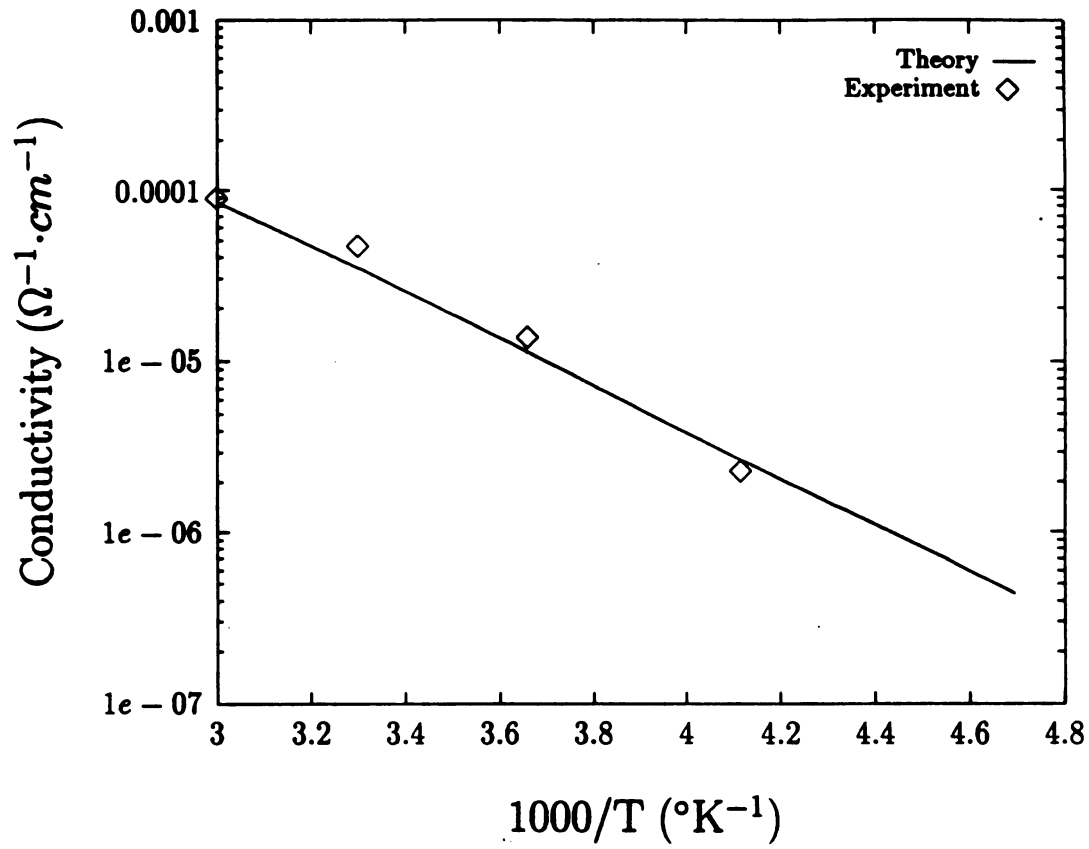


Figure 5.4. Conductivity vs.  $1000/T$  of NDF-S1

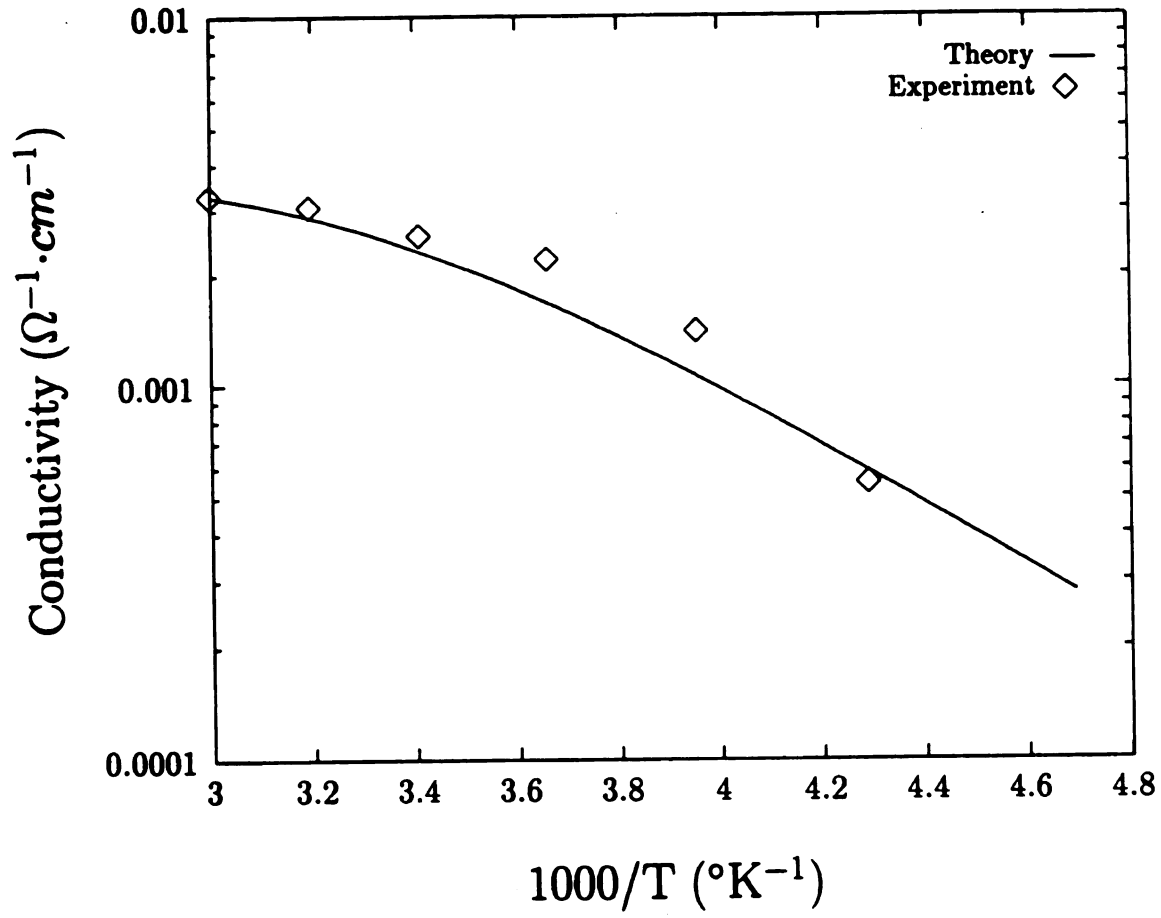


Figure 5.5. Conductivity vs.  $1000/T$  of NDF-S3

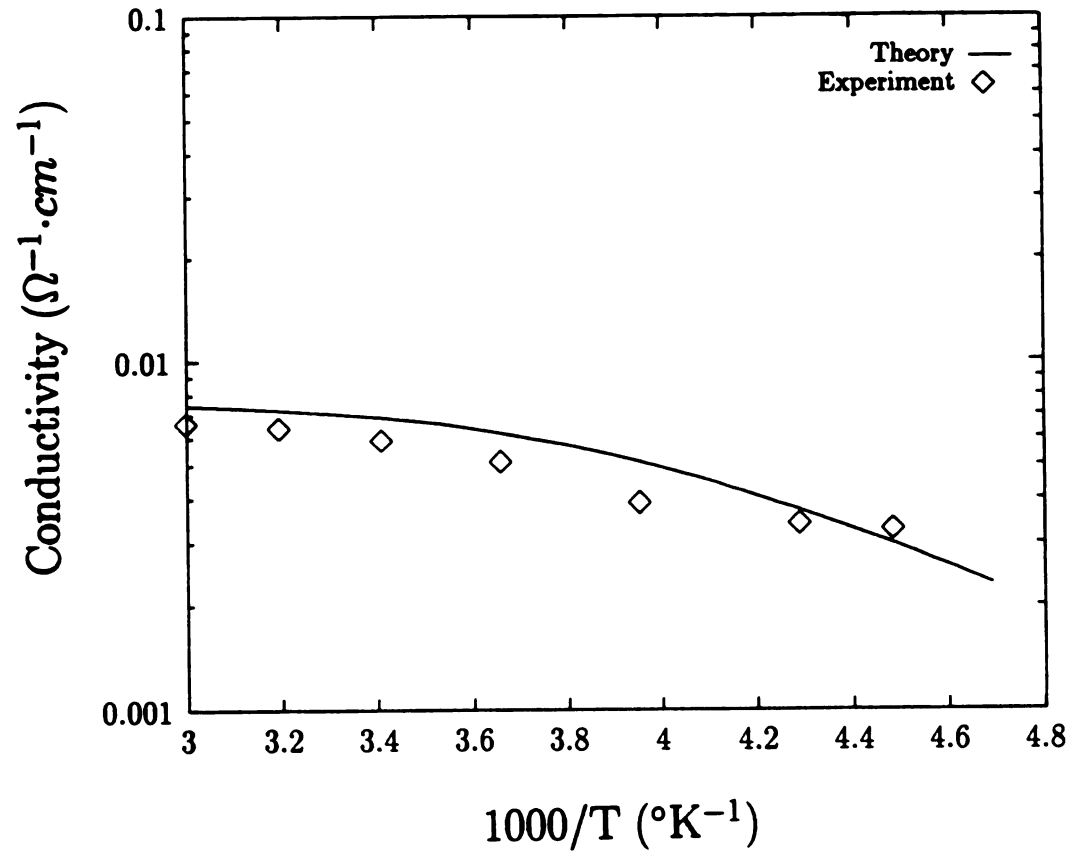


Figure 5.6. Conductivity vs.  $1000/T$  of NDF-S4

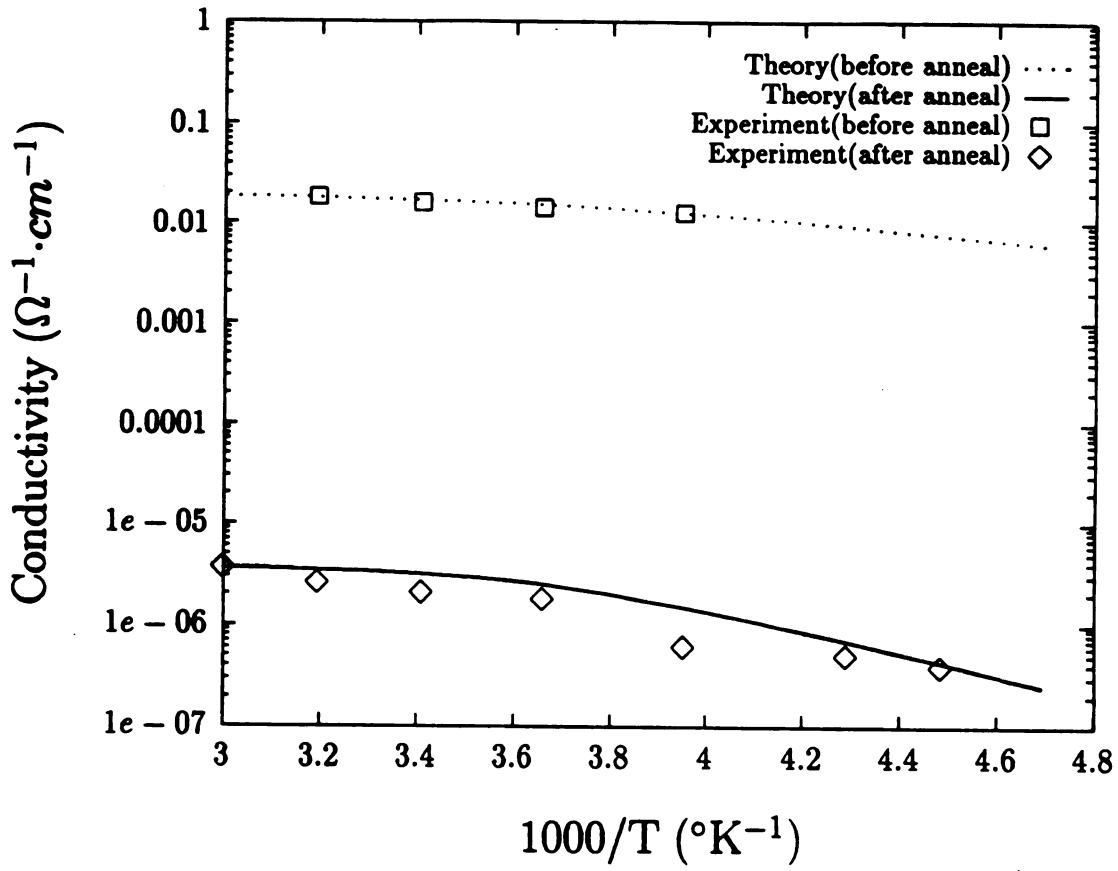


Figure 5.7. Conductivity vs. 1000/T of NDF-S6

this investigation, that is greater than  $10^{10} \Omega/\square$ .

The calculated  $E_a - E_v$  and  $N_a$  for NDF-S6-anneal are 0.44 eV,  $1.9 \times 10^{10} \text{ cm}^{-3}$  when  $\mu_p = 1200 \text{ cm}^2/\text{V}\cdot\text{s}$  and 0.36 eV,  $2.2 \times 10^{12} \text{ cm}^{-3}$  when  $\mu_p = 12 \text{ cm}^2/\text{V}\cdot\text{s}$  respectively. No matter what the value of the mobility is, the significant decrease of the acceptor concentration indicates that part of the defects or impurities are expelled from the samples during the annealing process. The increase of the activation energy suggests that there are multiple impurity energy levels existing in the forbidden gap. When one level is annealed out, the previous minor level becomes dominant.

Landstrass and Ravi presented a specific explanation for such an annealing effect; a model of hydrogen passivation of deep donor-like traps in the inter-band states. Hydrogenation electrically neutralizes the traps and the resistivity is governed by shallow acceptor levels, the effective acceptor concentration increases and the conductivity increases. The annealing process on the other hand causes de-hydrogenation resulting in electrical activation of deep traps. These donor-like traps cause the effective acceptor concentration to decrease because of compensation and the conductivity decreases. When the hydrogenated diamond films are heat treated in a neutral ambient, the hydrogen can be expelled from the crystals, restoring the high resistivity. For example, with a  $780 \text{ }^\circ\text{C}$ , 2 hour treatment in flowing nitrogen ambient, the resistivity increases from  $\sim 10^5$  to  $\sim 10^{14} \Omega\cdot\text{cm}$ . [122, 123] Albin *et al.* [124] also had a similar observation that the conductivity of the diamond films will increase several orders of magnitude after hydrogenation by the hydrogen plasma. However these measurements were performed by the two probe method instead of the four point probe method.

Defects states due to dangling bonds and grain boundaries and inter-band levels due to impurities play major roles in the conduction mechanism of the diamond films. Consequently, from the four point probe experiment, there are indeed multiple inter-band energy levels existing in the forbidden gap and some of the impurities, such as

h

d

5

5

T

d

a

t

in

a

w

d

in

st

F

a

as

di

ef

be

hydrogen, can be expelled from the samples by the annealing process. The effect of defects states will be discussed in chapter 5 (section 3).

## 5.3 Back-Etched Samples.

### 5.3.1 The Back-Etched Samples and I-V Measurement Set-Up

Typical deposition parameters and some physical characterization of diamond films deposited for back-etched samples are described as follows. A mixture of methane and hydrogen, with flow rates of 0.75 sccm and 150 sccm respectively, was allowed to flow into the chamber and a gas discharge was maintained with 600 W microwave input power. The plasma pressure was 50 Torr and the substrate temperature was approximately 1000°C. Films were deposited on a sacrificial silicon substrate that were diamond powder polished.

Scanning electron microscopy of the top surface of the resulting films showed well defined crystallites with an average grain size of 0.55  $\mu\text{m}$  as determined by the linear intercepts method. A surface profile as measured by a stylus profileometer showed a standard deviation of 630 Å. Raman characterization of the films, as illustrated in Figure 5.8, showed the characteristic diamond peak at 1332  $\text{cm}^{-1}$  and indicates an absence of appreciable non-diamond carbonaceous material.

After deposition, dual side contacts were made to the top and bottom of the film as described in chapter 3 (section 5.3). The top metal contacts are circular with a diameter of 400  $\mu\text{m}$  and approximately 20 contacts are on each transferred film. This effectively provides 20 two-terminal devices for electrical characterization, with the bottom contact being common to all devices.

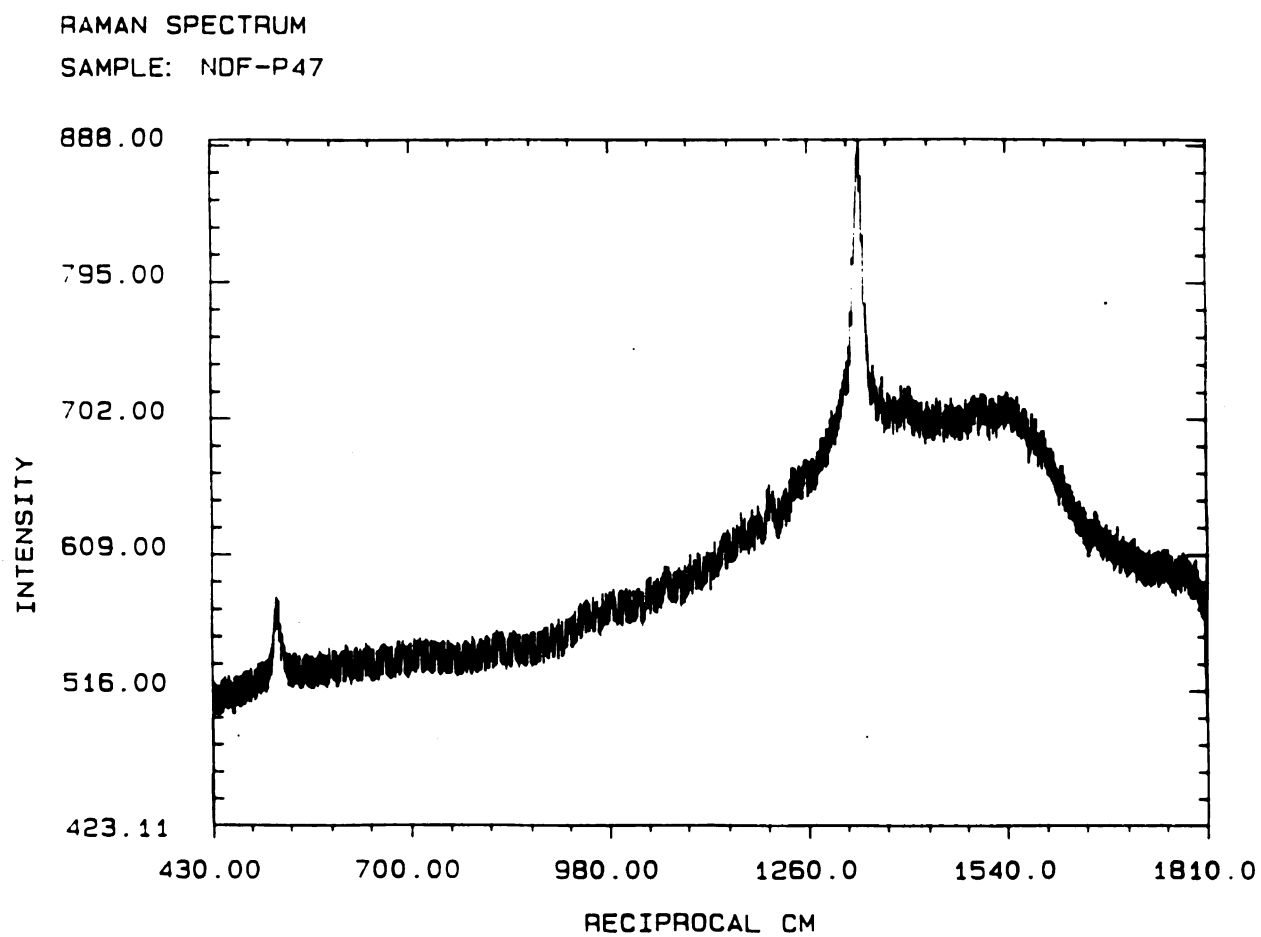


Figure 5.8. Raman spectrum of the diamond film as deposited on the silicon substrate with substrate temperature at 1000 °C. (From Dr. Gray)

The measurement set-up is illustrated in Figure 5.9. The sample was placed on the Signatone microprobe station. Current-voltage (I-V) characteristics were measured at room temperature, with and without photo-excitation. For voltages up to 100 V, an HP 4145B semiconductor parameter analyzer was used to collect the data, with a current resolution of approximately 100 pA. For higher voltages, a Tektronix 577 curve tracer was used.

### 5.3.2 Contact Effects on Back-Etched Samples

In this study, Au, Ag, and In contacts were used in order to investigate the contact effect of different metal work functions. The work functions for Au, Ag, and In are 5.2 eV, 4.42 eV, 3.97 eV respectively [125].

For low voltages, less than 35 V, the I-V characteristic of powder-polished samples were nearly linear and symmetric for gold, silver, and indium contacts, as shown in Figure 5.10. For a film thickness of 3.5  $\mu\text{m}$ , 35 V corresponds to an electric field of  $10^5$  V/cm. This indicates that for electric fields below  $10^5$  V/cm, the films exhibited predominantly ohmic behavior with a conductivity that was independent of the applied voltage for the high work function metal contacts (Au) and low work function metal contact (In). However, for large grain films described later in chapter 5 (section 4), results show that under certain conditions, metal-diamond contacts are non-ohmic and dominate device I-V characteristics.

### 5.3.3 High Field Effect

The combination of dual-side contacts and relatively thin films facilitates measurement of electrical properties at higher electric fields than have been generally reported for previous studies of diamond films with metallic contacts [126]. In the last section, it is shown that ohmic behavior was predominant at low voltages for different metal

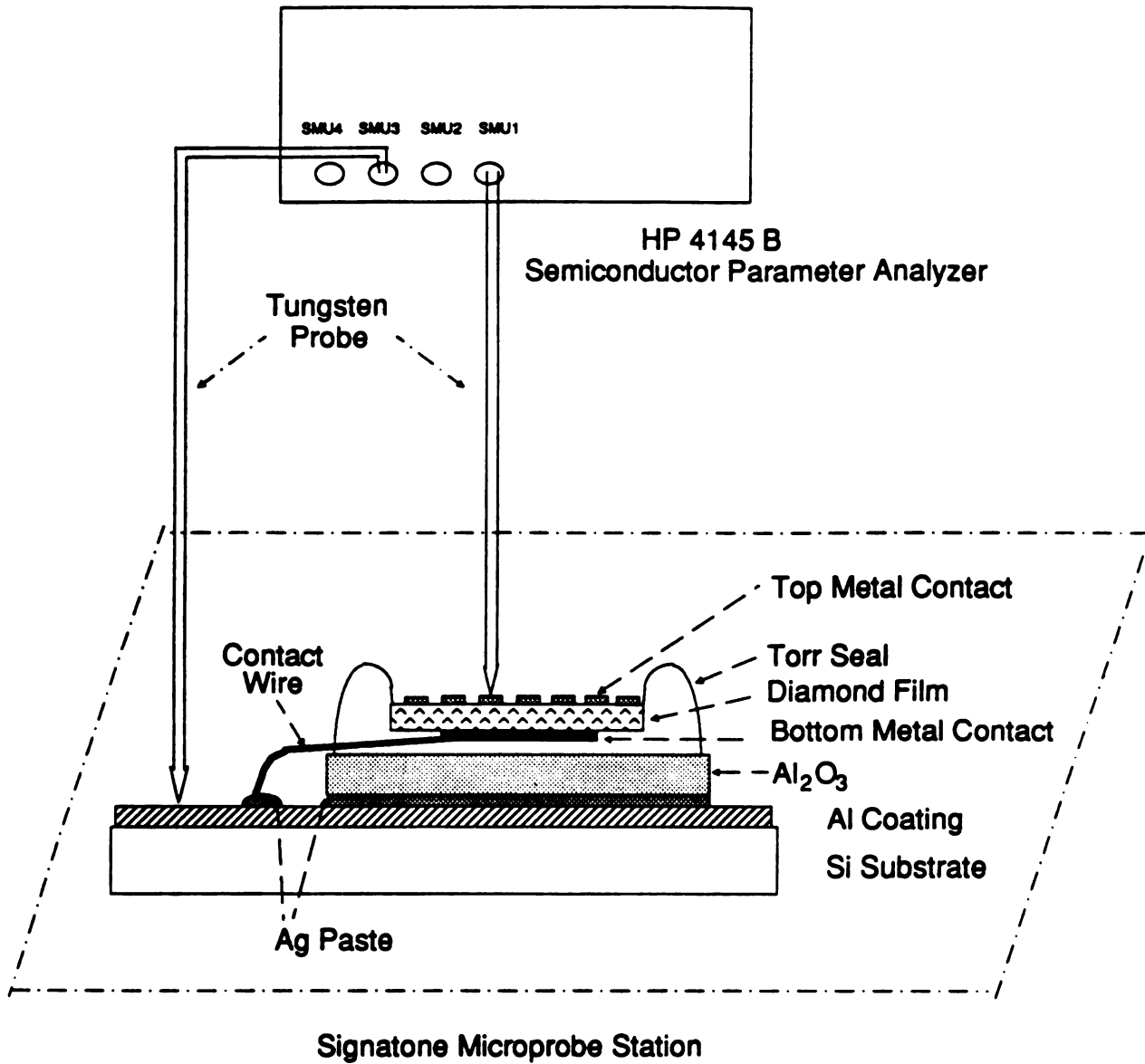


Figure 5.9. The I-V measurement set-up of the back-etched samples.

(3)  
C

Fig  
and  
sam

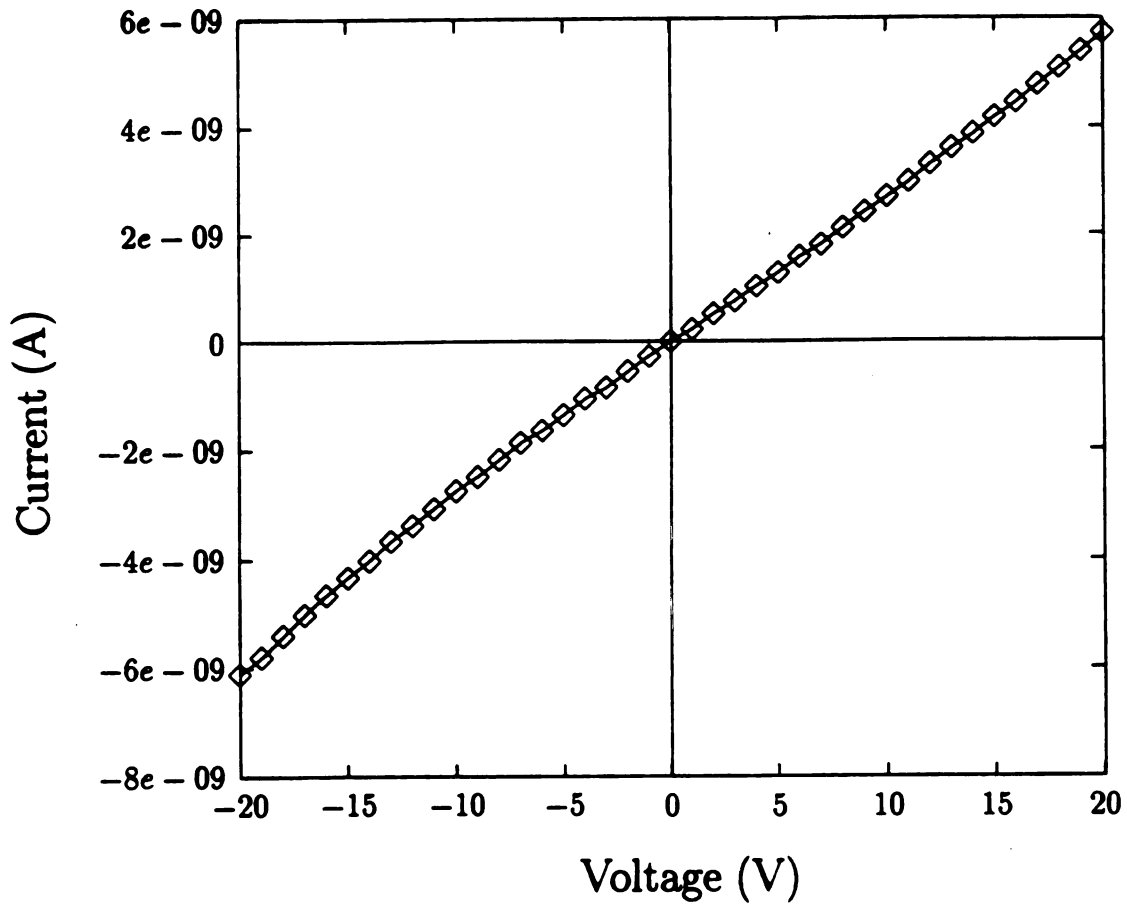


Figure 5.10. I-V characteristics of a small grain size sample with gold contacts top and bottom. It shows linear and symmetric behavior at low voltages. (Electrical sample : P47-T1)

co

as

th

lo

ac

as

wi

tic

vo

m

on

fi

en

Fe

se

de

ch

I.V

otl

at.

con

con

contacts. However, at high voltages, the current increases more rapidly than linearly, as shown in Figure 5.11.

As shown in Figure 5.12 (a) and (b), current-voltage relationship did not follow the space charge limited current-voltage power law where in (a)  $I \propto V^{3/2}$  and in (b)  $I \propto V^2$ .

However, the nonlinear behavior at high voltages is well modeled by a voltage activated conductivity. The total dark conductance of the device may be expressed as

$$G = G_{00} + G_0 \exp(aV) \quad (5.12)$$

where the first term represents ohmic behavior corresponding to low field conduction in the diamond film and second term represents the nonlinear behavior at high voltages, with  $V$  being the applied voltage and  $a$  representing the slope of the curve.

Figure 5.13 and Figure 5.14 show that this model fits the data over the entire measurement range for both Au-Au contacts on the top and bottom, and In contacts on the top and Au contact on the bottom respectively. For both cases the diamond film thickness was 3.5  $\mu\text{m}$ . At voltages higher than 250 V, a breakdown regime is entered in which a negative resistance state is followed by an irreversible breakdown. For voltages less than 250 V, however, no hysteresis in the I-V characteristic is observed. The experimental data is repeatable and the same for increasing voltage as for decreasing voltage. Since both contact combinations gave the same low and high field characteristics, the work function of the contact does not appear to contribute to the I-V characteristics of the small grain size samples. This result is consistent with some other reported work on metal-diamond contacts [127]. The slopes  $a$  of Figure 5.13 and Figure 5.14 are 0.042  $V^{-1}$  and 0.045  $V^{-1}$  respectively. Both Au-Au and In-Au contacts gave rise to nearly symmetric I-V characteristics and exhibited a low-field, constant conductance (ohmic) region with a conductivity  $\sigma_{00}$ . For Figure 5.13 and

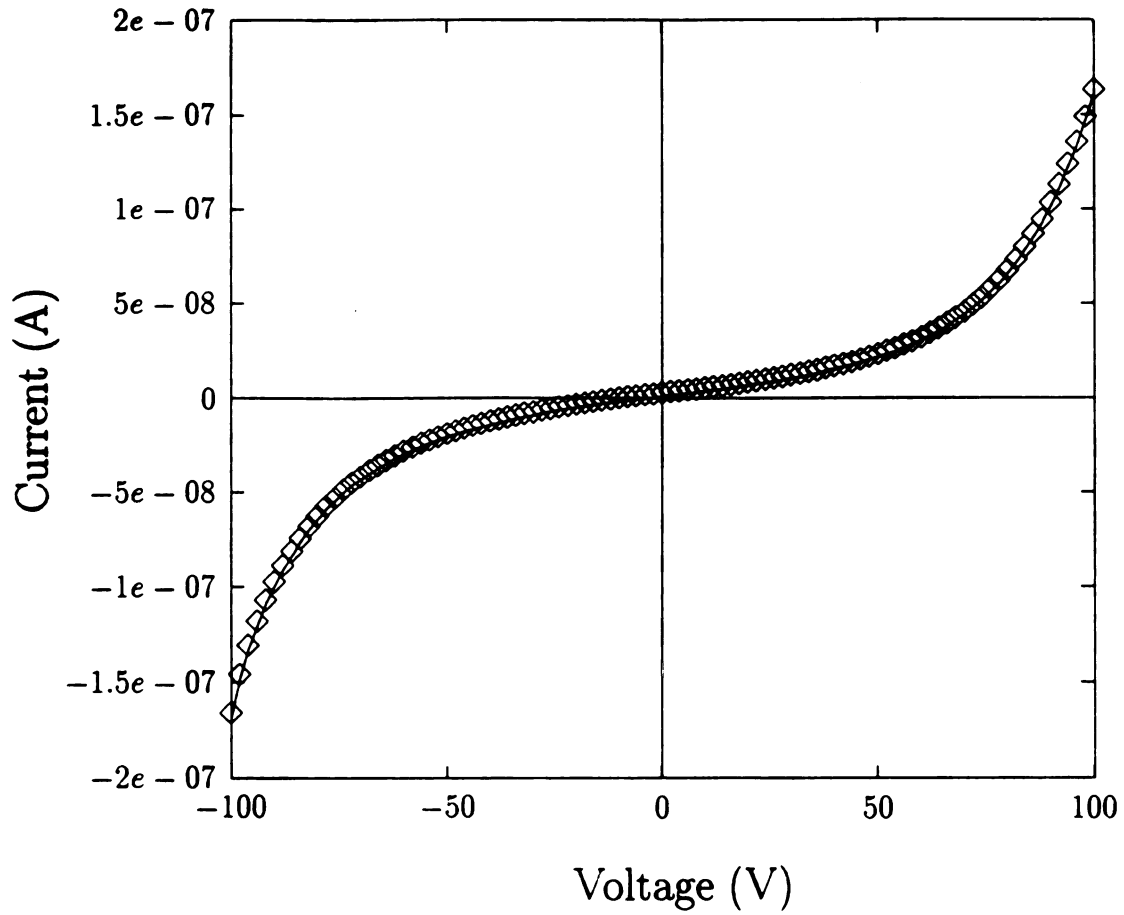


Figure 5.11. I-V characteristics of a small grain size sample with gold contacts top and bottom. It shows nonlinear behavior at high voltages. (Electrical sample : P47-T1)

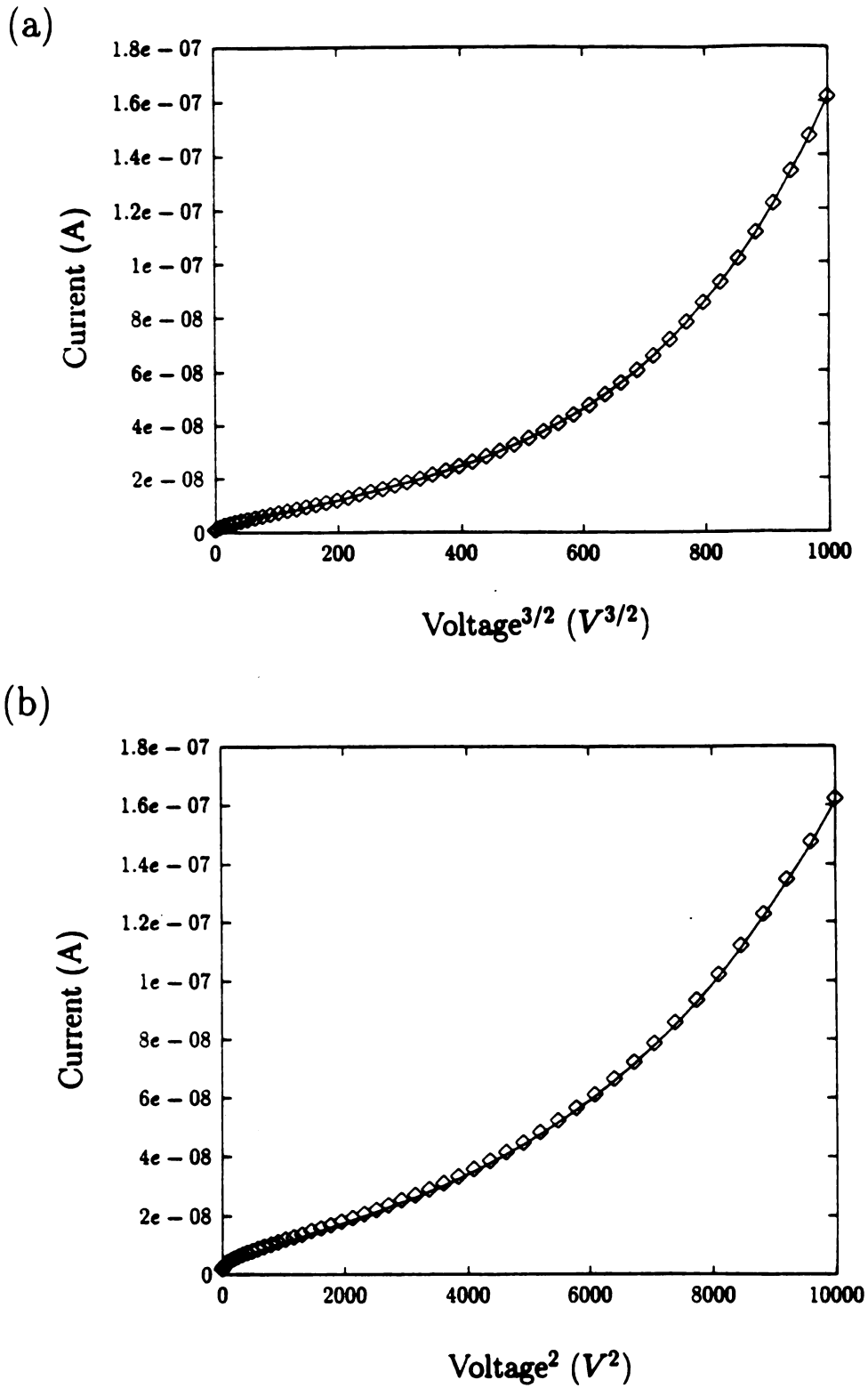


Figure 5.12. The  $I - V^{3/2}$  characteristic and (b) the  $I - V^2$  characteristic of Figure 5.11. (Electrical sample : P47-T1)

Fi

sh

Ap

hi

ga

co

4.

He

of

pr

ap

wl

vs

Fi

(V

to

de

wa

Figure 5.14,  $\sigma_{00}$  is equal to  $7.3 \times 10^{-11} (\Omega \cdot cm)^{-1}$  and  $5.9 \times 10^{-11} (\Omega \cdot cm)^{-1}$  respectively.

For samples deposited at similar conditions with a thickness of  $2 \mu m$ . Figure 5.15 shows that this model also fits the data over the entire measurement range for Ag-Ag contacts on the top and bottom. The breakdown regime happens at voltages higher than 150 V. The slope  $a$  of Figure 5.15 is  $0.08 V^{-1}$ . The Ag-Ag contacts also gave rise to nearly symmetric I-V characteristics and exhibited a low-field, constant conductance (ohmic) region with a conductivity  $\sigma_{00}$ . For Figure 5.15,  $\sigma_{00}$  is equal to  $4.6 \times 10^{-11} (\Omega \cdot cm)^{-1}$ .

The slope  $a$  is approximately  $0.045 V^{-1}$  for a sample with a thickness of  $3.5 \mu m$ . However, the slope  $a$  is  $0.08 V^{-1}$  for a sample with a thickness of  $2 \mu m$ . For samples of varying thickness, the slope of the conductivity vs. voltage is found to be inversely proportional to the sample thickness, indicating that this increase is related to the applied electric field. Consequently, the conductivity may be expressed as

$$\sigma = \sigma_{00} + \sigma_0 \exp(\alpha F) = \sigma_{00} + \sigma_0 \exp(F/F_0) \quad (5.13)$$

where  $F$  is the electric field and  $\alpha$  represents the slope of the log of the conductivity vs. electric field and  $F_0$  is the inverse of the  $\alpha$ . The value of  $\alpha$  and  $F_0$  for Figure 5.13, Figure 5.14 and Figure 5.15 are  $1.47 \times 10^{-5} (V/cm)^{-1}$ ,  $6.8 \times 10^4 V/cm$ ;  $1.58 \times 10^{-5} (V/cm)^{-1}$ ,  $6.3 \times 10^4 V/cm$ ; and  $1.6 \times 10^{-5} (V/cm)^{-1}$ ,  $6.25 \times 10^4 V/cm$  respectively.

In order to investigate whether the high voltage increase in conductance is due to an increase in dark carrier concentration or an increase in mobility, the voltage dependence of the photoconductivity was also investigated. A tungsten light source was used to illuminate the devices so that the current increased by an amount  $\Delta I_{ph}$ .

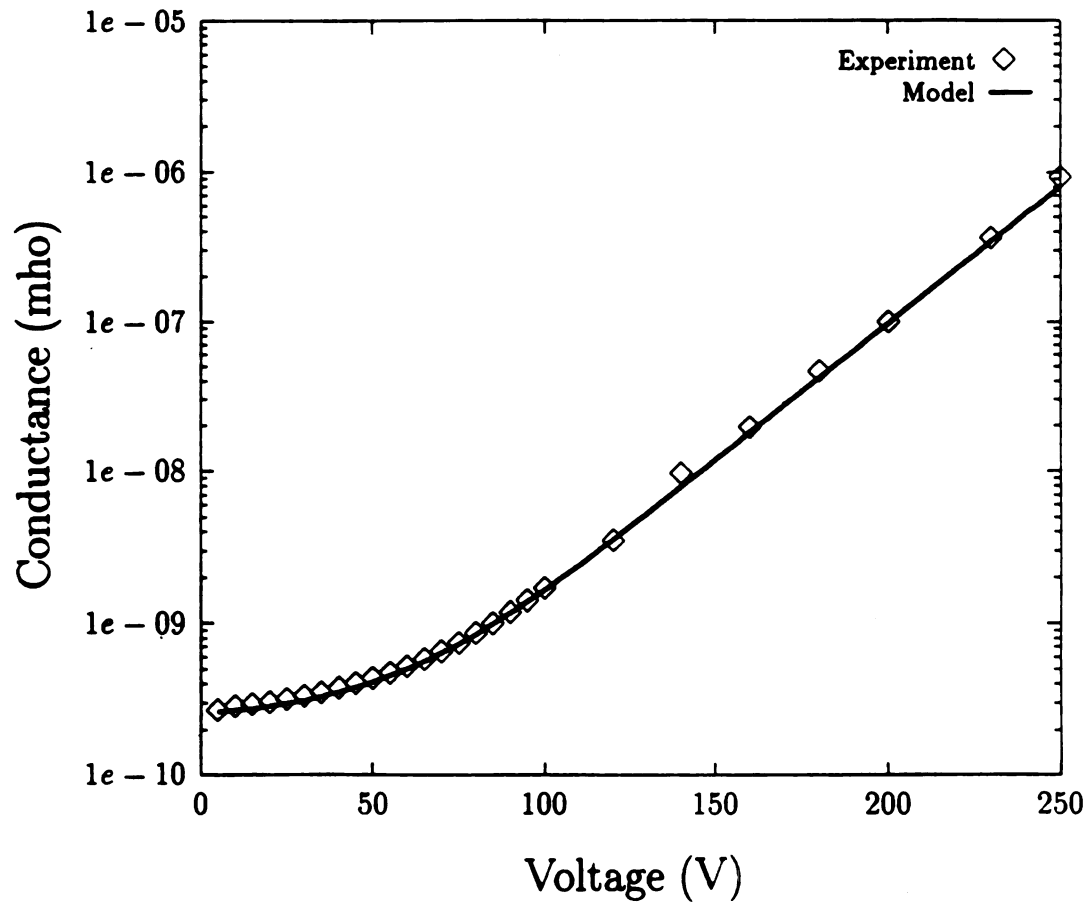


Figure 5.13. I-V characteristic of diamond film with gold contacts top and bottom. Experimental data is shown by data points. The solid line represents the model results of Eq. (5.12) with  $G_{00}=2.6 \times 10^{-10} \Omega^{-1}$ ,  $G_0 = 2.1 \times 10^{-11} \Omega^{-1}$ , and  $a = 0.042 \text{ V}^{-1}$ . (Electrical sample : P47-T1)

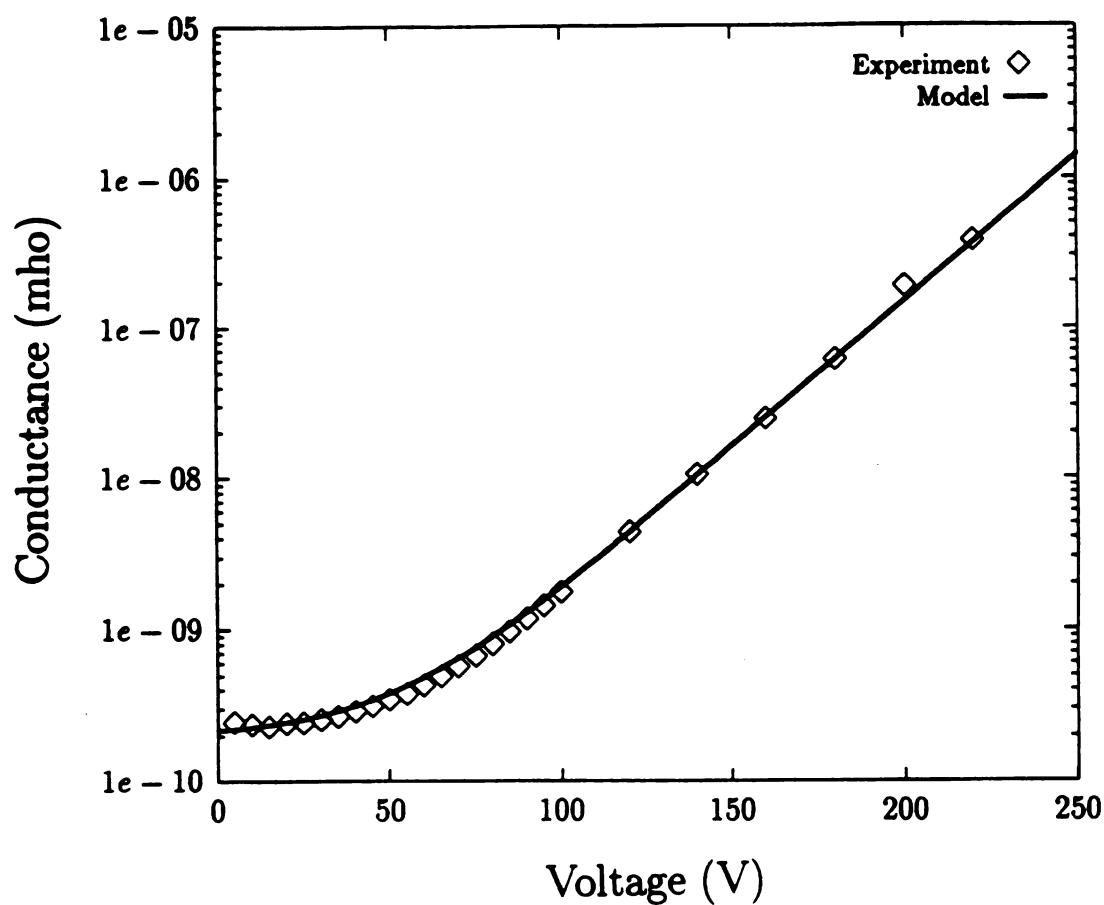


Figure 5.14. I-V characteristic of diamond film with top indium contacts and bottom gold contact. Experimental data is shown by data points. The solid line represents the model results of Eq. (5.12) with  $G_{00}=2.1 \times 10^{-10} \Omega^{-1}$ ,  $G_0 = 2.0 \times 10^{-11} \Omega^{-1}$ , and  $a = 0.045 \text{ V}^{-1}$ . (Electrical sample : P47-T3)

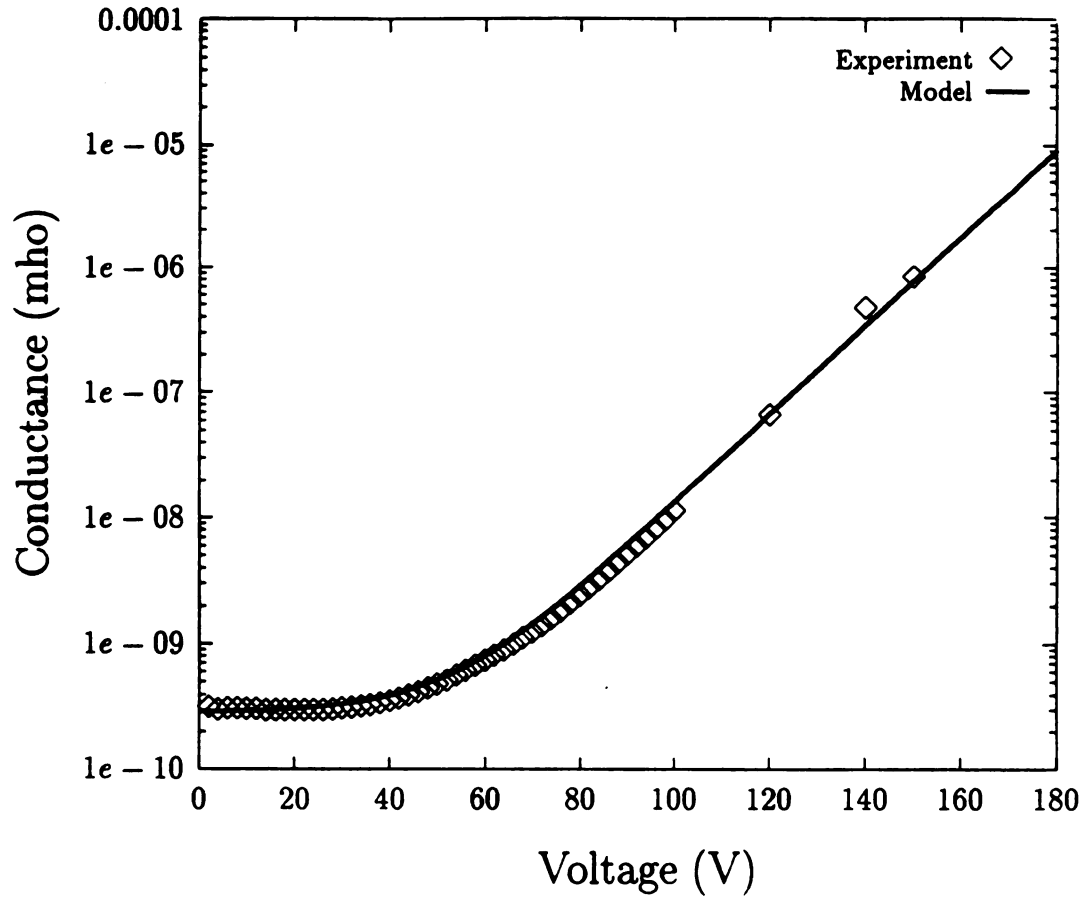


Figure 5.15. I-V characteristic of diamond film with silver contacts top and bottom. Experimental data is shown by data points. The solid line represents the model results of Eq. (5.12) with  $G_{00}=2.9 \times 10^{-10} \Omega^{-1}$ ,  $G_0 = 4.0 \times 10^{-12} \Omega^{-1}$ , and  $a = 0.08 \text{ V}^{-1}$ . (Electrical sample : P49-T2)

The photoconductance is defined here as

$$G_{ph} = \Delta I_{ph}/V. \quad (5.14)$$

The results of the photoconductance are shown in Figure 5.16 for several photon flux intensities. In all cases, the photocurrent was less than 10 % of the dark current, and so may be considered as a small signal contribution to the total current. For a given light intensity, the photoconductance is

$$G_{ph} = q\Delta n_{ph}\mu A/t \quad (5.15)$$

where  $A$  is the area of the top contact,  $t$  is the film thickness,  $\mu$  is the carrier mobility, and  $\Delta n_{ph}$  is the increase in carrier concentration due to photo-excitation. Eq. (5.15) is written generally for any carrier type, that is  $\Delta n_{ph}$  may refer to photo-generated electrons, or holes, or both. If the increase in dark conductivity at high voltages is primarily due to a field activated mobility, then the photoconductance would be expected to show a similar increase at high voltages. In fact, however, the data in Figure 5.16 shows that  $G_{ph}$  is essentially constant with respect to voltage. Over the same voltage range, the dark conductivity increased by approximately an order of magnitude. Consequently, the field activated dark conductivity seems to be primarily due to an increase in carrier concentration.

An electric field activated conductivity has been previously reported in a wide variety of non-single crystal insulating and semiconductor films. A linear plot of the logarithm of the conductivity versus the applied field is evidence of **Poole's Law** and is often interpreted as being a result of Poole-Frenkel reduction of the ionization energy associated with Coulombic potentials surrounding ionizable sites resulting from impurities, local non-stoichiometry, or defects. [128, 129, 130] The

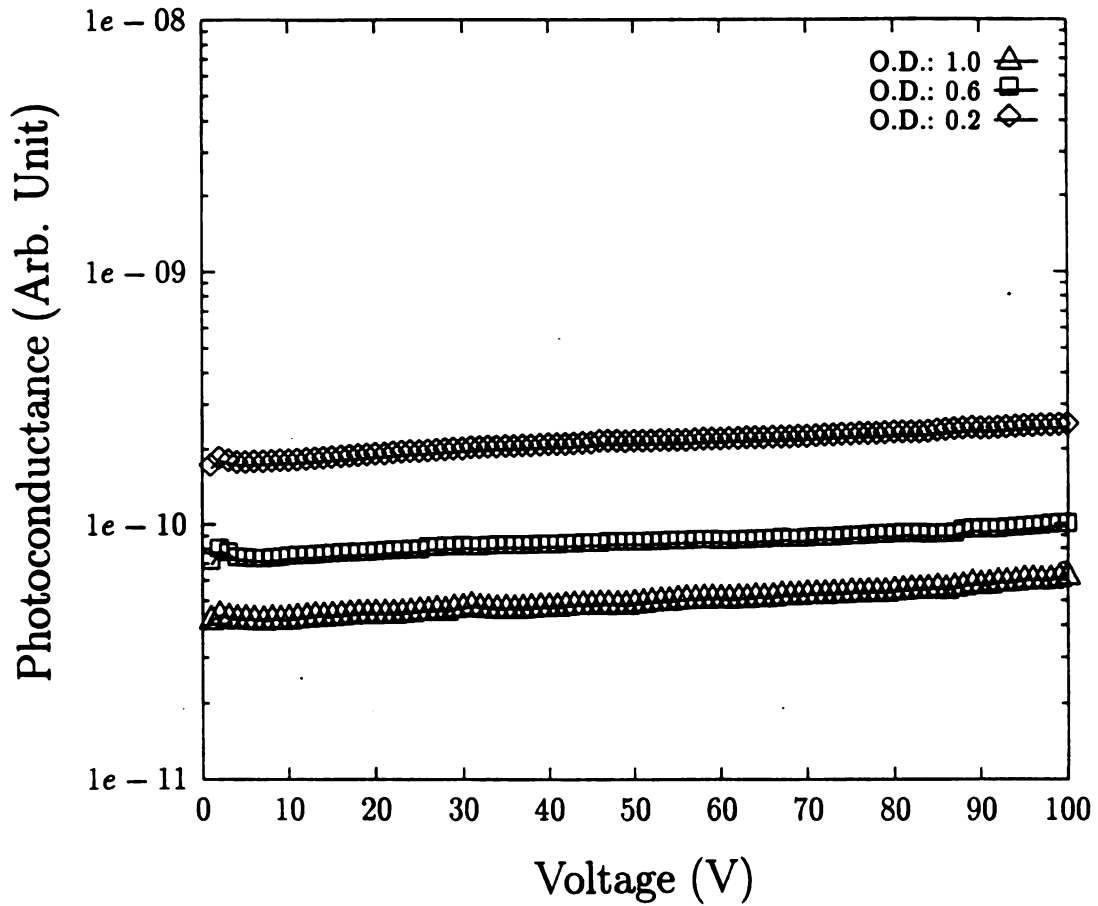


Figure 5.16. The photoconductance is nearly independent of the applied voltage. Shown here are data for different photon fluxes corresponding to different optical density (O.D.) filter values. (Electrical sample : P47-T1)

Poole-Frenkel mechanism causes an increase in conductivity due to an increase in carrier concentration, resulting from ionization of Coulombic centers by the applied electric field. This is consistent with our experimental evidence that it is a carrier concentration increase, not a mobility increase, that gives rise to the field activated conductivity.

When Coulombic potentials may be considered as non-overlapping, their contribution to conductivity is proportional to  $\exp(\beta F^{1/2}/kT)$  where  $\beta$  is the Poole-Frenkel constant, equal to  $e^{3/2}(\pi\epsilon)^{-1/2}$ , and  $F$  is the electric field [130]. However, when the Coulombic center density is sufficiently high that there is appreciable overlap of the Coulombic potentials, then the contribution of the Coulombic centers to the conductivity is proportional to  $\exp(\alpha F)$  where  $\alpha$  is a function of temperature and distance between centers [130]. The conductivity exhibited by the films in this study are examples of the latter case, as indicated by Eq. (5.13) and Figure 5.13 to Figure 5.15.

A direct indication of the density of the Coulombic centers may be found from the slope of the log of conductivity vs. voltage in Figure 5.13 to Figure 5.15. From Hill, the expected slope would be  $es/2kTt$  where  $s$  is the separation of Coulombic centers (or defect centers) and  $t$  is the sample thickness. [130] For the experimental slope of  $0.045 V^{-1}$  for  $t = 3.5 \mu\text{m}$ , the corresponding value of  $s$  is  $4 \times 10^{-7}$  cm. Taking  $s$  to be equal to  $N^{-1/3}$  where  $N$  is the Coulombic center density, the value of  $N$  is  $1.6 \times 10^{19} \text{ cm}^{-3}$ . The overlap of Coulombic potentials is a matter of degree, and setting a maximum separation for overlap is necessarily arbitrary. Following Hill, the maximum separation which still produces appreciable overlap may be taken, as an approximation, as twice the distance from a site to the maximum in the barrier. The lower limitation of the density for overlapping is  $(e\beta^{-1}F^{1/2})^3$  [130]. Taking

$$\left(\frac{1}{s}\right)^3 = N = (e\beta^{-1}F^{1/2})^3 \quad (5.16)$$

this approximation leads to a relationship between  $s$  and the electric field according to  $s = \beta/eF^{1/2}$ . As the electric field increases, this maximum separation decreases. For  $s = 4 \times 10^{-7}$  cm, the corresponding electric field is calculated to be  $6 \times 10^5$  V/cm. This value is within the range of fields at which we observed field activated conductivity and, given the rough approximation used as an overlap criteria, is an indication that overlap of Coulombic potentials is a reasonable hypothesis at these densities.

Since the lattice constant of diamond is  $3.567 \text{ \AA}$  and the lattice configuration is face center-cubic structure, the diamond crystal has  $1.76 \times 10^{23}$  atoms/cm<sup>3</sup>. The calculated Coulombic center density corresponds to approximately one center per 10,000 host atoms. While this value is high by single crystal semiconductor standards, it would not necessarily be unexpected for polycrystalline films deposited by chemical vapor deposition. States at grain boundaries may be a contributor to these centers. Additionally, thin film deposition system purity considerations are also a factor in terms of impurity or defects states within individual crystallites.

Because of the field activated conductivity, the current is substantially larger at high electric field than would otherwise be the case. The negative resistance observed prior to breakdown is evidence of thermal effects which apparently cause thermal runaway. For  $3.5 \text{ }\mu\text{m}$  and  $2 \text{ }\mu\text{m}$  thick films, this occurs at a voltage of 250 V and 150 V respectively. It corresponds to a breakdown field of  $7.2 \times 10^5$  and  $7.5 \times 10^5$  V/cm. Consequently, the dielectric strength of the polycrystalline diamond samples in this study are substantially less than those reported for single crystal diamond ( $0.6 - 1 \times 10^7$  V/cm) [131].

### 5.3.4 Photo Effect

If an incident photon has sufficient energy to excite a valence electron into the conduction band, then, with a certain probability, that photon will be absorbed in the

material creating a hole-electron pair. Alternatively, a valence electron may be excited to a higher lying defect state, creating a free hole, or a trapped electron may be excited to the conduction band, creating a free electron. In any case, these photo-generated carriers, being in thermal equilibrium with their surroundings, recombine after some time, generally via trapping dynamics. During the lifetime of the photo-generated carriers, an increase in electrical conductivity will be observed.

Photon absorption in high purity, single crystal semiconductors and insulators is generally characterized by an absorption edge which occurs at the minimum energy required to free a valence electron and cause band-to-band excitation. Below this energy there is little photon absorption, above it the absorption increases sharply. The presence of defects and impurities allow different absorption phenomena which may be exhibited by a tail on the absorption edge which extends into the energy gap, or by structure in the absorption spectra within the energy gap. This investigation studied photo-conductivity due to photon energies smaller than the energy gap, and therefore corresponding to excitation involving defects or impurities.

In this research, two sets of optical filters, which are visible light filters and infrared filters, were used to study the photo-effect. The monopass wavelengths of the visible filters are between 412 nm and 714 nm and those of the infrared filters are between 775 nm and 1480 nm. Consequently, the covered range corresponds to photon energies between 3 eV and 0.84 eV. Before the measurement were conducted on the back-etched samples, the relative power density for each filter was measured. A Newport power meter (model 815) with Si photodetector (model 818-SL) and Ge photodetector (model 818-IR) were used to measure the power for photon energies above 1.2 eV and below 1.6 eV respectively. As shown in Figure 5.17 (a), a calibration factor was applied to the power meter for different wavelengths of light for each photodetector in order to get the accurate readings. Since the photon flux passing through each

filter is different, the relative power intensities corresponding to each filter are shown in Figure 5.17 (b).

The photoconductance versus photon energy at -20 V and 20 V for the Au-Au contact sample is shown in Figure 5.18(a) before the normalization of the relative power intensity factors and in Figure 5.18(b) the normalized photoconductance versus photon energy is shown. Similarly, for the In-Au (In contact on the top) contact sample, the relationship of the photoconductance versus energy before and after the normalization are shown in Figure 5.19(a) and (b) respectively.

For both the Au-Au contact sample and the In-Au contact sample, the relationship of photoconductance versus photon energy is nearly the same for positive and negative bias. The existence of appreciable photoconductance well below the band gap indicates many defect states existing in the polycrystalline diamond films. The phenomenon of increasing sub-bandgap photo-conduction with increasing photon energy is also observed by a group with an international cooperation effort using a different approach [132]. They found that all CVD diamond films exhibited an almost monotonically increasing absorption with increasing photon energy. As the absorption increases, the generation of electron-hole pairs increases and the photo current increases.

## **5.4 The Metal/Diamond/Silicon Samples**

### **5.4.1 The I-V Measurement Set-up**

The metal/diamond/silicon samples as described in chapter 3 (section 5.2) were placed on the Signatone microprobe station as shown in Figure 5.20. Current-voltage (I-V) characteristics were measured at room temperature, with and without photo-excitation. As for the back-etched samples, an HP 4145B semiconductor parameter

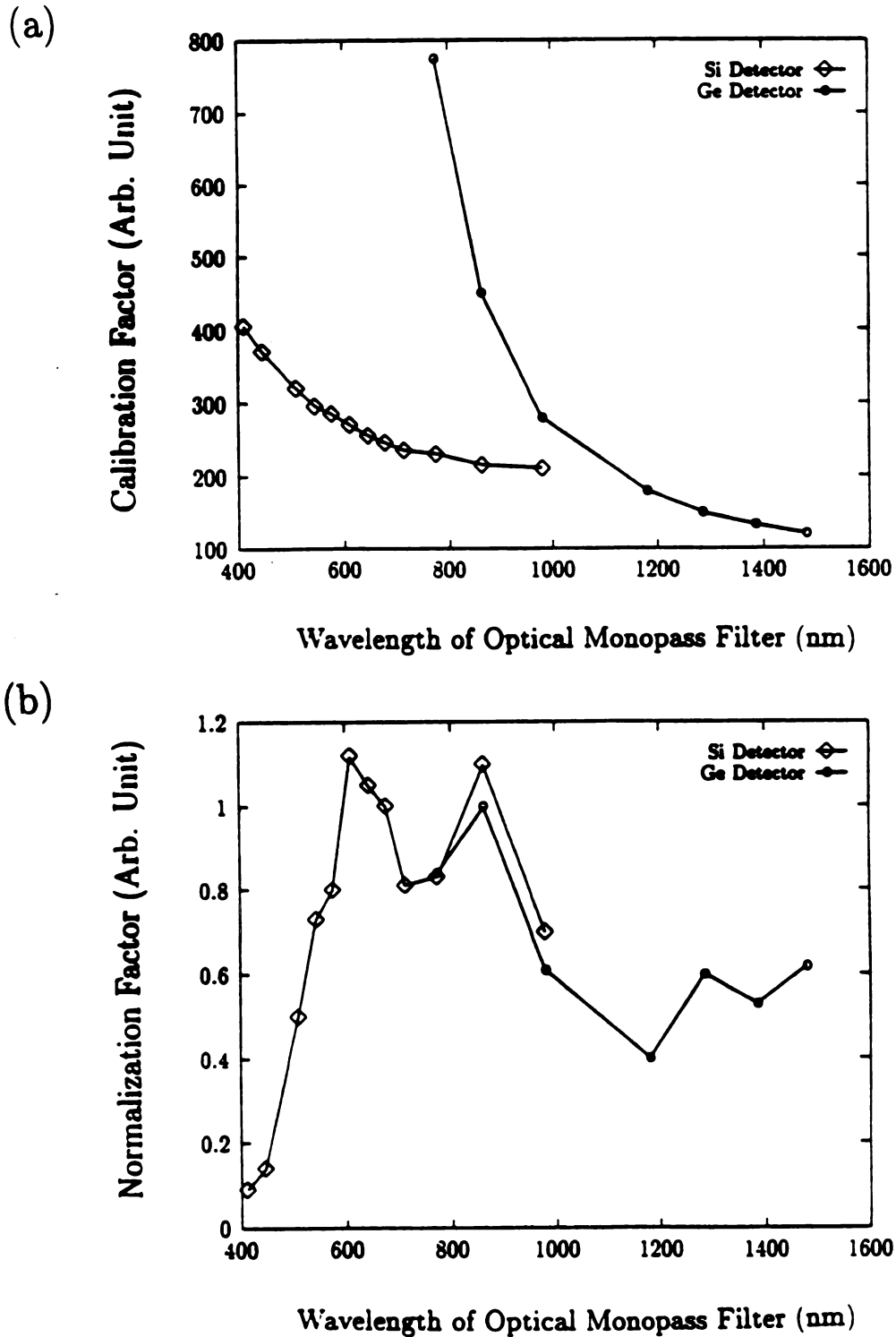
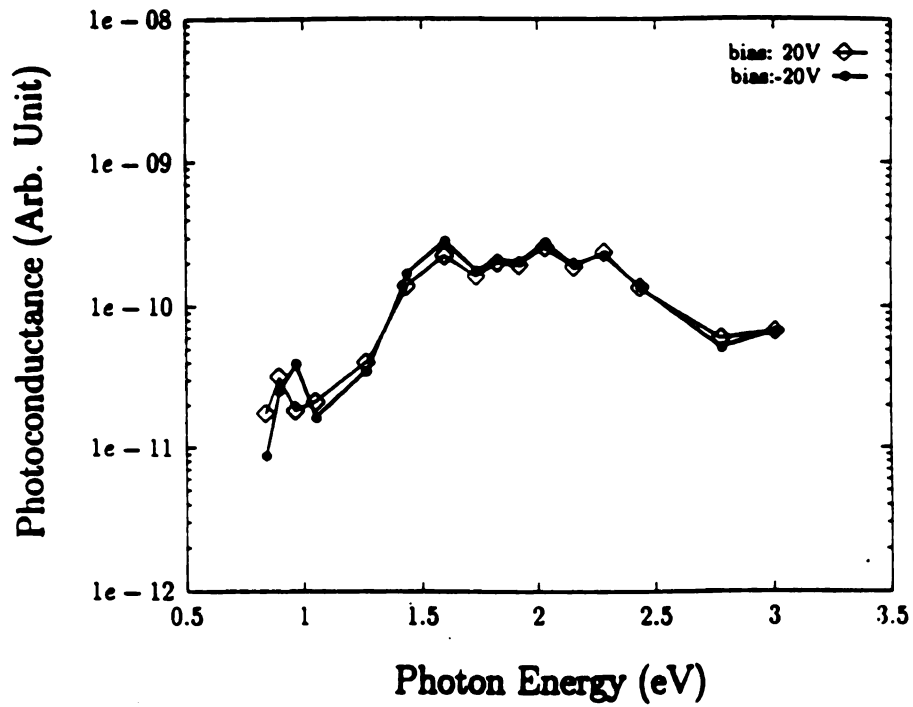


Figure 5.17. (a) The calibration factors corresponding to different optical wavelength for Si and Ge photodetector. (b) The relative power intensity factors for Si and Ge photodetector at different wavelength of the optical monopass filters.

(a)



(b)

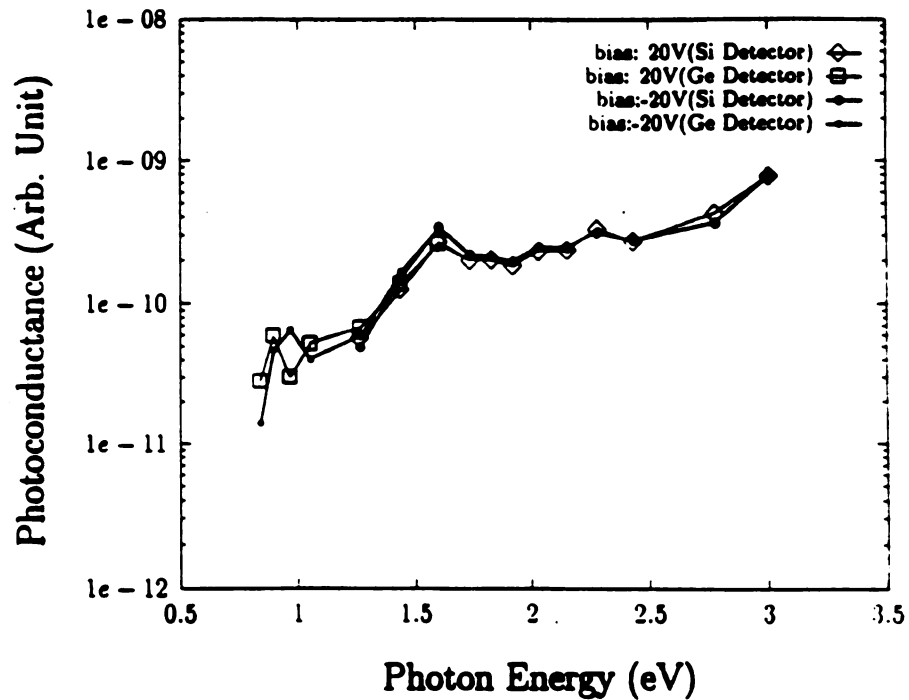
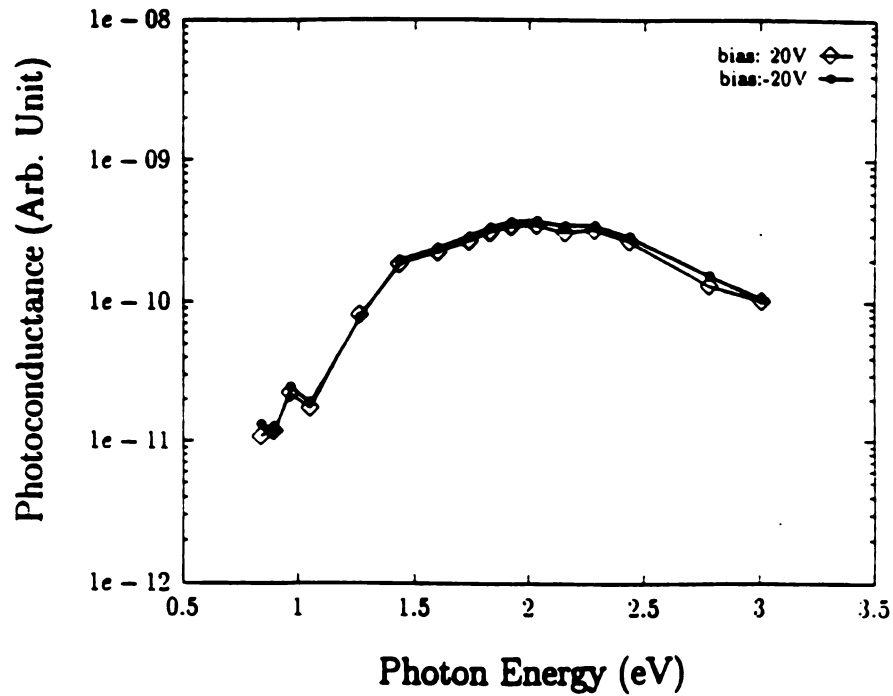


Figure 5.18. Relation of photoconductance vs. photon energy for Au-Au contact sample (a) before normalization and (b) after normalization. (Electrical sample : P47-T1)

(a)



(b)

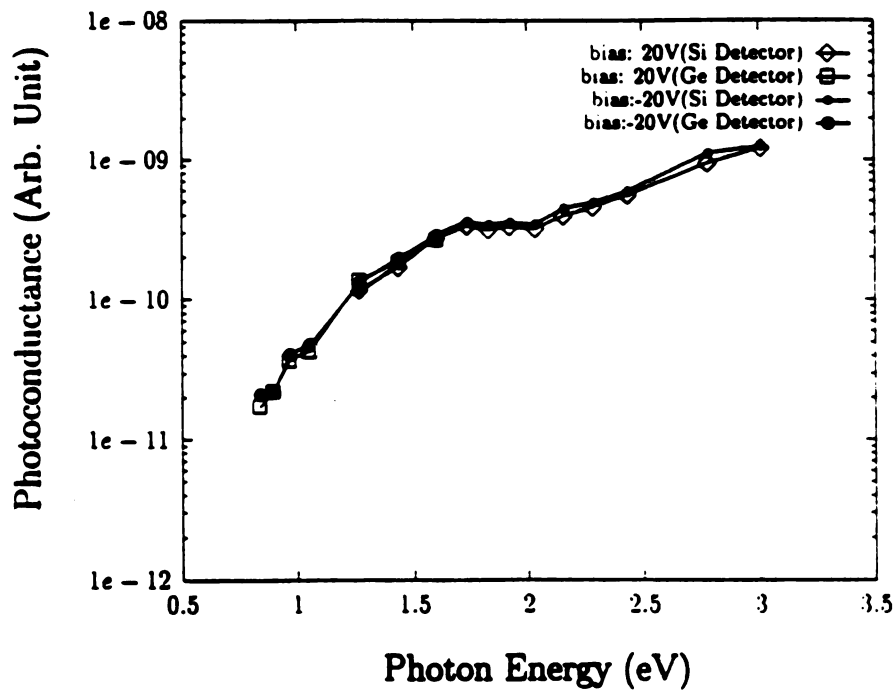


Figure 5.19. Relation of photoconductance vs. photon energy for In-Au contact sample (a) before normalization and (b) after normalization. (Electrical sample : P47-T3)

analyzer was used to collect the data with a current resolution of approximately 100 pA. In all cases, p-type silicon was used as the substrate.

#### **5.4.2 Contact Effects on Metal/Diamond/Silicon Samples**

There are two ways of fabricating the metal/diamond/silicon samples as previously mentioned in chapter 3 (section 5.2). The I-V characteristic of the large grain size diamond samples (paste-polished samples) with Al contacts and the small grain size diamond samples (powder-polished samples) with Au, Ag, and In contacts will be described and compared to the results reported in the last section for back-etched samples. Silver paste was used to form contact on the back side of the silicon wafer. For the p-type silicon used here, the paste contact was ohmic.

For low voltages, less than 25 V, the current-voltage (I-V) characteristics were nearly linear and symmetric for all the Au, Ag, and In contacts as shown in Figure 5.21 and Figure 5.22 on fine grain, diamond-powder prepared samples. It is strongly believed that in these small grain size diamond films, the defect state density is so high that the tunneling process dominates the metal/diamond contact I-V properties. Consequently, ohmic behavior is observed for both high work function metal contacts (Au) and low work function metal contacts (In) of the metal/diamond contact. This is consistent with the metal/diamond contacts on the back-etched samples.

The data in Figure 5.21 and Figure 5.22 also indicate that there is no rectifying behavior at the diamond/silicon interface. On the diamond side of this interface, it is reasonable to assume that, if a barrier did exist, a high defect density again produces such a thin barrier that tunneling allows ohmic behavior. For the silicon, the starting wafer which has been severely abraded as shown in Figure 3.5. Consequently, the defect density in the powder abraded silicon is also expected to be high, which would result in a silicon barrier that was also sufficiently thin to tun-

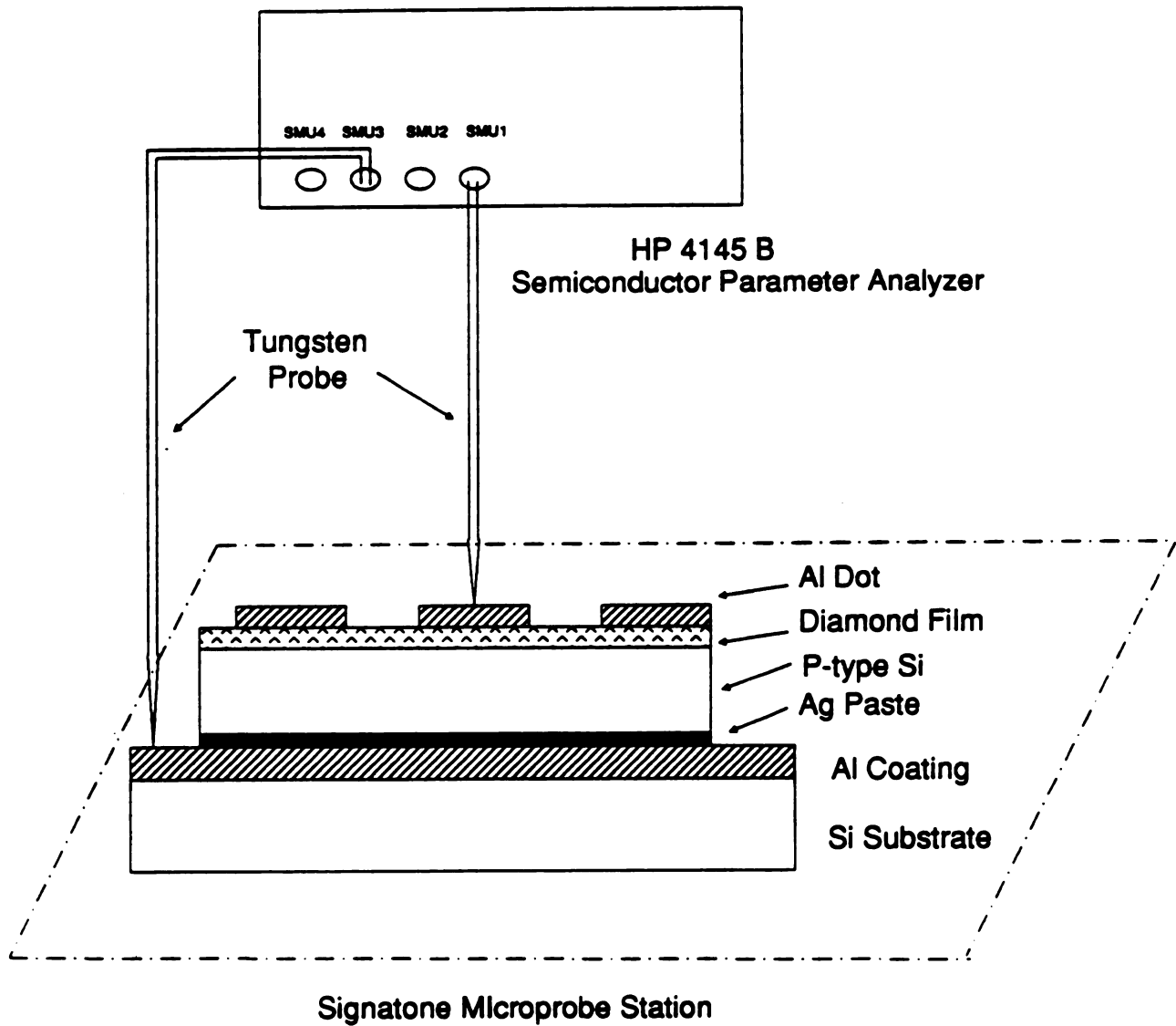


Figure 5.20. The I-V measurement set-up of the metal/diamond/silicon samples.

nel through. In fact, several decades ago, ohmic contacts to semiconductors were sometimes made by abrading the semiconductor with sandpaper in order to create a defect-laden surface. Alternately, the lack of a rectifying barrier may also be due to a lack of appreciable band bending in the silicon. As will be elaborated on later, the results of photo-excitation experiments described in the next section indicate that there is no significant band bending in the silicon, either for powder-polished samples or for paste-polished samples.

In contrast to the powder polished, small grain samples, for the large grain size paste-polished diamond samples, the I-V characteristics of the Al/diamond/silicon structure showed rectifying behavior as shown in Figure 5.23 and Figure 5.24. This indicates that the defect density is not as high as in the small grain size diamond films. It is reported that polycrystalline diamond films have a much higher defect density than the single crystal, and the concentration of defect increases as the concentration of methane increases [132]. This research indicates that different nucleation techniques and/or different grain sizes are also factors contributing to defect states in the films.

Rectifying phenomena of metal/diamond/silicon structures have been previously reported by several groups [133, 134] in recent years, and similar behavior was also observed for bulk boron-doped diamond synthesized under ultrahigh pressure conditions [135]. The rectifying property has been variously attributed to the band bending at the top-contact/diamond interface [133] and back-contact/diamond/silicon interface [134]. It is important to know which interface in fact contributes to the rectifying characteristics in our case. Further investigation using additional information from photo-excitation will be discussed in the next subsection.

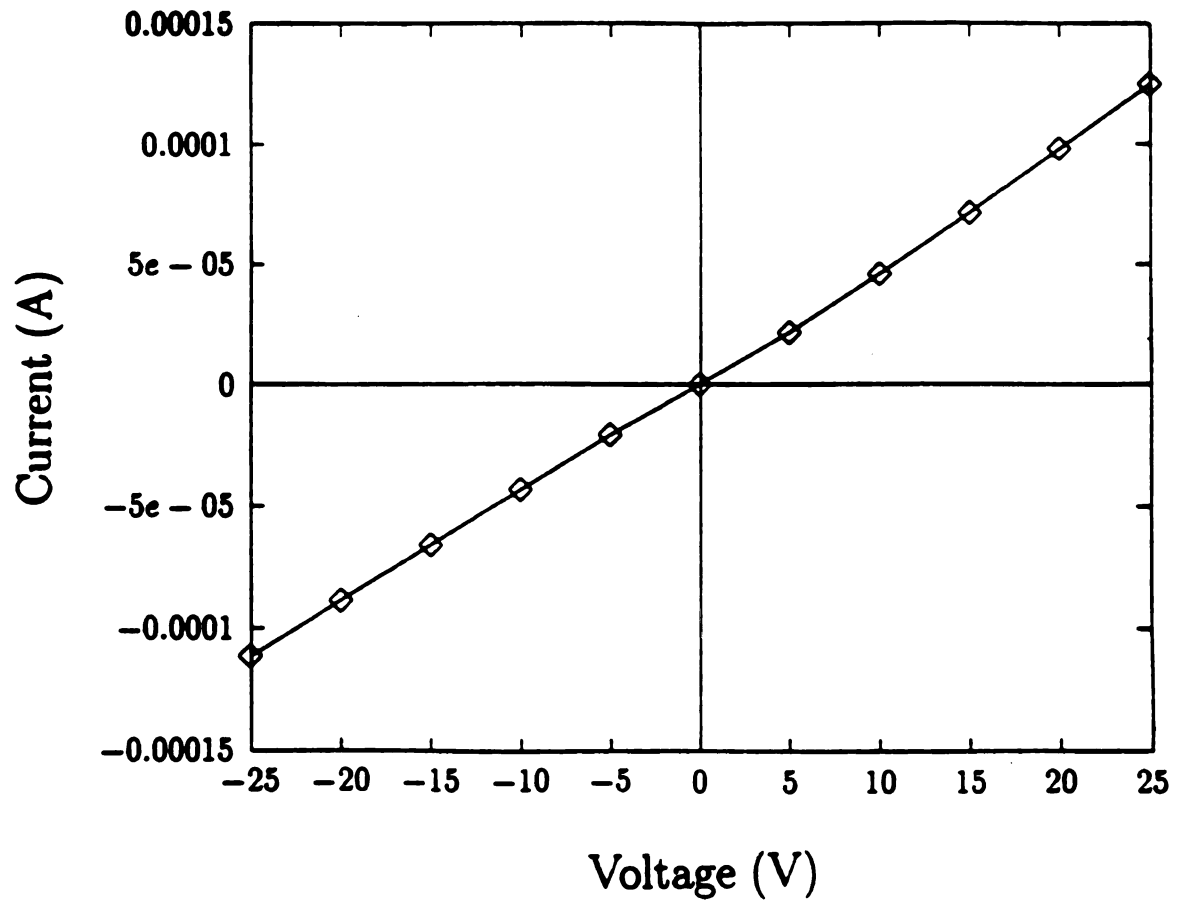


Figure 5.21. I-V characteristic of the small grain size Au/diamond/silicon samples. (Electrical sample : P39)

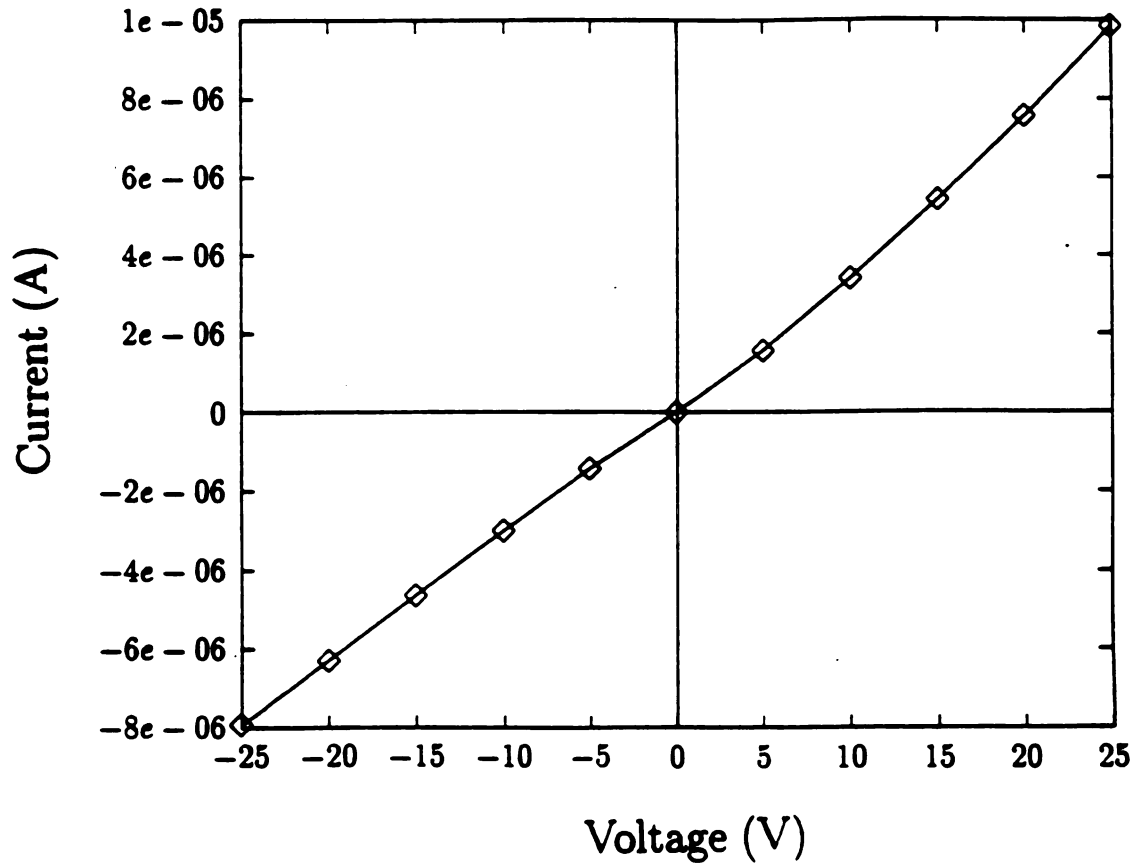


Figure 5.22. I-V characteristic of the small grain size In/diamond/silicon samples. (Electrical sample : P39)

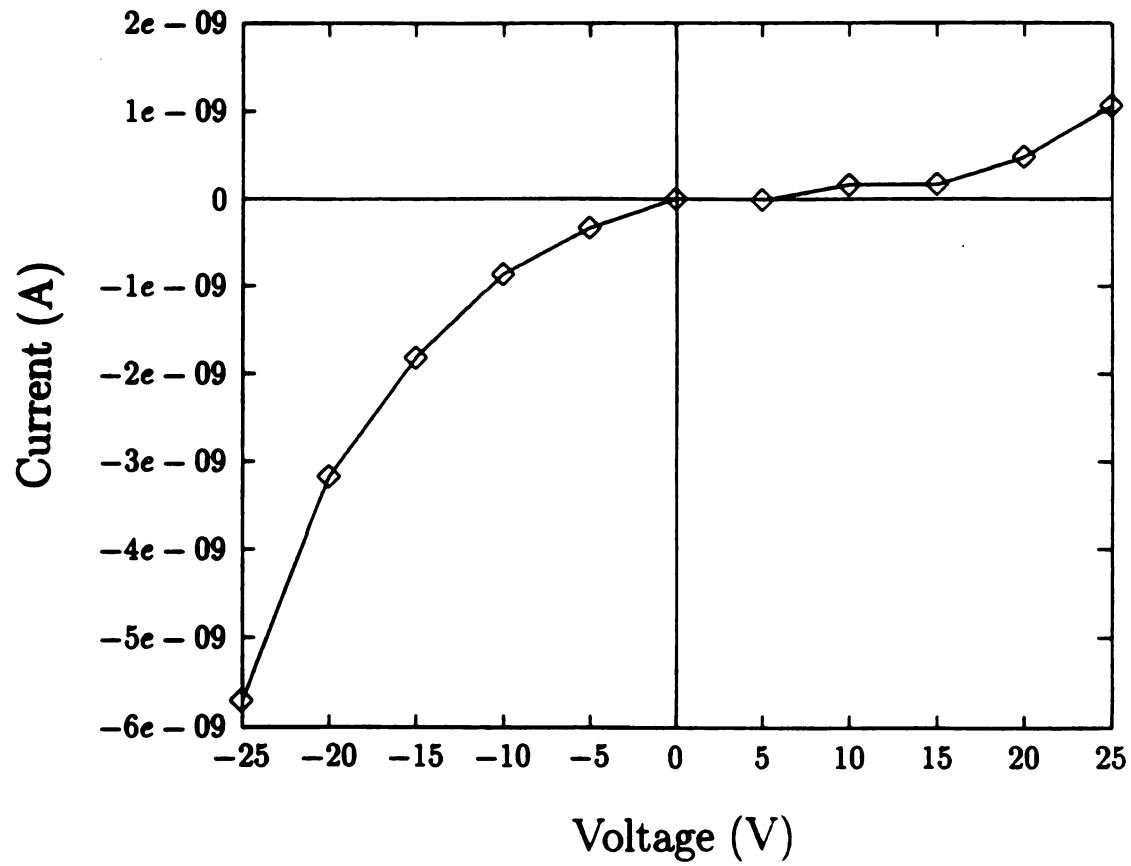


Figure 5.23. I-V characteristic of the large grain size Al/diamond/silicon samples. The average grain size is  $2.1 \mu\text{m}$ . (Electrical sample : P6)

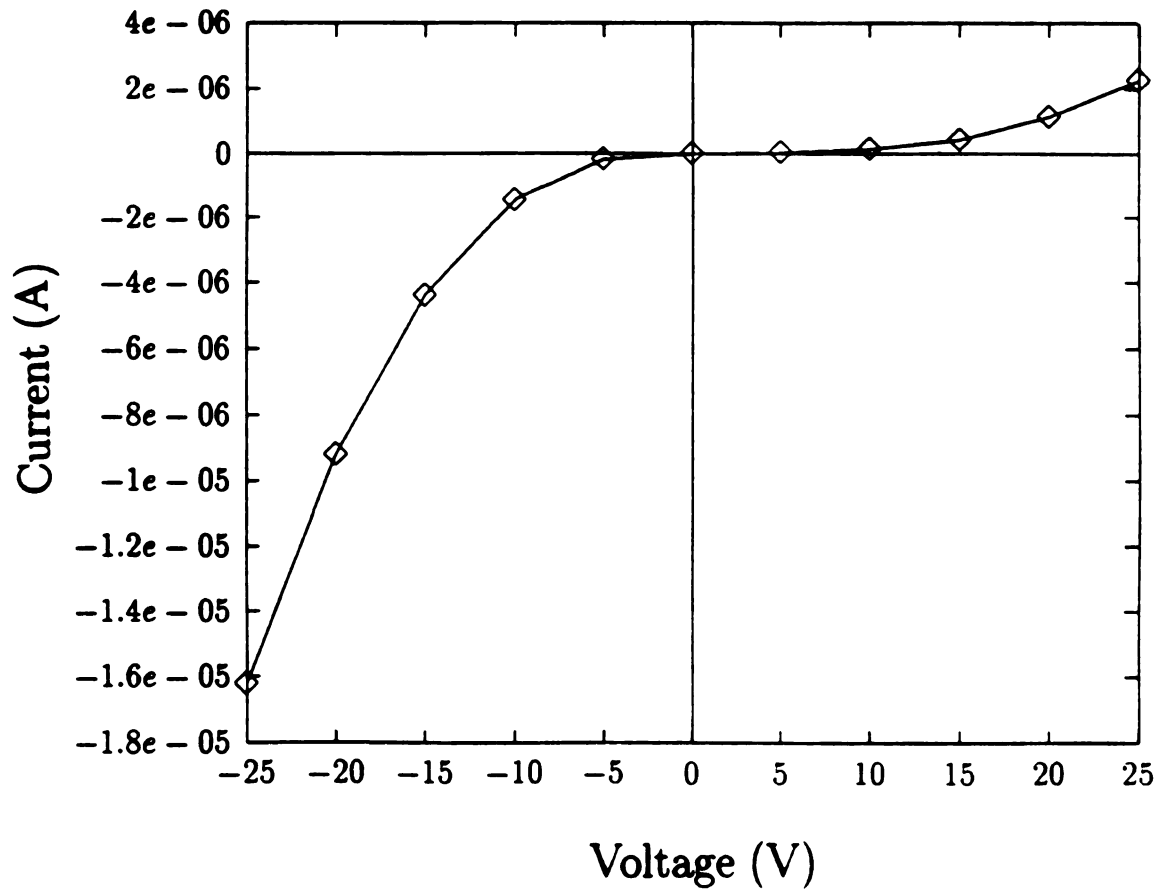


Figure 5.24. I-V characteristic of the large grain size Al/diamond/silicon samples. The average grain size is  $1.4 \mu\text{m}$ . (Electrical sample : P7)

### 5.4.3 Photo Effect

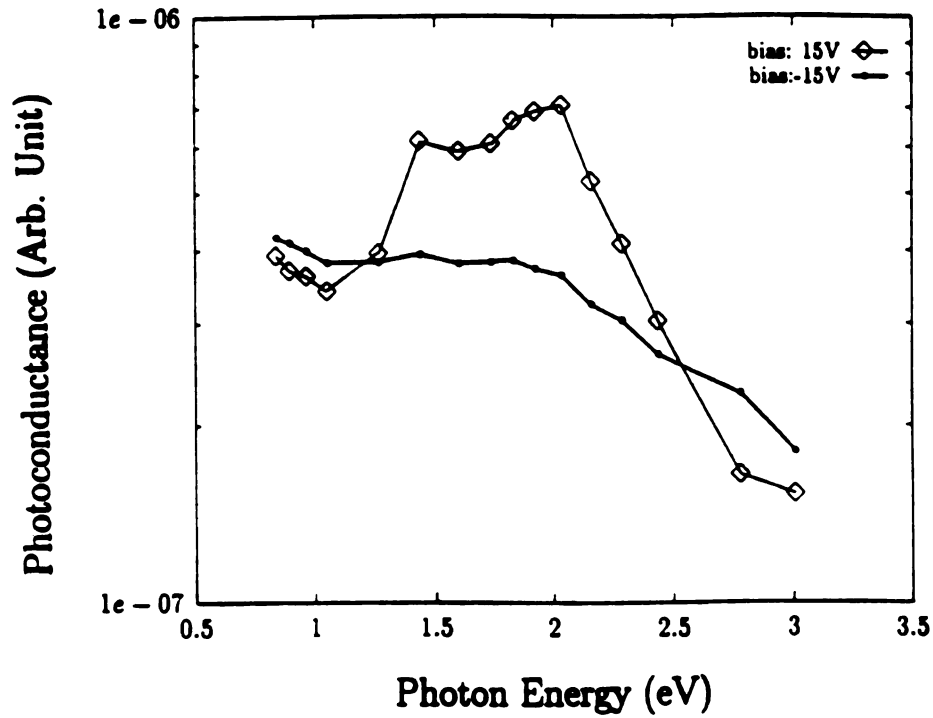
The experiments of the photo effects on the metal/diamond/silicon samples used the same method and technique as that described in chapter 5 (section 3.4).

Figure 5.25 and Figure 5.26 show the relationship of photoconductance versus photon energy for the small grain size Au/diamond/silicon sample and the small grain size In/diamond/silicon sample respectively. Similarly, the photoconductance versus photon energy characteristics for different large grain size Al/diamond/silicon samples are shown in Figure 5.27, Figure 5.28 and Figure 5.29. If the rectification happens at the diamond/silicon interface and is a result of silicon band bending, then silicon should play a role in contributing to the photo current. Consequently, the photo current should abruptly increase as the photon energy increases above 1.1 eV, which is the energy gap of the silicon. However, in both large and small grain size metal/diamond/silicon samples there are no indications that photoconductance abruptly increases at photon energies above 1.1 eV. This showed that the rectifying properties are not contributed by the diamond/silicon interface but rather by the Al/diamond interface and that band bending happens at the Al/diamond interface.

It is also observed that a negative bias did generate more photo current than a positive bias in Figure 5.27, Figure 5.28, and Figure 5.29. Figure 5.30 shows a possible energy band diagram of the Al/p-type diamond interface. During the photo-excitation the valence electrons are excited into the higher lying acceptor level creating more holes in the valence band. Since the band bending happens at the Al/diamond interface, that a negative bias drawing more photo current from the diamond is reasonable.

Generally, this research indicates that large grain size diamond films prepared by the paste-polished method provided better metal/diamond rectifying properties

(a)



(b)

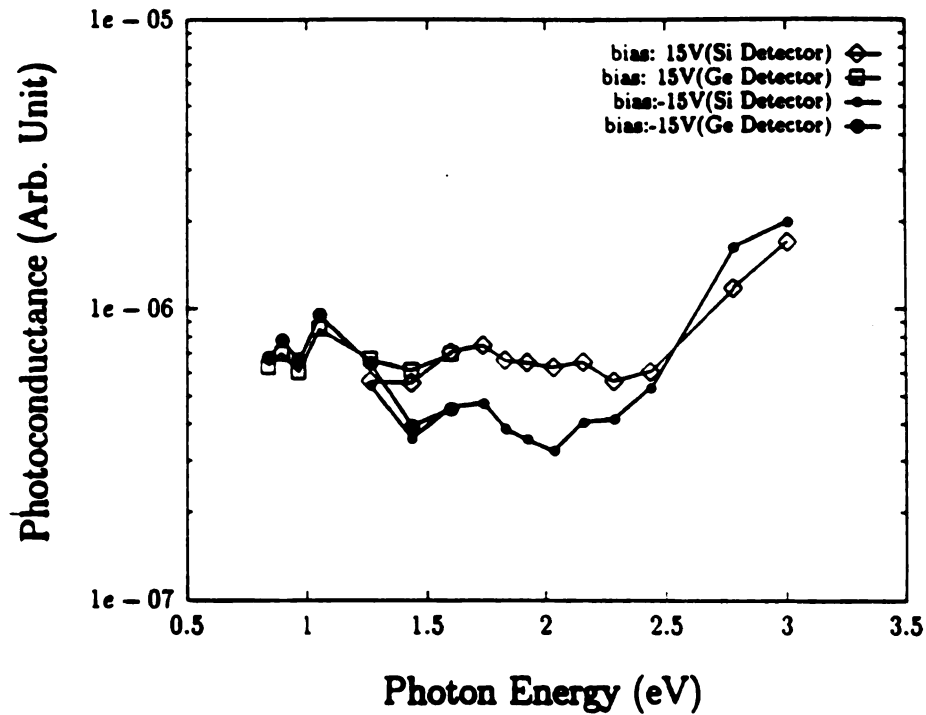
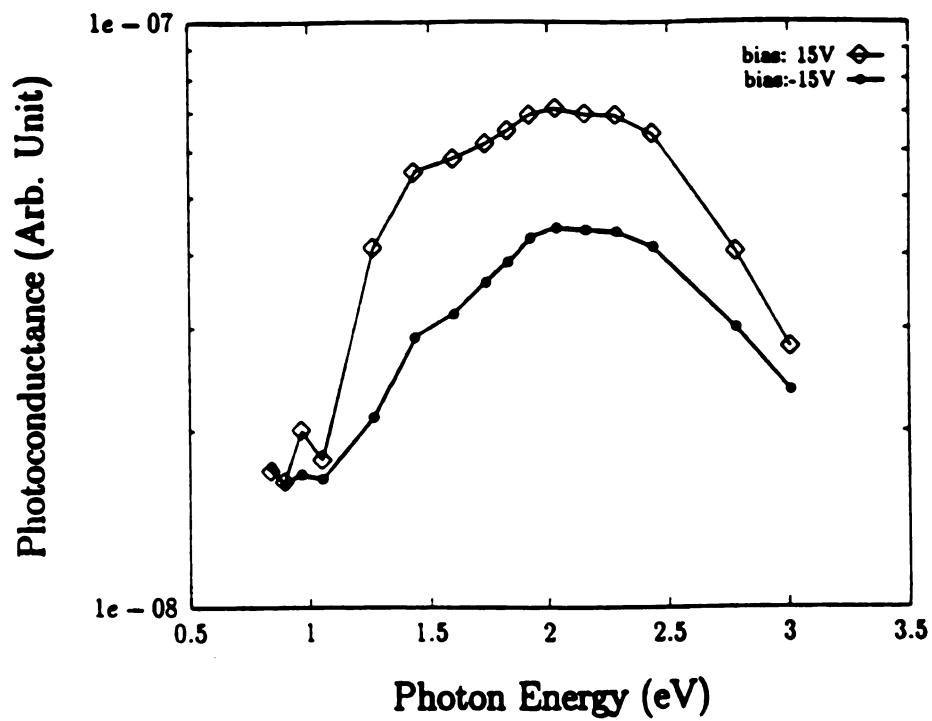


Figure 5.25. Photoconductance versus photon energy (a) before normalization and (b) after normalization for the small grain size Au/diamond/silicon sample. (Electrical sample : P39)

(a)



(b)

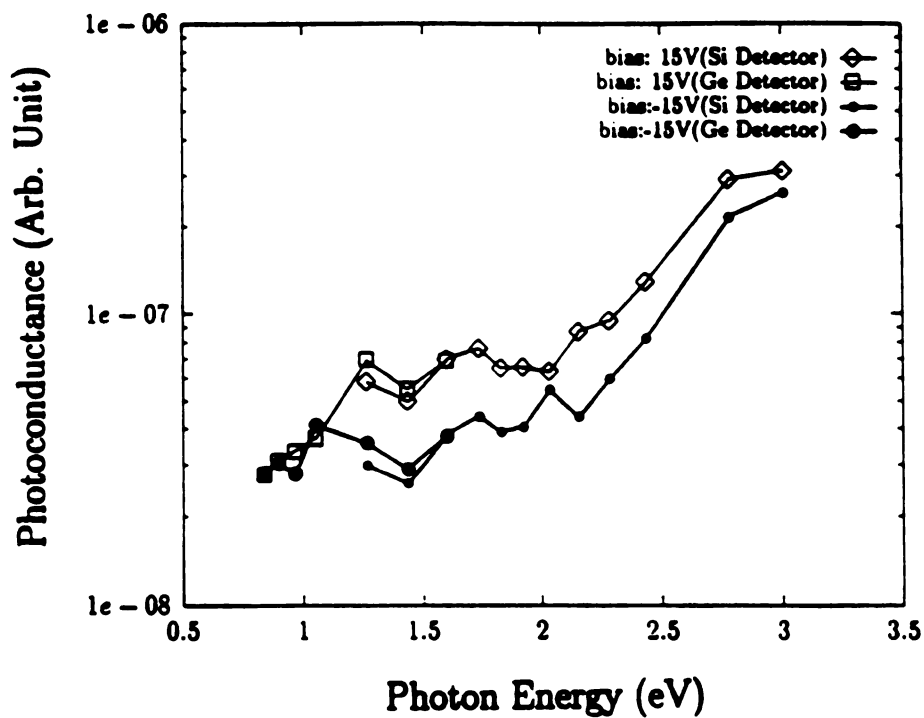
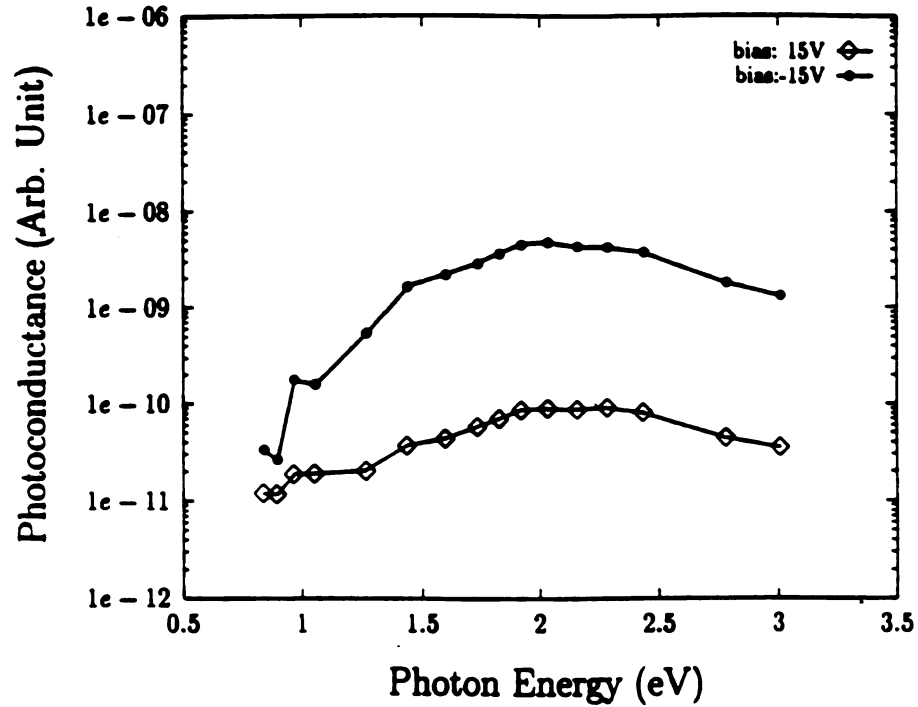


Figure 5.26. Photoconductance versus photon energy (a) before normalization and (b) after normalization for the small grain size In/diamond/silicon sample. (Electrical sample : P39)

(a)



(b)

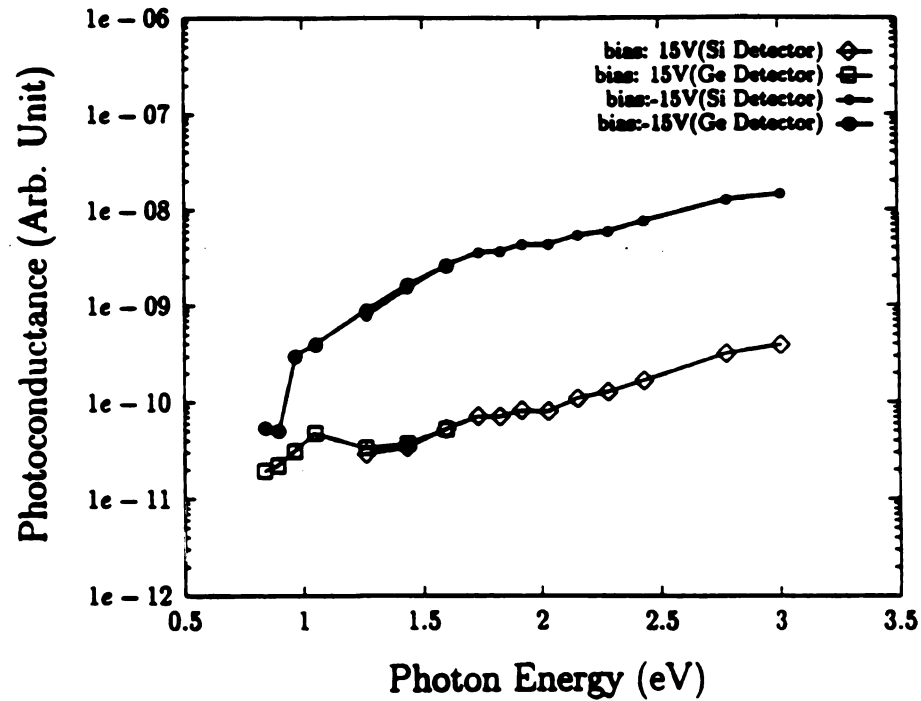
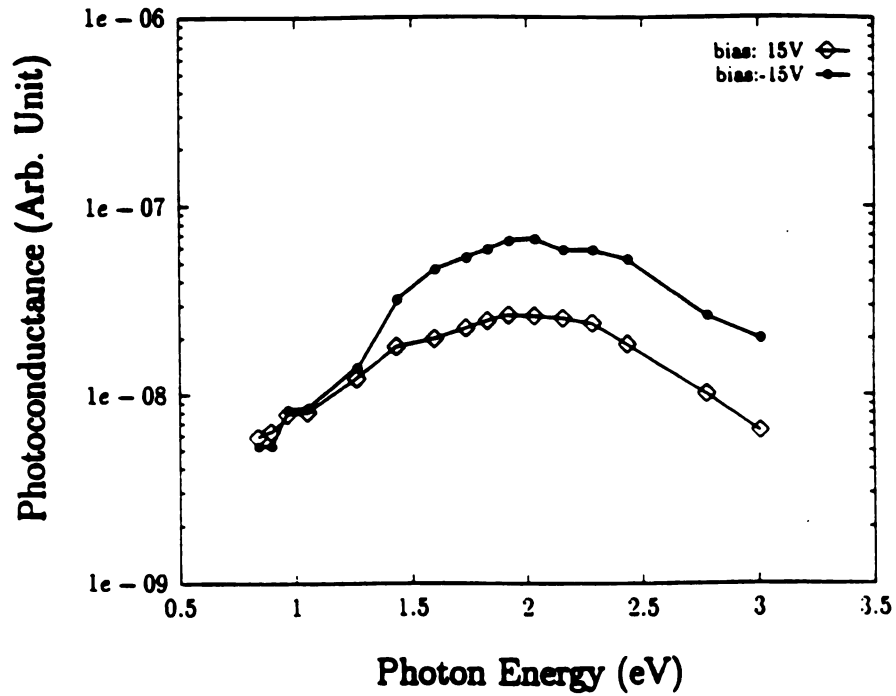


Figure 5.27. Photoconductance versus photon energy (a) before normalization and (b) after normalization for the large grain size Al/diamond/silicon sample. The average grain size is  $2.1 \mu\text{m}$ . (Electrical sample : P6)

(a)



(b)

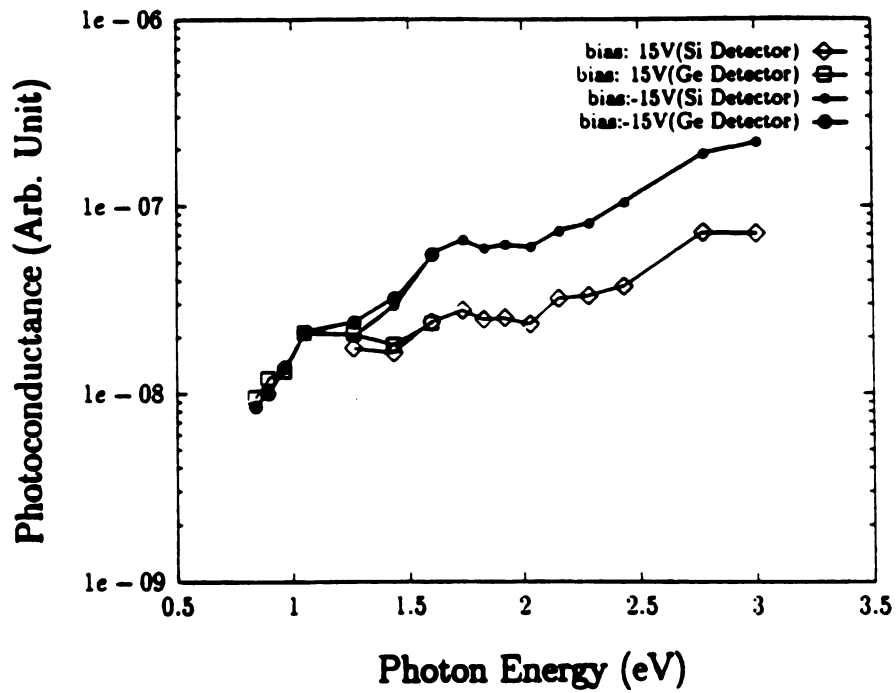
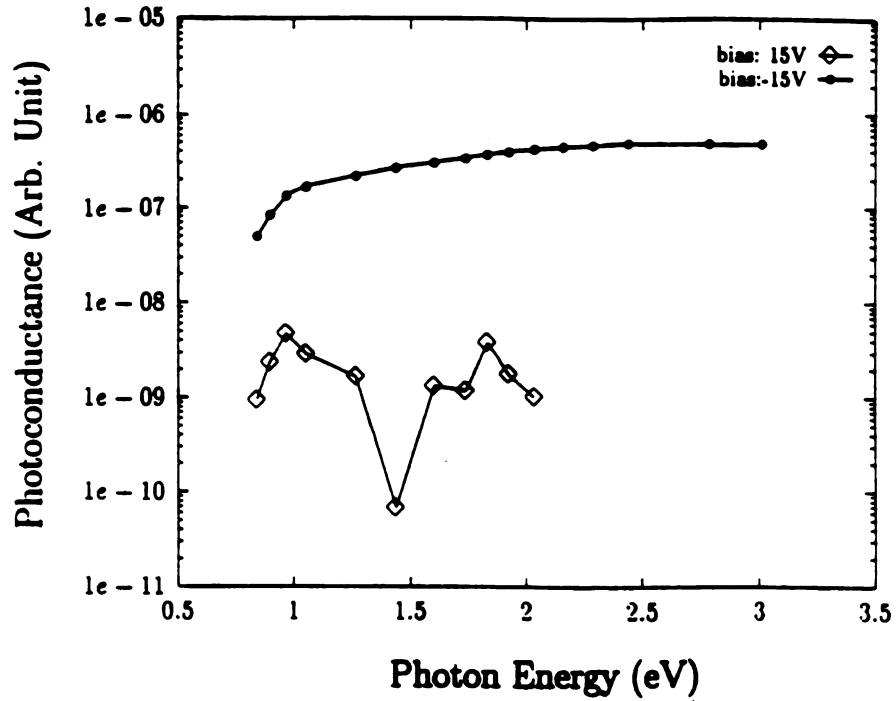


Figure 5.28. Photoconductance versus photon energy (a) before normalization and (b) after normalization for the large grain size Al/diamond/silicon sample. The average grain size is  $1.4 \mu\text{m}$ . (Electrical sample : P7)

(a)



(b)

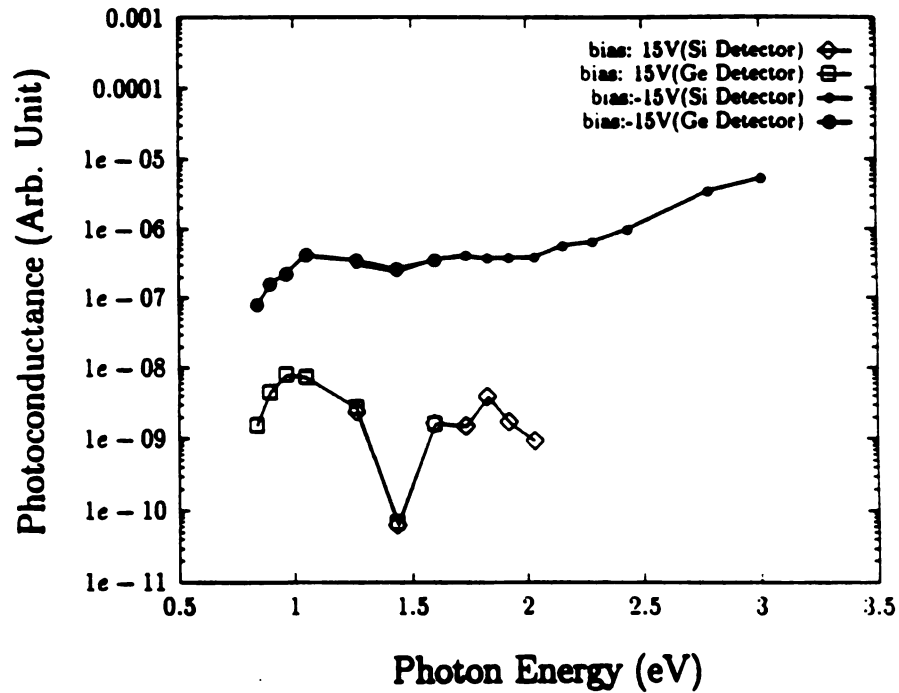


Figure 5.29. Photoconductance versus photon energy (a) before normalization and (b) after normalization for the large grain size Al/diamond/silicon sample. The average grain size is 1.1  $\mu\text{m}$ . Electrical sample : P20)

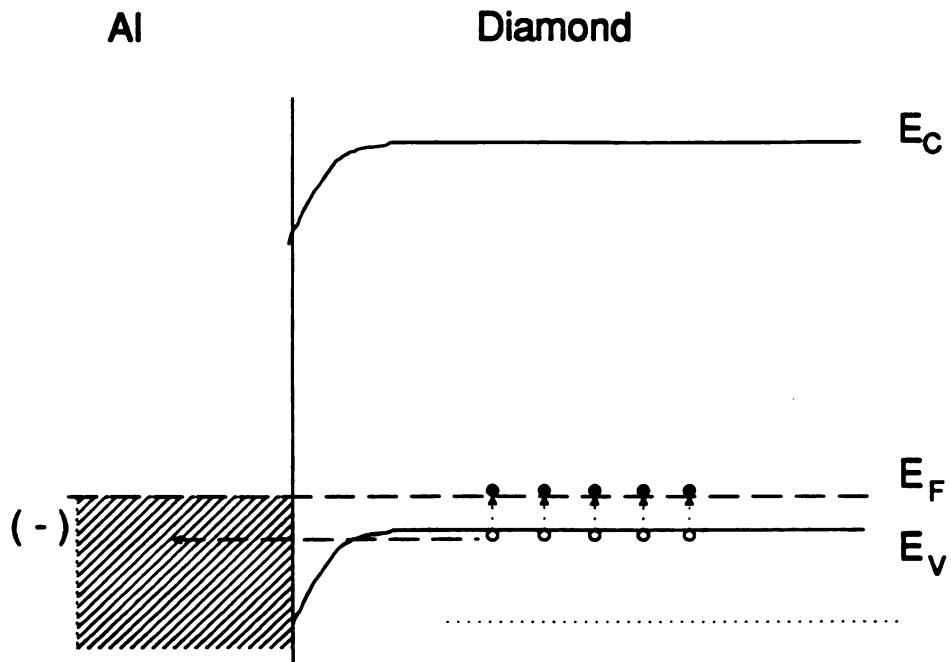


Figure 5.30. The energy band diagram in the Al/p-type diamond interface.

than the small grain size diamond films prepared by the powder-polished method. However, it doesn't mean that the larger the grain size the better the rectifying properties, independent of other variable. In this work, the sample which has the best rectifying properties is not the sample with biggest grain size diamond crystal. The degree of rectifying is also dependent on other properties of the metal/diamond interface. Details of studies on the device with the best rectifying properties in this study will be discussed in the next subsection.

#### 5.4.4 Diamond Schottky Barrier Diode

The best metal/diamond/silicon rectifying structures were prepared by the paste-polished method. The best of these rectifying characteristics were formed on film NDF-P20, deposited at conditions of 700 W microwave input power, 60 Torr pressure, 1 % methane/hydrogen concentration (1.5 sccm : 150 sccm). Typical I-V characteristics of the tungsten point contact/diamond/silicon and Al/diamond/silicon structures on the film are shown in Figure 5.31 and Figure 5.32 respectively. The Raman spectrum of NDF-P20 is shown in Figure 5.33. The point contact structure shows the ohmic behavior which again supports the mechanism that the rectifying property is a result of the Al/diamond interface. When two coplanar contacts are made, with one contact being the evaporated aluminum circle and the other being the tungsten point probe, SBD characteristics are again observed as shown in Figure 5.34. In this case the current passes via the rectifying diamond/Al contact through the diamond film to the silicon, through the silicon, and back up through the diamond film to the ohmic tungsten point contact.

Figure 5.35 shows that the forward bias current ( $I_F$ ) to the reverse bias current ( $I_R$ ) ratio at 10 V is almost  $2 \times 10^5$ . However, the ratio drops to  $2 \times 10^2$  when the voltage increases up to 25 V. Similar phenomena have been reported by other groups

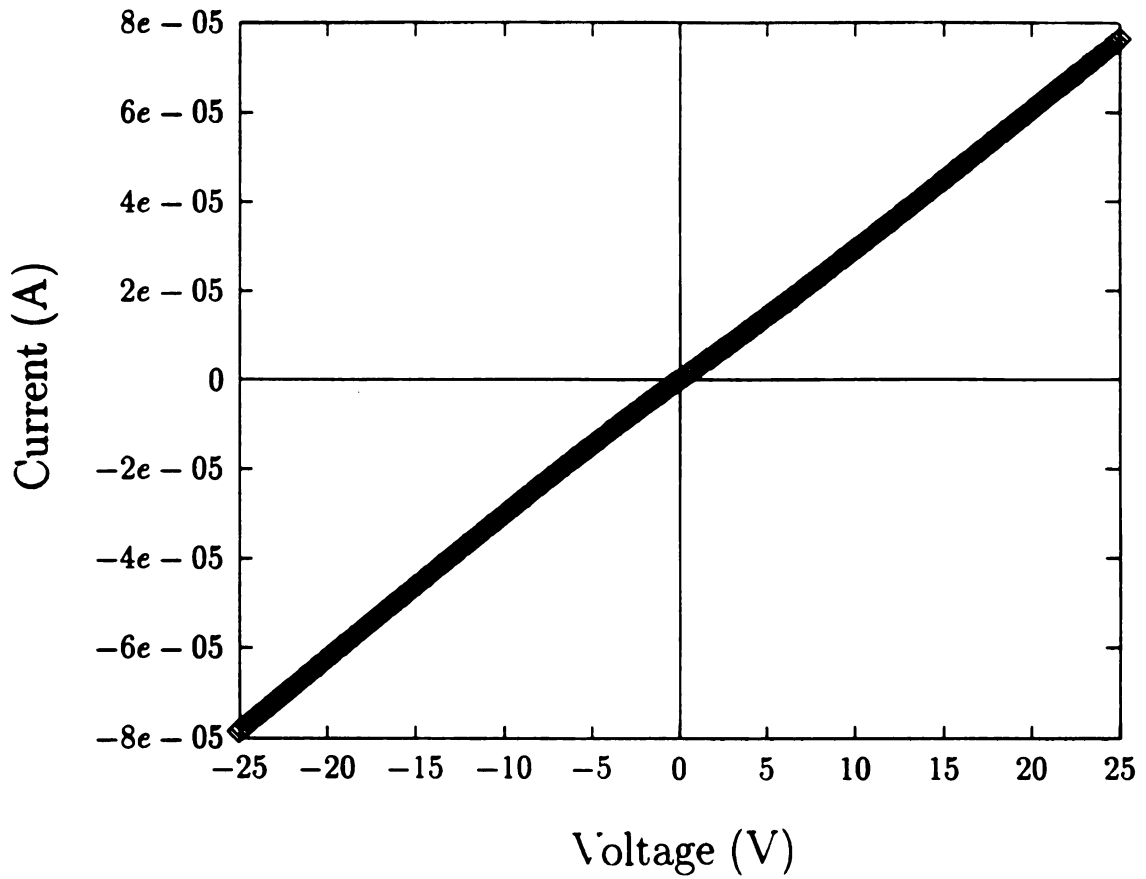


Figure 5.31. The I-V characteristic of the point contact/diamond/silicon structure showed ohmic behavior. The top contact is a tungsten point probe and the bottom contact is the silicon wafer. (Electrical sample : P20)

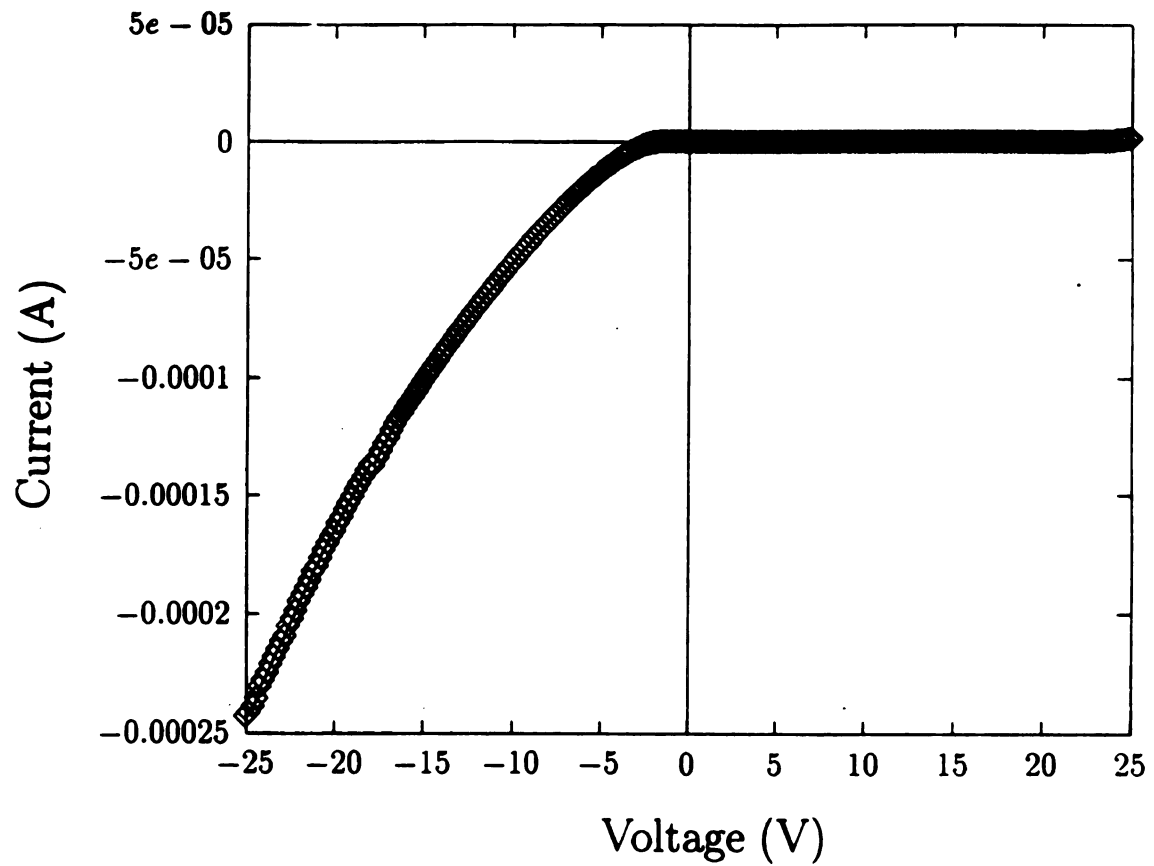


Figure 5.32. The best Schottky barrier diode (SBD) characteristic of the large grain size Al/diamond/silicon samples. The top contact is aluminum and the bottom contact is the silicon wafer. (Electrical sample : P20)

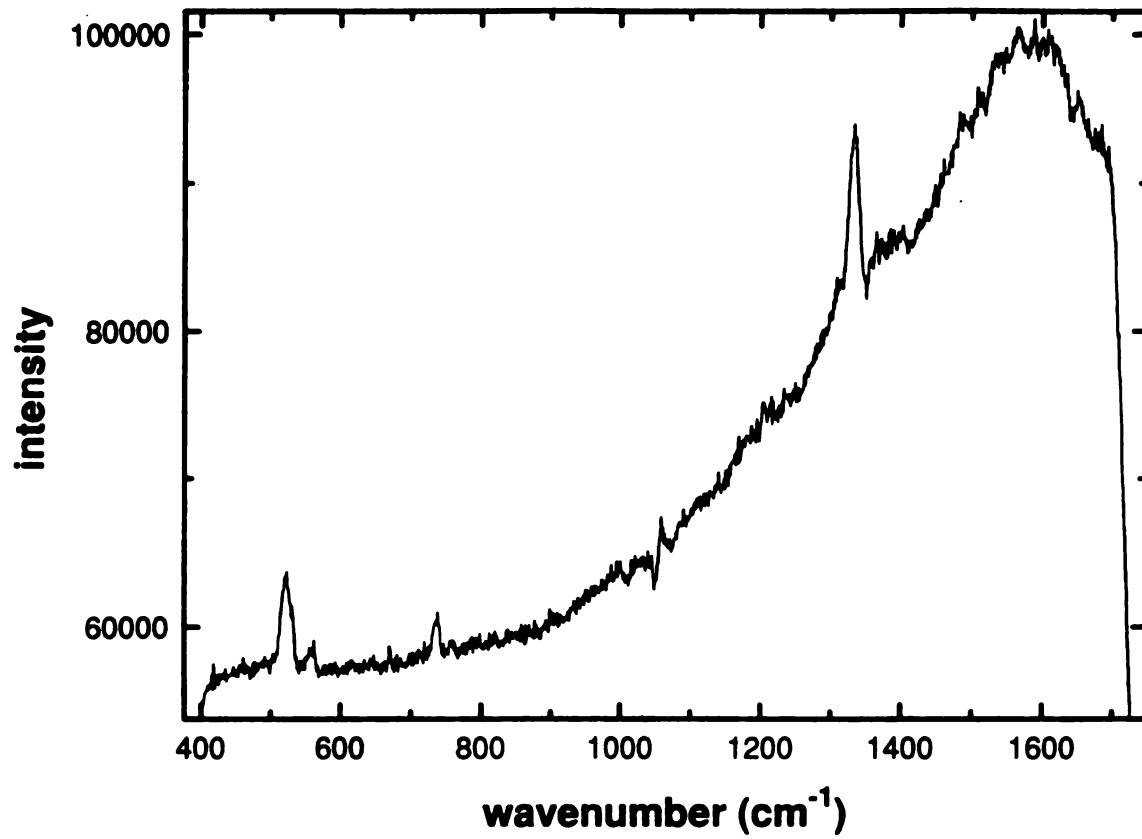


Figure 5.33. The Raman spectrum of NDF-P20. The peak between  $1550\text{cm}^{-1}$  and  $1600\text{cm}^{-1}$  indicates that the existence of graphitic component in the film.

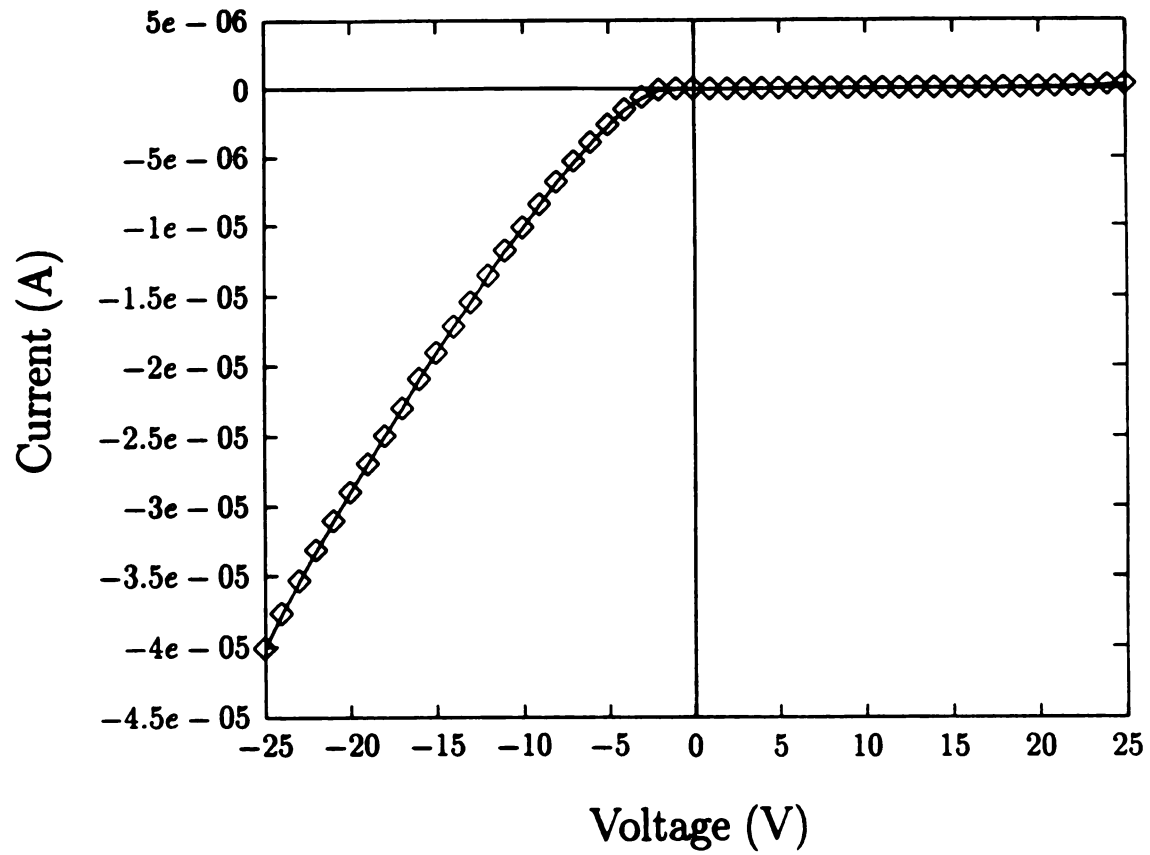


Figure 5.34. The SBD I-V characteristic of a film with coplanar surface contacts. One contact is aluminum and the other contact is a tungsten point probe. (Electrical sample : P20)

[76, 80, 137]. It is noted that the samples of [76, 80] are intentionally boron-doped and the samples of [133, 136, 137] and of this research are self-p-typed-doped during the deposition.

The current-voltage results of the diode are best analyzed by considering the current as a function of both the voltage across the junction and the voltage across the bulk region. For the former

$$I \approx I_0 \exp(qV_j / \eta kT) \quad (5.17)$$

where  $V_j$  is the junction voltage,  $\eta$  is the diode ideality factor ( $1 \leq \eta \leq 2$ ),  $T$  is temperature,  $k$  is Boltzmann's constant and  $I_0$  is the saturation current. Then for any current, the junction voltage is found to be

$$V_j = \frac{\eta kT}{q} \ln(I/I_0) \quad (5.18)$$

and the bulk voltage is next found from

$$V_b = V_{Applied} - V_j \quad (5.19)$$

Consequently, the forward I-V characteristic of the total structure is modeled by

$$V = \frac{\eta kT}{q} \ln(I/I_0) + f(I) \quad (5.20)$$

where  $V_b = f(I)$  represents the I-V characteristics of the bulk material. In its simplest form, the relationship between the bulk voltage and the current would be ohmic,

$$V_b = IR \quad (5.21)$$

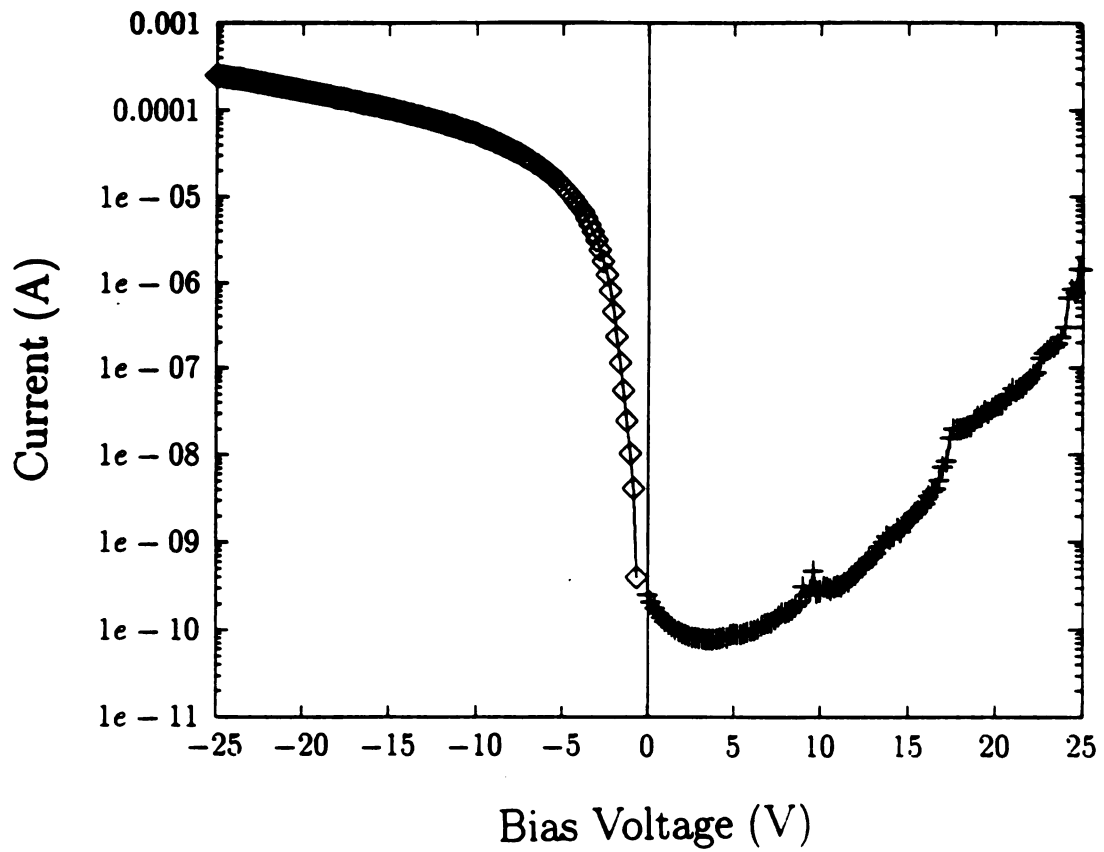


Figure 5.35. The  $\log(I)$ -V characteristic of the SBD. (Electrical sample : P20)

where  $R = \rho L/A$  is the resistance of the diamond film. However non-ohmic behavior is often observed in diamond films, an example being the field activated conductance reported in chapter 5 (section 3.3) of this research.

The data to be modeled by Eq. (5.20) is the forward I-V characteristic of the diode shown in the semilogarithmic plot of Figure 5.36. The parameters used in fitting the equation to the data are  $I_0$ ,  $\eta$ , and the functional relationship  $f(I)$ .

The data shown in Figure 5.36 doesn't show any straight line region in which the I-V characteristics are dominated by the diode portion of Eq. (5.20). For all currents in the range of measurements, the bulk voltage plays a major role in the total voltage. However, two straight lines representing the diode portion of the voltage are superimposed on the plot of Figure 5.36 which are consistent with the measured data. These straight lines correspond to quite different  $I_0$  and  $\eta$  values. The solid line shows the diode voltage versus current for  $I_0=5.2 \times 10^{-16}$  A and for  $\eta = 1$ . The dashed line shows the diode voltage versus current for  $I_0=2.9 \times 10^{-14}$  A and for  $\eta = 2$ . As will be shown below, both lead to similar conclusions about the bulk I-V relationship,  $f(I)$ .

One might expect that the  $f(I)$  relationship would follow the field activated conductivity model of Eq. (5.12). However Figure 5.37 shows that this is not the case. Above 10 V the data is consistent with a field activated conductivity with  $F_0=6 \times 10^4$  V/cm, consistent with the field activated model. However, below 10 V the model does not fit, since the conductivity decreases rapidly instead of approaching a constant value.

The data is better fit by assuming a power law for  $f(I)$  where

$$I \propto V_b^m \quad (5.22)$$

which  $m$  is the degree of power. As shown in Figure 5.38 and Figure 5.39 both  $m=3/2$  and  $m=2$  give a reasonable fit to the data, with the  $m=3/2$  fit being marginally

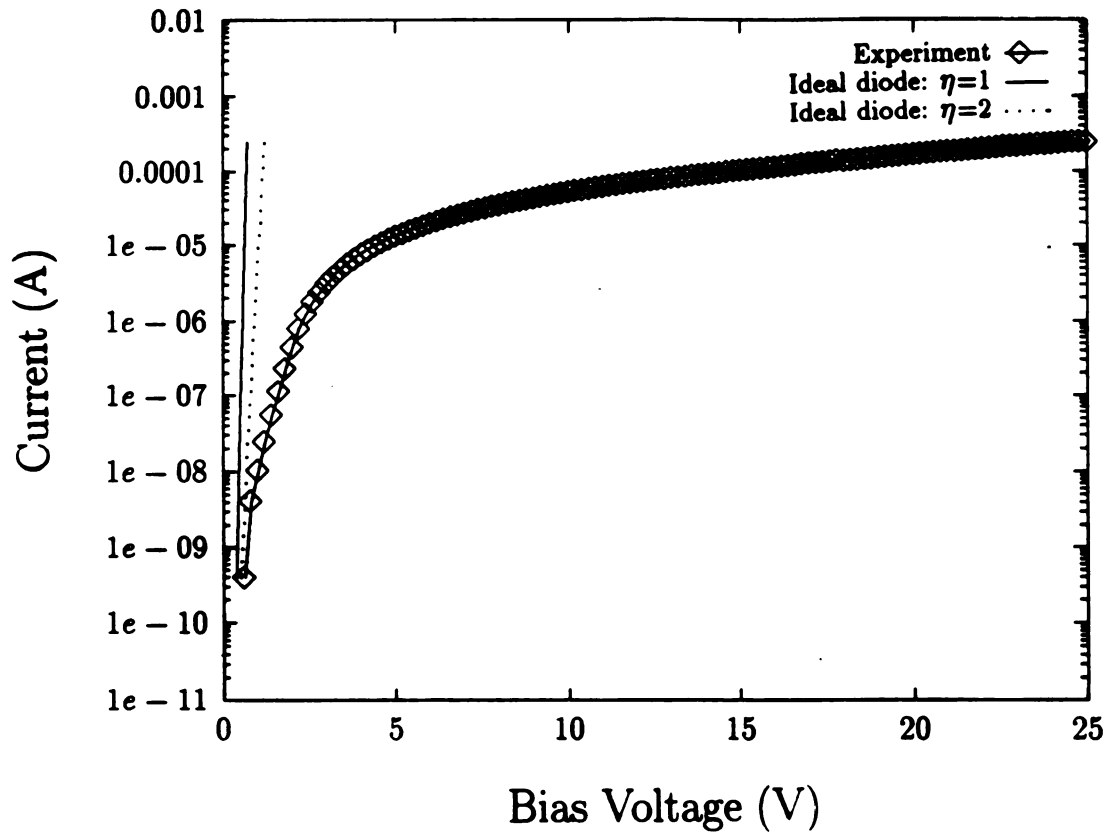


Figure 5.36. The forward bias I-V characteristic of the SBD. The  $\diamond$  represents the experimental data, the solid line shows the ideal diode with  $\eta = 1$ ,  $I_0=5.2 \times 10^{-16}$  A and the dashed line shows the ideal diode with  $\eta = 2$ ,  $I_0=2.9 \times 10^{-14}$  A. (Electrical sample : P20)

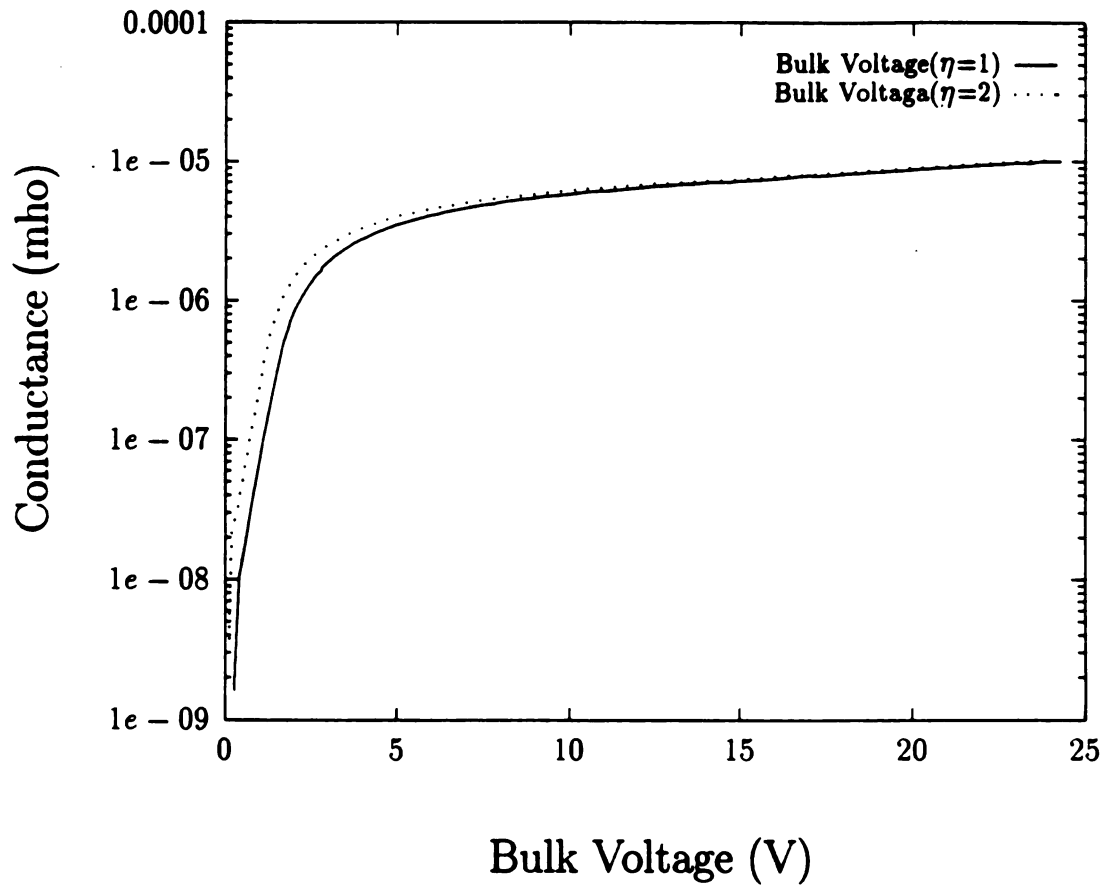


Figure 5.37. Conductance-bulk voltage characteristic. It follows the field activated model above 10 V. (Electrical sample : P20)

better. The energy band diagram and the equivalent circuit of the SBD are shown in Figure 5.40(a) and (b) respectively. The exact choice of  $I_0$  and  $\eta$  is not critical to the fits since the diode portion of the voltage drop is relatively negligible, especially at the higher range of voltages. The range of  $I_0$  values corresponds to a barrier height range of between 1.1 eV and 1.2 eV.

The significance of the power law dependence may be considered further as follows. Lampert and Mark loosely defined materials with band gap  $E_g \leq 2$  eV as semiconductors and those with  $E_g > 2$  eV as insulators [138]. By this definition, un-doped diamond with  $E_g = 5.5$  eV can be considered as an insulator. In a perfect trap free solid state insulator, the space-charge limited current-voltage relation can be expressed as

$$I \propto V^2 \quad (5.23)$$

rather than the  $V^{3/2}$ . In considering the difference it is noted that the derivation of Eq. (5.23) is based on the assumption that carriers drift at a velocity,  $v$ , with

$$v = \mu E \quad (5.24)$$

where  $\mu$  is carrier mobility and  $E$  is applied electric field. However, if the field strength is too high, the drift velocity of the carriers may vary as the square root of the applied electric field when above a certain critical field strength  $E_r$  [138]. This is known as a characteristic of "warm" carriers when acoustic phonon scattering is dominant. Then for

$$E > E_r, \quad v = \mu(E E_r)^{1/2} \quad (5.25)$$

The current-voltage relation becomes

$$I \propto E_r^{1/2} V^{3/2} \quad (5.26)$$

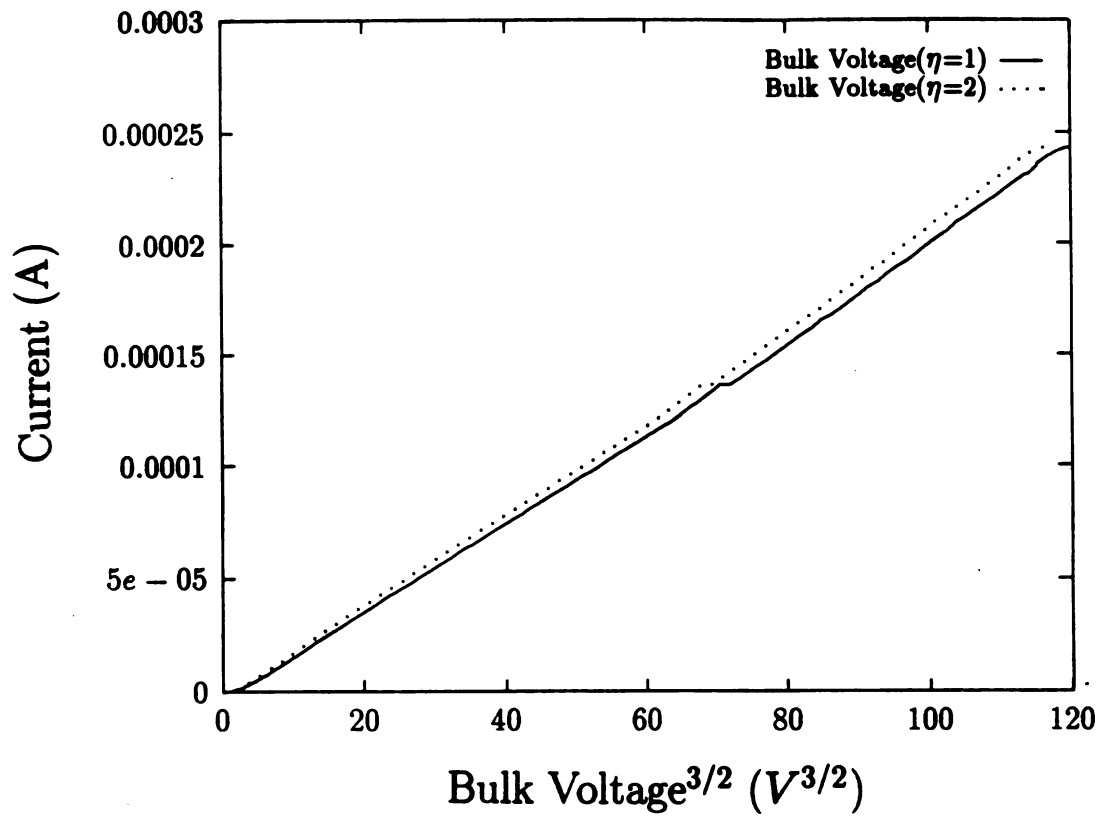


Figure 5.38. The  $I-V_b^{3/2}$  characteristic of the SBD. (Electrical sample : P20)

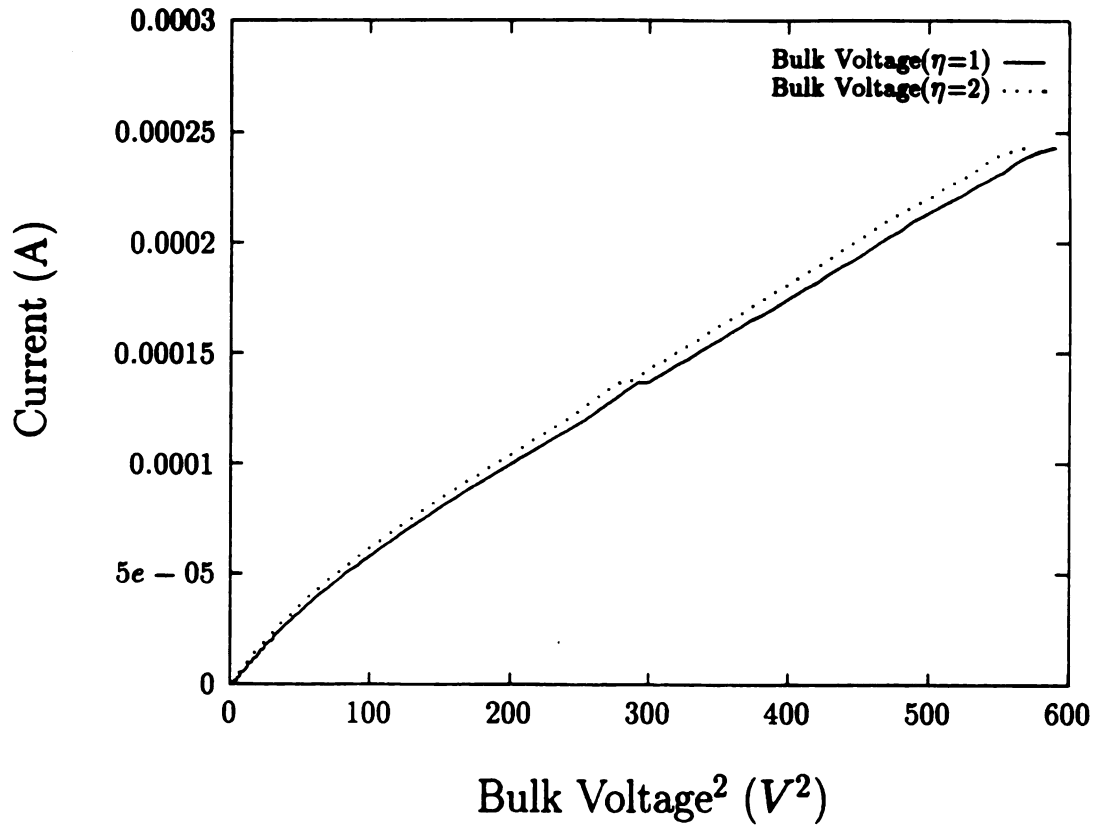
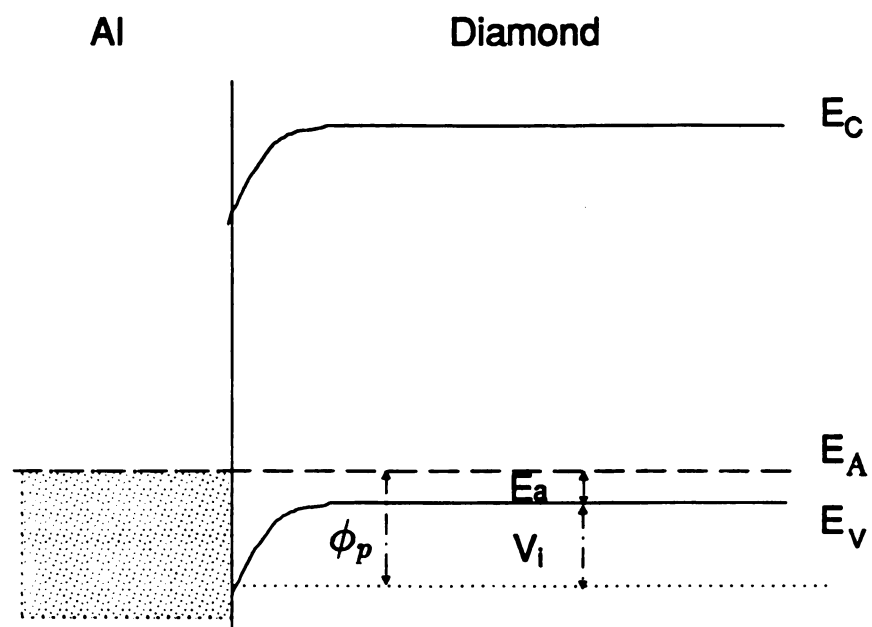


Figure 5.39. The  $I-V_b^2$  characteristic of the SBD. (Electrical sample : P20)

(a)



(b)

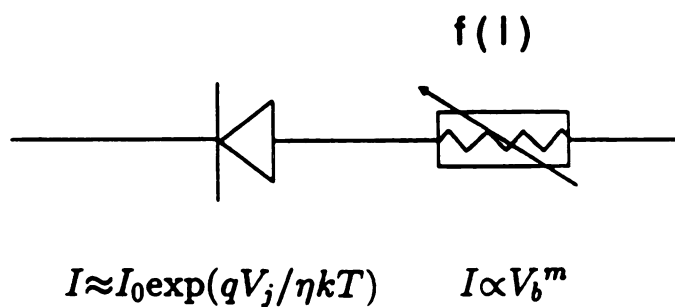


Figure 5.40. (a) The energy band diagram of the SBD. The barrier height  $\phi_p$  equals to the sum of built-in potential  $V_i$  and activation energy  $E_a$ . (b) The equivalent circuit of the SBD.

which has the same functional form as the observed data.

For single crystal diamond, the high field phenomenon happens above  $1 \times 10^5$  V/cm. In this case the film thickness is about  $4 \mu\text{m}$ , so a voltage of 10 V corresponds to an electric field of  $2.5 \times 10^4$  V/cm. The high field effect might not contribute to the phenomenon observed here.

An obvious point is that the powder-polished samples of chapter 5 (section 3.3) follow a field activated conductivity and exhibit ohmic, non-Schottky behavior whereas the paste-polished samples of this section follow a power law I-V and Schottky behavior. Both of these observations are consistent with the hypothesis that the powder-polished films have a larger defect concentration. Consequently, metal/diamond space charge layers are sufficiently thin to allow tunneling and ohmic behavior and their high field properties are dominated by ionizable defects.

It must also be noted here that some of the SBD exhibited a particular form of instability. The current becomes much smaller after several times of measurements. However, the rectifying behavior still exist.

Capacitance versus frequency measurement were also performed on the Al/diamond/silicon diodes with a HP4192A impedance analyzer and the data is presented in Figure 5.41 for different values of reverse bias.

The barrier height  $\phi_p$  can also be determined by the capacitance versus voltage measurement. By plotting  $1/C^2$  against reverse bias, one can get built-in potential  $V_i$  from the extrapolated intercept on the horizontal axis. From the slope of the straight line one can also calculate the doping concentration. As shown in Figure 5.40(a) the barrier height  $\phi_p$  can be found from

$$\phi_p \simeq V_i + E_a \quad (5.27)$$

where  $E_a$  is activation energy. However, from Figure 5.42 the data shown did not lie

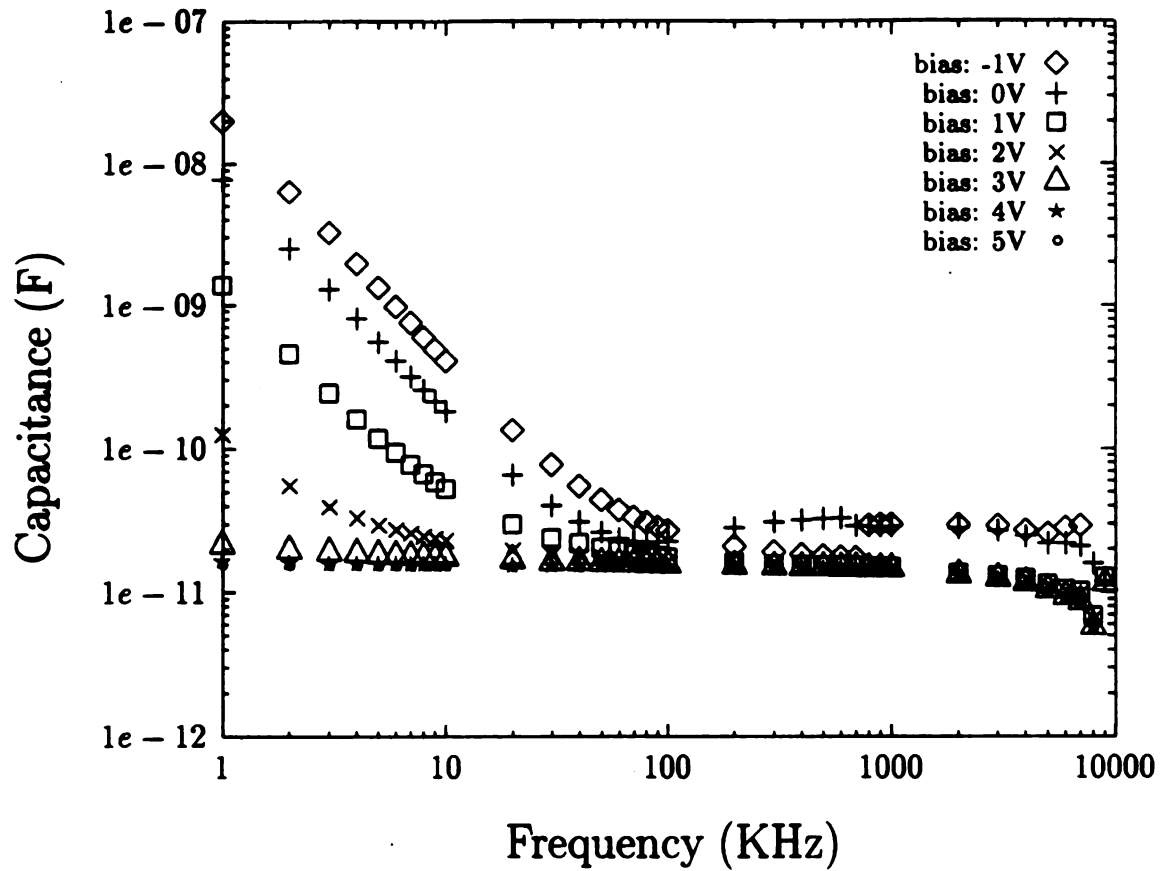


Figure 5.41. Capacitance versus frequency characteristic at different reverse bias. (Electrical sample : P20)

in a straight line. This may indicate that the self-doping of the film is non-uniform. Consequently, the barrier height can not be determined from Figure 5.42.

In Penn State University's work [133, 136, 137], they determine the ideality factor as 1.8, and the barrier height as 1.15 eV for Al and Au contacts to p-type CVD diamond films. They were not able to determine barrier height from the I-V curve, instead they use the technique of internal photoemission to determine the barrier height. In H. Shiomi, et al.'s work [76], an ideality factor of 2.1 and barrier height of 1.2 eV were all determined from the I-V measurement of the W contact to boron-doped diamond films. They noted that barrier height could not be obtained from C-V curve due to the high series resistance in the bulk. In D. G. Jeng, et al.'s work [80], they noted that an ideality factor of 1.85 was determined from the low voltage region (0.1-0.5 eV) slope for the Al/diamond Schottky diode. It is obvious that the understanding of the synthetic diamond film diodes is still preliminary. Many factors contribute to the film properties and since the deposition conditions are so different from group to group, more experiments are needed to further investigation.

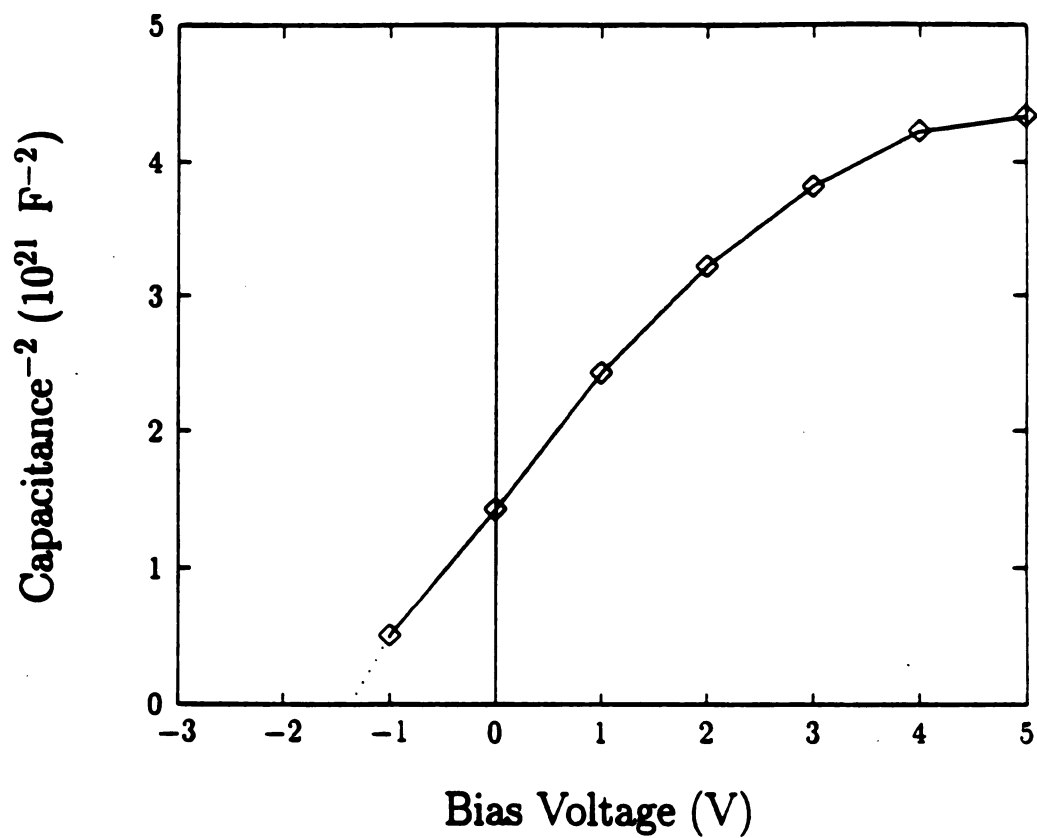


Figure 5.42. Capacitance versus reverse bias characteristic at 50 kHz. (Electrical sample : P20)

# CHAPTER 6

## Summary and Future Research

### 6.1 Summary of Important Results

The application of the microwave plasma disk reactor (MPDR) chemical vapor deposition system for diamond synthesis has been successfully developed. Good quality polycrystalline diamond films have been successfully deposited and characterized on silicon and silicon nitride substrates. Two sample preparation methods, which are paste-polished and powder-polished nucleation techniques have been used for depositing large grain size diamond films and small grain size diamond films respectively. A back-etching processing technique was also developed to isolate the deposited diamond films from the silicon substrate in order to study the diamond/silicon interface and allow access to evaporate metal contacts on both sides of the diamond films in order to study the electrical properties of the diamond films.

A goal of this research has been to provide an increased understanding about the relationship between properties of thin film diamond and the preparation conditions. Toward this purpose several important physical characterizations of the diamond films, such as Raman spectroscopy, X-ray photoelectron spectroscopy, DekTak profile measurement, scanning electron microscopy, and laser scanning microscopy were

carefully studied (see chapter 4). A particular focus of this research has been on the electrical properties of the films, and consequently several important electrical properties of the diamond films, such as activation energy, I-V characteristics, high field effect, and contact phenomenon were also studied (see chapter 5). The importance of preparation conditions on the nature of metal contacts is described in chapter 5 and new information about the relationship between defects and high electric field properties is provided by this research. The following subsections provide specific summary highlights.

### **6.1.1 Nucleation Method**

The nucleation method is important for the diamond synthesis since as was shown in this research, the density of nucleation sites is a major factor in determining the grain size of the diamond films.

The paste-polished nucleation method produced comparatively larger grain size diamond films than the powder-polished nucleation methods did since the latter method provides many more nucleation sites than the former method. It was also observed experimentally that the average grain size obviously increased as the methane concentration increased for the paste-polished nucleation method but not the powder-polished nucleation method. For both nucleation methods, the average grain size of diamond increased as the microwave power or plasma density increased, but the effect was smaller than the effect of increasing methane concentration in the case for the paste-polished nucleation method.

For both methods, the growth rate of diamond increased as methane concentration increases. The growth rate also increased as the microwave power or plasma density increased, however, the effect was smaller than the methane concentration. At the same deposition conditions, the growth rate of diamond by the powder-polished nu-

cleation method is slightly higher than that by the paste-polished nucleation method.

### **6.1.2 Quality of Diamond Films**

Raman spectroscopy is used as the major technique to distinguish the quality of the diamond films. The reported natural diamond peak is at  $1332\text{ cm}^{-1}$ . The larger the Raman signal at  $1332\text{ cm}^{-1}$  and the smaller the other peaks, the higher quality of the diamond films. It is known that the temperatures for depositing good quality diamond films is a critical variable for diamond synthesis. If the temperature is too low, an amorphous diamond-like component can become dominant and graphite becomes dominant instead of diamond if the temperature is too high.

Generally, from this research it was observed, based on Raman results, that at lower methane concentration one can get good quality diamond films in a wider temperature range than at higher methane concentration. It was found that for the range of power and pressure investigated, the preferential temperature range for good quality diamond films is between  $1030\text{ }^{\circ}\text{C}$  and  $1060\text{ }^{\circ}\text{C}$ . It was also noted that the two nucleation methods, under the same deposition conditions, appears to make no obvious difference in the quality of the diamond film.

### **6.1.3 Back-Etching Technique**

For film characterization, it is advantageous to have access to both sides of the film. In this research, a back-etching process was successfully developed in cooperation with Dr. Engemann at the University of Wuppertal (Germany) to transfer the diamond film from the silicon substrate to an epoxy substrate.

There are two kinds of back-etched samples fabricated by this technique. One kind of samples were used for physical characterizations (specifically XPS) of the back surface (diamond/silicon interface). The other kind of samples were processed

to have metal contacts on both sides of the film for electrical property studies of the diamond film.

#### 6.1.4 Diamond/Silicon Interface

From the back-etched samples prepared by the paste-polished nucleation method, it is found that a thin layer of  $SiC$  existed at the diamond/silicon interface by X-ray photoelectron spectroscopy analysis. This supports the hypothesis that the formation of a thin layer of  $SiC$  is an inherent part of the growth of diamond on the silicon substrate.

#### 6.1.5 Activation Energy of Diamond Films

A four-point probe technique was used for sheet resistance measurements of the diamond films. Diamond films were deposited on an insulating composite material, silicon nitride ( $Si_3N_4$ ), using both paste-polished and powder-polished nucleation methods. All the diamond films were determined as p-type by the hot probe technique.

The sheet resistance for the as-deposited samples prepared by the powder-polished nucleation method was on the order of  $10^5$  to  $10^6 \Omega/\square$ . By varying the temperature for the sheet resistance measurement, activation energies of 0.22 to 0.31 eV and 0.13 to 0.23 eV were obtained for carrier mobility equals to 1200 and  $12 \text{ cm}^2/V \cdot s$  respectively (see chapter 5, section 2.4). The samples were then annealed in a nitrogen ambient furnace at  $500^\circ C$  for one hour. This caused the sheet resistance to increase by at least four orders of magnitude and the activation energy to increase as well.

However, the sheet resistance of the as-deposited samples prepared by the paste-polished nucleation method was on the order of  $10^4 \Omega/\square$ . This occurred because a different system shut off procedure caused formation of a conducting layer by the

hydrogen plasma. When the sample was cleaned by a solution (see chapter 5, section 2.4) in order to remove the conducting layer, the sheet resistance was determined on the order of  $10^8 \Omega/\square$  with an activation energy of 0.51 eV and 0.42 eV for hole mobility equals to 1200 and  $12 \text{ cm}^2/\text{V}\cdot\text{s}$  respectively (see chapter 5, section 2.4).

### **6.1.6 Electric Field Dependent Conductivity of Diamond Films**

The dc electrical conductivity of polycrystalline diamond films with submicron grain sizes and ohmic contacts was studied as a function of the applied electric field up to the point of electrical breakdown. For electric fields below approximately  $10^5 \text{ V/cm}$ , the films exhibited predominantly ohmic behavior with a conductivity that was independent of the applied voltage for both high work function metal contacts (Au) and low work function metal contacts (In). For higher electric fields, however, the conductivity was field activated according to Poole's Law. The data is consistent with a Poole-Frenkel reduction of the ionization energy associated with Coulombic potentials surrounding ionizable centers, where the Coulombic potentials overlap. The ionizable centers may result from impurities or defects. In this study, experimental data showed that it is a carrier concentration increase, not a mobility increase, that gave rise to the field activated conductivity which is consistent with the Poole-Frenkel mechanism.

Because of the field activated conductivity, the current at high electric fields is substantially larger than would otherwise be the case. For  $3.5 \mu\text{m}$  and  $2 \mu\text{m}$  thick films, the breakdown happens at voltages higher than 250 V and 150 V respectively, corresponding to a breakdown field of  $7.1 \times 10^5$  and  $7.5 \times 10^5 \text{ V/cm}$  respectively. Consequently, the dielectric strength of the sub-micron grain size polycrystalline diamond films in this study are substantially less than those reported for single crystal dia-

mond ( $0.6 - 1 \times 10^7$  V/cm). The slope of the conductivity versus electric field indicates approximate one ionizable impurity or defect per 10,000 host atoms in such films.

### 6.1.7 Diamond Schottky Barrier Diode

Polycrystalline diamond Schottky barrier diodes were fabricated by using the large grain size diamond films with the Al/diamond/p-silicon structure. Rectifying behavior was determined in the Al/diamond interface as opposed to the diamond/silicon interface. The  $I_F/I_R$  ratio is almost  $2 \times 10^5$  at 10 V in the best device, but only  $2 \times 10^2$  at 25 V. The I-V characteristic can be modeled as an ideal Schottky diode in series with an insulator, for which the property ( $I \propto V^m$  relationship), is indicative of a space charge limited current effect in the bulk diamond. However, the metal/diamond/p-silicon samples for the small grain size diamond films exhibited ohmic property since the defect states in these films are so large that carriers can easily tunnel through the barrier.

## 6.2 Future Research

This research has studied the synthesis of diamond films in the MPDR deposition system; physical characterizations, and electrical characterization of the diamond films and diamond/silicon samples. However, the understanding of the relationship between the physical characterization and electrical properties is still in the early stage. More detailed investigation into the topics covered in this dissertation as well as the effects of other parameters (such as the vacuum purity, the addition of oxygen, and other gases, and lower plasma pressure) are still needed to complete our understanding of this research. Recommendations for future research follow.

### 6.2.1 Improvement for Diamond Deposition

The deposition system described in this research can be considerably improved with regard to system purity and with regard to deposition over larger area substrate. With regard to the latter, considerable progress has been made by a colleague, J. Zhang [139]. With regard to system purity, the vacuum system used in this research was mechanically pumped with a ultimate pressure of  $1 \times 10^{-4}$  Torr. Residual gas composition and leak/outgas rates were not specially quantified and monitored on a run-to-run basis. In order to better control impurities it would be useful to upgrade the system to a  $1 \times 10^{-7}$  Torr ultimate pressure and to perform residual gas analysis prior to runs. By providing a lower pressure capability, this also offers the opportunity to investigate ECR plasma deposition of diamond at lower pressures and temperatures. If the ECR plasma technique can be successfully used in an MPDR system, the deposition area could be quite large, 6 inches in diameter or larger.

Other things being equal, there is always a trade-off between a large deposition area and a high deposition rate since the amount of reaction species is fixed for a given reaction mixture, gas flow and microwave power. Consequently, the larger the deposition area, the lower the deposition rate. With the addition of oxygen, however, it is known that the quality and deposition rate can be improved. The extent to which oxygen affects the quality and deposition rate needs to be carefully studied on different configurations of this system.

### 6.2.2 The Techniques for Physical Characterization

It is known that Raman spectroscopy is the best technique to distinguish diamond, graphite, and amorphous carbon. However, Raman spectroscopy only provides limited information about the sample, specifically it determines if the film is similar to natural diamond having a sharp peak at  $1332 \text{ cm}^{-1}$ . For example, Raman spec-

troscopy can't show the difference between a sample with and without a very thin layer of conducting graphite or chemical contamination on top of the films. Also as shown in Figure 4.7, Raman spectroscopy can't show the difference between a large grain size diamond film and a small grain size diamond film deposited at the same conditions.

Other characterization techniques are therefore also needed in future work to provide the basic properties of the film to assist the Raman spectroscopy in order to have a better understanding of the over-all physical properties of the film. Examples include secondary ion mass spectroscopy (SIMS) and Auger electron spectroscopy (AES) to determine the elemental composition of the film; X-ray diffraction (XRD) to determine the crystal structure and lattice spacing; electron energy loss spectroscopy (EELS) to determine the localized bonding in the bulk film; X-ray photoelectron spectroscopy (XPS) to examine the chemical composition at the surface of the film; and scanning electron microscopy (SEM) to examine the surface morphology.

### **6.2.3 The Role of *SiC* at the Diamond/Silicon Interface**

It is known that a thin layer of *SiC* exists at the diamond/silicon interface from this and other research. It may be hypothesized that *SiC* contributed to the ohmic behavior of the diamond/p-silicon interface for both small and large grain size diamond films in this research. However, it is not clear at this point how *SiC* affects the electrical properties of the diamond/silicon heterojunction. It would be of interest in future research to carefully prepare back-etched samples with and without the *SiC* layer in order to study this further. It would also be interesting to investigate how the interfacial electrical properties vary if the nucleation methods is changed from abrasion to seeding since the abrasion nucleation method scratches the silicon surface and the seeding nucleation methods does not.

#### **6.2.4 Defects States in Diamond Films**

There are clearly defect states in polycrystalline diamond films because of the existence of grain boundaries. However, defect states in each single crystal is also possible since the methane and hydrogen gases used in this research are 99.99 % and 99.999 % pure respectively. In this research, it was shown that defect states play an important role contributing to the electrical properties. For small grain size metal/diamond/p-silicon samples, the number of defect states is so large that it contributes to the ohmic contact behavior. Large grain size Al/diamond/p-silicon samples, however, did show some rectifying properties since there are less defect states. Further knowledge of the defect states in the diamond films under different plasma pressure and different deposition system becomes an important future task for understanding the electrical properties of synthetic diamond films.

#### **6.2.5 Diamond Devices**

A major future goal of diamond synthesis research is to fabricate useful diamond devices, such as diamond diodes, diamond transistors, diamond metal-oxide-semiconductor structures, and diamond integrated circuits (IC) with performance advantages based on the excellent properties of diamond (see chapter 2, section 4). There is a need for considerable future work toward the development of electronic grade diamond.

A difficult, but important, future task for diamond device research is the development of the capability to synthesize epitaxial diamond films on non-diamond substrates. The existing techniques only can deposit epitaxial diamond films on diamond substrates and polycrystalline diamond films on non-diamond substrate. Furthermore, it is important to evaluate and improve the performance of the poly-diamond devices. Future device related tasks also include the development of improved tech-

niques for diamond doping and etching.

The investigation of the electrical properties of synthetic diamond is still in the preliminary stage and the fabrication of diamond devices is still far from mature. Consequently, much more future research effort is needed in order to explore the potential development of diamond devices.

# APPENDICES

# APPENDIX A

## Deposited Diamond Films

### ( 1 ) Samples by Diamond-Paste Nucleation Method

Sample Number ( NDF- # )	CH <sub>4</sub> / H <sub>2</sub> and Flow Rate ( sccm )	Microwave Input Power ( W )	Plasma Pressure ( Torr )	Time ( hour )	Date
N6	1.5 % ( 3 : 200 )	600	60	7	6/17/89
P6	1.5 % ( 3 : 200 )	600	60	7	6/18/89
N7	1.25 % ( 2.5 : 200 )	600	50	7	6/19/89
P7	1.25 % ( 2.5 : 200 )	600	50	7	6/20/89
P8, N8	0.5 % ( 1.25 : 250 )	700	80	6	8/31/89
P9, N9	0.5 % ( 1.25 : 250 )	700	80	6	9/2/89
P10, N10	0.5 % ( 1.25 : 250 )	700	80	6	9/3/89
P11, N11	0.5 % ( 1.25 : 250 )	825	80	6	9/4/89

Sample Number ( NDF- # )	CH <sub>4</sub> / H <sub>2</sub> and Flow Rate ( sccm )	Microwave Input Power ( W )	Plasma Pressure ( Torr )	Time ( hour )	Date
P12, N12	0.5 % ( 1.25 : 250 )	700	70	6	9/5/89
P13, N13	0.5 % ( 1.25 : 250 )	700	70	6	9/6/89
P14, N14	0.5 % ( 1.25 : 250 )	700	60	8	9/7/89
P15, N15	0.5 % ( 1.25 : 250 )	800	60	8	9/8/89
P16, N16	0.5 % ( 1.25 : 250 )	600	60	8	9/9/89
S1	0.5 % ( 1.25 : 250 )	600	60	6	9/10/89
S2	0.5 % ( 1.25 : 250 )	600	60	6	9/11/89
P17, N17	0.5 % ( 1.25 : 250 )	700	60	10	9/12/89
P18, N18	2 % ( 2 : 100 )	700	60	5	10/18/89
P19, N19	2 % ( 2 : 100 )	700	50	5	10/19/89
P20, N20	1 % ( 1.5 : 150 )	700	60	8	11/5/89
P21, N21	1 % ( 1.5 : 150 )	700	70	8	11/6/89
P22, N22	1 % ( 1.5 : 150 )	800	60	10	11/7/89

Sample Number ( NDF- # )	CH <sub>4</sub> / H <sub>2</sub> and Flow Rate ( sccm )	Microwave Input Power ( W )	Plasma Pressure ( Torr )	Time ( hour )	Date
P23, N23	1 % ( 1.5 : 150 )	800	50	10	11/8/89
P24, N24	1 % ( 1.5 : 150 )	700	70	10	11/9/89
P25, P26	1 % ( 1.5 : 150 )	700	70	14	11/10/89
P27, N27	1 % ( 1.5 : 150 )	700	70	10	1/11/90
P28, N28	1.5 % ( 2.25 : 150 )	700	70	6	1/22/90
P29, N29	1.33 % ( 2 : 150 )	700	70	6	1/23/90
P30, N30	1.1 % ( 1.75 : 150 )	700	70	6	1/24/90
P31, N31	1 % ( 1.5 : 150 )	700	70	5	2/6/90
P32, N32	1.2 % ( 1.8 : 150 )	700	70	6	2/8/90
N25, N26	0.7 % ( 1.05 : 150 )	700	70	6	2/13/90

## ( 2 ) Samples by Diamond-Powder Nucleation Method

Sample Number ( NDF- # )	CH <sub>4</sub> / H <sub>2</sub> and Flow Rate ( sccm )	Microwave Input Power ( W )	Plasma Pressure ( Torr )	Time ( hour )	Date
P33	0.5 % ( 0.75 : 150 )	600	80	6	3/9/90
P34	0.5 % ( 0.75 : 150 )	600	70	6	3/13/90
P35	1 % ( 1.5 : 150 )	600	70	5	3/15/90
P36	1.5 % ( 2.25 : 150 )	600	70	5	3/16/90
P37	1 % ( 1.5 : 150 )	600	60	5	3/19/90
P38	0.5 % ( 0.75 : 150 )	600	60	6	3/22/90
P39	0.5 % ( 0.75 : 150 )	600	50	6	3/23/90
P40	1 % ( 1.5 : 150 )	600	50	5	3/27/90
P41	1 % ( 1.5 : 150 )	750	50	5	3/29/90
P42	0.5 % ( 0.75 : 150 )	500	60	6	4/6/90
P43	0.5 % ( 0.75 : 150 )	500	50	6	4/9/90
S3	0.5 % ( 0.75 : 150 )	500	50	6	4/11/90
S4	0.5 % ( 0.75 : 150 )	400	50	6	4/12/90

Sample Number ( NDF- # )	CH <sub>4</sub> /H <sub>2</sub> and Flow Rate ( sccm )	Microwave Input Power ( W )	Plasma Pressure ( Torr )	Time ( hour )	Date
S5	0.5 % ( 0.75 : 150 )	600	50	6	4/13/90
P44	0.5 % ( 0.75 : 150 )	500	60	10	4/14/90
P45	0.5 % ( 0.75 : 150 )	400	60	10	4/15/90
P46	0.5 % ( 0.75 : 150 )	600	60	10	4/16/90
P47	0.5 % ( 0.75 : 150 )	600	50	10	4/17/90
P48	0.5 % ( 0.75 : 150 )	700	60	10	4/18/90
S6	0.5 % ( 0.75 : 150 )	320	50	6	4/19/90
P49	0.5 % ( 0.75 : 150 )	400	50	6	4/20/90
P50	0.5 % ( 0.75 : 150 )	800	60	6	4/23/90
P51	1 % ( 1.5 : 150 )	400	60	5	4/24/90
P52	1 % ( 1.5 : 150 )	500	60	5	4/25/90
P53	1 % ( 1.5 : 150 )	700	60	5	4/27/90
S7	1 % ( 1.5 : 150 )	400	50	5	4/29/90

# APPENDIX B

## Electrical Samples

### (1) Metal/Diamond/Silicon Samples

Film #	Metal Contact
P6	Al
N6	Al
P7	Al
N7	Al
P8	Al
N8	Al
P9	Al
N9	Al

Film #	Metal Contact
P10	Al
N10	Al
P20	Al
N20	Al
P21	Al
N21	Al
P39	Au
P39	Ag
P39	In
P49	Au
P49	Ag
P49	In

## ( 2 ) Metal/Diamond/Metal Back-Etched Samples

Film #	Top Metal Contact	Bottom Metal Contact
N14-T1	---	Cr/Au
N14-T2	---	Au
P33-T1	Ag	Ag
P33-T2	Ag	Pt/Ag
P33-T3	In	Pt/Ag
P44-T1	Au	Ag
P44-T2	In	In
P44-T3	In	Pt/Ag
P46-T1	Au	Ag
P46-T2	Au	Ag
P46-T3	In	In
P46-T4	Au	In

Film #	Top Metal Contact	Bottom Metal Contact
P45-T1	---	Ag
P45-T1	---	Ag
P45-T1	---	Ag
P47-T1	Au	Au
P47-T2	Au	Au
P47-T3	In	Au
P48-T1	---	Au
P48-T2	---	Au
P48-T3	---	Au
P49-T1	Ag	Ag
P49-T2	Ag	Ag
P49-T3	Au	Ag

# **BIBLIOGRAPHY**

## BIBLIOGRAPHY

- [1] F. P. Bundy, H. T. Hall, H. M. Strong, R. H. Wentorf Jr., *Nature*, 176, pp.51, 1955.
- [2] J. Asmusson and J. Root, "Characteristics of a Microwave Plasma Disk Ion Source", *Appl. Phys. Lett.*, 44, pp.396, 1984.
- [3] J. Root and J. Asmusson, "Experimental Performance of a Microwave Cavity Plasma Disk Ion Source", *Rev. of Sci. Inst.*, 56, pp.1511, 1985.
- [4] J. Hopwood, D. K. Reinhard, J. Asmusson, "Experimental Conditions for Uniform Anisotropic Etching of Silicon with a Microwave Electron Cyclotron Resonance Plasma System", *Journal of Vacuum Science and Technology, B*, 6, pp.268, 1988.
- [5] Dahimene, M., "Development of a Microwave Ion and Plasma Source Immersed in a Multicusp Electron Cyclotron Resonant Magnetic Field", Ph.D. dissertation, Michigan State University, 1987.
- [6] J. Hopwood, "Macroscopic Properties of a Multipolar Electron Cyclotron Resonance Microwave-Cavity Plasma Source for Anisotropic Silicon Etching", Michigan State University, 1990.
- [7] J. Hopwood, R. Wagner, D. K. Reinhard, J. Asmusson, "Electric Fields in a Microwave-Cavity ECR Plasma Source", *J. Vac. Sci. Technol. A*, 8, pp. , May/June 1990.
- [8] G. T. Salbert, D. K. Reinhard, and J. Asmusson, "Oxide Growth on Silicon Using a Microwave Electron Cyclotron Resonant Oxygen Plasma", *J. Vac. Sci. Technol. A*, 8, pp. May/June 1990.
- [9] T. Roppel, D. K. Reinhard, and J. Asmusson, "Low Temperature Oxidation of Silicon Using a Microwave Plasma Source", *J. Vac. Sci. Technol. B*, 4, pp.295, 1986.

- [10] J. Zhang, B. Huang, D. K. Reinhard, and J. Asmussen, "An Investigation of The Effects of Electromagnetic Field Patterns on Microwave Plasma Diamond Thin Film Deposition", *J. Vac. Sci. Technol. A*, *8*, pp.2124, 1990.
- [11] R. F. Curl and R. E. Smalley, "Fullerenes", *Scientific American*, *265*, pp.54, 1991.
- [12] P. W. Bridgman, "Synthetic Diamond", *Scientific American*, *42*, pp.42, 1955.
- [13] P. K. Bachmann, R. Messier, "Emerging Technology of Diamond Thin Films", *C&EN*, pp.24, 1989.
- [14] S. Aisenberg, R. Chabot, "Ion Beam Deposition of Thin Films of Diamondlike carbon", *J. Appl. Phys.*, *42*, pp.2953, 1971.
- [15] E. G. Spencer, P. H. Schmidt, D. J. Joy, and F. J. Sanssalone, "Appl. Phys. Letter.", *29*, pp.118, 1976.
- [16] C. Weissmantel, K. Bewilogua, D. Dietrich, H. Erler, H. Hinneberg, S. Klose, W. Nowick, and G. Reisse, *Thin Solid Films*, *72*, pp.19, 1980.
- [17] T. J. Moravec, T. W. Orent, *J. Vac. Sci. Technol.* *18*, pp.226, 1981.
- [18] B. V. Derjaguin, B. V. Spitsyn, L. L. Bouilov, A. A. Klochkov, A. E. Gorodestskii, and A. V. Smol'yanov, *Sov Phys. Dokl*, *21*, pp.767, 1976.
- [19] S. Matsumoto, Y. Sato, M. Kamo, and N. Setaka, "Vapor Deposition of Diamond Particles from Methane", *Japanese J. Appl. Phys.*, *21*, pp.L183, 1982.
- [20] W. D. Kingery, H. K. Bowen, D. R. Uhlmann, "Introduction to Ceramics", 2nd edition, pp.313, John Wiley & Sons, Inc. 1976.
- [21] R.C. DeVries, "Synthesis of Diamond under Metastable Conditions." *Ann. Rev. Mater. Sci.*, *17*, pp.161, 1987.
- [22] M. Tsuda, M. Nakajima, S. Oikawa, "Epitaxial Growth Mechanism of Diamond Crystal in  $CH_4$ -2 plasma." *J. Am. Chem. Soc.*, *108*, pp.5780, 1986.
- [23] S. J. Harris, "Mechanism For Diamond Growth From Methyl Radicals." *Appl. Phys. Lett.* *56(23)*, pp.2298, 1990.
- [24] M. Frenklach, K. E. Spear, "Growth Mechanism of Vapor-deposited Diamond." *J. Mater. Res.* *3(1)*, pp.133, 1987.

- [25] Y. Hirose, Y. Terasawa, *Jpn. J. Appl. Phys.*, *25*, pp.L519, 1986.
- [26] T. Kawato, K-I Kondo, "Effects of Oxygen on CVD Diamond Synthesis." *Jpn. J. Appl. Phys.*, *26(9)*, pp.1429, 1987.
- [27] S. J. Harris and M. Weiner, "Effects of Oxygen on Diamond Growth." *Appl. Phys. Lett.*, *55(21)*, pp.2179, 1989.
- [28] Y. Liou, R. Weimer, D. Knight, and R. Messier, "Effect of Oxygen in Diamond Deposition at Low Substrate Temperatures." *Appl. Phys. Lett.*, *56(5)*, pp.437, 1990.
- [29] Y. Matsui, H. Yabe, Y. Hirose, "The Growth of Diamond Crystals in Acetylene Flames." *Jpn. J. Appl. Phys.*, *29(8)*, pp.1552, 1990.
- [30] Y. Tzeng, C. Cutshaw, R. Phillips, T. Srivinyunon, "Growth of Diamond Films on Silicon From an Oxygen-acetylene Flame." *Appl. Phys. Lett.* *56(2)*, pp.134, 1990.
- [31] M. Frenklach, "The role of Hydrogen in Vapor Deposition of Diamond." *J. Appl. Phys.* *65(12)*, pp.5142, 1989.
- [32] J. A. Mucha, D.L. Flamm, D. E. Ibbotson, "On the Role of Oxygen and Hydrogen in Diamond-forming Discharge." *J. Appl. Phys.*, *65(9)*, pp.3448, 1990.
- [33] A. Sawaba and T. Inuzuka, "Growth of Diamond Thin Films by Electron Assisted Chemical Vapor Deposition." *Appl. Phys. Lett.*, *46(2)*, pp.146, 1985.
- [34] Y. Hirose and Y. Terasawa, "Synthesis of Diamond Films by Thermal CVD Using Organic Compounds." *Jpn. J. Appl. Phys.*, *25(6)*, pp.L159, 1986.
- [35] H. Aikyo and K. I. Kondo, "Diamond Synthesis Suppressing the Thermal Decomposition of Methane in a Hot-Filament CVD." *Jpn. J. Appl. Phys.*, *28(9)*, pp.L1631, 1989.
- [36] Y. H. Lee, P. D. Richard, K. J. Bachmann, J. T. Glass, "Bias-Controlled Chemical Vapor Deposition of Diamond Thin Films." *Appl. Phys. Lett.*, *56(7)*, pp.620, 1990.
- [37] M. Ihara, H. Maeno, K. Miyamoto, and H. Komiyama, "Diamond Deposition on Silicon Surface Heated to Temperature as low as 135 °C." *Appl. Phys. Lett.*, *59(12)*, pp.1473, 1991.

- [38] K. Suzuki, A. Sawabe, H. Yasuda, T. Inuzuka, "Growth of Diamond Thin Films by Dc Plasma Chemical Vapor Deposition." *Appl. Phys. Lett.*, *50(12)*, pp.728, 1987.
- [39] S. Koizumi, T. Murakami, T. Inuzuka, "Epitaxial Growth of Diamond Thin Films on Cubic Boron Nitride (111) Surfaces by DC Plasma Chemical Vapor Deposition." *Appl. Phys. Lett.*, *57(6)*, pp.563, 1990.
- [40] S. Nakao, M. Noda, H. Kusakabe, H. Shimizu, "Deposition of Diamond onto an Aluminum Substrate by DC Plasma CVD." *Jpn. J. Appl. Phys.*, *29(8)*, pp.1511, 1990.
- [41] K. Kurihara, K. Sasaki, M. Kawarada, N. Koshino, "High Rate Synthesis of Diamond by DC Plasma Jet Chemical Vapor Deposition." *Appl. Phys. Lett.*, *52(6)*, pp.437, 1988.
- [42] F. Akatsuka, Y. Hirose, K. Komaki, "Rapid Growth of Diamond Films by Arc Discharge Plasma CVD." *Jpn. J. Appl. Phys.*, *27(9)*, pp. L1600, 1988.
- [43] S. Matsumoto, I. Hosoya, T. Chounan, "Substrate Bias Effect on Diamond Deposition by DC Plasma Jet." *Jpn. J. Appl. Lett.*, *29(10)*, pp.2082, 1990.
- [44] S. Matsumoto, M. Hino, T. Kobayashi, "Synthesis of Diamond Films in a rf induction Thermal Plasma." *Appl. Phys. Lett.*, *51(10)*, pp.737, 1987.
- [45] D. E. Meyer, R. O. Dillon, J. A. Woollam, "Radio-frequency Plasma Chemical Vapor Deposition Growth of Diamond." *J. Vac. Sci. Technol., A* *7(3)*, pp.2325, 1989.
- [46] M. Kamo, Y. Sato, S. Matsumoto, N. Setaka, "Diamond synthesis from Gas Phase in Microwave Plasma." *J. Crys. Growth*, *62*, pp.642, 1983.
- [47] C. P. Chang, D. L. Flamm, D. E. Ibbotson, J. A. Mucha, "Diamond Crystal Growth by Plasma Chemical Vapor Deposition." *J. Appl. Phys.*, *63(5)*, pp.1744, 1988.
- [48] I. Watanabe and K. Sugata, "Diamond Films Synthesized by Microwave Plasma CVD of Ethyl Alcohol,etc." *Jpn. J. Appl. Phys.*, *27(8)*, pp.1397, 1988.
- [49] J. S. Ma, H. Kawarada, T. Yonehara, J. I. Suzuki, J. Wei, "Selective Nucleation and Growth of Diamond Particles by Plasma-assisted Chemical Vapor Deposition." *Appl. Phys. Lett.*, *55(11)*, pp.1071, 1989.

- [50] H. Shiomi, K. Tanabe, Y. Nishibayashi, N. Fujimori, "Epitaxial Growth of High Quality Diamond Film by the Microwave Plasma-assisted Chemical Vapor Deposition." *Jpn. J. Appl. Phys.*, *29(1)*, pp.34, 1990.
- [51] D. G. Jeng, H. S. Tuan, R. F. Salat, G. J. Fricano, "Oriented Cubic Nucleations and Local Epitaxial During Diamond Growth on Silicon (100) Substrates." *Appl. Phys. Lett.*, *56(20)*, pp.1968, 1990.
- [52] Y. Mitsu, T. Yoshida, K. Akashi, "Development of a New Microwave Plasma Torch and Its Application to Diamond Synthesis." *Rev. Sci. Instrum.*, *60(2)*, pp.249, 1989.
- [53] J.-I. Suzuki, H. Kawarada, K. S. Mar, J. Wei, Y. Yokota, A. Hiraki, "The Synthesis of Diamond Films at Lower Pressure and at Lower Temperature Using Magneto-Microwave Plasma CVD." *Jpn. J. Appl. Phys.*, *28(2)*, pp.L281, 1989.
- [54] J. Wei, H. Kawarada, J.I. Suzuki, A. Hiraki, "Low Temperature Synthesis of Diamond Films Using Magneto-Microwave Plasma CVD." *Jpn. J. Appl. Phys.*, *29(8)*, pp.L1483, 1990.
- [55] W.L. Hsu, D. M. Tung, E. A. Fuchs, K. F. McCarty, "Low-Temperature Diamond Growth in a Microwave Discharge." *Appl. Phys. Lett.*, *55(26)*, pp.2739, 1989.
- [56] Y. Liou, A. Inspektor, R. Weimer, R. Messier, "Low-temperature Diamond Deposition by Microwave Plasma-enhanced CVD." *Appl. Phys. Lett.*, *55(7)*, pp.631, 1989.
- [57] D. J. Pickrell, W. Zhu, A. R. Badzian, R. Messier, "Downstream Plasma-enhanced Diamond Film Deposition." *Appl. Phys. Lett.*, *56(20)*, pp.2010, 1990.
- [58] D. E. Patterson, B. J. Bai, C. J. Chu, R. H. Hauge, and J.L. Margrave, "Halogen Assisted CVD of Diamond", pp.14, Abstract of 2nd international conference on the New Diamond Science and Technology, Washington,DC, Sep.23-27, 1990.
- [59] C. Weissmantel, *Thin Solid Films*, *35*, pp.255, 1976.
- [60] T. Mori and Y. Namba, "Hard diamondlike carbon films deposited by ionized deposition of Methane Gas." *J. Vac. Sci. Technol. A* *1(1)*, pp.23, 1983.
- [61] T. Mori and Y. Namba, "Crystal Structure of Diamondlike Carbon Films Prepared by Ionized Deposition from Methane Gas." *J. Appl. Phys.* *55(9)*, pp.3276, 1984.

- [62] M. Kitabatake and K. Wasa, "Growth of Diamond at Room Temperature by A Ion-beam Sputtering Deposition." *J. Appl. Phys.*, *58(4)*, pp.1693, 1985.
- [63] J. W. Rabalais and S. Kasi, "Growth of Thin Chemically Bonded Diamondlike Films by Ion Beam Deposition." *Science*, *239*, pp.623, 1988.
- [64] J. C. Angus and C. C. Hayman, "Low-Pressure, Metastable Growth of Diamond and Diamondlike Phases." *Science*, *241*, pp.913, 1988.
- [65] personal discussion with Dr. Richard Guarnier, senior engineer in IBM Watson research center.
- [66] A. Masood, M. Aslam, M. A. Tamor, and T. J. Potter, "Techniques for Patterning of CVD Diamond Films on Non-Diamond Substrates." *J. Electrochem. Soc.*, *138(11)*, pp.L67, 1991.
- [67] S. Iijima, Y. Aikawa, and K. Baba, "Growth of Diamond Particles in Chemical Vapor Deposition." *J. Mater. Res.*, *6(7)*, pp.1491, 1991.
- [68] L. C. Conner, "CVD Diamond : Beyond the Laboratory." , Gorham Advanced Material Institute at The Global Business and Technical Outlook for High Performance Inorganic Thin Film Coatings, 1988.
- [69] W. A. Yarbrough, "Diamond and Diamond-Like Coatings by CVD." , Gorham Advanced Material Institute at The Global Business and Technical Outlook for High Performance Inorganic Thin Film Coatings, 1988.
- [70] R. Orr, "The Impact of Thin Film Diamond on Advanced Engineering Systems." , Gorham Advanced Material Institute at The Global Business and Technical Outlook for High Performance Inorganic Thin Film Coatings, 1988.
- [71] K. Shenai, R. S. Scott and B. J. Baliga, "Optimum Semiconductors for High-Power Electronics." *IEEE transaction on electron devices*, *36(9)*, pp.1811, 1989.
- [72] J. F. Prins, "Bipolar transistor action in ion implanted diamond." *Appl. Phys. Lett.*, *41(10)*, pp.950, 1982.
- [73] M. W. Geis, D. D. Rathman, D. J. Ehrlich, R. A. Murphy, and W. T. Lindley, "High-Temperature Point-Contact Transistor and Schottky Diodes Formed on Synthetic Boron-Doped Diamond." *IEEE Electron Device letters*, *8(8)*, pp.341, 1987.

- [74] N. Fujimori, T. Imai, and A. Doi, "Characterization of Conducting Diamond Films." *Vacuum*, *36*, pp.99, 1986.
- [75] J. Mort, D. Kuhman, M. Machonkin, M. Morgan, F. Jansen, and K. Okumura, "Boron Doping of Diamond Thin Films." *Appl. Phys. Lett.*, *55(11)*, pp.1121, 1989.
- [76] H. Shiomi, H. Nakahata, T. Imai, Y. Nishibayashi, and N. Fujimori, "Electrical Characteristics of Metal Contacts to Boron-Doped Diamond Epitaxial Film." *Jpn. J. Appl. Phys.*, *28(5)*, pp.758, 1989.
- [77] N. Fujimori, H. Nakahata, T. Imai, "Properties of Boron-Doped Epitaxial Diamond Films." *Jpn. J. Appl. Phys.*, *28(5)*, pp.824, 1990.
- [78] K. Okana, H. Naruki, Y. Akiba, T. Kurosu, M. Iida, and Y. Hirose, "Synthesis of Diamond Thin Films Having Semiconductive Properties." *Jpn. J. Appl. Phys.*, *27*, pp.L173, 1988.
- [79] S. A. Grot, G. SH. Gildenblat, C. W. Hatfield, C. R. Wronski, A. R. Badzian, T. Badzian and R. Messier, "The Effect of Surface Treatment on the Electrical Properties of Metal Contacts to Boron-Doped Homoepitaxial Diamond Film.", *IEEE Electron Device Letters*, *11(2)*, pp.100, 1990.
- [80] D. G. Jeng, H. S. Tuan, R. F. Salat, and G. J. Fricano, "Thin-Film Al/Diamond Schottky Diode over 400V Breakdown Voltage." *J. Appl. Phys.*, *68(11)*, pp.5902, 1990.
- [81] H. Shiomi, Y. Nishibayashi, and N. Fujimori, "Field-Effect Transistor Using Boron-Doped Diamond Epitaxial Films." *Jpn. J. Appl. Phys.*, *28(12)*, pp.L2153, 1989.
- [82] K. Okana, H. Kiyota, T. Iwasaki, T. Kurosu, and M. Iida, "P-N Junction Diode Made of Semiconducting Diamond Films." *Appl. Phys. Lett.*, *58(8)*, pp.840, 1991.
- [83] G. Sh. Gildenblat, S. A. Grot, C. W. Hatfield, and A. R. Badzian, "High-Temperature Thin-Film Diamond Field effect Transistor Fabricated Using a Selective Growth Method." *IEEE Electron Device Letters*, *12(2)*, pp.37, 1991.
- [84] W. Tsai, M. Delfino, D. Hodul, M. Riazat, L. Y. Ching, G. Reynold, and C. B. Cooper, "Diamond MESFET Using Ultrashallow RTP Boron Doping." *IEEE Electron Device Letters*, *12(4)*, pp.157, 1991.

- [85] M. W. Geis, J. A. Gregory, and B. B. Pate, "C-V Measurements on Metal-SiO<sub>2</sub>-Diamond Structures Fabricated with (100) and (111) Oriented Substrates." IEEE Transaction on Electron Devices. *38(3)*, pp.619, 1991.
- [86] T. Inoue, H. Tachibana, K. Kumagai, K. Miyata, K. Nishimura, "Selected-Area Deposition of Diamond films." J. Appl. Phys., *67(12)*, pp.7329, 1990.
- [87] R. Ramesham, T. Roppel, C. Ellis, D. A. Jaworske, W. Bough, "Selective and Low Temperature Synthesis of Polycrystalline Diamond." J. Mater. Res., *6(6)*, pp.1278, 1991.
- [88] K. Okumura, J. Mort, and M. Machonkin, "Lithium Doping and Photoemission of Diamond Thin Films." Appl. Phys. Lett., *57(18)*, pp.1907, 1990.
- [89] M. W. Geis, H. I. Smith, A. Argoitia, J. Angus, G.-H. M. Ma, J. T. Glass, J. Butler, C. J. Robinson, R. Pryor, "Larg-area Mosaic Diamond Films Approaching Single-Crystal Quality." Appl. Phys. Lett., *58(22)*, pp.2485, 1991.
- [90] J. Asmussen, H.H. Lin, B. Manring, and R. Fritz, Rev. of Sci. Inst., *58*, pp.1497, 1987.
- [91] W. Kern and D. A. Puotinen, RCA Rev., *31*, pp.187, 1970.
- [92] R.F. Harrington, "Time Harmonic Electromagnetic Fields." pp. 216, McGraw-Hill, New York, 1961.
- [93] L. Mahoney, M. Dahimene, and J. Asmussen, Rev. Sci. Instrum. *59*, pp.448, 1988.
- [94] S. Whitehair, J. Asmussen, and S. Nakanishi, J. of Propul. Power, *3*, pp.136, 1987.
- [95] J. Engemann and H. Keller, D. K. Reinhard, B. Huang, and J. Asmussen, "Dual-side Contact Formation on Isolated Diamond Films." Appl. Phys. Lett. *57(23)*, pp.2461, 1990.
- [96] *Torr-Seal<sup>TM</sup>* is manufactured by Varian Industrial Components Division, 3100 Jay Street, Santa Clara, CA 95054.
- [97] *Epo-Tek<sup>TM</sup>* is manufactured by Epoxy Technology Inc., Billerica, MA 01821.
- [98] M. Balkanski, editor, "Light Scattering in Solids." pp.65, Flammarion Sciences, Paris, 1971.

- [99] S. A. Solin and A. K. Ramdas, "Raman Spectrum of Diamond." *Physical Review B*, *1(4)*, pp.1687, 1970.
- [100] M. Yoshikawa, G. Katagiri, H. Ishida, and A. Ishitani, "Characterization of Crystalline Quality of Diamond Films by Raman Spectroscopy." *Appl. Phys. Lett.* *55(25)*, pp.2608, 1989.
- [101] M. Yoshikawa, G. Katagiri, H. Ishida, and A. Ishitani, "Raman Spectra of Diamondlike Amorphous Carbon Films." *J. Appl. Phys.* *64(11)*, pp. 6464, 1988.
- [102] R. G. Buckley, T. D. Moustakas, Ling Ye, and J. Varon, "Characterization of Filament-assisted Chemical Vapor Deposition Diamond Films Using Raman Spectroscopy." *J. Appl. Phys.* *66(8)*, pp.3595, 1989.
- [103] Diane. K. Knight and William B. White, "Characterization of Diamond Films by Raman Spectroscopy." *J. Mater. Res.*, *4(2)*, pp.385, 1989.
- [104] The diagram of the set-up of the Raman spectroscopy is a courtesy from Dr. Kevin Gray in Norton company.
- [105] P. E. Sobol, "A comparison of Techniques for Compositional and Chemical Analysis of Surface." technical reprint by Perkin Elmer, Physical Electronics Division.
- [106] J. Ruan, W. J. Choyke, and W. D. Partlow, "Si Impurity in Chemical Vapor Deposited Diamond Films." *Appl. Phys. Lett.*, *58(3)*, pp.295, 1991.
- [107] Y. Mizokawa, T. Miyasato, S. Nakamura, K. M. Geib and C. W. Wilmsen, *J. Vac. Sci. Technol., A* *5(5)*, pp.2809, 1987.
- [108] B.E. Williams and J.T. Glass, "Characterization of Diamond Films: Diamond Phase Identification, Surface Morphology, and Defect Structures." *J. Mater, Res.*, *4(2)*, pp.373, 1989.
- [109] D.N. Belton, S.J. Harris, S.J. Schmieg, A.M. Weiner, and T.A. Perry, "In *situ* Characterization of Diamond Nucleation and Growth." *Appl. Phys. Lett.*, *54(5)*, pp.416, 1989.
- [110] R. Meilunas, M.S. Wong, K.C. Sheng and R.P.H. Chang, "Early stages of plasma synthesis of diamond films." *Appl. Phys. Lett.*, *54(22)*, pp.2204, 1989.

- [111] T. Hartnett, R. Miller, D. Montanari, C. Willingham, and R. Tustison, "Intermediate Layers for the Deposition of Polycrystalline Diamond Films." *J. Vac. Sci. Technol., A* 8(9), pp.2129, 1990.
- [112] D.-W. Kweon and J.-Y. Lee, "The Interface Morphology of Diamond Film Grown on Si." *J. Appl. Phys.* 68(8), pp.4272, 1990.
- [113] D.J. Pickrell, W. Zhu, A.R. Badzian, R.E. Newnham, and R. Messier, "Near-interface Characterization of Diamond Films on Silica and Silicon." *J. Mater. Res.*, 6(6), pp.1264, 1991.
- [114] B. L. Gabriel, "SEM: A User's Manual for Material Science." pp.1-5, published by American Society for Metals, Metal park, Ohio 44073.
- [115] J.F. Denatale, J.F. Flintoff, and A.B. Harker, "Microstructural Control of Diamond Thin Films by Microlithographic Patterning." *J. Appl. Phys.*, 68(8), pp.4014, 1990.
- [116] P. Baurschmidt, CLSM for biomedical research, Carl Zeiss, Inc., 1988.
- [117] F. M. Smits, "Measurement of Sheet Resistivities with the Four Point Probe." *Bell System Technical Journal* (May 1958), pp.711.
- [118] S. M. Sze, "Physics of Semiconductor Physics." 2nd edition, Chapter 1, John Wiley & Son, New York, 1981.
- [119] K. Okano, H. Naruki, Y. Akiba, T. Kurosu, M. Iida, Y. Hirose, and T. Nakamura, "Characterization of Boron-Doped Diamond Film." *Jpn. J. Appl. Phys.*, 28(6), pp.1066, 1989.
- [120] J. E. Field, "Properties of Diamond", Academic Press, London, Chap. 3, pp.79, 1979.
- [121] J. P. Mckelvey, "Solid State and Semiconductor Physics." , Robert E. Krieger publishing company, Malabar, Florida, 1971.
- [122] M. I. Landstrass and K. V. Ravi, "Hydrogen Passivation of Electrically Active Defects in Diamond." *Appl. Phys. Lett.*, 55(14), pp.1391, 1989.
- [123] M. I. Landstrass and K. V. Ravi, " Resistivity of Chemical Vapor Deposited Diamond Films." *Appl. Phys. Lett.*, 55(10), pp.975, 1989.

- [124] S. Albin and L. Walkins, "Electrical Properties of Hydrogenated Diamond." *Appl. Phys. Lett.*, *56(15)*, pp.1454, 1990.
- [125] E. H. Rhoderick, "Metal-Semiconductor Contacts." Clarendon Press, Oxford, pp.54, 1980.
- [126] Y. Tzeng, C. C. Tin, R. Phillips, T. Srivinyunon, and Y. Chen, "High Electrical Resistivity Diamond Films Deposited from an Oxyacetylene Flame." *Appl. Phys. Lett.*, *57(8)*, pp.789, 1990.
- [127] A. T. Collins, E. C. Lightowers, and W. S. Williams, *Diamond Res. (Suppl. Ind. Diamond Rev.)*, pp.19, 1970.
- [128] H. H. Poole, *Lond. Edinb. Dubl. Phil. Mag.*, *33*, pp.112, 1916.
- [129] J. Frenkel, *Phys. Rev.*, *54*, pp.647, 1938.
- [130] R. M. Hill, *Phil. Mag.*, *23*, pp.59, 1971.
- [131] A. V. Bogdanov, I. M. Vikulin, and T. V. Bogdanova, *Sov. Phys. Semicond.*, *16*, pp.720, 1982.
- [132] A. T. Collins, M. Kamo and Y. Sato, "A Spectroscopic Study of Optical Centers in Diamond Grown by Microwave-Assisted Chemical Vapor Deposition." *J. Mater. Res.*, *5(11)*, pp.2507, 1990.
- [133] G. Sh. Gildenblat, S. A. Grot, C. R. Wronski, A. R. Badzian, T. Badzian, and R. Messier, *Appl. Phys. Lett.*, *53*, pp. 586, 1988.
- [134] C. L. Ellison, R. M. Cohen, and J. T. Hoggins, *Materials Research Society Conference Record*, Boston, MA, pp.213, 1989.
- [135] G. H. Glover, *Solid State Electronics*, *16*, pp.973, 1973.
- [136] M. C. Hicks, C. R. Wronski, S. A. Grot, and G. Sh. Gildenblat, "The Barrier Height of Schottky Diodes with a Chemical Vapor Deposition Diamond Base." *J. Appl. Phys.*, *65(5)*, pp.2139, 1989.
- [137] S. A. Grot, S. Lee, G. Sh. Gildenblat, C. W. Harfield, C. R. Wronski, A. R. Badzian, T. Badzian and R. Messier, "Rectification and Internal Photoemission in Metal/CVD Diamond and Metal/CVD Diamond/Silicon Structures." *J. Mater. Res.*, *5(11)*, pp.2497, 1990.

- [138] M. A. Lampert and P. Mark, "Current Injection in Solids." Academic Press, Inc., New York, pp.14-30, 1970.
- [139] J. Zhang, "Diamond Film Deposition By Microwave Plasma Assisted Chemical Vapor Deposition" Ph.D dissertation, Michigan State University, (in progress).